Study of the Hoyle State in ^{12}C

using the Lund-York-Cologne-Calorimeter (LYCCA) array

Inaugural-Dissertation

zur

Erlangung des Doktorgrades

der Mathematisch-Naturwissenschaftlichen Fakultät

der Universität zu Köln

vorgelegt von

David Werner

aus Solingen

September 2024

Berichterstatter: Prof. Dr. Peter Reiter
Prof. Dr. Dennis Mücher

The current state of knowledge can be summarized thus:
In the beginning, there was nothing, which exploded.

— Sir Terry Pratchett, *Lords and Ladies*

Abstract

This thesis presents an analysis of the particle-decay behavior of excited ^{12}C states using the LYCCA detector setup. The setup was upgraded to 24 mounted DSSSDs and 18 AIDA FEE data acquisition modules, allowing for the detection of over 3×10^{10} scattered ions across two experiments performed in December 2019 and January 2020. Among these, more than 6×10^6 particle-decay events, consisting of 4 alpha particles each, of the Hoyle state decay were identified and analyzed, representing the largest dataset for Hoyle state decay studies to date.

The thesis details a series of methodological improvements, including the development of a new event-analysis pipeline, time-walk correction, and refined analysis logic, which collectively improved the precision and efficiency of data processing. Additionally, new gate conditions and detector position offset corrections were implemented to enhance data selection and spatial resolution. The calibration and analysis tools developed during this work also contributed to reducing the time required from data acquisition to center-of-mass frame analysis of the detected particles.

These developments have improved the capabilities of the LYCCA setup, providing a solid foundation for future studies of excited nuclear states and their decay pathways.

While the energy resolution in the center-of-mass frame of the particle decay of the excited Carbon nuclei did not allow for establishing a new upper limit, the measured branching ratios are consistent with previous studies, providing additional data points for investigating the structure of higher-lying states in ^{12}C. Additionally, ongoing improvements in the data analysis pipeline have shown promising results for future studies, even on the current dataset.

Zusammenfassung

In dieser Arbeit wird das Teilchenzerfallsverhalten angeregter ^{12}C-Zustände unter Verwendung des LYCCA-Detektoraufbaus analysiert. Der Aufbau wurde auf 24 DSSSDs und 18 AIDA FEE-Datenaufnahmemodule erweiter, was es ermöglichte, über zwei Experimente, die im Dezember 2019 und Januar 2020 durchgeführt wurden, mehr als 3×10^{10} gestreute Ionen zu detektieren. Darunter wurden mehr als 6×10^6 Zerfallsereignisse des Hoyle-Zustands, jeweils bestehend aus 4 Alphateilchen, identifiziert und analysiert, was den bisher größten Datensatz für Zerfallsstudien der Hoyle-Anregung darstellt.
In dieser Arbeit wird eine Reihe von methodischen Verbesserungen beschrieben, darunter die Entwicklung einer neuen Analysearchitektur zur Verarbeitung gemessener Ereignisse, Korrekturen für energieabhängige Verschiebungen der Detektionszeiten und eine verfeinerte Analyselogik, die insgesamt die Präzision und Effizienz der Datenverarbeitung verbessert haben. Außerdem wurden neue Filterbedingungen und Korrekturen für die Detektorposition eingeführt, um die Auswahl der Ereignisse und die räumliche Auflösung zu verbessern. Die im Rahmen dieser Arbeit entwickelten Kalibrierungs- und Analysewerkzeuge trugen ebenfalls dazu bei, die Zeit von der Datenerfassung bis zur Analyse der detektierten Teilchen im Schwerpunktsystem deutlich zu verkürzen.
Diese Entwicklungen haben die Möglichkeiten des LYCCA-Aufbaus erweitert und stellen eine gute Grundlage für künftige Untersuchungen angeregter Kernzustände und ihrer Zerfallswege dar.
Limitiert durch die Energieauflösung der gemessenen Alphateilchen im Schwerpunktsystem der zerfallenden angeregten Kohlenstoff-Kerne konnten keine neuen Obergrenzen für die Verzweigungsverhältnis der direkten Teilchenzerfallskanäle bestimmt werden. Jedoch stimmen die gemessenen Verzweigungsverhältnisse mit früheren Messungen überein und liefern zusätzliche Datenpunkte für die Untersuchung der Struktur höherliegender Zustände in ^{12}C. Darüber hinaus haben die laufenden Verbesserungen in der Datenanalyse vielversprechende Ergebnisse für künftige Messungen gezeigt und auch der aktuelle Datensatz ist durch neue Verbesserungen noch nicht vollständig ausgereizt.

Contents

Chapter 1

Stellar Nucleosynthesis and the Hoyle State

Since the dawn of time, humans have been fascinated by the inner workings of our Universe. Their desire to unravel the mysteries of the cosmos has led to scientific advancements that have shaped our understanding of the world around us. One of the most profound questions is what our everyday world is made of and how its constituents came to be. This question about the origin of elements has been a central theme in the field of nuclear astrophysics and even has philosophical implications considering that with just minor changes in production processes of the building blocks of our everyday world, life itself might not have been possible.

1.1 The Origin of Elements

Initially, after the Big Bang, the Universe was mostly composed of hydrogen, as well as about 25 % helium by mass, and trace amounts of lithium. Almost all other elements were created in the cores of stars during their burning and in supernova explosions [1].

The mechanisms behind this elemental synthesis were first thoroughly described in the famous "alphabet" paper by Alpher, Bethe, and Gamow, commonly referred to by the initials of its authors and published in 1948 [2]. This pioneering work explored the implications of nucleosynthesis in the early universe but lacked knowledge of the different production mechanisms of heavier elements.

This work was substantially expanded upon in one of the most foundational papers in the field of nuclear astrophysics, the B^2FH paper, published in 1957 [3]. Named after its famous authors, Margaret Burbidge, Geoffrey Burbidge, William Fowler, and Fred Hoyle, it describes the nucleosynthetic pathways, reaching from hydrogen burning and helium burning to the s-, r-, and p-processes, and how these contribute to the observed abundance patterns in the universe (Figure 1.1). A more recent refinement of these theories on the origin of elements is presented in the periodic table of elements in Figure 1.2, in which

the production process for each element is shown as a colored graph over time. The plot highlights that the production of heavier elements from primordial nuclei is a multi-step process, which started with the first light of the first stars and is ongoing ever since.
Elements up to the iron-peak (around mass number 56-62) can be produced through fusion and capture-reactions within stars during their burning cycles or later during core-collapse supernovae [4], which are the final stage of a massive star's life [5]. Thus, the study of stellar nucleosynthesis processes is of great importance to understand the origin of the elements. Of these, carbon is of particular interest, as it is not only the fourth most abundant element in the Universe and an important intermediary in the production of heavier elements [6], but also an essential building block of life as we know it. To

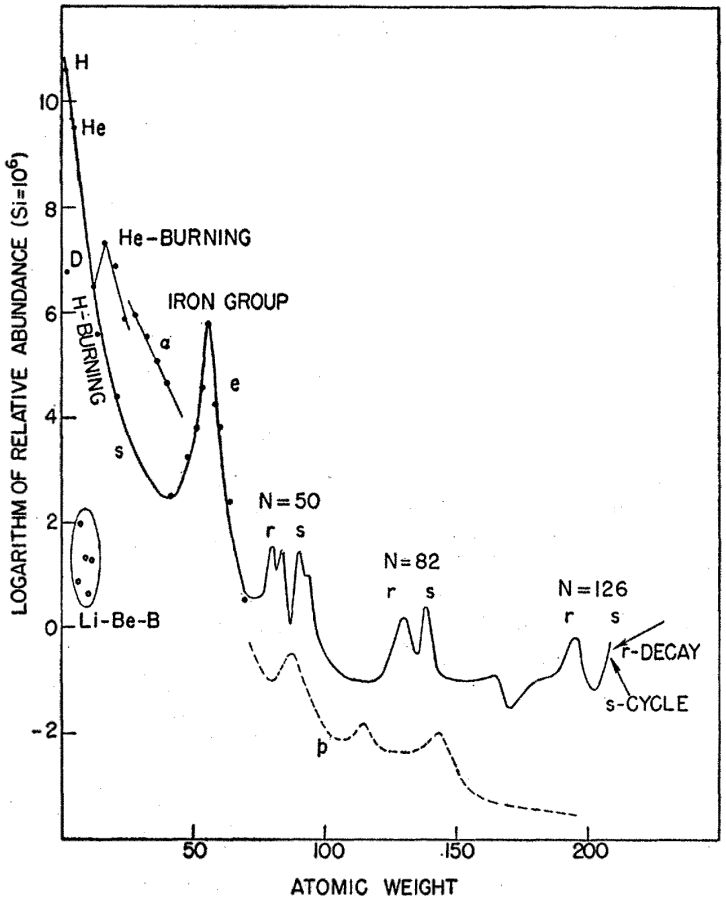

Figure 1.1: Abundances of the elements as a function of atomic number. The presented data is based on galactic and solar abundance data. The figure is taken from the paper by Burbidge, Burbidge, Fowler, and Hoyle [3].

understand the production of carbon and the elements leading up to it, it is essential to consider the evolution of and nucleosynthesis within stars. Most stars in the Milky Way Galaxy are main sequence stars, a category defined by their prolonged stable phase of hydrogen fusion in their cores which forms ^{4}He. These *alpha particles*, the nuclei of ^{4}He, are particularly stable due to their doubly magic nature, corresponding to a high binding energy per nucleon which can even affect the nuclear structure of heavier elements. This

also contributes to the high abundance of helium in the Universe [7].
After the long period of hydrogen burning, the relative abundance of hydrogen in a star's core depletes too far to sustain nuclear fusion rates sufficient to counteract the gravitational force compressing the star. This imbalance causes the core to contract and its temperature and pressure increase. During this phase, as density spikes and the temperature increases to around 100 million Kelvin, conditions become favorable for the fusion of helium nuclei into heavier elements and the star's next burning phase begins. For lighter stars below $2M_{\odot}$ (solar masses), this coincides with a brief runaway phase, where the still collapsing helium core fuels the core burning, while the radiation pressure cannot counteract the inertia of the outer layers, which is known as the *helium flash* [4]. After this, the core settles into a stable helium burning phase [8]. During this phase, which lasts for less than 10 % of the star's lifetime, temperatures of the core are now sufficient for positively charged helium nuclei to reach kinetic energies high enough to overcome the Coulomb barrier between them to form heavier elements [9, 10]. To reach ^{12}C from ^{4}He, two distinct reaction paths are possible: Either a step-by-step build-up, forming ^{8}Be as an intermediary, or the direct fusion of three ^{4}He nuclei into ^{12}C. There are, however, hindrances to both of these processes, challenging the explanation of the high mass-fraction of carbon in the Universe: The direct ^{4}He + ^{4}He + ^{4}He fusion of helium nuclei into carbon is highly unlikely due to the low probability of three helium nuclei coming together at the same time with sufficient energy. A gradual process also faces difficulties, as the intermediate steps formed in ^{4}He + ^{4}He or ^{4}He + ^{1}H would result in products which are inside the mass A = 5 and A = 8 gaps. These refer to the fact that no stable isotopes exist for these mass numbers, with half-lives of the reaction products in the order of $3 \cdot 10^{-22}$ seconds for the unbound ^{5}Li which undergoes prompt decay into ^{4}He and a proton [11] and $9 \cdot 10^{-17}$ seconds for ^{8}Be [4]. This severely lowers the probability to use these as intermediate steps in the production of carbon and heavier elements. A relevant factor for the fusion reactions is that the high mass and density of stellar cores result in a low equilibrium population of ^{8}Be which can then capture another ^{4}He nucleus. This process is unlikely due to the higher Coulomb barrier for the ^{8}Be + ^{4}He interaction. This issue is often referred to as the "carbon problem" - the fact that despite its evident abundance the production of carbon in stars is not as straightforward as it might seem [7, 12].

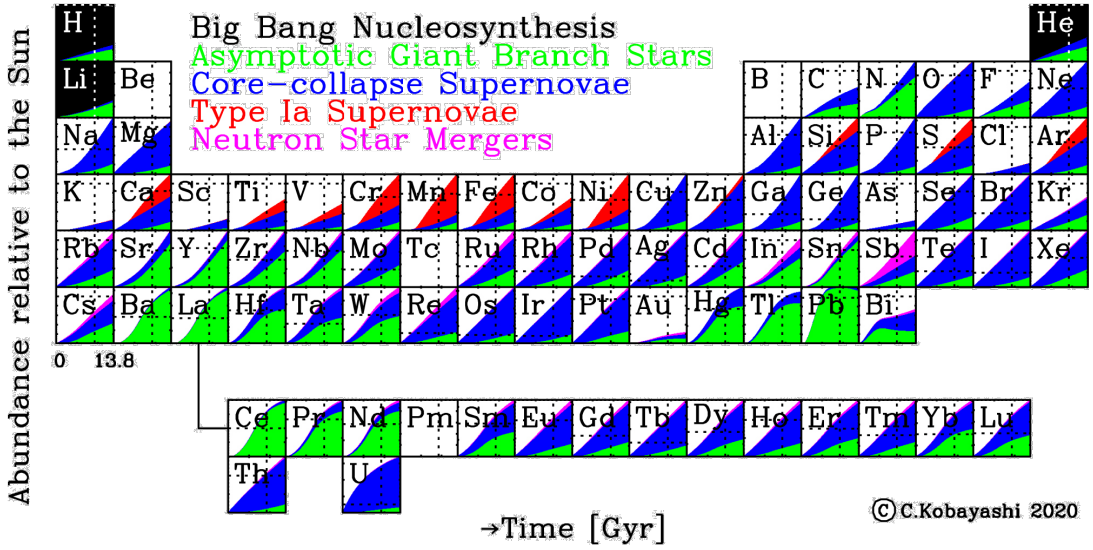

Figure 1.2: The origin of elements in the periodic table. Each element shows the production process as a colored graph, where the x-axes represent the time since the Big Bang and the y-axis represents the relative abundance. The three primordial elements hydrogen, helium, and lithium are initially completely filled black, as the majority of them is produced in the Big Bang nucleosynthesis. Due to stellar mass loss and ^{4}He synthesis, small amounts of hydrogen and helium are returned to the interstellar medium. All other elements are initially empty, as they are only produced subsequently. Reprinted from Ref. [13], Copyright (2020), with permission from IOP Publishing.

1.2 Stellar nucleosynthesis and reaction probabilities

Stellar nucleosynthesis, as briefly touched upon in the previous section, is the process by which elements are formed in the cores of stars through nuclear fusion reactions. The energy generated by these reactions is what powers the star and allows it to shine. The fusion of lighter elements into heavier ones up to the iron-peak elements (e.g., ^{56}Fe, ^{62}Ni, and ^{59}Co) is exothermic, meaning that it releases energy, which counteracts the gravitational force trying to collapse the star. This balance between gravity and outward pressure gradient determines the stability and evolution of the star. As they govern the energy generation and conditions for the nuclear processes, the temperature and density profiles within the star are significant factors in determining the reaction rates and the elements produced. In the following section, the overall dependence of the reaction rates on the temperature and density of the stellar core will be discussed.

1.2.1 Stellar equation of state and hydrostatic equilibrium

During their burning phase, on a macroscopic scale, stars are in a state of hydrostatic equilibrium. This equilibrium is maintained by a balance between the inward gravitational pull and the outward pressure forces inside the star. Stellar matter can be approx-

imated as an ideal gas, where the pressure is determined by the temperature, density, and composition of the gas, following the ideal gas law

$$P_{\text{gas}} = \frac{\rho k_{\text{B}} T}{\mu m_{\text{u}}}, \tag{1.1}$$

where P_{gas} is the gas pressure, ρ is the mass-density, k_{B} is Boltzmann's constant, T is the temperature, μ is the mean molecular weight, and m_{u} is the atomic mass unit.

In addition to the gas pressure, radiation pressure can contribute significantly in stellar interiors at high temperatures (e.g., in massive stars). The nuclear energy generated in the core is transported outward by a combination of radiative diffusion and convection, and the associated photon energy density gives rise to a radiation pressure P_{rad},

$$P_{\text{rad}} = \frac{1}{3} a T^4, \tag{1.2}$$

where a is the radiation constant ($a = \frac{4\sigma}{c}$, with σ being the Stefan-Boltzmann constant and c the speed of light).

The total pressure within a star can then be written as the sum of the gas and radiation contributions

$$P = \frac{\rho k_{\text{B}} T}{\mu m_{\text{u}}} + \frac{1}{3} a T^4, \tag{1.3}$$

which serves as a common approximation for the equation of state in the stellar interior [9].

In the context of hydrostatic equilibrium, the pressure gradient has to compensate the gravitational force per unit volume at every point within the star. This balance is described by the hydrostatic equilibrium equation

$$\frac{dP}{dr} = -\frac{GM(r)\rho}{r^2}, \tag{1.4}$$

where $\frac{dP}{dr}$ is the pressure gradient, G is the gravitational constant, $M(r)$ is the mass enclosed within radius r, and ρ is the density. Combining the stellar equation of state with the hydrostatic equilibrium condition, one gets:

$$\frac{d}{dr}\left(\frac{\rho k_{\text{B}} T}{\mu m_{\text{u}}} + \frac{1}{3} a T^4\right) = -\frac{GM(r)\rho}{r^2}, \tag{1.5}$$

which is one of the differential equations that describe the structure of a star during its burning phases. Due to its dependence on the temperature and density, the equation is tightly coupled to the nuclear reactions in the stellar core, which determine the energy generation rate and the temperature profile of the star. These, in turn, are dependent on the reaction rates, which are determined by the temperature and density of the stellar core. Large modern state-of-the-art stellar models attempt to simulate this strongly

coupled, nonlinear feedback dynamic, but for accurate modeling, a profound understanding of the underlying nuclear reaction conditions is foundational - especially the precise energy dependence of the reaction rates [14].

1.2.2 Nuclear reaction rates and the Gamow window

To further understand nuclear reaction rates in stars, it is essential to consider the probabilities of the reaction steps as well as the amount of available reactants at sufficient energy. This window of opportunity for nuclear reactions is known as the *Gamow window*. The Gamow window defines the range of energies at which nuclear reactions in stars are most likely to occur. It arises from the interaction between the Maxwell-Boltzmann distribution of particle energies and the quantum-mechanical tunneling probability through the Coulomb barrier [15–17].
The probability for a nuclear reaction to occur is quantified by its cross-section, defined as

$$\sigma = \frac{N_R}{N_T\, N_P}, \tag{1.6}$$

where N_R is the number of reactions (yield), N_T is the target areal density (number of target nuclei per unit area), and N_P is the number of incident projectiles. This definition assumes a thin target with full beam-target overlap; for a beam with particle rate $\Phi(t)$ and irradiation time t, $N_P = \int_0^t \Phi(t')\,\mathrm{d}t'$. The reaction cross-section as a function of energy, $\sigma(E)$, is commonly factorized (for non-resonant charged-particle reactions) as

$$\sigma(E) = \frac{S(E)}{E}\, e^{-2\pi\eta}, \tag{1.7}$$

using the Gamow factor $e^{-2\pi\eta}$, where η is the Sommerfeld parameter

$$\eta = \frac{Z_1 Z_2 e^2}{4\pi\epsilon_0\, \hbar v} = Z_1 Z_2\, \alpha\, \frac{c}{v} = Z_1 Z_2\, \alpha \sqrt{\frac{\mu c^2}{2E}}. \tag{1.8}$$

with v being the relative velocity of the interacting particles, Z_1 and Z_2 the atomic numbers of the reactants, and the astrophysical S-factor $S(E)$. This factor encapsulates the nuclear physics of the reaction by removing the exponential dependence on energy due to the Coulomb barrier, yielding a smoother and more manageable function for analysis. The cross-section, $\sigma(E)$, decreases exponentially with decreasing energy due to the Coulomb barrier's tunneling probability factor $e^{-2\pi\eta}$. This exponential dependence can obscure the underlying nuclear reaction mechanisms. By factoring out the Coulomb barrier effect, the S-factor $S(E)$ isolates the intrinsic nuclear reaction probabilities, which typically vary less dramatically with energy. This makes it easier to study and compare different nuclear reactions. Furthermore, it allows for more accurate extrapolations to the low-energy regime relevant in stellar environments, where direct measurements are

often challenging.

Despite factoring out the Coulomb barrier in the S-factor to simplify analysis, the overall reaction rate still depends on the probability of particles having sufficient energy to overcome this barrier. The Maxwell-Boltzmann energy probability density describes this probability:

$$P(E) = \frac{2}{\sqrt{\pi}} \frac{E^{1/2}}{(k_{\mathrm{B}}T)^{3/2}} e^{-E/k_{\mathrm{B}}T}. \tag{1.9}$$

Additionally, the particles must overcome the Coulomb barrier to react, which can be approximated by the tunneling probability

$$\mathcal{T}(E) = e^{-\sqrt{E_G/E}}. \tag{1.10}$$

Here, E_G is the characteristic Gamow energy (also sometimes written as b^2 in the literature) defined as

$$E_G = 2\mu c^2 (\pi \alpha Z_1 Z_2)^2, \tag{1.11}$$

with μ being the reduced mass of the interacting particles, and the fine-structure constant α. The Gamow window is defined by the product $P(E)\,\mathcal{T}(E)$ of the Maxwell-Boltzmann distribution and the tunneling probability [18]:

$$G(E) = \frac{2}{\sqrt{\pi}} \frac{E^{1/2}}{(k_{\mathrm{B}}T)^{3/2}} e^{-E/k_{\mathrm{B}}T} e^{-\sqrt{E_G/E}}. \tag{1.12}$$

The reaction rate can be computed by integrating over all possible energies while considering the reaction cross-section $\sigma(E)$:

$$\langle \sigma v \rangle = \left(\frac{8}{\pi \mu} \right)^{1/2} \frac{1}{(k_{\mathrm{B}}T)^{3/2}} \int_0^\infty S(E)\, e^{-E/k_{\mathrm{B}}T - \sqrt{E_G/E}}\, dE. \tag{1.13}$$

The width of the Gamow window, ΔE, can be estimated by

$$\Delta E = \left(\frac{16 E_0 k_{\mathrm{B}} T}{3} \right)^{1/2}, \tag{1.14}$$

where E_0 is the peak energy of the Gamow window. To find its value, the derivative of $G(E)$ with respect to E is set to zero:

$$\frac{d}{dE} \left(\frac{2}{\sqrt{\pi}} \frac{E^{1/2}}{(k_{\mathrm{B}}T)^{3/2}} e^{-E/k_{\mathrm{B}}T} e^{-\sqrt{E_G/E}} \right) = 0. \tag{1.15}$$

By solving this equation, the approximate peak energy of the Gamow window can be found to be

$$E_0 = \left(\frac{\sqrt{E_G} k_{\mathrm{B}} T}{2} \right)^{2/3}, \tag{1.16}$$

which places it at around 3 keV to 30 keV for typical stellar core temperatures during hydrogen burning and at 200 keV to 300 keV during early stages of helium burning [19]. Figure 1.3 illustrates the Maxwell-Boltzmann distribution, the tunneling probability, and the resulting Gamow window.

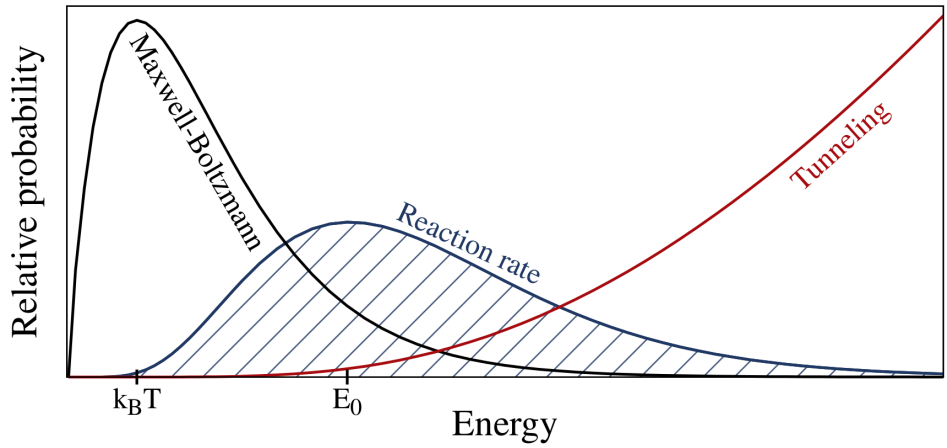

Figure 1.3: Illustration of the Gamow window, showing the Maxwell-Boltzmann distribution (black line), the tunneling probability (red line), and the resulting function showing where nuclear reactions are most likely to occur (shaded area). From [17].

1.2.3 Resonant reactions

Apart from the general approach to calculating reaction rates, resonant reactions play an essential role in stellar nucleosynthesis. Resonances are excited states of the compound nuclei formed during the fusion reactions. They are characterized by their angular momentum, parity, energy and mean lifetime. The mean lifetime is directly related to the width of the resonance by the Heisenberg uncertainty principle: $\Gamma\tau = \hbar$. Their existence can significantly enhance the reaction rates, which is described by the Breit-Wigner formula, which gives the cross-section of a resonance as a function of energy

$$\sigma(E) = \pi\lambda\!\!\!^{-2}\frac{2J+1}{(2s_p+1)(2s_T+1)}\frac{\Gamma_i\Gamma_f}{(E-E_R)^2+\Gamma^2/4}. \tag{1.17}$$

Here, $\lambda\!\!\!^{-}$ is the reduced de Broglie wavelength of the incident particle, J is the spin of the resonance, s_p and s_T are the spins of the projectile and target particles, E_R is the resonance energy, and Γ is the total width of the resonance. The total width of the resonance is the sum of the partial widths for all possible decay channels [4].
For a single, narrow resonance where the total width Γ is much smaller than the thermal

energy $k_{\mathrm{B}}T$, the reaction rate is then given by

$$\langle \sigma v \rangle_{\mathrm{res}} = \left(\frac{2\pi}{\mu\, k_{\mathrm{B}} T} \right)^{3/2} \hbar^2 \, (\omega\gamma) \, e^{-E_R/(k_{\mathrm{B}}T)}. \tag{1.18}$$

with the resonance strength $(\omega\gamma)$, given by

$$\omega\gamma = \frac{2J+1}{(2s_p+1)(2s_T+1)} \frac{\Gamma_i \Gamma_f}{\Gamma}. \tag{1.19}$$

The Breit-Wigner formula is a cornerstone in the study of nuclear reactions and is used to describe the behavior of resonances in a wide range of nuclear physics experiments [18]. Since it depends on the partial widths of the resonances' decay channels, the knowledge of these is necessary to accurately determine the reaction rate [20].

1.3 The Hoyle State

The predominant process for the production of carbon in stars is called the triple-alpha process. It is a two-step reaction during which three ^{4}He nuclei are converted into a ^{12}C nucleus. The first step,

$$^4\mathrm{He} + {}^4\mathrm{He} \rightleftharpoons {}^8\mathrm{Be}, \tag{1.20}$$

involves the fusion of two ^{4}He nuclei to form an unstable ^{8}Be nucleus. The second step then involves the fusion of a third ^{4}He nucleus with the ^{8}Be,

$$^8\mathrm{Be} + {}^4\mathrm{He} \rightleftharpoons {}^{12}\mathrm{C}, \tag{1.21}$$

to form a ^{12}C nucleus.

Given the short half-life of ^{8}Be, it usually decays back into two ^{4}He nuclei almost instantaneously. Its production, however, is enabled by the binding energy of the ^{8}Be nucleus, which is unbound by just 92 keV above its ^{4}He + ^{4}He separation threshold [21]. This energy is within available energy range for temperatures of red giant stars [22], which are the primary site for the triple-alpha process [23]. Still, despite the continuous production, its short half-life only allows a low population of ^{8}Be.

This problem was first discussed by E. J. Öpik in 1951 and E. E. Salpeter in 1952 [24, 25], who both independently concluded that the triple-alpha process should not be able to produce significant amounts of carbon in stars. Without anything increasing the capture probability, even in the dense stellar core environment, the concentration of helium nuclei is not high enough that a third ^{4}He will react with the ^{8}Be in time, inhibiting the formation of ^{12}C. This issue was first addressed by Sir Fred Hoyle in 1954, who proposed the existence of a resonance above the particle-separation energy of ^{12}C nucleus with a Q-

value inside the Gamow window for the helium-burning temperature in stars that would enhance the probability of the triple-alpha process [12]. In his honor, this resonance is now commonly referred to as the Hoyle state.

The Hoyle state is an excited state of the ^{12}C nucleus with an energy of 7.654 MeV above the ground state. Initially proposed to be either a $J^\pi = 0^+$ or a 2^+ state, since the capture probability for *s-wave* and *p-wave* is higher than for higher angular momenta, it was later determined to be a 0^+ state [26, 27]. The confirmation of this was achieved by studying the decay modes of the Hoyle state using detectors sensitive to γ-radiation. These measurements did not find any direct gamma-ray transitions to the ground state which were predicted if the Hoyle state was a 2^+ state. For a 0^+ configuration, the only direct photonic decay channel of the Hoyle state is the two-photon decay. Alternatively, a e^+e^- pair production process is available. These are both much less likely, as they are of higher order, as shown in recent measurements [28]. The existence of this resonance, right above the alpha separation energy of ^{12}C, increases the reaction rate significantly compared to non-resonant fusion processes, making it a pivotal factor in the synthesis of carbon. The existence of the Hoyle state explains how carbon can be produced efficiently in stellar environments [29]. Based on the fundamental properties of the Hoyle state, the existence of a rotational band of its configuration has been suggested, as its proposed high degree of deformation [30] would allow for relatively low excitation energies of the first excited states above it.

Additionally, form factor measurements have shown that the Hoyle state has a substantial spatial extension compared to the ground state of ^{12}C [31, 32], with a radius 1.5 to 2 times larger. This suggests a more dilute, gas-like configuration of the Hoyle state. The level scheme of ^{12}C is shown in Figure 1.4.

Further studies indicate that at low-temperatures (below 0.1 GK), the triple-alpha fusion rate is significantly enhanced by the inclusion of direct particle-decay channels. Nguyen *et al.* (2012) demonstrated using the Continuum Discretized Coupled Channel (CDCC) method, detailed in [33], that non-resonant contributions significantly increase the reaction rate at low temperatures compared to the NACRE compilation, a comprehensive collection of reaction rates for astrophysical processes [34, 35]. In 2013, Nguyen *et al.* refined this approach using the Hyperspherical Harmonics Expansion (HHR) method, identifying a transition between resonant and non-resonant processes around 0.06 GK. It was found that off-diagonal Coulomb couplings enhance the reaction rate by several orders of magnitude at low temperatures [36].

Additional work by Garrido *et al.* (2011) supported these findings through a detailed investigation using a three-body model that compares direct and sequential capture mechanisms. Their study revealed that at temperatures below 0.1 GK, direct capture dominates, leading to significantly higher reaction rates than those predicted by sequential models. At higher temperatures, the particle-decay of the Hoyle state in ^{12}C proceeds

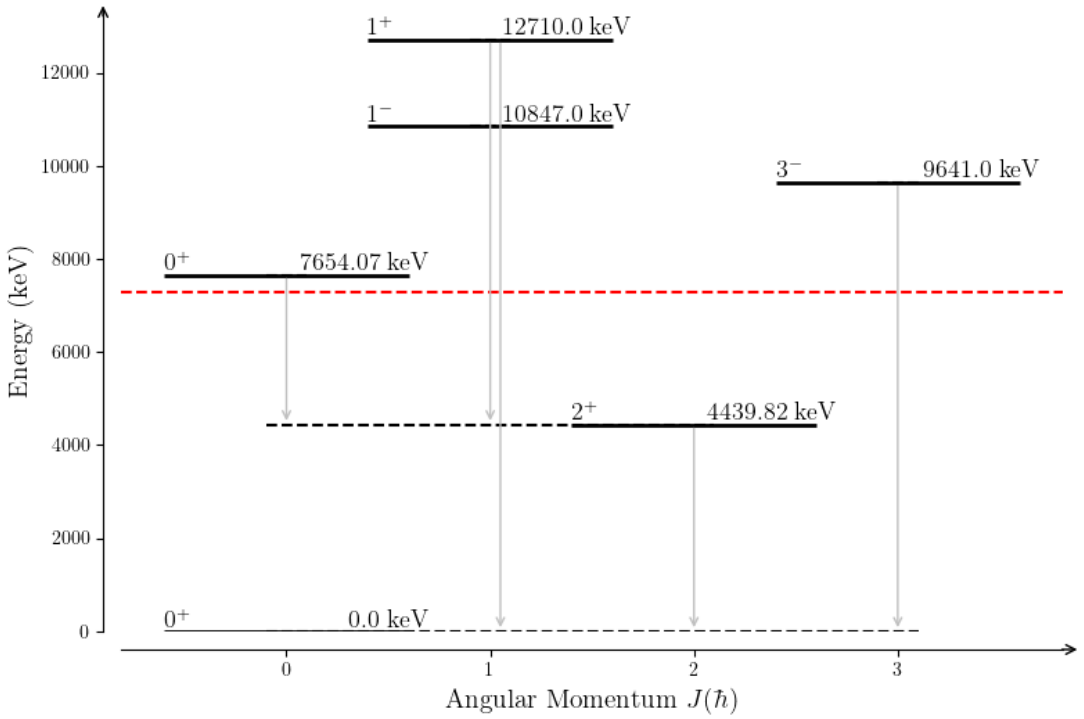

Figure 1.4: Level scheme of ^{12}C showing the ground state and known excited states below 13 MeV including the second 0^+ state, the Hoyle state at 7.654 MeV. The plot also shows the 3-alpha separation energy at 7.274 MeV in red.

almost fully sequentially. However, at lower temperatures, direct decay becomes more significant, substantially increasing the reaction rate [37].

The Hoyle state is not only interesting from a stellar nucleosynthesis perspective but also from a nuclear structure point of view, as it provides significant insights into nuclear clustering phenomena and internal nuclear configurations. In nuclear physics, *clustering* refers to the formation of substructures, such as alpha particles, within a nucleus. The structure of these clusters can be dependent on the excited state. The Hoyle state, in particular, is of interest due to its unique configuration and the possibility of different cluster configurations.

1.4 Modeling the Hoyle State in ^{12}C

To further the understanding of the internal structure and dynamics of ^{12}C, a variety of modeling approaches have been undertaken. Throughout the years many different modeling approaches for the structure of nuclei have been developed. One of the most important models is the nuclear shell model, developed by Maria Goeppert Mayer and J. Hans D. Jensen in 1949. It posits that nucleons occupy discrete energy levels within an effective potential, often modeled as a harmonic oscillator potential with a strong

spin-orbit coupling term. It predicts certain "magic numbers" of protons and neutrons in a nucleus that correspond to particularly stable nuclei, including the doubly-magic ^{4}He. Valence nucleons, outside closed shells, influence nuclear properties and participate in excitations by moving to higher orbitals. The shell model has been successful in describing the structure of many nuclei, but it has limitations when describing collective phenomena and clustering effects.

Underpinning the shell model is the mean-field approach, which simplifies the complex interactions among nucleons by approximating them with an average potential created by all nucleons. This allows for the calculation of nucleon behavior within this collective potential field formed by all nucleons. In ^{12}C, the mean-field approach successfully reproduces the binding energy of the ground state and the excitation energies of the 2^+ and 3^- states. The Hoyle state, however, could not be described accurately, incorrectly predicting its energy and decay properties, indicating that a pure mean-field (shell-model) approach is insufficient to describe the Hoyle state [38].

Given these limitations, alternative modeling approaches have been explored to account for phenomena that the shell model and mean-field approach struggle to describe [21, 39]. Cluster models, in particular, offer a promising solution. These describe nuclei as aggregates of tightly bound clusters of nucleons rather than individual particles, which is particularly effective for light nuclei. Its low-lying alpha decay channels and high lying first excited states indicate that the dynamics in ^{12}C are dominated by these clustering effects.

Complementary to these, other techniques, such as models describing alpha-particle condensation or the *ab initio* method, which uses first-principles calculations to predict nuclear properties without empirical data, have been used to describe carbon and, in particular, the Hoyle state. Some of the most prominent models are *lattice effective field theory* (EFT), *Quantum Monte Carlo* (QMC), and the *No-Core Shell Model* (NCSM), as well as the broadly related *Antisymmetrized Molecular Dynamics* (AMD) model. Another technique treats the Hoyle state as a *Bose-Einstein Condensate* (BEC) of alpha particles to describe its collective behavior and spatial configuration [31, 40].

1.4.1 Cluster Models

The influential alpha clustering framework describes ^{12}C as a system of three alpha particles. The model, initially based on groundwork by Eugene Wigner and later expanded by Margenau [41], was significantly advanced by David M. Brink and Wilhelm Boeker [42].

In it, the clusters (alpha particles) are treated as point-like entities without internal degrees of freedom, and their dynamics are governed solely by an effective alpha-alpha

interaction. Each alpha particle is described by a wave packet, and the total wave function of the system is constructed by antisymmetrizing the product of these wave packets. This antisymmetrization is necessary because, although alpha particles behave as composite bosons, the nucleons (protons and neutrons) that constitute them are fermions and must obey the Pauli exclusion principle. Therefore, the overall wave function must be antisymmetric with respect to the exchange of any two nucleons to ensure that no two fermions occupy the same quantum state simultaneously. This antisymmetrization is typically achieved using a Slater determinant. For nucleon states $\phi_i(\mathbf{r}_j)$, where i labels the nucleon state and j labels the position of the nucleon, the Slater determinant for N nucleons is given by:

$$\Psi(\mathbf{r}_1, \mathbf{r}_2, \ldots, \mathbf{r}_N) = \frac{1}{\sqrt{N!}} \begin{vmatrix} \phi_1(\mathbf{r}_1) & \phi_1(\mathbf{r}_2) & \cdots & \phi_1(\mathbf{r}_N) \\ \phi_2(\mathbf{r}_1) & \phi_2(\mathbf{r}_2) & \cdots & \phi_2(\mathbf{r}_N) \\ \vdots & \vdots & \ddots & \vdots \\ \phi_N(\mathbf{r}_1) & \phi_N(\mathbf{r}_2) & \cdots & \phi_N(\mathbf{r}_N) \end{vmatrix}$$

The determinant ensures that the wave function changes sign upon the exchange of any two nucleons, thus enforcing antisymmetry. This approach maintains the correct quantum statistics of the nucleons while simplifying the complex many-body problem into a more manageable bosonic interaction framework. Based on this, a minimization approach is used to determine the optimal geometric configuration of the alpha particles, resulting in two primary triangular configurations - equilateral and bent-arm (obtuse) - and, as an extreme case, the linear chain (collinear mode).

Further insights into the structure of cluster states in nuclei can be obtained from the group theoretical approach discussed by Bijker and Iachello. In their work, they describe cluster states in nuclei as representations of a U($\nu + 1$) group, providing a framework that unifies various clustering phenomena within a common mathematical structure [43]. This model is referred to as the algebraic cluster model (ACM). Its predictions on the geometry of the cluster configurations can also be used to infer moments of inertia and thus the rotational band structure of the nucleus as well as vibrational rigidity. It suggests that the Hoyle state can be understood as a "breathing mode", increasing the distance between the alpha particles. As this configuration increases the separation of the alpha clusters from the center of the mean Coulomb potential, this suggests that their position can fall outside of the potential threshold of the alpha separation energy facilitating its decay. Its properties would be directly linked to the direct decay properties of the state. This energy comparison cannot be directly obtained from the ACM, as it does not provide full energy spectra, but only relative energies of states, requiring a scaling factor to be applied to the ACM predictions.

Using these scaled data points, the algebraic cluster model's predictions for the spectrum of low-lying states in ^{12}C are in good agreement with experimental data, as can be seen

in Figure 1.5.

Later experimental work by Marín-Lámbarri *et al.* showed consistency with predictions

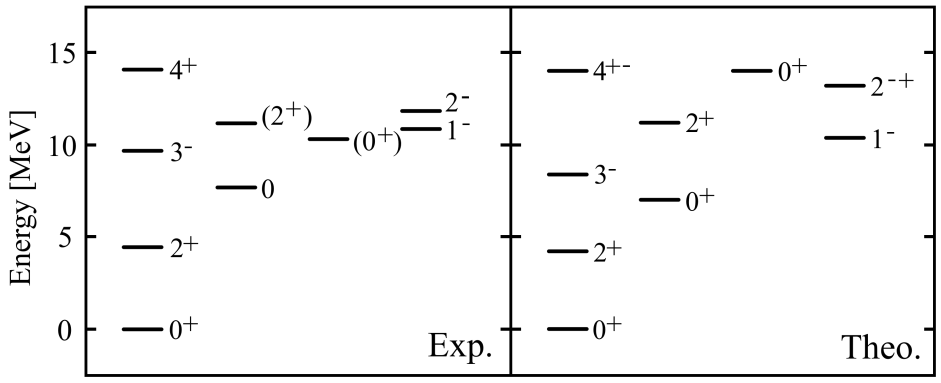

Figure 1.5: Comparison of the experimental spectrum of ^{12}C with the predictions of the algebraic cluster model. Modified from [43].

of the algebraic cluster model, lending support to a clustered description of ^{12}C [44]. Another key feature of cluster models is their description of breakup phenomena near the α-breakup thresholds. This is illustrated by the Ikeda diagram (Figure 1.6), which predicts that states close to the α-breakup thresholds exhibit a pronounced α-cluster structure. The configuration of the Hoyle state, located only ∼379.2 keV [45] above the three-alpha threshold, is therefore an ideal probe for this hypothesis.

1.4.2 Alpha particle condensation (Bose-Einstein Condensate-like States)

In addition to the ACM framework, recent studies by Tohsaki, Horiuchi, Schuck, and Röpke (THSR) introduced a novel α-cluster wave function that suggests a different nature of cluster states in nuclei like ^{12}C [40]. Their work proposes that certain excited states in these nuclei can be understood as α-particle condensates, analogous to Bose-Einstein condensates (BEC) observed in atomic gases when cooled to temperatures near absolute zero. This concept extends to nuclear physics, where α-clustered nuclei exhibit similar behavior due to the bosonic nature of α particles. These states are characterized by weakly interacting α particles forming a gas-like structure, with α-particle condensation predicted to occur in low-density, near-threshold states.

The THSR approach uses a variational method to explore the energy landscapes of these configurations, suggesting that the Hoyle state exhibits characteristics of a dilute α-particle gas [40]. This state is significant in stellar nucleosynthesis, facilitating the fusion of three α particles into carbon. Theoretical models predict that the α particles in this state interact predominantly in relative S-waves, supporting the idea of a condensate-like behavior. The calculated root-mean-square (rms) radii for these states are larger

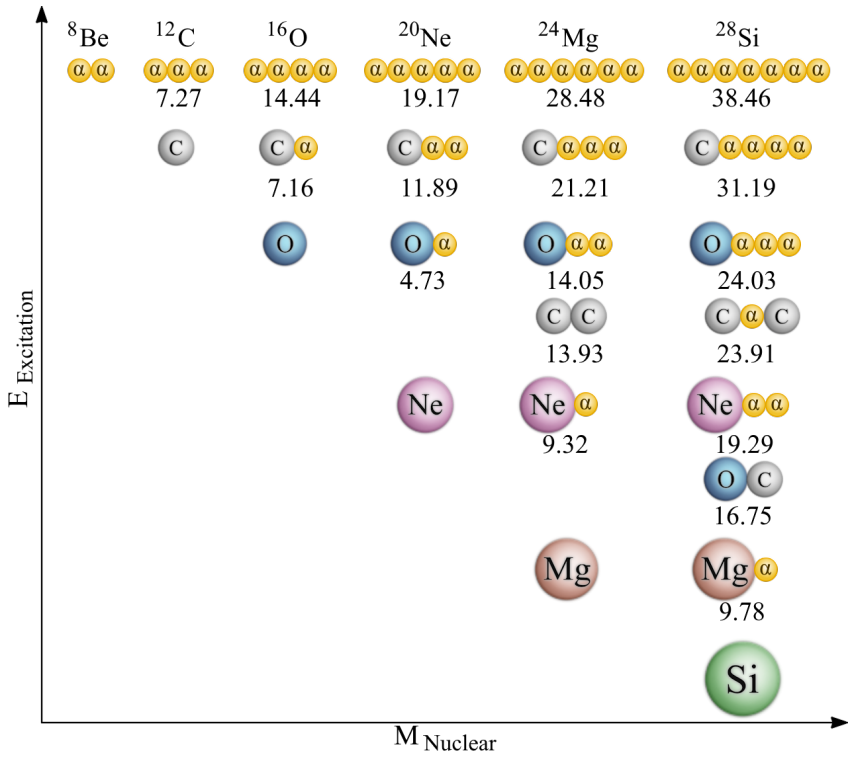

Figure 1.6: Ikeda diagram showing the clustering configurations near the alpha-decay thresholds for light nuclei up to Si. Adapted from Ref.[46, 47], Copyright (2006), with permission from Elsevier.

than those of the ground states, indicating a more extended structure, aligning with experimental observations of the Hoyle state's decay properties and its relatively low density [48].

The ground state of bosonic systems can be described using the Gross-Pitaevskii equation, based on the Hartree-Fock approximation (which reduces to the Hartree mean field for bosons):

$$i\hbar\frac{\partial}{\partial t}\Psi = \left(-\frac{\hbar^2}{2m}\nabla^2 + V(\mathbf{r}) + g|\Psi|^2\right)\Psi, \tag{1.22}$$

where $V(\mathbf{r})$ is the external potential, g is the interaction strength (for dilute, weakly interacting gases $g = 4\pi\hbar^2 a_s/m$ with s-wave scattering length a_s), and Ψ is the condensate order parameter [49]. For dilute atomic gases, this equation yields condensate density profiles and collective excitation modes. Analogously, the Hoyle state has been described as a condensate-like state of α particles within the THSR framework.[40]

The Uegaki *et al.* (1977) model proposes a microscopic α-cluster approach using the generator coordinate method (GCM) to study ^{12}C, which also predicts cluster structures but with a different methodological focus. Their model successfully reproduces various energy levels, including the Hoyle state, by treating the α-clusters' center-of-mass motions. This model suggests that the structure of the excited positive-parity states in ^{12}C should be considered as configurations of α-clusters rather than traditional shell model

structures [50].

The 2003 paper by Funaki *et al.* demonstrates that the wave function of the Hoyle state is almost completely equivalent to the wave function of a 3 α-particle condensate, supporting the interpretation of the Hoyle state as an α-particle condensate [31]. Their subsequent publication in 2006 provides further analysis of the inelastic form factors, which also supports the interpretation of the Hoyle state as a condensate by demonstrating sensitivity to the spatial extension of the Hoyle state and reinforcing the proposed gas-like structure [32].

However, while the condensate models suggest a gas-like structure of α particles, other models, such as the ACM, propose different, more discrete geometries [43]. Another weakness of the BEC-like approach is the difficulty of directly observing the condensate nature of the α particles due to their short-lived states and the complexity in measuring the low-density configurations experimentally, as low densities can also be caused by a widely separated configuration of clusters. The THSR model's reliance on the variational method requires careful selection of parameters, which can introduce uncertainties.

1.4.3 Molecular Dynamics Models

The Antisymmetrized Molecular Dynamics (AMD) method has also been employed to model the Hoyle state [51]. Without assuming preformed clusters as other mentioned techniques, it implicitly captures cluster dynamics. The intrinsic wave function is constructed as a Slater determinant of Gaussian wave packets, using a comparable optimization approach as the condensate models. The calculation of the Hoyle state in the AMD framework employs the Variational After Projection (VAP) method, projecting the wave function onto eigenstates of angular momentum and parity before variation. This allows an accurate description of excited states. A key feature of the 0_2^+ state is its pronounced 3α clustering. The AMD framework naturally reveals this structure, forming a loosely bound, spatially extended configuration. AMD calculations yield accurate binding energies and excitation spectra, closely matching empirical observations.
The AMD technique combines classical molecular dynamics with quantum mechanical antisymmetrization. Each nucleon is represented by a Gaussian wave packet:

$$\phi_i(\mathbf{r}) = \exp\Big(- \nu \, |\mathbf{r} - \mathbf{Z}_i|^2 \Big) \, \chi_i \, \xi_i,$$

where $\mathbf{Z}_i$ is the centroid of the wave packet, ν is the width parameter, χ_i is the spin component, and ξ_i is the isospin component. A Slater determinant, $\Psi = \mathcal{A}\{\phi_1, \phi_2, \ldots, \phi_A\}$, ensures antisymmetry. The total energy E is minimized:

$$E = \langle \Psi | H | \Psi \rangle,$$

where H denotes the Hamiltonian. AMD predicts an α-cluster structure for the Hoyle state, with three α-particles in a loosely bound arrangement, accurately predicting its larger radius and lower density relative to the ground state [52]; this aligns with the early 3α-cluster hypothesis [30]. An example of AMD predictions for different mass densities in excited states of ^{12}C is shown in Figure 1.7.

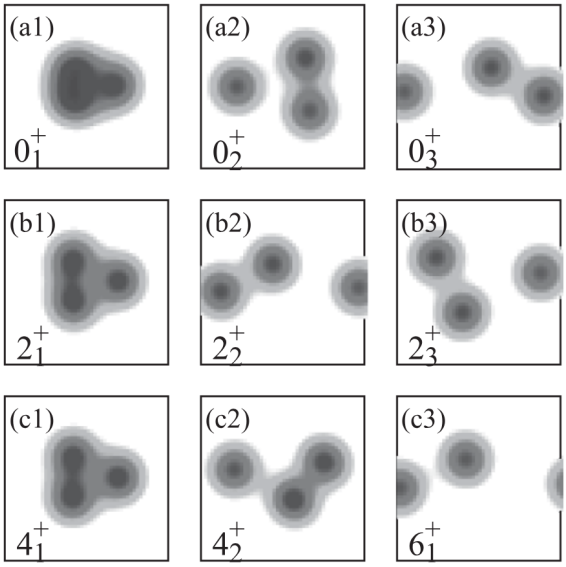

Figure 1.7: Simulation results showing different mass densities for excited states in ^{12}C using the AMD model. Reprinted from Ref. [53], Copyright (2007), with permission from the Physical Society of Japan.

Fermionic Molecular Dynamics (FMD) uses a generalized wave function, including Gaussian and non-Gaussian components, to describe various nuclear states. Unlike AMD, the width parameter ν in the Gaussian wave packet is not fixed. FMD does not accurately predict the Hoyle state's binding energy but successfully predicts the form factor and thus the spatial extension of the Hoyle state [48, 51].

1.4.4 Ab Initio Approaches

While cluster models can provide insights into the spatial configuration of nucleons, *ab initio* methods offer a complementary approach, using first-principles calculations that start from realistic nucleon-nucleon and three-nucleon interactions constrained by few-body data and avoid phenomenological adjustments to reproduce observables in ^{12}C. Among the prominent *ab initio* approaches relevant to the Hoyle state are *Lattice Effective Field Theory (EFT)*, *Quantum Monte Carlo (QMC)*, and *No-Core Shell Model (NCSM)*:

Lattice Effective Field Theory (EFT): The Lattice Effective Field Theory (EFT) technique discretizes space-time onto a periodic cubic lattice, modeling nucleons as point-like particles at the lattice sites. These nucleons interact through pions and multi-nucleon

operators generated by auxiliary fields, such as meson exchange fields. As some of the other introduced approaches, this method employs quantum mechanical operators and wave functions to describe the system's evolution and interactions.

The projection of low-energy states is achieved by Euclidean time propagation, where the amplitude is obtained by $\langle\psi|e^{-Ht}|\psi\rangle$. Here ψ is the wave function, H is the Hamiltonian operator, and t is the Euclidean time. As t increases, e^{-Ht} enhances low-energy state signals by suppressing wave function contributions with higher energy eigenvalues. This method allows determination of energy levels by analyzing the decay of these projected states.

In the recent study by Epelbaum *et al.*, [54], the lattice has a spatial spacing of 1.97 fm and a length of 12 fm. The temporal step size is 1.32 fm. While using distance units for time may seem unconventional, this choice is common in lattice simulations that adopt natural units with the speed of light set to unity ($c = 1$), where time and length share the same unit (e.g., 1 fm/$c \approx 3.34 \times 10^{-24}$ s). To investigate different states of ^{12}C, various initial and final state configurations are used. For example, in the case of ^{4}He, the initial state consists of four nucleons at zero momentum. For ^{8}Be, the process involves the initial ^{4}He configuration, followed by the injection of four additional nucleons at zero momentum. For ^{12}C, the method measures four-nucleon correlations to reveal the formation of alpha clusters, which are crucial for understanding its structure.

The lattice calculations indicate that the ground state and first excited spin-2 state of ^{12}C show best agreement with a compact triangular configuration of alpha clusters. In contrast, the Hoyle state and the second excited spin-2 state align best with a bent-arm triangular configuration. The calculated electromagnetic transition rates among these low-lying states generally agree with experimental data, lending support to the configurations proposed by the lattice calculations. These configurations are illustrated in Figure 1.8.

However, there are some limitations to the technique. The use of a fixed lattice spacing may not capture all fine details of the nuclear interactions, and the results may be sensitive to the chosen lattice parameters. Additionally, higher-order corrections and smaller lattice spacings could improve accuracy but at the cost of increased computational resources. Lattice Effective Field Theory (Lattice EFT) calculations are typically run on supercomputers due to their high computational demands. The mentioned study by Epelbaum *et al.*, for example, used resources provided by the Jülich Supercomputing Centre. Despite these limitations, the application of chiral EFT up to next-to-next-to-leading order (NNLO) [54] provides a robust model of the structure and rotational excitations of the Hoyle state.

Quantum Monte Carlo (QMC) Quantum Monte Carlo (QMC) methods are stochastic techniques used to solve the Schrödinger equation for many-body quantum systems

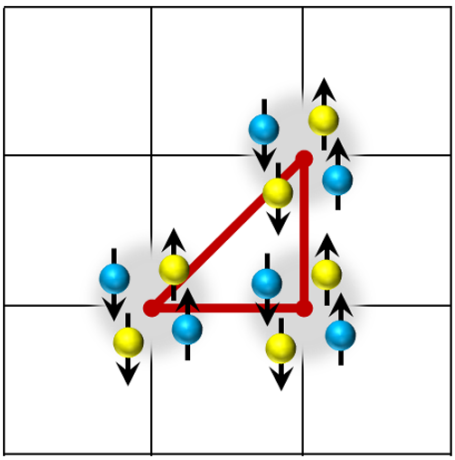

(a) Ground state of ^{12}C, predicted by Lattice EFT.

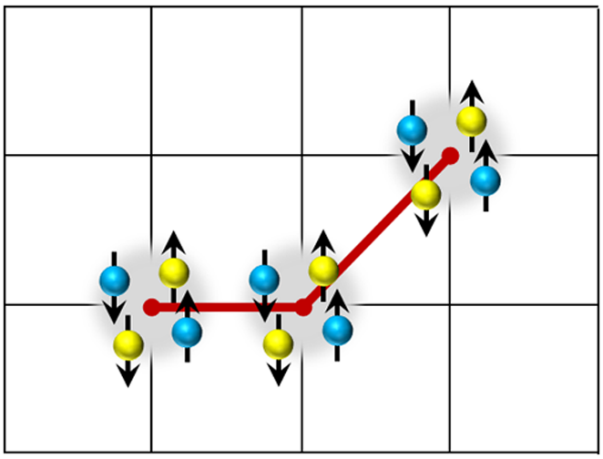

(b) Hoyle state of ^{12}C, predicted by Lattice EFT.

Figure 1.8: Predictions of the ground state and Hoyle state configurations of ^{12}C using Lattice EFT. Reprinted from Ref. [54], Copyright (2012), with permission from the American Physical Society.

through random sampling, making it possible to study computationally intractable systems. Key methods include Variational Monte Carlo (VMC), which optimizes a trial wave function to approximate the ground state energy, and Green's Function Monte Carlo (GFMC), which refines this wave function by projecting out the ground state via stochastic diffusion. In Quantum Monte Carlo (QMC) calculations [55, 56], VMC was used to construct a trial wave function Ψ_V with optimized variational parameters to minimize the Hamiltonian's expectation value, employing the Argonne v18 (AV18) two-body and Illinois-7 (IL7) three-body potentials. GFMC further refined Ψ_V by projecting out the lowest energy eigenstate using $\exp[-(H - E_0)\tau]$.

QMC methods accurately describe ground- and excited-state energies for light nuclei up to $A \leq 12$ and show good agreement with experimental data for energy levels and electromagnetic moments. However, these methods are computationally intensive, limiting their application to heavier nuclei. Statistical errors increase with larger systems, and the mixed estimator approach introduces potential systematic errors. Significant computational resources and time are required for convergence. Despite these challenges, QMC methods are renowned for their precision in modeling strong many-body correlations and quantum fluctuations. The application to the Hoyle state successfully models this crucial state for stellar nucleosynthesis, though it faces challenges in fully capturing all transition rates and electromagnetic properties [57].

No-Core Shell Model (NCSM) Complementary to other *ab initio* techniques, the no-core shell model (NCSM), here specifically its symmetry-guided realizations, the symmetry-adapted NCSM (SA-NCSM) and the no-core symplectic model (NCSpM), overcomes tra-

ditional limitations by utilizing a symmetry-guided approach and a single many-nucleon interaction parameter. For ^{12}C, this realization effectively captures the ground-state rotational band and α-clustering phenomena in low-lying states, especially the Hoyle state and its first 2^+ and 4^+ excitations. By focusing on the long-range components of the interaction together with a spin-orbit term, this realization simplifies complex interactions yet retains fundamental physical characteristics. Results, such as those by Dreyfuss *et al.* [58], show that this approach captures key features of the Hoyle state, with calculated energy levels, matter radii, and nuclear deformation parameters closely matching experimental data. The root-mean-square (rms) matter radius of the Hoyle state predicted by this approach is 2.93(5) fm [58], aligning with recent experimental extractions that yield 2.89(4) fm [48]. This agreement reinforces the α-cluster structure hypothesis, as the work by Dreyfuss *et al.* demonstrates that this framework, even with simplified many-body interactions, accurately describes large-deformation and cluster phenomena, indicating that precise symmetry-guided no-core descriptions are feasible within this framework.
However, the NCSM also has its shortcomings and disadvantages. One significant challenge is the computational complexity associated with solving the many-body Schrödinger equation without assuming an inert core, which requires substantial computational resources. Additionally, the truncation of the model space can introduce uncertainties in the results, as not all possible configurations of nucleons are included. Another limitation is the dependence on effective interactions that are derived from realistic nucleon-nucleon potentials, which might not fully capture all many-body correlations. Finally, while the NCSM provides valuable information for light nuclei, extending this approach to medium and heavy nuclei remains a formidable challenge due to the exponential growth of the model space.

1.4.5 Summary

Many different approaches have been employed throughout the years to model the Hoyle state in ^{12}C. The cluster models, in particular, have been successful in describing the Hoyle state as a 3α cluster (and, in some approaches, as an α-particle condensate), with the ACM and BEC-like models providing valuable insights into the spatial configuration and dynamics of it. The AMD model, on the other hand, implicitly captures the cluster dynamics without assuming preformed clusters, which reaffirms the cluster models' base assumption. The *ab initio* methods, such as Lattice EFT, QMC, and NCSM, provide a complementary approach by using first-principles calculations to predict nuclear properties without empirical data, offering insights into the many-body dynamics of the Hoyle state. Whereas each model has its strengths and limitations, their differences indicate the need for further experimental data to improve the observational constraints on the models to refine the understanding of the Hoyle state in ^{12}C.

1.5 Decay modes of the Hoyle state

Since the three-particle fusion process is inaccessible in the laboratory, the inverse reaction, the decay of the Hoyle state, can be used to study the properties of the state and its branching ratios. The Hoyle state can decay via two different pathways: The sequential (SD) and the direct decay (DD) modes. During the sequential decay, the ^{12}C nucleus in the Hoyle state breaks up into an alpha particle and the unbound ^{8}Be resonance, which then decays into two alpha particles. A schematic overview of this decay mode is shown in Figure 1.9. This mode is dominant with a branching ratio shown to be greater than 99.9 % [59]. The competing direct decay is a rare process with a branching ratio of less than 0.1 %. During this process, the Hoyle state decays directly into three alpha particles.

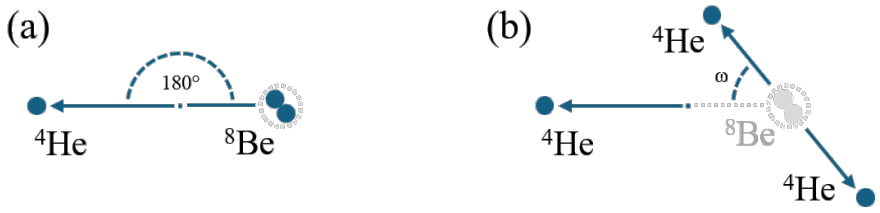

Figure 1.9: Sequential decay mode of the Hoyle state. (a) The Hoyle state decays into the ^{8}Be and an alpha particle, (b) The ^{8}Be resonance then decays into two alpha particles. The only degree of freedom in this decay mode is the angle difference between the two reaction axes ω.

The branching ratios will be discussed in more detail in Section 1.7. Having more degrees of freedom, the direct decay process has multiple possible configurations, which are shown in Figure 1.10. The direct decay is of particular interest, as it provides information

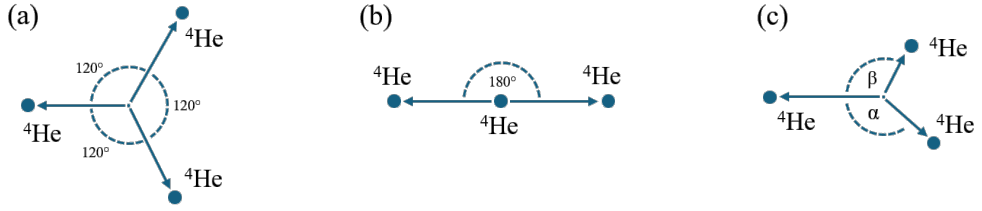

Figure 1.10: Direct decay mode of the Hoyle state, showing (a) the DDE configuration, (b) the DDL configuration, and (c) the DDΦ configuration.

about the structure of the Hoyle state and the nature of the three-alpha interaction. The primary direct decay modes are thought to correlate to structural configurations of the Hoyle state, as the short time scale of the decay process may not allow for a significant

rearrangement of the pre-formed alpha particles. The two extreme cases are the linear chain (DDL) and the equilateral triangular configuration (DDE), which correspond to an internal triangular configuration with equal decay energies for the three alpha particles. Other possible modes are linear combinations of these two configurations. This mixture also corresponds to the broadest phase space for the decay, as it can be either described by a triangular configuration with variable opening angles or as a product of the dilute gas-like configuration which, on the other hand, is linked to a more extended and less clustered state, was later discussed in Section 1.4. This decay mode is referred to as the DDΦ decay.
Another possible decay mode of the Hoyle state is the radiative decay

$$^{12}\mathrm{C}^{*}(7.654\ \mathrm{MeV}) \rightarrow {}^{12}\mathrm{C} + \gamma\gamma, \text{ or} \tag{1.23}$$

$$^{12}\mathrm{C}^{*} \rightarrow {}^{12}\mathrm{C} + e^{+} + e^{-}. \tag{1.24}$$

Due to its high photon energy compared to available photon energies in stellar environments, the radiative decay is a one-way process, producing ^{12}C in its ground state. Since the ground state of ^{12}C is stable in regard to the ^{8}Be + ^{4}He or the direct three-alpha decay channel (see 1.21), this process enables the creation of ^{12}C in a stellar environment. The leakage through the radiative decay channels is very small though, as recent measurements place the $\Gamma_{\mathrm{rad}}/\Gamma$ branching ratio at $\Gamma_{rad}/\Gamma = 4.0(0.3_{stat})(0.16_{sys}) \cdot 10^{-4}$ [28].
In summary, the two step reaction process forming ^{12}C from three alpha particles can be understood as a sequence of the initial 3-alpha capture, enhanced by the Hoyle state resonance, with a subsequent decay of the Hoyle state into the ground state of ^{12}C via radiative decay.

The radiative decay out of the $^{12}\mathrm{C}^{*}$ state further branches into the two-photon decay and an electron-positron pair production decay

$$\Gamma_{\mathrm{rad.}} = \Gamma_{\gamma\gamma} + \Gamma_{\mathrm{e^{+}e^{-}}}, \tag{1.25}$$

while the competing particle-decay channel consists of the sequential and direct three-alpha decay channels

$$\Gamma_{3\alpha} = \Gamma_{\mathrm{seq.}} + \Gamma_{\mathrm{dir.}} \tag{1.26}$$

where $\Gamma_{\gamma\gamma}$ and $\Gamma_{\mathrm{e^{+}e^{-}}}$ are the partial decay widths for the radiative decay channels and $\Gamma_{\mathrm{seq.}}$ and $\Gamma_{\mathrm{dir.}}$ are the partial decay widths for the sequential and direct three-alpha decay channels, respectively. As discussed in Section 1.2.3, the resonance strength of the entire formation process is given by

$$\omega\gamma = \frac{\Gamma_{3\alpha}\Gamma_{\mathrm{rad.}}}{\Gamma} = \frac{(\Gamma_{seq.} + \Gamma_{dir.})\Gamma_{\mathrm{rad.}}}{\Gamma_{seq.} + \Gamma_{dir.} + \Gamma_{\mathrm{rad.}}}. \tag{1.27}$$

1.6 The Dalitz plot

The Dalitz plot is a tool often used in the analysis of three-body decays. First developed to study the decay of K mesons by Richard Dalitz [60] in 1953, it was soon widely used in the particle physics community. The general idea is to find a two-dimensional representation of a three-dimensional problem by using constraints such as momentum and energy conservation. The plot can be constructed using the reduced energies of the decay products $\epsilon_i = E_i/Q$ where E_i is the energy of the decay product and Q is the decay energy of the parent nucleus. This equation by definition results in

$$\sum_{i=1}^{3} \epsilon_i = 1. \tag{1.28}$$

Using this constraint, the problem reduces to a two-dimensional plane. This can be seen in Figure 1.11. The coordinates of the Dalitz plot are derived by projecting the 3D plane

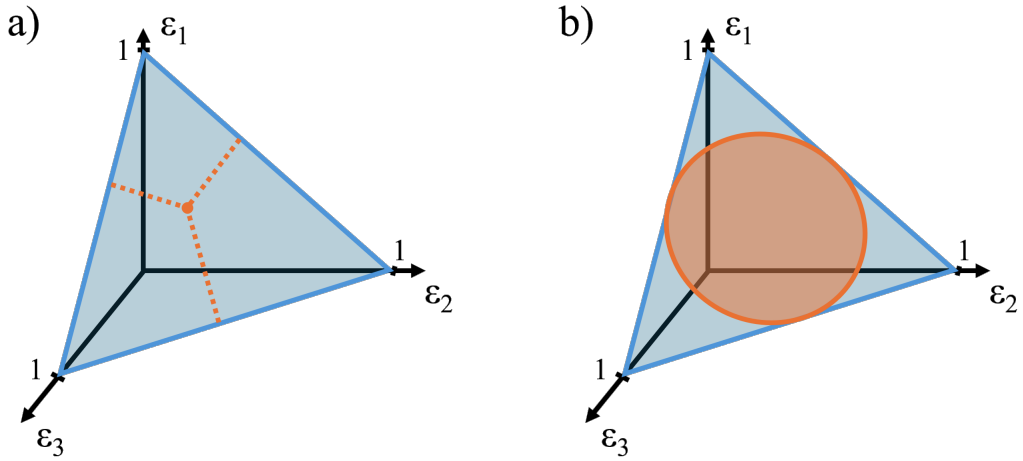

Figure 1.11: The construction of a Dalitz plot: (a) Due to the constraint in equation 1.28, the projection plane is formed. It also indicates the position of each data-point on this plane, as further detailed in Figure 1.12. (b) Shows the constraints of the plot: The triangle constraints in the Energy domain, and the orange ellipse restricts valid events based on momentum conservation. Dalitz plot construction based on Ref.[60].

into a 2D plane using the following equations:

$$x = \frac{\epsilon_2 - \epsilon_1}{\sqrt{3}} \tag{1.29}$$

$$y = \frac{2\epsilon_3 - \epsilon_2 - \epsilon_1}{3} \tag{1.30}$$

This creates the triangular shape of the Dalitz plot, as shown in Figure 1.12. The overall Dalitz plot contains two distinct shapes: A large triangular region, which follows from the conservation of energy and the circular shape which is a result of the conservation of

momentum. A derivation of this is provided in the appendix A.4.

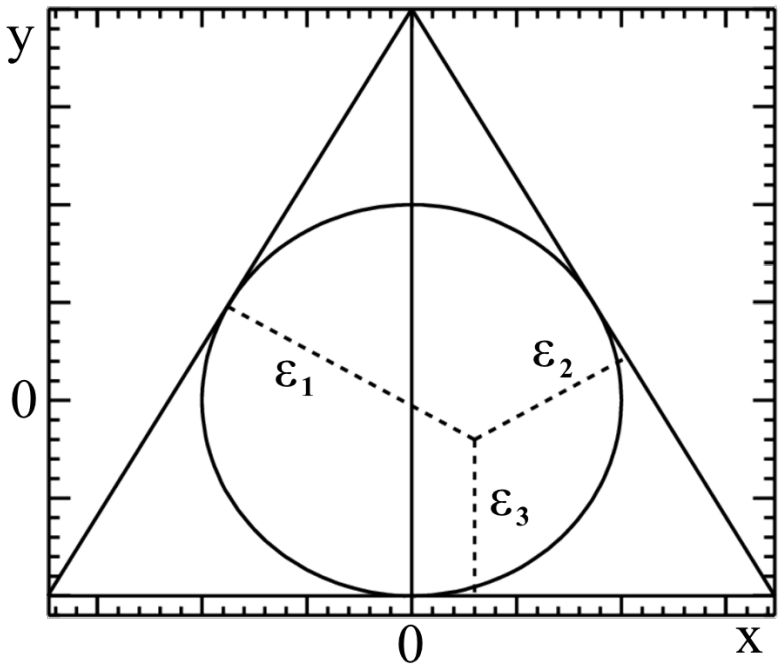

Figure 1.12: The Dalitz plot showing the dependencies of its coordinates to the reduced energies ϵ_i of the decay products.

In its 2D-representation, the Dalitz plot can be used to identify different decay modes of the Hoyle state, as shown in Figure 1.13: While the sequential decay, with its single degree of freedom, is represented by a triangle (due to symmetry), the direct decay modes are represented different shapes: The DDE mode, where all three decay products have equal energy, has zero degrees of freedom and is represented by a single point in the center of the Dalitz plot. The DDL modes also do not have a degree of freedom in their relative energy distribution in the center-of-mass system and are represented by three points towards the corners of the sequential triangle. This is intuitive, as the sequential decay where all particles decay in-line has a very similar momentum composition as the DDL mode. The DDΦ mode, however, has two degrees of freedom and is thus able to fill the entire momentum-constrained region of the Dalitz plot. This is due to the fact that the decay products can have different energies, as long as the total energy is conserved.

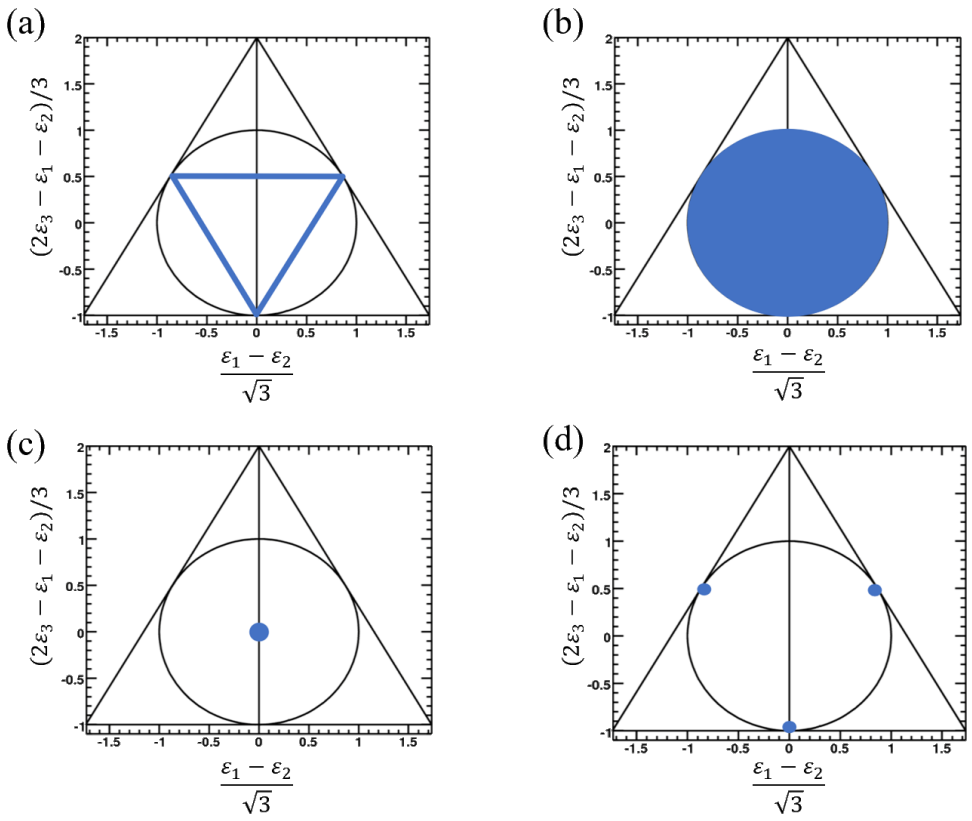

Figure 1.13: The Dalitz plot showing the different decay modes of the Hoyle state: (a) Sequential decay, (b) the DDΦ configuration, (c) the DDE mode, and (d) the DDL mode.

1.7 Prior experimental studies of the Hoyle state

The particle-decay branching ratio of the Hoyle state has been studied in several experiments: Initial studies in the 1940s and 1950s focused on the existence of excited states in ^{12}C. The first experiment claiming to observe a resonance in the 7 MeV range was conducted by Holloway and Moore in 1940 [61], who used a $^{14}\mathrm{N}+^{2}\mathrm{D} \rightarrow {}^{12}\mathrm{C}+{}^{4}\mathrm{He}$ reaction and measured an excitation energy at around 7.6 MeV. Due to their limited understanding of the underlying mechanisms, no further conclusions could be drawn at the time.
More than a decade later, in 1957, at the nuclear physics department of the California Institute of Technology (Caltech), the existence of the excitation now known as the Hoyle state was definitively confirmed [27]. (An excited level near $E_x \approx 7.65\,\mathrm{MeV}$ in ^{12}C had already been reported at Caltech in 1953 by Dunbar, Pixley, Wenzel, and Whaling [26].) This confirmation was achieved three years after Sir Fred Hoyle's postulation of the resonance, as discussed in Section 1.3. During Hoyle's visit from Cambridge, he suggested further measurements above 7.6 MeV in ^{12}C; subsequent experiments revealed a resonance at the predicted energy. Thus, the 1957 Caltech work by Cook, Fowler, and C. C. and T. Lauritsen established the state's properties and astrophysical significance [27].
The first attempt to directly measure the direct particle-decay branching ratio of the

Hoyle state was undertaken by Freer *et al.* in 1994 [62] using a ^{12}C(^{12}C, 3^{4}He)^{12}C reaction to populate the Hoyle state and measured the decay products using a $\Delta E - E$ telescope and a Double-Sided Silicon Strip Detector (DSSSD). Their measurement yielded an upper limit for the direct decay branching ratio of the Hoyle state of 4 %. In the following years, advances in experimental techniques and the development of new detector systems allowed for more precise measurements of the Hoyle state decay properties. Multiple later studies have subsequently lowered the upper limits for the direct decay branching ratio of the Hoyle state, with two publications also providing lower limits [63, 64]. Although the results by Raduta and Rana have since been superseded by more advanced measurements due to progress in the employed methodology, such as the study by Kirsebom *et al.* in 2012 [65], which placed the upper limit for the direct decay branching ratio of the Hoyle state at 6.8×10^{-3}, their findings contributed to the growing interest in the measurement of the direct decay branching ratio.
Recent direct measurements have been published by Dell'Aquila *et al.* in 2017 [66], Smith *et al.* in 2017 and 2020 [59, 67], Rana *et al.* in 2019 [68], and Bishop *et al.* in 2020, as listed in Table 1.1. Most measurements place the upper limit for the direct 3α decay branching ratio of the Hoyle state at around 10^{-4}. The study by Bishop *et al.* in 2020 [69] placed a first lower limit on the direct 3α decay branching ratio of the Hoyle state at 5.8×10^{-5}, close to the sensitivity limit of the work of this thesis. To better understand the different approaches to the branching ratio measurements, the experimental setups and techniques used in some of the latest and most notable studies will be discussed briefly in the following sections.

Dell'Aquila *et al.* (2017) Dell'Aquila *et al.* used a ^{14}N(d,^{4}He)^{12}C reaction at a beam energy of 10.5 MeV at the *INFN-LNS* facility in Catania, Italy, to populate the Hoyle state. The decay products were measured using a $\Delta E - E$ telescope and a high-granularity hodoscope detector to measure the trajectory of the resulting alpha particles. This enabled reconstruction of the complete kinematics of the reaction and an effective background suppression. In total, about 28 000 decay events were recorded and analyzed. A Monte-Carlo simulation was used to evaluate the results and determine the branching ratio of the direct decay of the Hoyle state to be below 4.3×10^{-4} [66].

Smith *et al.* (2017) The initial study performed by Smith *et al.* in 2017 used a combination of five DSSSD detectors in a geometrical configuration where one detector was specifically set up to detect the ejectile and the other four to detect the coincident alpha particles from the breakup of the excited carbon nuclei. Their employed methodology is comparable to the one used in this thesis, although the limited number of detectors increased the Combinatorial uncertainty inherent in multi-particle detections of comparable energy using DSSSDs. A 40 MeV α-particle beam at the MC40 cyclotron at the

University of Birmingham was used to populate excitations in ^{12}C. During the measurement a total of about 93 000 events were registered, of which approx. 24 000 remained after suppressing the ambiguous detector combinations. The branching ratio of the direct decay of the Hoyle state was determined to be below 4.7×10^{-4} [59].

Rana *et al.* (2019) Rana *et al.* (2019) also studied the decay width of the Hoyle state in ^{12}C, using inelastic alpha scattering to populate the Hoyle state and measure its decay products [68]. The experiment was performed at the Variable Energy Cyclotron Centre in Kolkata, using a 60 MeV alpha beam on a ^{12}C target. The emitted alpha particles were detected using two double-sided silicon strip detectors. Similar to the measurement performed by Smith *et al.* in 2017, the use of inelastic scattering allowed for a complete kinematic reconstruction of the Hoyle state decay, increasing the separation efficiency between particles originating from sequential and direct decays. During the experimental campaign, about 1.95×10^5 events were recorded of which 1.6×10^5 remained after background suppression, a large increase over previous measurements. This enabled the determination of an upper limit on the direct 3α decay branching ratio of the Hoyle state of 1.9×10^{-4} at the 95 % confidence level, more than a factor of two lower than the previously determined upper limits

Smith *et al.* (2020) In a follow-up study using a different approach, Smith *et al.* used a ^{12}C(γ, 3α) reaction to place a new upper limit on the direct 3α decay branching ratio of the Hoyle state [67]. The experiment was conducted at the High Intensity Gamma-ray Source (HIγS) facility, utilizing an Optical Time Projection Chamber (O-TPC) for the detection of the decay events. The O-TPC allowed for three-dimensional visualization of the decay process, capturing the trajectories of the emitted alpha particles. By analyzing the events where all three alpha particles were detected, they identified two distinct classes: events where two alpha particles emerged close together, indicative of a sequential decay through the ground state of ^{8}Be, and events with large opening angles between the alpha particles, suggestive of direct decay. This indirect technique, however, relies heavily on the accurate modeling of the decay process and the interpretation of the detected events. The authors utilized the three-body WKB approach [70] to calculate the penetrability ratio between the Hoyle state and its 2^+ excitation, from which they inferred the direct decay width of the Hoyle state. Despite the indirect nature of the technique, the experiment achieved a substantially lower upper limit on the direct 3α decay branching ratio of 5.7×10^{-6}, which is over an order of magnitude lower than previous experimental limits.

Bishop *et al.* (2020) Bishop *et al.* (2020) employed the Texas Active Target Time Projection Chamber (TexAT TPC) to measure the direct 3α decay component of the

Hoyle state with high sensitivity [69]. Their method utilized beta-delayed charged-particle spectroscopy of ^{12}N to populate the Hoyle state, followed by the detection of the resulting 3α decay events. The TexAT TPC setup allowed for a nearly medium-free environment, reducing background contributions and avoiding pile-up events that have limited previous measurements. By tracking the three-dimensional trajectories of the alpha particles, the experiment distinguished between sequential decay via ^{8}Be and the direct 3α decay by analyzing the energy partition and angular correlations of the alpha particles. Bishop *et al.* reported an upper limit on the direct 3α decay branching ratio of 4.3×10^{-4} and a lower limit of 5.8×10^{-5} at the 95 % confidence level. This result contrasts with the significantly lower upper limit of 5.7×10^{-6} reported by Smith *et al.* (2020) [67], highlighting discrepancies that may arise from the different experimental techniques. The higher limit obtained by Bishop *et al.* suggests that further investigation and refinement of both experimental and theoretical approaches are necessary to reconcile these differences and achieve a more accurate determination of the direct 3α decay branching ratio of the Hoyle state.

Table 1.1: Previously obtained upper and lower limits on the direct 3α decay branching ratio of the Hoyle state

Author	Lower Limit	Upper Limit
Kirsebom *et al.* (2012) [65]	-	$< 6.8 \times 10^{-3}$
Dell'Aquila *et al.* (2017) [66]	-	$< 4.3 \times 10^{-4}$
R. Smith *et al.* (2017) [59]	-	$< 4.7 \times 10^{-4}$
R. Smith *et al.* (2020) [67]	-	$< 5.7 \times 10^{-6\dagger}$
T.K. Rana *et al.* (2019) [68]	-	$< 1.9 \times 10^{-4}$
J. Bishop *et al.* (2020) [69]	$> 5.8 \times 10^{-5}$	$< 4.3 \times 10^{-4}$

† This upper limit is indirectly calculated from measurements of the 2^{+} state in ^{12}C.

Chapter 2

The experiment

To study the particle-decay modes of the Hoyle state in ^{12}C, a series of experiments using the Lund-York-Cologne-CAlorimeter (LYCCA) array were conducted at the Institute for Nuclear Physics at the University of Cologne using its 10 MV FN-Tandem accelerator. The two primary experiments were conducted in December 2019 and January of 2020. The measurement setup used in these, the employed experimental procedure, and the utilized data acquisition system are described in the following sections.
To obtain data on the Hoyle state decay, a ^{12}C(α,$\alpha\prime$)^{12}C reaction was used to populate excited states in ^{12}C. The reaction was chosen because the direct population of the Hoyle state allows efficient selection of the resulting decay products. The reaction was performed using a 27 MeV ^{4}He beam, ensuring that each emitted alpha particle has sufficient energy to leave the target and be detected by the LYCCA setup. This enables the detection of all fragments, which allows to study the reaction using complete kinematics. The beam current was kept between 0.8 and 2 nA intensity.

2.1 Cologne FN-Tandem accelerator

The Cologne FN-Tandem accelerator is a 10 MV Tandem van de Graaff particle accelerator and is used to supply ions for a multitude of experiments in the field of nuclear structure physics, accelerator mass spectrometry, and nuclear astrophysics. It can provide a wide range of ions, from protons to heavy ions, with beam currents up to 800 nA. It is supplied by a sputter ion source and a Duoplasmatron ion source [71].
Due to the requirement of negatively charged ions for the accelerator and the challenge to create negative ions from the noble gas helium, a Duoplasmatron ion source is used for the ion-beam experiments described in this thesis. The source creates the ions in a dense plasma: The generation occurs in two stages: initially, a primary plasma is formed in a cathode-anode discharge chamber where electrons emitted from a heated filament ionize helium gas. These α^{2+} ions capture low-energy electrons, forming α^{-} ions. An extraction voltage is then applied to draw the α^{-} ions through an aperture, resulting in a well-defined ion beam. This beam is then accelerated towards the positive terminal of the

Tandem accelerator, which was charged to 9 MV for the experiment. Here a stripper foil is used to remove electrons from the ions, resulting in an ion beam consisting of positively charged alpha particles. These are subsequently accelerated again by the terminal. After this terminal, the ions are accelerated again using the same terminal voltage, reaching the final beam energy of 27 MeV. A 90° bending magnet is used to verify the energy, select the correct charge state for transmission and suppress background ions. The beam is then focused by multiple quadrupole magnets and steered towards the LYCCA setup, which is set up in the *Osiris* hall, one of the laboratory halls in Cologne.

2.2 The Lund-York-Cologne-Calorimeter (LYCCA)

The LYCCA setup consists of an array of segmented double-sided silicon strip detectors (DSSSDs) with supplementary CsI(Tl) scintillators in a subset of its detector telescopes. It is currently installed at the 10 MV FN-Tandem accelerator facility at the institute for nuclear physics in Cologne.

The array was previously employed for a GSI-PreSPEC campaign, in preparation for future work as part of the HISPEC-DESPEC collaboration at FAIR, the Facility for Antiproton and Ion Research in Darmstadt, Germany. Although in an initial, limited configuration, the array was successfully employed in a relativistic Coulomb excitation experiment to study the transition strengths of excited states in the neutron-deficient sd shell nucleus ^{33}Ar [72].

The LYCCA array, now consisting of 18 telescope modules, was at the time comprised of 12 modules. At the time, each telescope paired a DSSSDs with a grid of 9 CsI-crystals to be used in a $\Delta E - E$ configuration (see Figure 2.4 for a schematic drawing). During later experiments not all telescopes were outfitted with CsI-crystals, as the primary capability of the LYCCA setup is based on its highly segmented DSSSDs with 1024 pixels per detector.

The LYCCA modules were used in conjunction with a position-sensitive time projection chamber (TPC) and a subset of the RISING germanium detector array consisting of 15 high-purity germanium (HPGe) detectors and the HECTOR BaF_2 detector array. The experiment used a 450 $\frac{\text{MeV}}{\text{u}}$ ^{36}Ar beam impinging on a ^{9}Be target. The FRS fragment separator was used to select the ^{33}Ar ions and focus them on the secondary ^{197}Au target at 145 $\frac{\text{MeV}}{\text{u}}$. A group of two plastic scintillators was used for time-of-flight measurements in conjunction with the DSSSDs to identify the incoming ions by their mass and charge. The LYCCA setup was used to detect the outgoing particles and measure their energy loss and total kinetic energy as can be seen in the $\Delta E - E$ plot in Figure 2.1, where its resolving power of fragments is demonstrated. The primary physics case for this setup was the investigation of isospin symmetry in sd shell nuclei by measuring the mirror-energy differences (MED) and reduced transition strengths in ^{33}Ar.

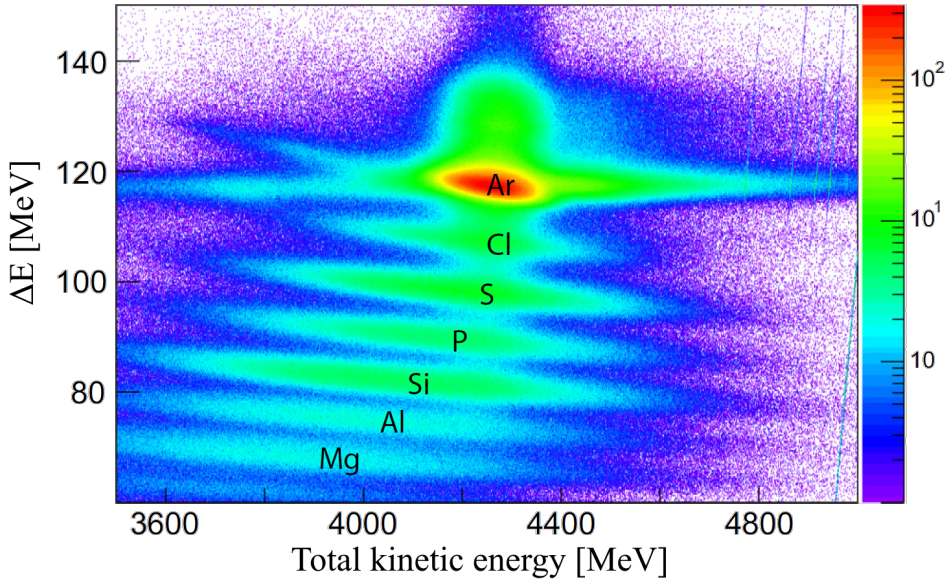

Figure 2.1: A ΔE-E plot obtained during the GSI-PreSPEC campaign, showing the separation of different isotopes. Reprinted from Ref. [72], Copyright (2014), with permission from the American Physical Society.

2.2.1 LYCCA detector configuration

The array can be mounted in multiple geometric configurations, dependent on the physics case of interest. For FAIR a planar configuration in a 5x6 grid was chosen, since the beam energies in excess of 3 GeV result in a narrow scattering angle range compared to beam energies available at the FN-Tandem accelerator in Cologne (up to 30 MeV for ^{4}He, for example). To accommodate this wider scattering angle range, a different detector configuration with larger angle coverage was required. In the experiment presented in this thesis, this new configuration was utilized. The new geometry covers scattering angles from 11° up to 83° in the laboratory frame, spanning almost the entire kinematic range of ^{12}C(α,$\alpha\prime$)^{12}C reactions. The used configuration consist of three detector groups: One plane (the "wall"), and two barrels (the "rings"), containing 8 detectors each. For the experiment presented in this thesis only the DSSSDs were employed, as lower energies compared to the FAIR configuration result in most particles of interest being completely stopped in the silicon detectors. The configuration employed in Cologne can be further customized, as one of the rings can be mounted in backwards direction ($\theta > 90°$), with respect to the beam axis and there are two potential ring positions under forward angle, as can be seen in Figure 2.2. The average detector positions and angular coverage of the current detector configuration in Cologne are given in Table 2.1. The total angular coverage of the current configuration is 3.25 sr, which equates to 51.7 % of the forward hemisphere.

In the performed experiment though, kinematic considerations governed that both rings were mounted in forward configuration. The barrel configuration of one of the detector

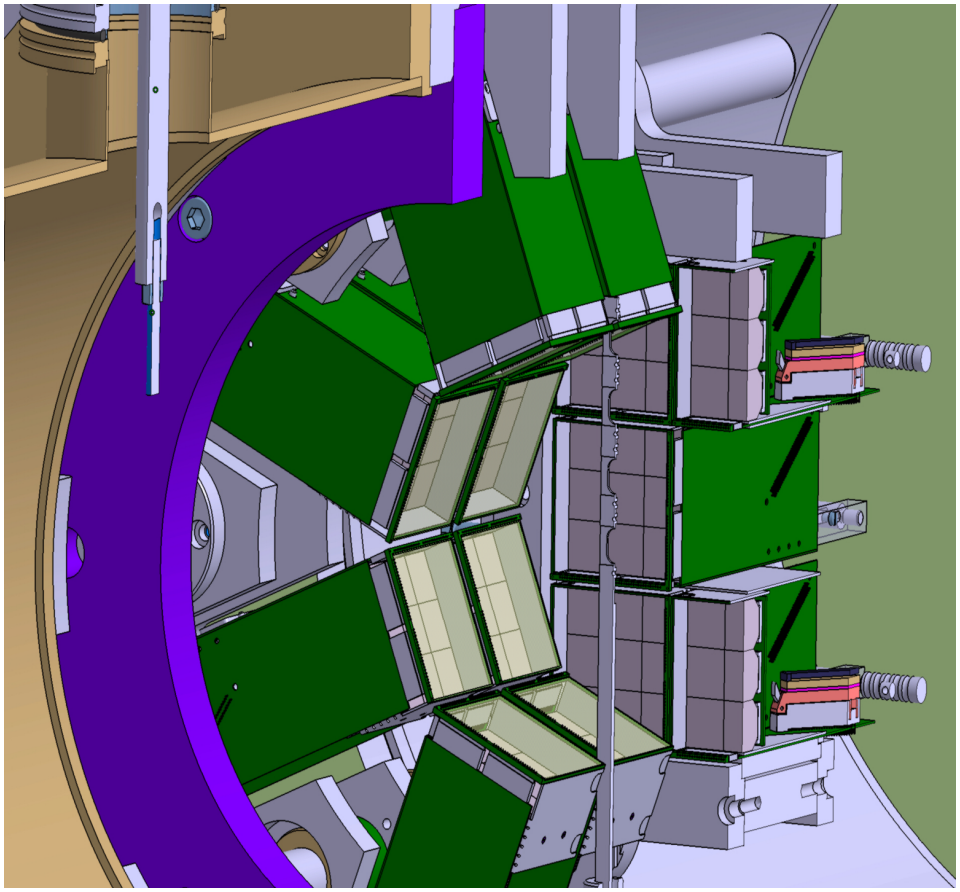

Figure 2.2: A cut-through CAD-drawing of the target chamber containing the LYCCA telescopes. The render demonstrates a mixed configuration of the LYCCA setup where one ring is mounted under backward angles. During the experiment, both rings were mounted in forward direction. In the plot, the beam enters from the left. Between the two rings shown, a cutout of the target ladder assembly is visible. Half of the wall detectors are visible on the right side.

rings can be seen in Figure 2.3a, while the wall configuration is shown in Figure 2.3b. The setup in Cologne also contains further upgrades, such as the new fully digital integrated data acquisition system using the AIDA modules, which will be discussed in Section 2.4 [73].

The setup also consists of a target ladder assembly with four positions, containing a 3 mm diameter tantalum aperture for focusing the beam on the target and three target positions. These were filled with the primary 0.114 $\frac{\text{mg}}{\text{cm}^2}$ ^{nat}C target, used for the experiment, a backup 0.133 $\frac{\text{mg}}{\text{cm}^2}$ ^{nat}C target, only used for testing, and a 0.35 $\frac{\text{mg}}{\text{cm}^2}$ ^{197}Au target for kinematic calibration purposes.

Additional equipment includes a set of collimators, which prevents initial scattering into the target chamber and which can be read out to measure the beam rate impinging on the apertures. Additionally, during the second beam time in January 2020, the four inner detectors in the wall-mounting were equipped with a set of protective tantalum covers to

Module	Avg. θ (deg)	Avg. ϕ (deg)	Solid Angle coverage (sr)
1	65.8	203.6	0.149
3	64.7	247.4	0.146
7	64.3	291.9	0.151
16	63.9	21.3	0.159
21	63.9	66.5	0.157
23	63.9	112.9	0.160
4	39.1	203.6	0.139
6	39.8	247.2	0.134
10	38.6	291.7	0.143
13	39.1	333.9	0.139
17	38.5	21.3	0.142
18	38.2	66.6	0.144
19	38.1	112.8	0.144
20	38.7	159.9	0.141
14	20.8	269.8	0.299
15	20.3	0.4	0.301
24	20.5	181.8	0.293
25	20.8	90.1	0.293
Total	43.3		3.235 (1.03π)

Table 2.1: Average θ, ϕ and angular coverage per detector module grouped by their assembly.

stop beam-like alpha particles scattered under low angle, which can damage the detectors and create high background rates. The setup is also equipped with a set of standard beam diagnostics equipment, including a Faraday cup, which was used for the initial focusing of the beam. Despite the shielding measures, a certain extent of radiation damage is unavoidable for the given geometry, as even the wanted reaction products have energies greatly exceeding the lattice binding energies of the silicon detectors' crystals. Additionally charge trapping in the detectors' passivation layers can occur. This results in a degradation of the detectors' performance over time, which was continuously monitored through the leakage current of the detectors. This effect will be further discussed in Section 3.5 and exemplary leakage current plots are presented in the appendix in Section A.3.

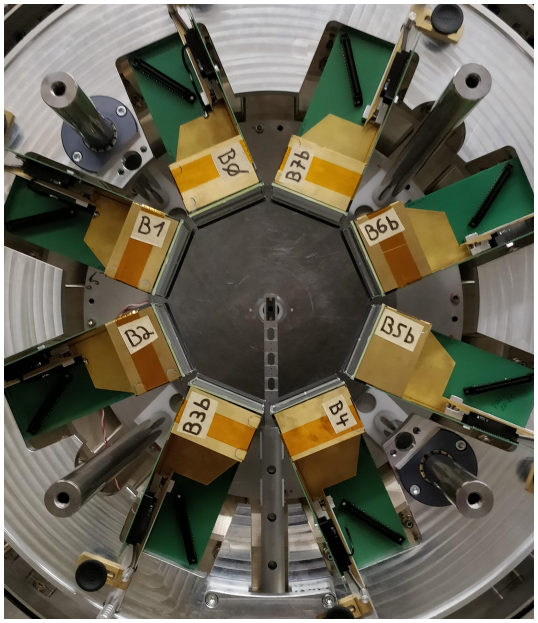

(a) Photo of one LYCCA ring , with eight barrel detectors facing the beam axis. The target (in the aperture position) is visible as is the added aperture at the chamber entrance in the background. The view is upstream towards the accelerator.

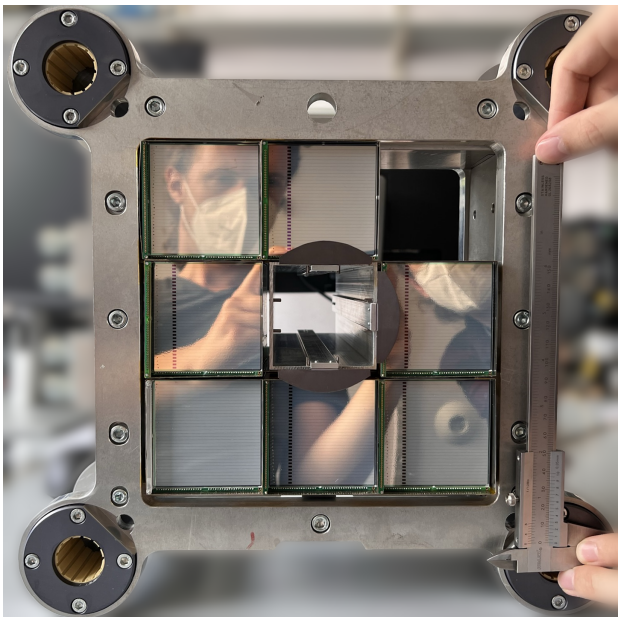

(b) The wall detector assembly containing seven out of eight detectors. Clearly visible are three of the four tantalum shields used to reduce the scattering of high-energy alphas into the delicate detectors and the gap in the center to allow the beam to pass through.

Figure 2.3: The two sub-assemblies of the LYCCA setup: Wall and ring detector groups.

2.2.2 LYCCA telescope

Each LYCCA telescope comprises of a DSSSD detector and a CsI-crystal scintillator with photo-diode (PD) readout, which enables the application of the ΔE-E measurement technique for particles which have sufficient energy to pass through the DSSSDs. While in the experiment discussed in this thesis only the DSSSD was used, the detector assembly will still be referred to as a telescope. The telescopes also provide structural support for the detectors as well as a robust electrical connection for readout and biasing. The telescopes are interchangeable and are mounted on a custom-built aluminum frame, which enables the aforementioned reconfiguration of the angular detector coverage.

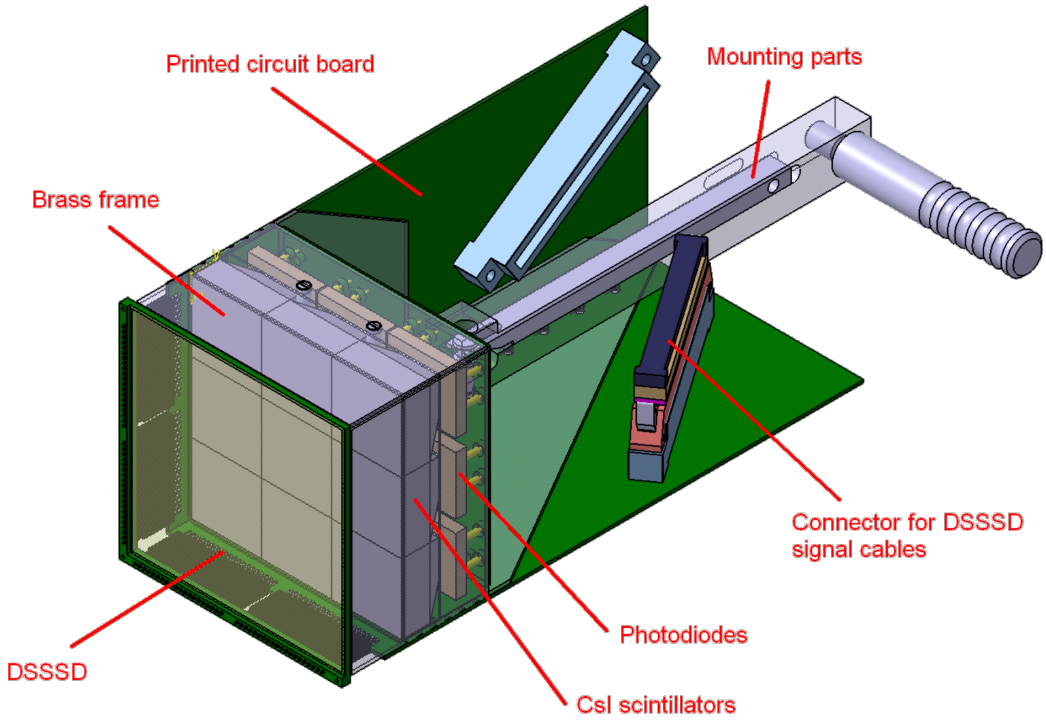

Figure 2.4: Schematic of a LYCCA telescope, showing the DSSSD and the CSI scintillator, as well as the mechanical assembly. Reprinted from Ref. [74], Copyright (2013), with permission from Elsevier.

2.2.3 DSSSD

The primary detection device of the LYCCA telescope is its double-sided silicon strip detector (DSSSD). The employed silicon detectors were produced by RADCON and are bonded to a custom printed circuit board (PCB) at the Lund University. The final assembly of the LYCCA telescope and integration testing was also performed there.
DSSSDs are position-sensitive semiconductor detectors that serve as a versatile tool for charged particle detection. A key advantage of DSSSDs is their ability to operate at room temperature while still providing good energy resolution.
The function of a semiconductor detector is governed by its electronic band structure, which determines the behavior of charge carriers (electrons and holes) in the material. The band model describes the energy levels available to electrons in a semiconductor. In this model, the band structure consists of a valence band, where electrons are bound to atoms, and a conduction band, where electrons are free to move and conduct electricity. The energy difference between these bands, known as the band gap, is 1.12 eV for silicon with 3.6 eV required to produce an electron-hole pair in the material at room temperature [75]. Due to its larger band gap, silicon has a low population of thermally excited electrons in the conduction band at room temperature. This results in a lower intrinsic carrier concentration and reduced leakage current compared to the often-used germanium

detectors. In comparison, Germanium detectors, with their smaller band gap of 0.67 eV, have higher intrinsic carrier concentrations and leakage currents at room temperature, necessitating cryogenic cooling to reduce thermal noise and maintain performance [76]. This cooling adds complexity and typically involves packaging that impedes charged particles, the primary detection focus of the LYCCA setup.

To enhance detection efficiency, semiconductor detectors typically employ p- or n-doping, introducing specific intentional impurities into the silicon to create regions with excess positive (p-type) or negative (n-type) charge carriers, forming a p-n junction. This creates an in-built electric field which allows charge carriers to migrate along the junction along the field. This diffusion leads to the establishment of an opposing adverse electric field which builds up until an equilibrium is reached. This equilibrium zone is known as the depletion zone, where mobile charge carriers are absent due to the diffusion of electrons and holes across the junction, which renders it highly sensitive to ionizing radiation. Applying a reverse bias-voltage to the p-n junction increases the electric field and widens the depletion zone. This increases the volume in which charge carriers can be generated by incoming radiation [75]. This layout is shown in Figure 2.5a. When charged ions

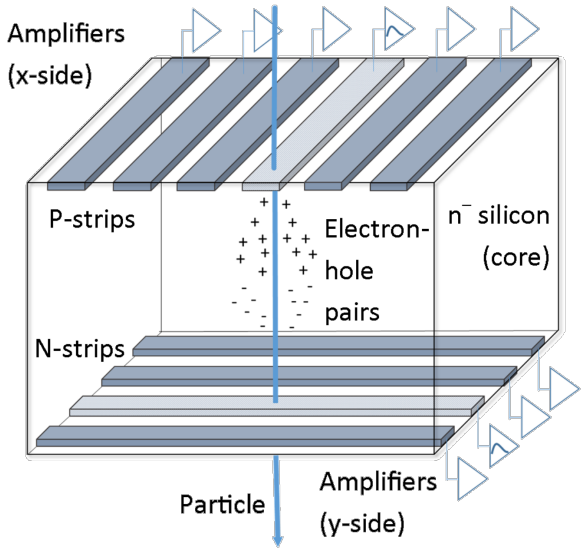

(a) Schematic of a DSSSD like the ones used in the LYCCA setup. The detector is operated in reverse bias, which creates a depletion zone in the silicon crystal. In the DSSSDs used in the LYCCA setup, the p-side faces the beam axis and will be referred to as the front side. Reprinted from Ref. [77], Copyright (2015), with permission from John Wiley and Sons.

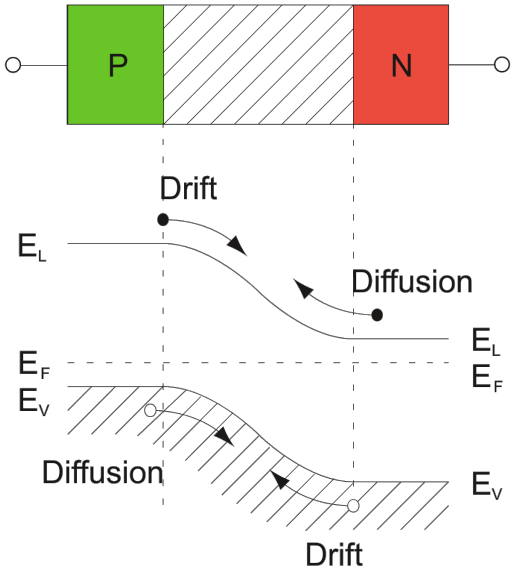

(b) Illustration of a p-n junction with the depletion in the center. The depicted energy levels are E_V for the valence band, E_L for the conduction band, and E_F for the Fermi level, where the probability of finding an electron is 50 %. Reprinted from Ref. [76], Copyright (2016), with permission from Springer Nature.

Figure 2.5: Schematic of a DSSSD and a p-n junction.

interact with the semiconductor material in the depletion zone, they lose energy through

ionization and excitation, resulting in the creation of electron-hole pairs. The electric field in the depletion zone promptly separates these pairs, with electrons moving towards the n-type region and holes towards the p-type region on the opposite side, generating a measurable electric current.
Due to the segmented structure of the DSSSDs, the charge carriers drift towards the nearest electrode, creating a measurable current pulse at the strips that overlay the particle's path inside the detector. Conversely this introduces the inter-strip effect, when a particle's energy deposition is either between two strips or the trajectory is not orthogonal to the detector surface.
The LYCCA-DSSSD consists of 32 conductive strips on each side, which then form 1024 virtual pixels, the intersect between each distinct strip pair on front- and back-side. The details of the LYCCA-DSSSDs are given in Table 2.2.

Table 2.2: Technical details of the LYCCA-DSSSDs. Data taken from [78].

Parameter	Value
Wafer dimensions	$(60 \pm 0.2) \times (60 \pm 0.2)\,\mathrm{mm}^2$
Active area	$58.5 \times 58.5\,\mathrm{mm}^2$
Thickness	$(303 \pm 3)\,\mu\mathrm{m}$
Number of strips	32×32
Strip width (p-side)	$1.8\,\mathrm{mm}$
Strip width (n-side)	$1.63\,\mathrm{mm}$
Interstrip gap (p-side)	$30\,\mu\mathrm{m}$
Interstrip gap (n-side)	$200\,\mu\mathrm{m}$
Dead layers (p-side)	$0.48\,\mu\mathrm{m}$
Dead layers (n-side)	$0.55\,\mu\mathrm{m}$
Full depletion voltage	typically $40\,\mathrm{V}$
Operating voltage	$50 - 70\,\mathrm{V}$
Leakage current	$10 - 15\,\mathrm{nA}$ per strip
Capacity	$33\,\mathrm{pF}$ per strip
Resistivity	$6.3\,\mathrm{k}\Omega\,\mathrm{cm}$

2.3 Inter-Strip Effects and Detector Dead Layer

Inter-strip effects in DSSSDs arise from the region between conductive strips, known as the inter-strip gap. These effects include partial energy deposition per strip and mixed charge collection, occurring when a charged particle passes close to or between adjacent strips, leading to multiple smaller current pulses instead of a single larger pulse. This effect is also known as inter-strip charge division and affects energy resolution and position determination [75]. While higher segmentation typically improves position resolution, it can also lead to energy being deposited in multiple strips, especially at slope angles.

Transverse diffusion and induced signals distribute charge across strips in a Gaussian manner, with a standard deviation related to the strip pitch [79]. Inter-strip capacitance introduces noise, and inter-strip gaps can create dead zones. In the LYCCA setup, these effects are minimized by ensuring the ion entrance angle is below 60° and using a high bias voltage to reduce capacitance [76].
Each detector surface is passivated with silicon dioxide (SiO_2), and the sensitive area is surrounded by guard rings. This forms a dead layer, 0.48 µm on the p-side and 1.55 µm on the n-side, with only the p-side dead layer contributing to the energy loss of incident particles. This layer can absorb incident particle energy, reducing effective detection energy. This is accounted for in the energy calibration, which maps the deposited energy in the DSSSDs and uses correction terms to ensure linearity, which will be further discussed in the following sections.
For this analysis, inter-strip effects are negligible due to their low event fraction given the relatively low area compared to the active area of a strip, as shown in Table 2.2 and can be excluded from the dataset using the analysis techniques described in the following sections.

2.3.1 Energy loss in matter

Since the LYCCA setup is only sensitive to the ions' energies deposited in the active area of the detector, the energy loss in matter of these ions as they pass through the detector needs to be considered. The differential energy loss of ions in matter, $-\frac{dE}{dx}$ per unit path length dx, commonly referred to as stopping power, can be described by the Bethe-Bloch formula

$$\frac{dE}{dx} = \frac{4\pi e^4 z^2 NZ}{m_e \beta^2 c^2} \left[\ln\left(\frac{2m_e\beta^2c^2}{I}\right) + \ln\left(\frac{1}{1-\beta^2}\right) - \beta^2 \right], \tag{2.1}$$

where e is the elementary charge, z is the charge of the ion, β is the velocity of the ion in units of the speed of light c, N is the target electron density, Z is the atomic number of the target material, m_e is the electron mass, and I is the mean excitation energy of the target material [80]. As the energies in the LYCCA setup are in the range of a few MeV, $\beta \ll 1$, resulting in simplification [73], which can be written as

$$\frac{dE}{dx} = \frac{4\pi e^4 z^2 NZ}{m_e c^2} \left[\ln\left(\frac{2m_e c^2}{I}\right) \right]. \tag{2.2}$$

This formula is a good approximation for heavy ions [81]. For lighter ions empirical data is used, which is tabulated in the SRIM database [82]. The energy loss of ions in matter is described by the stopping power, which is the negative derivative of the energy loss with respect to the distance traveled by the ion. The stopping power is given in units of

$\frac{\text{MeV}}{\text{cm}}$.

Two instances of energy loss are of particular interest in the LYCCA setup: The energy loss in the target material, and the energy loss in the silicon detectors before entering the sensitive depletion zone, commonly referred to as the dead layer. Both depend on the ion's energy before entering the medium and the effective path length given by

$$d_{\text{eff}} = \frac{d_0}{\cos(\omega)}, \tag{2.3}$$

where d_0 is the thickness of the material, ω is the angle of the ion with respect to the normal vector of the material, and d_{eff} is the distance the ion travels in the material. The incidence angle in the target is very close to the scattering angle θ, which is the angle between the beam axis and the scattered ion. The target is only rotated by $1.0(5)^\circ$ with respect to the beam axis, which was indirectly determined during the calibration process, explained in Section 3.4.2, which is corrected for during the analysis by rotating the incident angle by 1° in the opposite direction.

As the angular dependency in equation 2.3 also holds for the silicon detectors' dead layers, the entrance-angle of the ions into the detectors must be obtained to calculate the effective path lengths. This angle is dependent on the relative position of the individual pixel to the reaction position and is referred to as β in this work. It is defined as the deviation of the projectile's trajectory vector from the normal vector of the detector surface. It is computed using

$$\beta = \arctan\left(\frac{\vec{n} \cdot \vec{r}}{|\vec{n} \times \vec{r}|}\right), \tag{2.4}$$

where $\vec{n}$ is the normal vector of the detector surface, and $\vec{r}$ is the vector connecting the reaction point and the pixel center, which is the trajectory vector of an ion entering the detector. The θ-dependency of β is shown in Figure 2.6. As can be seen, the relationship between θ and β is linear in the wall detectors, because the wall plane is orthogonal to the beam axis. Since the barrel detectors are mounted to face the beam axis, the β-angles range from about 20° up to 60°, at which point the path length of the ions through the dead layer reaches double the path length of an ion entering a detector vertically. Due to its non-linear nature, energy losses cannot be fully compensated by the employed second-order polynomial calibration, as is evident in the deviation graphs for these calibrations, exemplified in Figure 3.13. Thus, the calibration maps the deposited energy in the DSSSDs, and not the actual energy of the scattered ions after the reaction. The latter is subsequently calculated by the energy loss in the target material and the dead layer.

The energy loss in the target material is dependent on the reaction position within the target, as the energy losses comprise of the initial loss of the beam particles before the reaction and the losses of the four reaction products after the reaction. As can be seen in

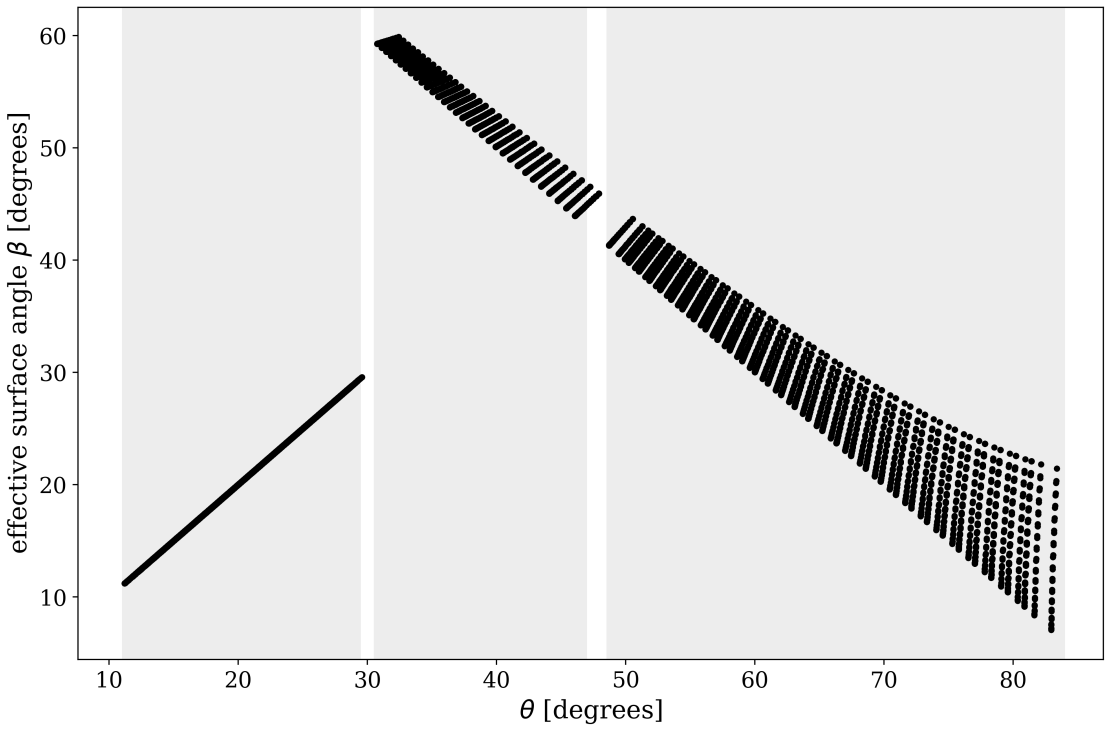

Figure 2.6: Dependency of the entrance-angle β for ions originating from the reaction position on the target on the scattering angle θ for all detectors in the LYCCA setup. As can be seen, the surface angle β reaches its maximum at about $\theta = 31°$, the end of angle range of the barrel detectors and the beginning of the wall detectors.

Figure 2.7, the energy loss at the beam energy (27 MeV) before the reaction is significantly lower compared to the losses for post-reaction energies. Additionally, the trajectory before the reaction is orthogonal to the target surface, minimizing the path length, while after the reaction the path length is substantially increased based on the scattering angle. This can be seen in Figure 2.8, where the energy losses for a reaction at the beginning of the target are compared to a reaction at the end of the target. The highest detectable angles, for example, at 83°, result in a path length increase by a factor of 8.2. Lastly, as ejectile, fragments and beam all consist of alpha particles, the increased number of four particles after the reaction also contributes to increased energy losses. To mitigate this, a *depth factor* is computed based on the measured energy of the ejectile, as its reference energy and angle are directly related. This factor is then used to scale the energy losses of the other particles, further increasing the energy resolution of the setup.

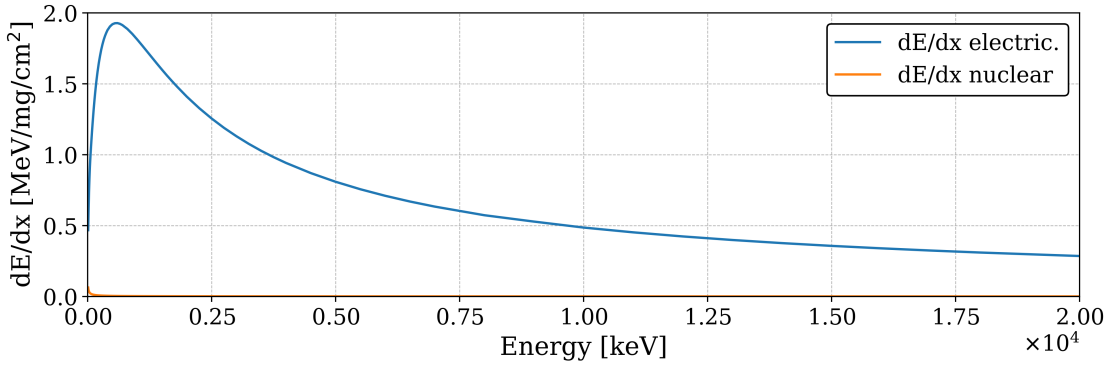

Figure 2.7: Energy loss of alpha particles in ^{12}C dependent on their energy. Data from the SRIM database [81]. As can be seen, the influence of the nuclear stopping power is negligible at and below the beam energy of 27 MeV.

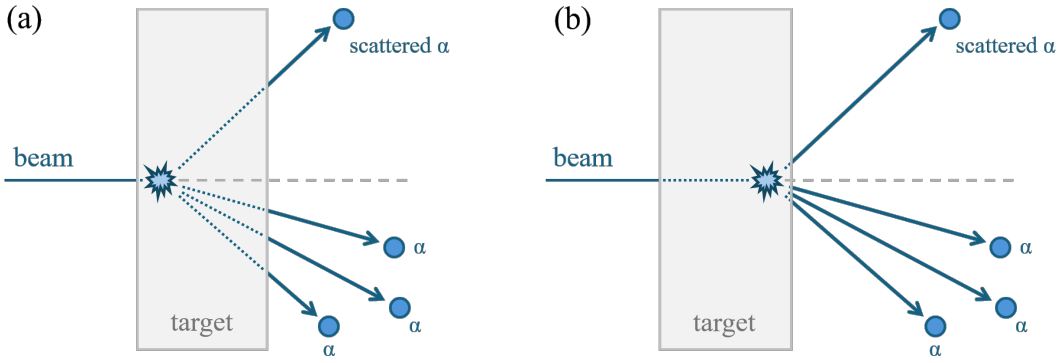

Figure 2.8: Energy loss in the target material dependent on the reaction position within the target. (a) depicts the energy losses for a reaction directly at the beginning of the target, (b) for a reaction at the end of the target. The comparison shows the increased path length through the target material for reactions occurring at the beginning of the target.

CsI-crystals

In the FAIR configuration only a part of the kinetic energy of the incoming ions is deposited in the DSSSDs. To enable readout of the entire energy of the ions, each DSSSD is paired with a set of CsI-crystals, enabling ΔE-E readout to allow for particle discrimination. The CsI-crystals, supplied from a manufacturer in Kharkiv, Ukraine [78], are wrapped in reflective foil to prevent light leakage. Each scintillator is read out by a PIN (positive-intrinsic-negative) type photo-diode. The mounting of the CsI-crystals inside a LYCCA telescope is shown in Figure 2.9.

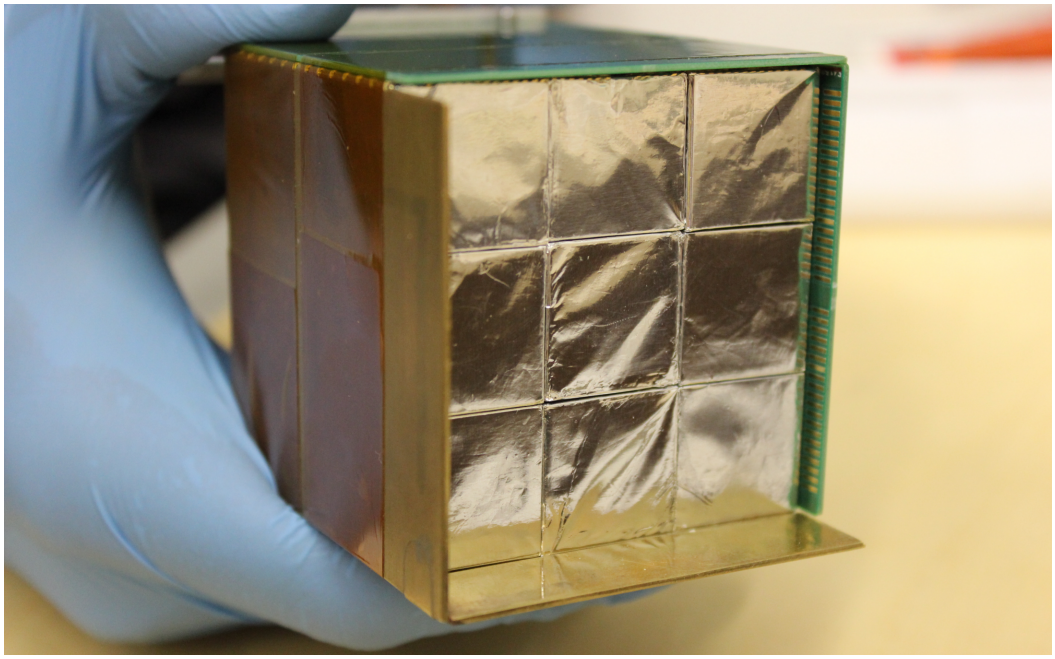

Figure 2.9: A LYCCA telescope without the DSSSD, showing the 3x3 grid of wrapped CsI-crystals. The photo-diodes are mounted on the backside of the crystals. From [73]

2.4 Data acquisition

As the complete LYCCA array, containing 26 DSSSDs in its final configuration, requires the readout of 1664 signal channels, a powerful data acquisition system is required. For this reason, integrated digital Front End Electronics (FEE) modules, which were originally developed for the Advanced Implantation Detector Array (AIDA) [83], were used, as their high integration density allows to read out one LYCCA DSSSD with only one FEE module. Each module comprises of four Application Specific Integrated Circuits (ASICs), which are installed on a separate Printed Circuit Board (PCB), the *mezzanine board*. This board is connected to the main FEE board using four connectors, shown on the left side of Figure 2.10. The ASICs contain signal processing electronics, such as preamplifiers, shapers, as well as threshold-comparators, peak-hold circuits, and control logic, allowing the output of triggered timestamp signals and shaped signal pulses for further processing. As each ASIC can process 16 channels, this enables the readout of all 64 channels of a DSSSD using one FEE module [84]. The entire system can operate in two energy ranges: low-energy (up to about 25 MeV) and high-energy (up to 1 GeV). Only the former was used during the experiment, to fully utilize the dynamic range of the system, as during the experiment only particles with energies up to 25 MeV were of interest.

After initial signal processing the ASICs output pulses are fed to one of eight eight-channel 16-bit ADC Analog-to-Digital Converters (ADCs) where the pulses are digitized.

The resulting signals from ASICs and ADCs are then processed by a Field Programmable Gate Array (FPGA) which can send control signals to the previously mentioned components and collects the readout of the previously mentioned components. It also contains a *MicroBlaze* processor running *Linux*, which is used to interface the FPGA with the data acquisition software. The acquired data is then passed to a central data server for storage using a Gigabit Ethernet connection [73]. The output is sent as data blocks, containing events sorted by their readout time. Each AIDA module also contains support electronics, such as power distribution circuitry, temperature sensors, and a timing synchronization link, which is used to synchronize the time stamps of the individual modules. To ensure low operating temperatures, each FEE module contains a water cooling loop which can be hooked up to the common cooling water supply of the LYCCA setup. One AIDA FEE board is shown in Figure 2.10. Each module provides a 10 ns discriminator timing signal, as well as 16-bit ADC signals with a readout frequency of 5 MHz (200 ns per sample) [73].

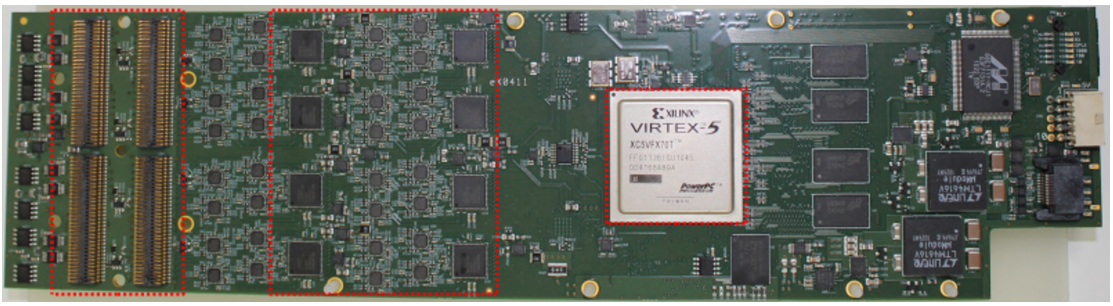

Figure 2.10: An AIDA FEE board, which is used to read out the LYCCA detectors. The three outlined sections (from left to right) are the transmission circuits, onto which the mezzanine boards containing the ASICs are mounted (not shown in the image), the eight ADCs, and the FPGA, which controls the FEE module.

The FEE modules are mounted in a ring shape, as can be seen in Figure 2.11, to minimize the cable length between the detectors and the FEE modules. The modules' common grounding was provided using a wide low-ohmic copper band, which was connected to the LYCCA setup's ground. The modules are supplied with water from a central chiller unit and power from a rack-mounted power supply unit. The data connection is established using a standard Ethernet connection through a Gigabit Ethernet switch, which enables the separate control of each FEE module and the data readout.

Since the only electrical connection to the DSSSDs is the signal cable, the detectors have to be supplied with the necessary bias voltage through the FEE modules. The applied bias voltage is 50 V, but was slightly reduced to 40 V during the second beam time to limit the increase of the leakage current of the detectors. The bias voltage is delivered by four four-channel Mesytec MHV-4 high-voltage power supplies [85] mounted in a NIM crate.

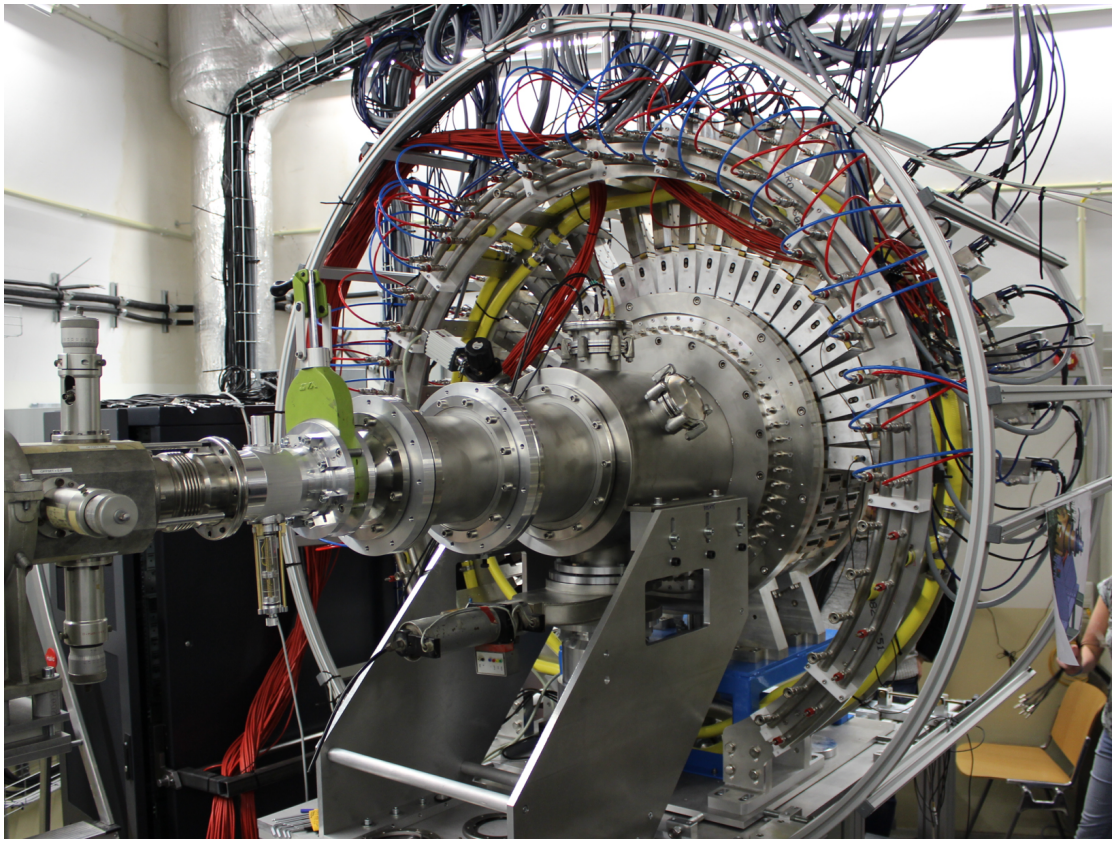

Figure 2.11: The LYCCA setup in the *OSIRIS* hall at the Institute for Nuclear Physics in Cologne. The beam line enters from the left. The AIDA front-end electronics (FEE) modules are arranged radially around the chamber, accompanied by their red and blue cooling water supply tubes.

As during the beam time, 20 detectors were connected, of which 18 were used for the experiment, a few channels had to be shared between detectors. The 16 available bias channels allowed 12 detectors to be supplied separately and the remaining eight active during the experiment to be supplied in pairs. No problems were observed for the detectors sharing a bias channel.

The time synchronization of the modules was achieved by using the *MACB* modules. These NIM mounted components form a hierarchical high resolution time synchronization network [86]. The MACB modules send and distribute 50 MHz clock signals, which are distributed to all modules, to synchronize the timing. The cables used were common HDMI cables due to their good high-frequency characteristics and availability. In the MACB topology, one AIDA FEE module is selected as the reference module (in this case the first module, *nnlycca1*, was used) and its timing signal is broadcast to the other FEE modules [87].

The primary control and data acquisition are run on a separate computer, which was connected to the FEE modules via Ethernet. The computer, which runs the control and data acquisition server (historically named the *tape server*), uses the Multi-Instance Data

Acquisition System (MIDAS) software, developed and maintained by the STFC laboratory in Daresbury, UK [88], for electronics control and data acquisition [73]. The data is split into runs and subruns, where each run corresponds to a single data acquisition cycle, comprising of several subruns, which are automatically incremented once about 2 GB of data is collected. During the beam time electronic instabilities mandated multiple system reboots, the data taking was also briefly interrupted twice due to source current instabilities. This, including the system being shut down and restarted between the two beam times, incremented the run number each time. The primary analysis consisted of 2436 subruns in 20 runs, with 865 subruns in 8 runs taken during the first beam time in December 2019, and 1571 subruns in 12 runs taken during the second measurement campaign in January 2020.

2.4.1 Energy thresholds

Each electronic discriminator system must be able to differentiate between noise and actual signals. Different approaches are used to achieve this, the most direct one being a direct threshold comparison. Each experiment must strike a balance between capturing noise events and potentially discarding valid experimental data. In the described measurement, the threshold can be set lower to rarely accept noise contributions, since the later analysis stages combine four separate signals (front side: ADC + discriminator, back side: ADC + discriminator) to form a valid detector hit event, which reduces random background (further detailed in Section 3.3.3). Still, erroneous triggering of the discriminators increases dead times and can lead to data loss. During tests the very high erroneous trigger rates saturated the DAQ, inducing high dead times up to 90 %. This causes the data acquisition system to become overloaded by high trigger rates, leading to instability or even crashes as experienced multiple times during the preparatory test measurements leading up to the experiment.
During these initial tests, idle detector rates were taken without calibration sources or pulser input. These rates are detailed in Figure 2.12, which shows the trigger rates of the detectors dependent on their energy threshold. It must be noted that this shows an ideal scenario without beam and with reduced equipment active. The shown energy dependency is only roughly calibrated, as more precise calibrations were only performed at a later stage. The rates increase exponentially with decreasing threshold, which is expected as the detectors are more likely to trigger on noise events. The high noise band is clearly visible and also varies greatly from module to module. This was a known limitation of the AIDA modules at the time [89]. The problem was remedied by imposing high veto-thresholds of up to 1.35 MeV on the detectors, which reduced the trigger rates to a manageable level. The thresholds, set per-detector, are listed in Table 2.3. The

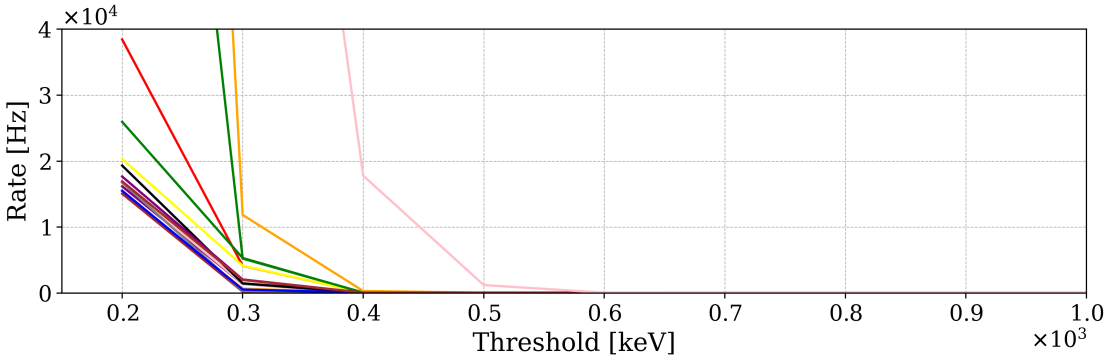

Figure 2.12: Plot of the trigger rate of the detectors in the LYCCA setup dependent on their energy threshold. As can be seen the rates increase exponentially with decreasing threshold. The energies are only roughly calibrated and use a proportional scaling to map them to equivalent energies. Each detector is a single line in the plot. The pink line shows the rate of detector 26, which showed very noisy energy and time spectra and was not used for the subsequent experiment. The scale is cut off at 40 kHz to show the lower rates, but the highest values reached up to 170 kHz.

values were obtained from the analysis codes during event combination.
Vetoing all event below a certain energy also discards valid detectors, which reduces the efficiency of the setup, especially for the decay products of the Hoyle state. The effects of this were modeled using the Monte Carlo simulation, discussed in chapter 5.

Table 2.3: Energy thresholds of the LYCCA detectors during the Hoyle state campaign.

Detector	Threshold [keV]	Detector	Threshold [keV]
Mod 1	600	Mod 16	800
Mod 3	450	Mod 17	1250
Mod 4	1350	Mod 18	1350
Mod 6	1050	Mod 19	1150
Mod 7	800	Mod 20	1350
Mod 10	1050	Mod 21	800
Mod 13	1450	Mod 23	800
Mod 14	800	Mod 24	850
Mod 15	950	Mod 25	900

2.5 Targets

Multiple ^{nat}C targets were produced for the experiment, out of which two with different thicknesses were selected to be used during the measurement campaign. The primary target was a 0.114 $\frac{\text{mg}}{\text{cm}^2}$ ^{nat}C target, which was used during both beam times. It is depicted in Figure 2.13a. The secondary fallback target was a 0.133 $\frac{\text{mg}}{\text{cm}^2}$ ^{nat}C target, which was not used for the primary experiment. Additionally, gold targets were produced using

rolling, which were used to test the overall performance of the setup, as the high mass of the gold nuclei results in a different kinematic behavior compared to the carbon targets due to the low momentum transfer. The carbon targets were produced using vacuum

(a) The 0.114 $\frac{\text{mg}}{\text{cm}^2}$ ^{nat}C target which was used in both beam times, glued onto an aluminum support frame before being mounted onto the target ladder assembly.

(b) The target ladder with (top to bottom) a 3 mm diameter aperture, the two ^{nat}C, and the ^{197}Au target. The used target shows the darkened beam spot.

Figure 2.13: Close-up of the used target and a view of the target ladder assembly showing the targets mounted during the beam time.

evaporation of graphite onto a glucose covered glass substrate. The target material on the substrate was then cut and lowered into a water bath, to dissolve the glucose. This leaves a thin floating layer of carbon on the water surface, which can then be placed onto an aluminum support frame and weighed to determine the mass per area. As the used targets are sufficiently thick, they are considered self-supporting and do not require a backing foil.

During a brief test measurement in 2019 to commission the new setup geometry using a $^{nat}\text{C}(\alpha, \alpha\prime)^{12}\text{C}$ reaction, kinematic background from scattering of the beam's alpha particles on ^{16}O and ^{1}H in the target material was observed. This was unsurprising, as the target production process involves floating the target material on water and contact to

the glucose substrate as well as the atmosphere, which can lead to surface-incorporation of trace amounts of oxygen and hydrogen. To test the suppression of this background, a backup target was produced in the same way, but was heated to 100 °C to allow surface contaminants to evaporate. While this was successful in reducing the background as demonstrated in a brief test measurement, the target surface was impacted by the heating process, as can be seen by the wrinkling on the target surface in Figure 2.13b. This downgraded the target to a backup target, as the surface structure increased the energy-loss uncertainty and made the target more susceptible to beam-induced damage. The primary target was subsequently not heated, as the background was deemed acceptable for the experiment. Another reason to use the primary target was to use the inverse kinematics of the ^{1}H(^{4}He,^{4}He)^{1}H reaction to enable tracking of the beam spot position during the beam time, which will be further discussed in Section 3.7.
The use of an enriched ^{12}C target was considered, but since the natural abundance of ^{12}C is 98.93 % and the abundance of the heavier isotope ^{13}C is only 1.1 % [90] this was deemed unnecessary as the reaction kinematics between ^{12}C and ^{13}C differ sufficiently due to the mass difference of 8.4 %. However, the minimal improvement in the signal-to-background ratio did not justify the additional cost and extended lead time necessary to procure the enriched target externally.
As discussed, the thicknesses of the used ^{nat}C target and the backup target were obtained by weighing the target foils and calculating the area density by dividing by the area of the target. Since the target thickness directly impacts the energy losses of the reaction products in the target material, it is an important parameter for the analysis. For this reason, a follow-up validation of the target properties was performed at the *RUBION* facility in Bochum using Rutherford backscattering [91]. The result, 0.1155(58) $\frac{\text{mg}}{\text{cm}^2}$, is consistent with the weight-based measurement. Given the errors of the measurements, the results can be considered consistent. The RUBION study is further detailed in the appendix (Section A.1). The measured values are slightly below the optimum value for the calibration, which varies between 1.05 and 1.25 times the nominal value, which can be attributed to other parameters such as target roughness and variations between the dead layers of the detectors, which also impact the optimization process.

Chapter 3

Data processing

In this chapter, the general data preparation and preprocessing steps required for the analysis of the LYCCA data are described. The data analysis pipeline is outlined in Section 3.1, and the calibration of the detectors is explained in detail (Section 3.4). Lastly, correction approaches to mitigate effects such as energy losses in the target material and the dead layer of the detectors, detailled in Section 3.6 or the variation of the beam spot position during the beam time, described in Section 3.7, are discussed.
The raw initial data obtained from the data acquisition system consists of a binary stream which contains multiple types of entries. These are either related to the status of the setup, like sync signals, additional timestamp information, or are linked to a detection in a certain detector strip. The different entry types are detailed in Table 3.1.
These data need to be combined and prepared to reconstruct detector hits of particles.

Table 3.1: Raw data entry types obtained from the data acquisition system.

	ADC signal	**Discriminator signal**	**SYNC signal**
Location	Position (detector + strip)		-
Time	ADC clock 2 µs (500 kHz)	FEE clock 10 ns (100 MHz) (lower 32 bits)	FEE clock 10 ns (upper 32 bits)
Energy	16-bit	-	-

First, the input data needs to be converted into a more accessible format. Next, the energy and timing signals are combined to form events. The front- and back-side signals of the detectors are then combined to form a single event, creating a complete detector hit entry, which contains energy and timing information and the pixel coordinate of the hit. This pixel coordinate is then converted into spherical coordinates to determine the scattering angle of the detected particle.
This chapter closely follows the path one single detection event takes from the raw data to the final reconstructed event, which contains the entire information required to perform the physics analysis.

3.1 Data analysis pipeline

The processing of the data is performed using a sequence of programs, which were written for this purpose. The whole analysis software forms a pipeline, taking in raw data from the data acquisition system and outputs the complete detector hit information.
This data analysis pipeline consists of several programs which were developed throughout this thesis to process the raw data from the data acquisition system into processed background-suppressed events in the center-of-mass frame of our reaction of interest. The codes combine, calibrate and filter the data using *gates*, logical conditions that select which events are kept for further analysis. The pipeline is illustrated in Figure 3.1.

During the two weeks of beam time, about 5 TB of event data were recorded. To pro-

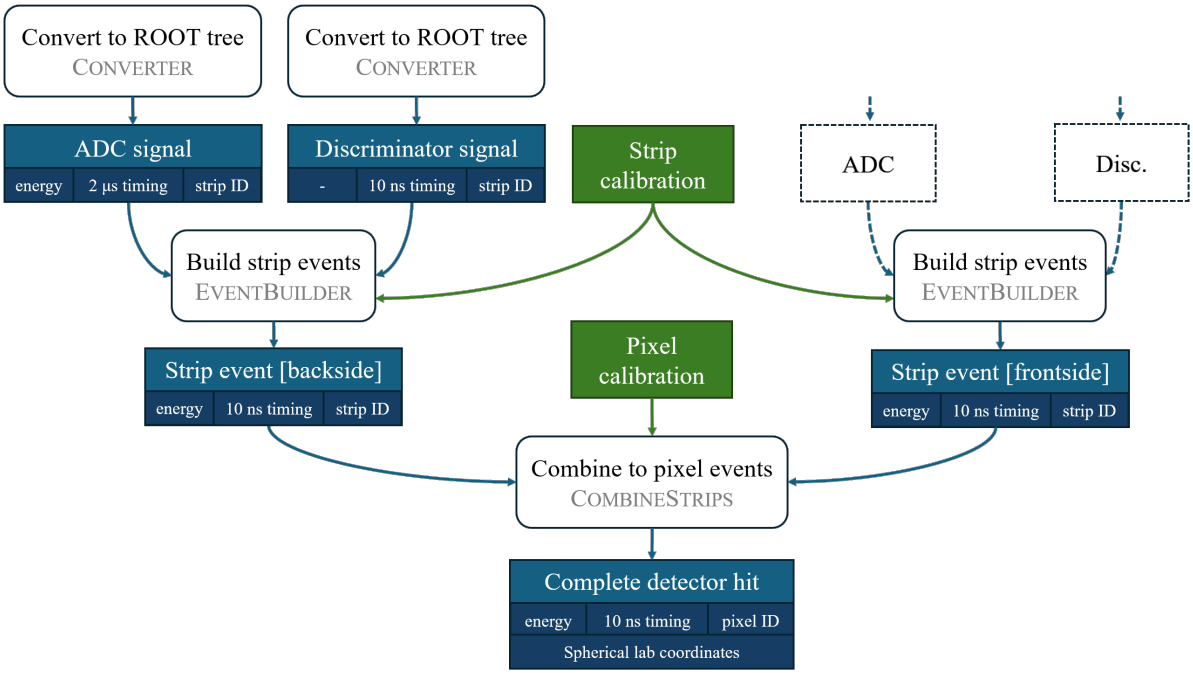

Figure 3.1: The LYCCA data analysis pipeline, showing the different steps from converted raw data to the final recombined events. After the initial events are obtained from the CONVERTER, strip events are built for front and back side signals. These are subsequently combined to form a single detector hit. The line below each shown entry shows the available information in that respective event.

cess this data quickly, the analysis pipeline was designed to run as efficiently as possible and utilize the available computing resources of the institute. The high number of 1152 detection channels also required a substantial degree of automation to ensure the analysis is reproducible and reliable. A list of the most important programs developed for this analysis can be found in the appendix (Section A.7). The analysis broadly consists of two phases: Data preparation, up to the combination of front- and back-side signals, and the analysis of the combined events.
The whole pipeline comprises the following sequential steps, not including smaller helper

scripts and gate-finding code:

1. Converter: The raw data from the data acquisition system is converted into the ROOT tree format.

2. EventBuilder: The ADC and discriminator entries are merged into one entry containing time and energy information for one detector strip.

3. CombineStrips: The front- and back-side signals of the detectors are combined into a single detector hit (pixel event) with position, energy, and timing information.

4. AnalysisKinematics: Sets of conditions are used to filter the data for the reaction of interest (not shown in the Figure, as this step is performed after the data is prepared) and transform the data into the center-of-mass frame.

3.2 The ROOT framework

The following analysis makes extensive use of utilities and classes provided by the ROOT analysis software framework [92]. The ROOT framework is a software package developed by CERN for data processing, statistical analysis, and data visualization which was initially released in 1994 [93] and has since become a standard tool in the field of high-energy physics. It is also widely used in nuclear physics and other fields. The ROOT framework is written in C++ and is provided as open-source software.
Over the years, the ROOT framework has grown to include a large number of classes and utilities and is still in active development. The analysis software in this work relies on several ROOT features: General data processing classes (such as ROOT trees), histogramming, fitting, and visualization classes provided by the ROOT framework.

3.3 Preprocessing

After data acquisition by the MIDAS system, different types of events are written to the output files: Signals from the analog-to-digital converters (ADCs) with 16-bit energy channel data and a 2 µs time resolution, and two different signals from the discriminator on the FEE modules: One general clock-synchronization signal, containing the upper 32 bits of the 64-bit timestamp, and the individual discriminator signals, which contain the lower 32 bits of the timestamp with a timing precision of 10 ns, but no energy information. Each signal also carries information about the module ID and the channel ID, which allows merging of ADC and discriminator data to create events with both energy and precise timing information.

3.3.1 Converter

The MIDAS system collects and writes its data in a binary data format, which is not directly usable for analysis. To prepare the data for further processing, the data is converted into the ROOT tree format. The pre-existing conversion code was heavily modified and extended. It now supports multithreading, and the merging of the two timestamps in the original format (one containing the upper 32 bit and the other the lower 32 bit of the 64-bit timestamp) into a single 64-bit timestamp. This is necessary to ensure that the timestamps are correctly ordered, as the timestamps are used to determine the time difference between events, which is crucial for the later coincidence gate, described in Section 4.1.1. Additionally, the converter has been extended to also detect copied discriminator events: In some cases, the discriminator circuits in the AIDA-FEE modules create multiple events per detected signal. The source of this seems to be related to an unreliable discriminator reset and the data readout. In the converter these erroneous entries can then either be tagged or removed from the data, depending on the configuration of the converter. In the following analysis the copied events are removed from the data.

3.3.2 Event building

As the recorded data consists of separate ADC and discriminator entries, a custom built tool called EventBuilder is used to merge the two data types into a single event.

Since each module has slightly different timing characteristics, which varies between power cycles (between runs), the gate widths for the EventBuilder are automatically deduced using the tool timetest, developed for this purpose. Figure 3.2 illustrates the time difference distribution for a single detector and run. A few features of the timing signals are shown here: Periodic spikes coinciding with clock frequencies of parts of the FEE modules, indicating unwanted signal pickup which caused false triggers. Since our follow-up analysis uses only the discriminator signals for timing information and the timing gates between ADC and discriminator are set wide (typically 7 µs), these artifacts do not impact the analysis. timetest is also used to determine the time offset between the ADC and discriminator signals, which typically is at about 8 µs.

At this stage each data event contains a timestamp, the ADC channel, the triggered strip and its containing module index, as well as some additional tracking information (such as if copies of the discriminator signal were detected). Using this information the EventBuilder is then used to obtain an initial energy calibration for each detector strip, as further described in Section 3.4.1. This calibration is then used to also store the energy information in the event data.

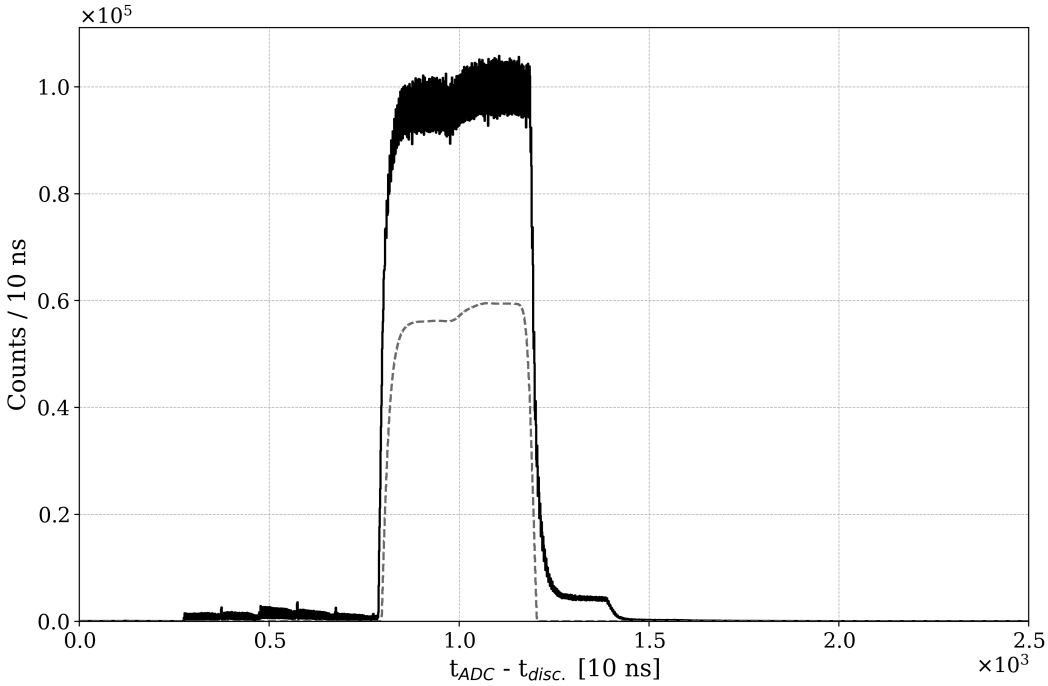

Figure 3.2: Time difference distribution between ADC and discriminator for module 21. The dashed line shows the filtered time curve after background subtraction.

3.3.3 Pixel event recombination

The data generated by the EventBuilder is still separated into front- and backside strip-detection events. These need to be combined to form a single detector hit. A good visualization of the prerequisites for this combination is shown in Figure 3.3 - this figure plots the energy of the p-side against the energy of the n-side of the same detector using a wide time-gate of 220 ns. The energies are obtained using the initial linear per-strip energy calibration created using the triple-alpha source. While the diagonal line shows events where the full energy of a detected particle is read out on both sides and demonstrates good linear behavior, the horizontal and vertical lines as well as the low-energy background indicate that narrow energy and time conditions are required to ensure that only full-energy events are combined. The horizontal and vertical lines are caused by particles which deposit parts of their energy in the inter-strip region between two active strips. These events should be excluded from the analysis, as the missing energy correlation information reduces the ability to distinguish between random coincidences. A reconstruction of events with partial energy deposition is computationally more complex and will be studied in future work. As seen in the figure, however, the majority of events are full-energy events and can be combined.

To combine the data from the detector's front and back side, a custom tool called CombineStrips was developed. Similar to the EventBuilder, two entries need to be matched to form a single registered hit. Since multiple events can be registered by each detector during a single tick (the time resolution of the discriminator), narrow gates are

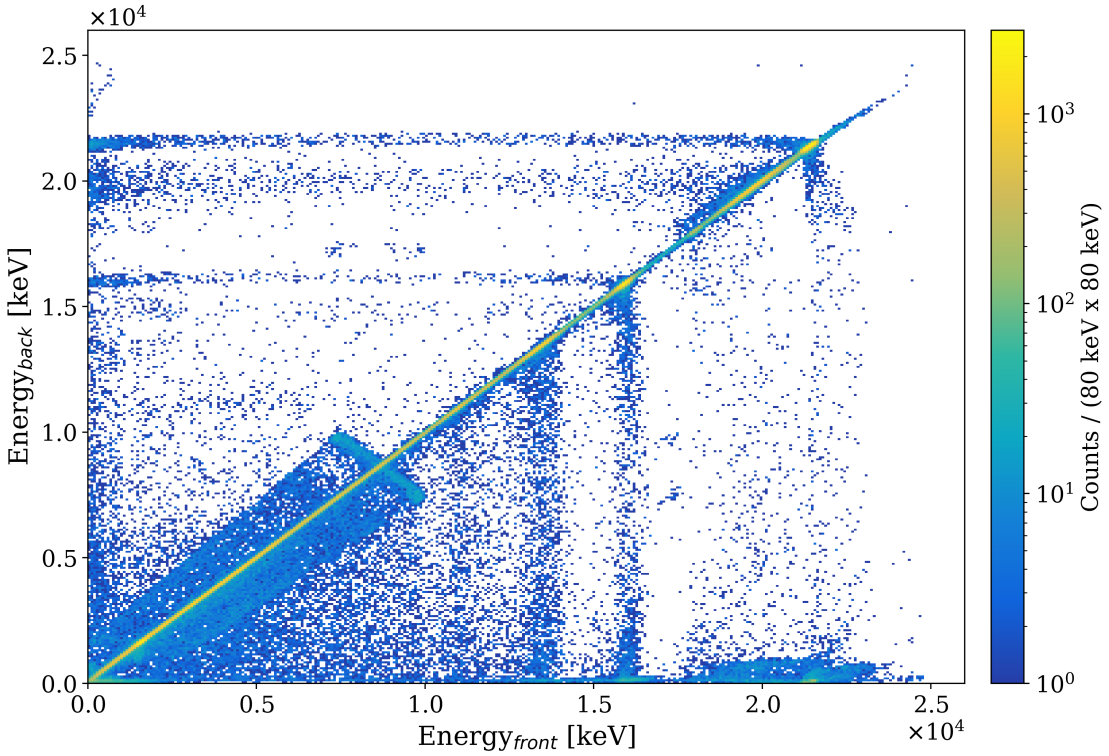

Figure 3.3: Energy correlation between front- and backside strips for module 14, showing data of one single run. The diagonal line shows events that can be combined. The horizontal and vertical lines are caused by partial energy depositions on one of the detector sides.

set to ensure that only events within a certain time window are combined. These gate widths are automatically determined using a tool called WINDOWTEST. This tool scans the entire entry list obtained from the DAQ and determines the time and energy difference distributions between events in the same detector. In contrast to Figure 3.3, the distributions just show the time and energy difference between the front- and back-side signals of the same detector against the energy of the front-side signal. The time distribution can be generated directly from the incoming data, while the energy distribution only includes energy entries within a 60 ns window around a time difference of zero. Examples for a ΔE and ΔT spectrum for a single detector are shown in Figure 3.4. These distributions are not constant with respect to energy over the entire sensitive range of the detectors, though. To take into account this dependence, the COMBINESTRIPS tool uses energy-dependent gates for the time and energy signals. This is done by fitting projections for every 400 keV energy bin, which yields the mean and standard deviation for each energy bin. These values are then used as the boundary of the gated region. Values between these fits are interpolated to ensure a continuous gate width function and be more robust against event-count differences per energy bin. The Figures 3.5 and 3.6 contain example plots demonstrating the energy and time difference distributions between strips on the front- and back-side of the same detector, used for determining appropri-

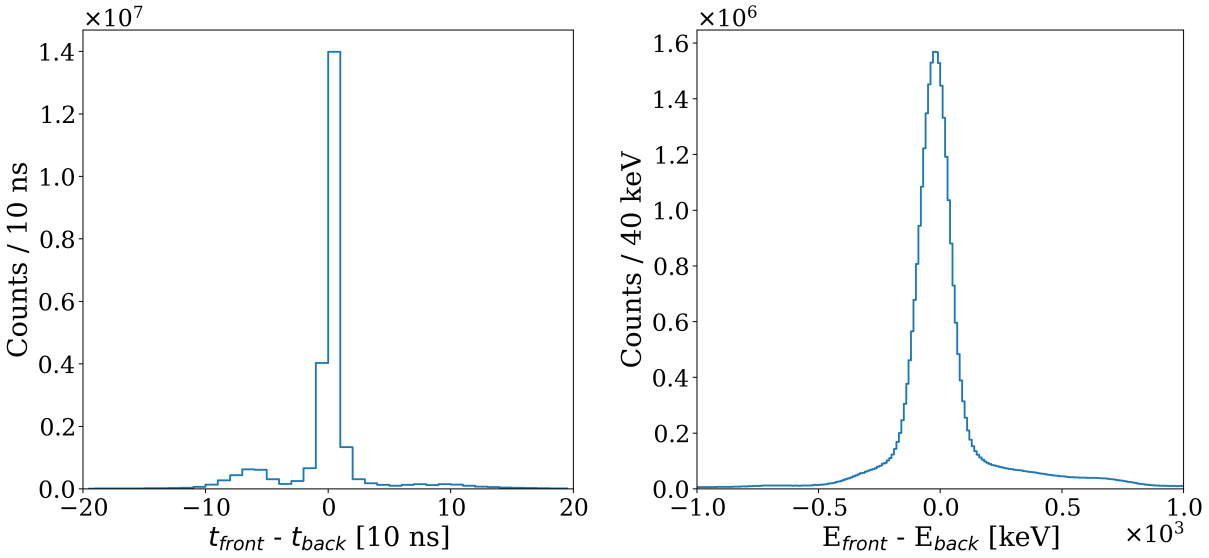

(a) Time difference distribution for the front- and back-side signals for module 24.

(b) Energy difference distribution for the front- and back-side signals.

Figure 3.4: Example distributions for the determination of the width of the employed conditional gates for the pixel combination for module 24.

ate gate widths for accurate pixel combination. This is done on a per-detector basis, since each strip and ADC / discriminator channel has slightly different energy resolution and timing characteristics. Typical gate parameters obtained by this approach for the performed experiments are detailed in Table 3.2.

Table 3.2: Gate parameters for the CombineStrips data processing software.

Parameter	Width	Typical width (Det. 18, Run 5, 10 MeV)
Energy gate width	3.0 σ	$\pm$128 keV
Time gate width	2.5 σ	$\pm$20 ns (2 discriminator ticks)

Another option of the CombineStrips tool is the possibility to export partial events: Since each event consists of a front and back side signal, each of which contains an ADC and a discriminator entry, events can also be built when only three of these four entries are present. While these events will be further explored in the future, for the current analysis they are not used, as the loss of one of the gate conditions when combining the front- and back-side signals does lead to a worse signal-to-noise ratio for the events, as the missing conditions reduce the background suppression.

The overall combination efficiency averages 55 % for the runs from December 2019 and about 47 % for the runs from January 2020, reflecting the slightly degraded performance of the detectors due to radiation damage from the prior beam time. The effect of radiation damage on the detector setup will be further discussed in Section 3.6.1.

One challenge in the combination of front- and back-side data are instances where multiple

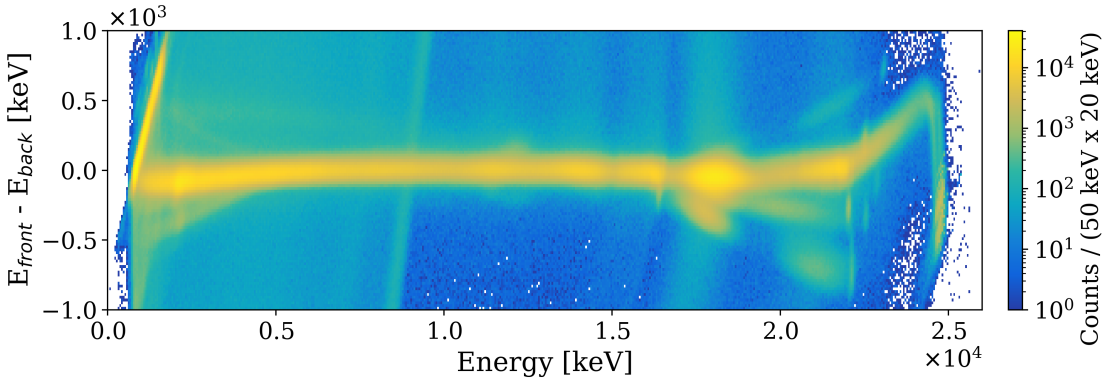

Figure 3.5: Example distribution of the energy difference between the front- and back-side signals on module 24 used to determine the energy-dependent gate condition width.

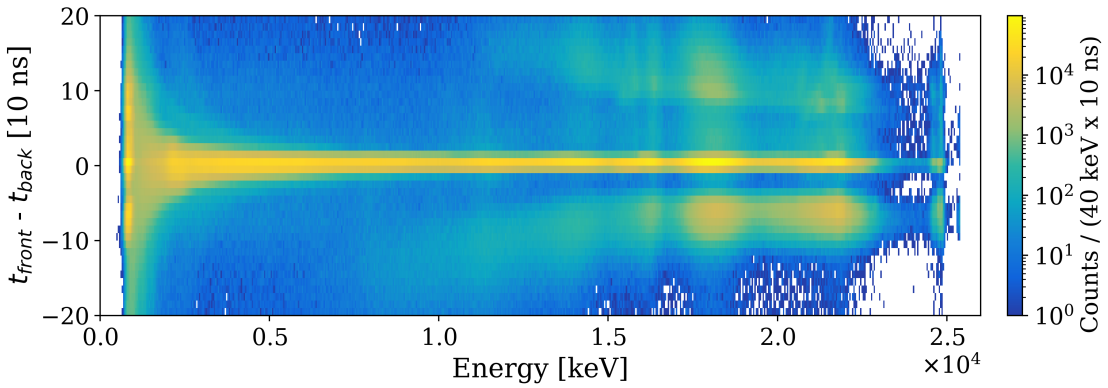

Figure 3.6: Example distribution of the time difference distribution for the front- and back-side signals on module 24 used to determine the energy-dependent gate condition widths.

alpha particles are detected in a single detector at the same time. Since our reaction products consist of up to four alpha particles, this has a non-negligible probability. The only way to distinguish between these events is the energy and time information of the signals. The impact difference of particles from one event is less than the time resolution of the data acquisition system, as further elucidated in Section 4.1, leaving just the energy information to distinguish between the events. If these alpha particle energies are closer than the typical energy difference between front- and back-side signals of about 130 keV, the pairing of the signals becomes ambiguous. This problem is demonstrated in Figure 3.7. The potentially mismatched pairings are still combined and their impact on the analysis will be resolved in later processing steps (see Section 4.1.6).

Lastly, the obtained events are sorted by their timestamp to ensure that the events are ordered correctly for the later analysis steps. The resulting output is then written to a ROOT tree, which allows easy access to the data and efficient processing.

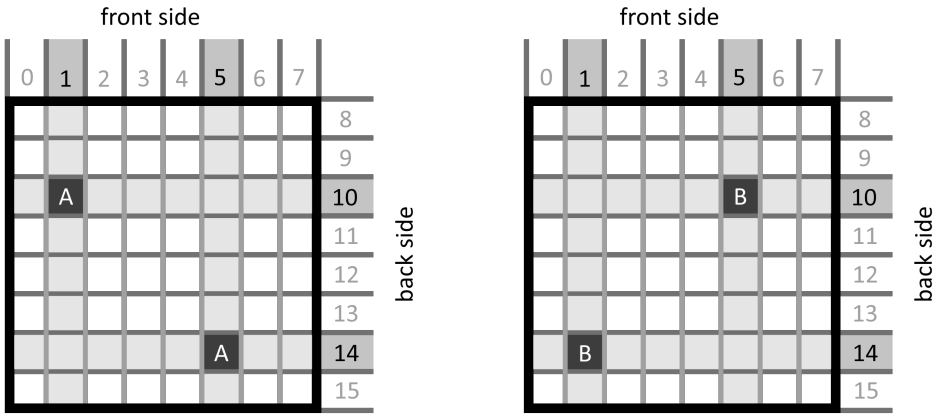

Figure 3.7: Combinatorial problem in the pairing of front- and back-side signals on a simplified proxy for the used DSSSDs. In this case strips 1,5,10, and 14 were activated by two alpha particles landing in both A locations. Based on the activated strips, the A and B combinations mark the two possible pairings.

3.4 Calibration

To analyze the data, the ADC channel information provided by the DAQ needs to be converted into energies. For this, two different types of calibrations are used:

- A calibration of the detector strips using a Triple-alpha-source.
- A pixel calibration using the kinematic lines of the scattered alpha particles (and the Triple-alpha-source, if sufficient statistics are available).

Statistics is a general problem for the calibration, as a sufficiently high number of events per pixel is needed to obtain a reliable calibration. Since each strip comprises 32 pixels, this limitation is especially relevant for the pixel calibration.

3.4.1 Strip calibration

To obtain an initial calibration of the LYCCA setup, a Triple-alpha-source was used. The used source consists of ^{239}Pu, ^{241}Am, and ^{244}Cm. These can decay into an alpha particle and a daughter nucleus, which is either in its ground state or in an excited state. The emitted alpha particles are observed and their known decay energies are used for the calibration. As each of the isotopes can decay into multiple states which are close in energy, first, the corresponding centroid energy of each isotopic decay must be determined. This is done by using a simulation of the decays, summing up the individual decay energies weighted by the branching ratio of the decay. The result of this simulation is shown in Figure 3.8. Since the energy resolution of the LYCCA setup does not allow to fully resolve the individual peaks per isotope, the effective peak position was then determined by fitting Gaussian functions to the sum of the simulated events using the known decay

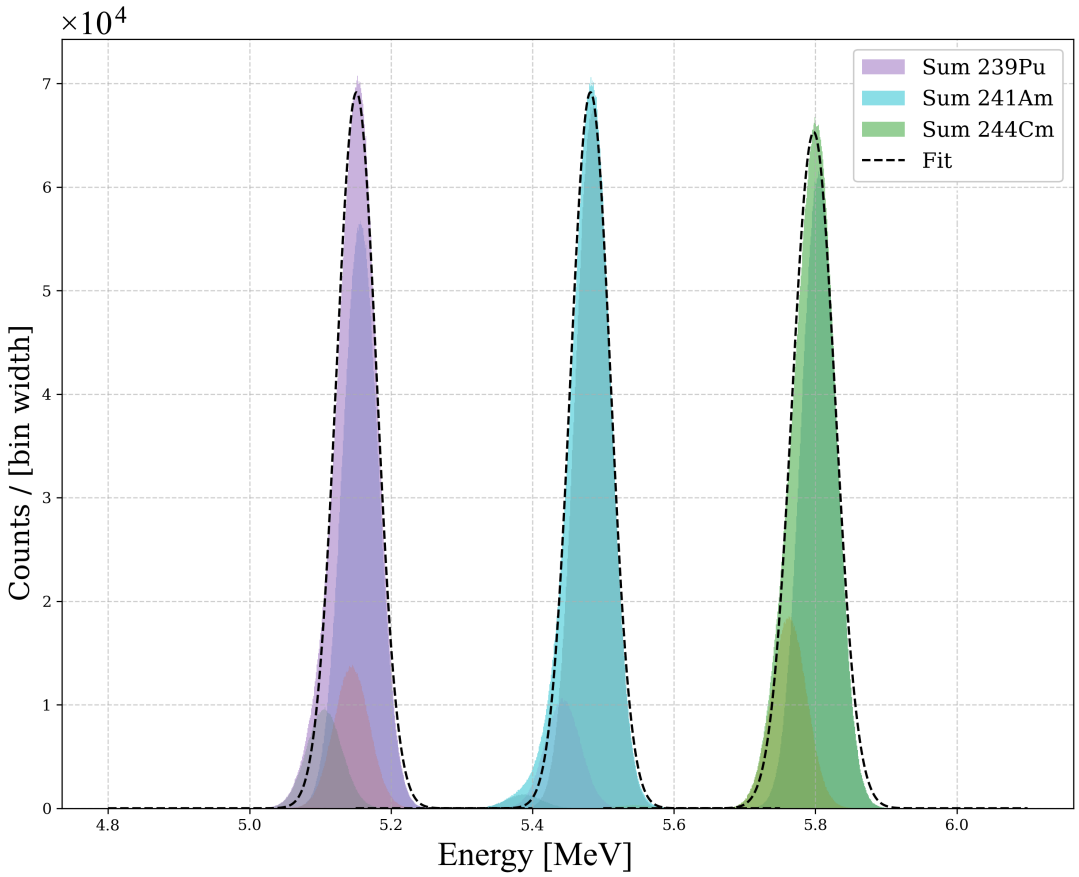

Figure 3.8: Spectra of the simulated triple-alpha source used for the calibration of the LYCCA setup. The peaks are fitted with Gaussian functions.

energies, weighted with their respective decay probability. The simulation also utilizes an average detector energy resolution of 45 keV, which is in agreement with the measured resolution of the detectors 3.5. The considered decays are listed in Table 3.3.

To obtain a calibration based on this reference data, a spectrum for each strip in each detector is created. A Gaussian fit is then performed to each of the three primary peaks of the triple-alpha spectrum. Using the expected mean positions obtained by the simulation, this can then be used to determine a linear calibration function for each strip. An example of a fit for detector 25 is shown in Figure 3.9. This mapping is later used for the recombination of front- and back strip-signals (see Section 3.3.3).

Table 3.3: Decay energies used for the calibration of the LYCCA setup [94–96].

Isotope	Energy [keV]	Branching ratio [%]
^{239}Pu	5156.59(14)	70.77(14)
	5144.3(8)	17.11(14)
	5105.5(8)	11.94(7)
	5076(8)	0.08(7)
^{241}Am	5485.56(12)	84.8(5)
	5442.8(13)	13.1(3)
	5388	1.66(20)
	5544.5(16)	0.37(3)
^{244}Cm	5804.77(5)	76.9(10)
	5762.64(3)	23.1(10)

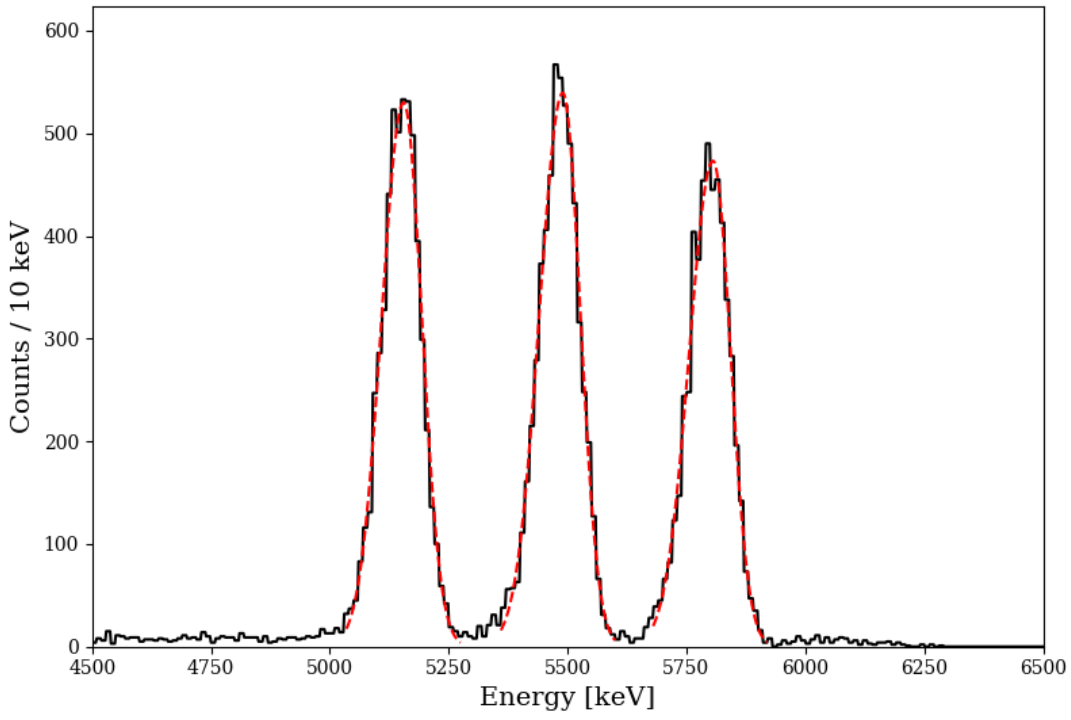

Figure 3.9: Triple alpha spectrum for detector 25, strip 1 including the fits to the peaks. The fit is performed on the sum of the simulated peaks. The peak widths (sigma) are 42.3 keV, 43.3 keV, and 44.0 keV respectively.

3.4.2 Pixel calibration

All emission energies of the three-alpha-source are below 5.9 MeV, yet the expected energies from the studied reactions reach up to 25 MeV (for low scattering angles). To not only rely on extrapolation, additionally measured kinematic lines of the scattered alpha particles which excited states in ^{12}C were utilized to improve the calibration and provide reliable reference points at higher energies. The energy of the scattered alpha is always directly correlated to the scattering angle off the beam axis, which allows us to use each pixel's position to compute the reference energies for each alpha particle, as can be seen in Figure 3.10. For each pixel this provides a set of reference peaks at low scattering

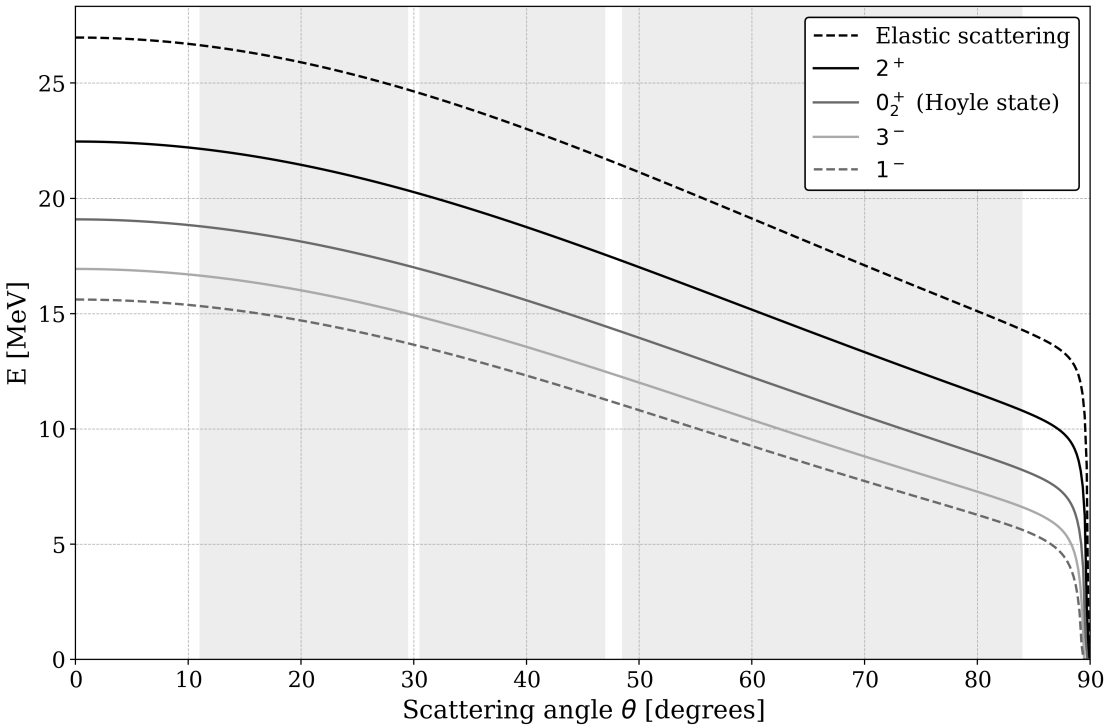

Figure 3.10: Kinematic lines for a selection of excited ^{12}C states below 11 MeV. The states indicated by solid lines were used for the kinematic calculation in conjunction with the triple-alpha source. The dashed lines indicate the elastic scattering of the alpha particles, and the 1^- state, not used for the calibration due to angular coverage, and statistics. The gray areas indicate the angular coverage of the detector array. Note the sharp decline in energy for higher scattering angles, caused by energy loss of the scattered alpha particle inside the target material.

angles in the wall detectors (10° - 29.5°) up to high angles in the second ring (48° - 84°), as demonstrated in Figures 3.11a and 3.11b. The calibration is then performed by fitting a second-order polynomial to the reference energies of the alpha particles in the DSSSDs. This is done on a per-pixel basis, since each pixel has slightly different incident angles for the alpha particles, which changes the expected energy as well as the energy loss in the target material and the dead layer.

Analogous to the triple-alpha source calibration, the particles used for the calibration are alpha particles. This is important, as alpha particles are the particle of interest in the primary study, and energy losses and deposition in the detector need to be consistent. An additional reaction used for validating the assumed dead layer and calibration was the ^{12}C(α,d)^{14}N reaction.

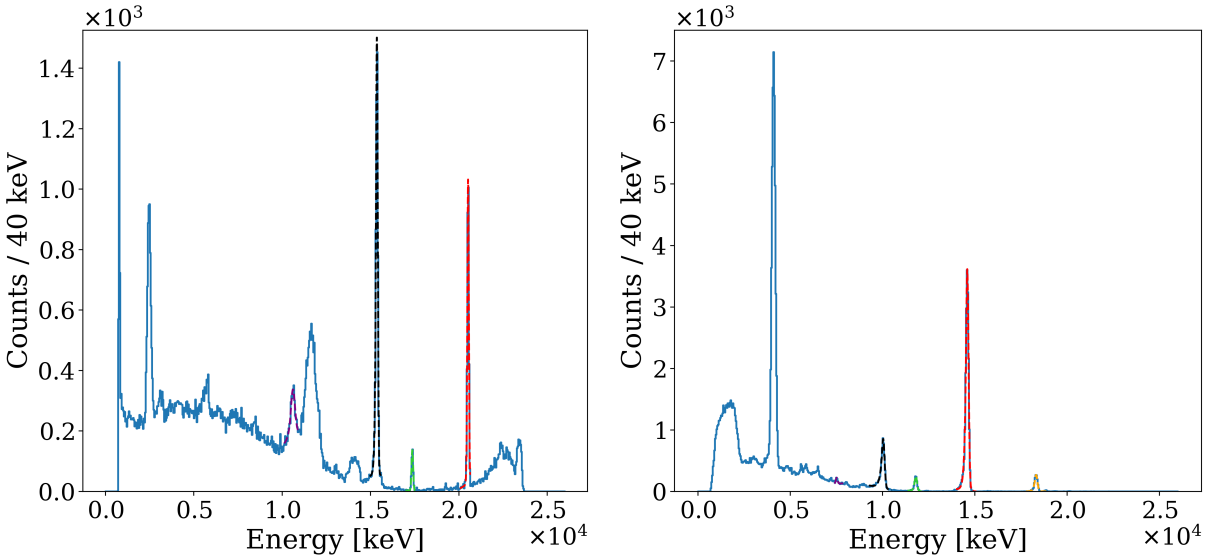

(a) Front-side energy spectrum of pixel (22,19), DSSSD 15 (wall)

(b) Front-side energy spectrum of pixel (0,28), DSSSD 1 (ring)

Figure 3.11: Energy spectra of one pixel in DSSSD 15 (wall detector, $\theta \approx 20°$) and one in DSSSD 1 (outer ring, $\theta \approx 65°$) using the front-side energy signal. The indicated peaks are from higher to lower energy: Elastic scattering (orange, only seen in detector 1), the 2^+ state (red), the Hoyle state (green), and the 3^- state (black) in ^{12}C, as well as the deuterium transfer reaction forming ^{14}N (purple).

After fitting the peaks for each pixel and mapping the fit positions to the expected reference values, a quadratic calibration function is obtained for each pixel, as seen in Figure 3.12. The shown data points corresponding to ejectiles of the deuterium transfer reaction was unused since the detected deuterium nuclei show different energy loss characteristics in the detector and energy losses in target and detector dead-layer. The ground state line was also not used for the calibration, as its ejectile energies are very close to the energy range of the used electronics, where linearity begins to degrade. Additionally, ejectiles of the elastic scattering reaction showed punch-through behavior, as can be seen by the back-bending of the kinematic line towards lower energies, visible in Figure 4.1. The scattering on the gold target showed a larger deviation and was therefore also not used for the calibration.

The obtained fit function is then used to convert the ADC channel information into energies for the further analysis. A quadratic function is sufficient, since the AIDA FEE modules provide a very low non-linearity in the energy signal [97]. Non-linearity contri-

butions by energy losses in the dead layer are compensated by the energy loss functions. The deviations of the calibration show slight deviations, introduced by differential non-

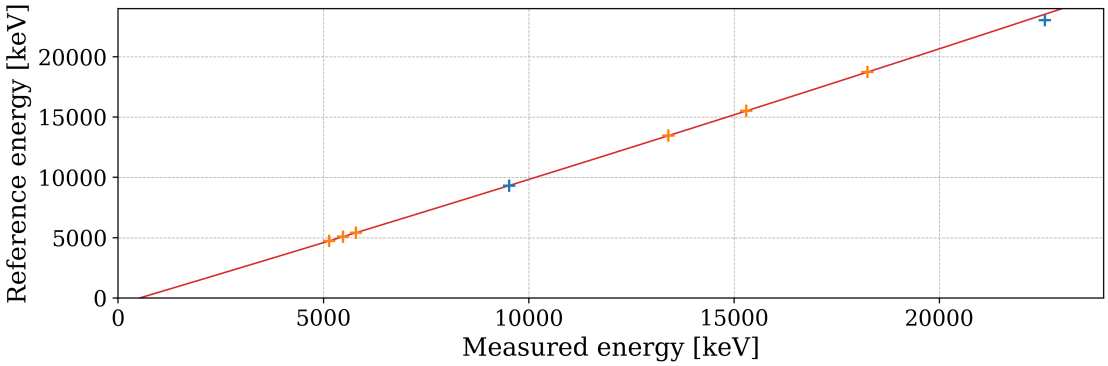

Figure 3.12: Quadratic calibration function for a single pixel in DSSSD 6 (index: 16,16) showing strong linearity in the calibration function. The orange data points denote the values used in the calibration: Triple-alpha source peaks, 2^+ excitation, 3^-, and 1^- excitation in ^{12}C. The blue points show the deuterium transfer reaction and the ground state. Error bars are plotted, but are smaller than the marker size (typical measurement uncertainty: 60 keV, typical reference uncertainty: 100 keV due to the angular uncertainty). The highest energy point is below the calibration line due to its partial energy deposition in the detector ("punch-through").

linearities [98] in the detector response and energy losses in target and dead layer. These deviations are shown in Figure 3.13 for the Hoyle state kinematic line in ^{12}C. Many cali-

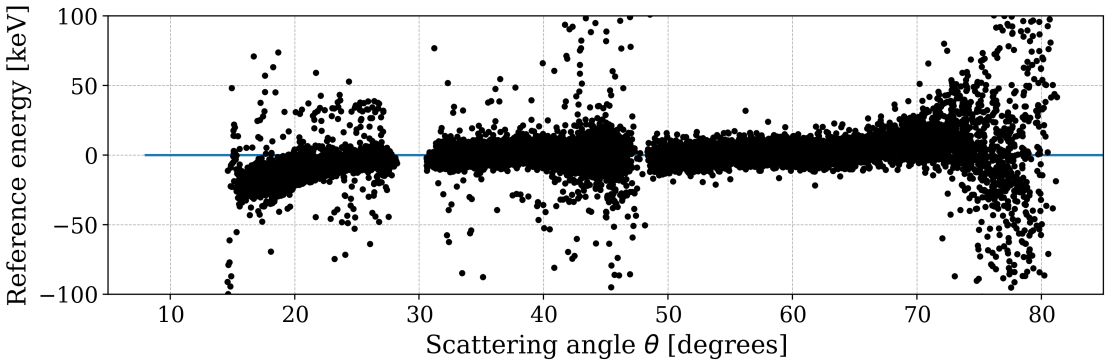

Figure 3.13: Deviation of the calibration function for the Hoyle state kinematic line in ^{12}C for the calibration peak positions from a quadratic calibration.

brations improvements, such as the determination of the ideal dead layer-target thickness combination, were performed by Alessandro Salice [99, 100]. Further details on this will be provided in his master thesis.

3.5 Energy resolution

The energy resolution of the detectors is an important metric for the analysis, as it directly impacts the distribution widths in later analysis stages. The resolution is determined per-pixel, as the energy loss in the dead layer, the ADC gain value / noise contribution, and the available kinematic scattering lines differ for each detector group. The obtained energy resolutions are shown in Figure 3.14. The obtained resolutions are

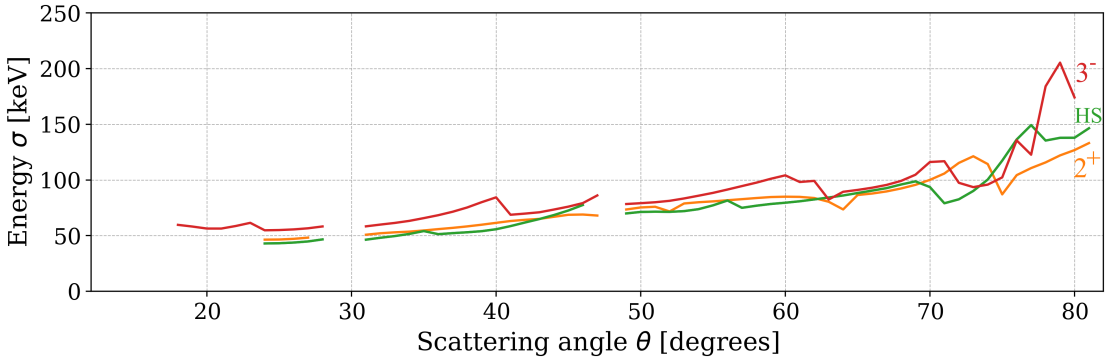

Figure 3.14: Comparison of the energy resolution for the kinematic line of different excited states in ^{12}C. The resolution is averaged over all detectors at the given angle. The orange line corresponds to the 2^+ state, the green line to the Hoyle state, and the red line to the 3^- state. The overall trend towards lower energy resolution for higher scattering angles is caused by the increased energy loss in the target material given by $\frac{1}{\cos(\theta)}$. The larger width increase towards higher energies for the Hoyle state is caused by low statistics in the fits compared to the other states. The gaps in the data are caused by the setup's gaps between the detector rings and wall assembly and the rings themselves. The inital gap below 24° for the 2^+ state and Hoyle state are caused by overlapping peaks of other reactions.

in the range of 40 keV to 45 keV for the triple-alpha calibration (see Figure 3.9) and between 40 keV and 120 keV for the kinematic lines of the scattered alpha particles.
While the in-beam energy distributions are wider than the triple-alpha source calibration, the higher energies of the incident particles still result in a better relative resolution compared to the source measurement. This has multiple reasons: The source activity is very limited compared to the on average 25.7 kHz alpha detection rate (after CombineStrips) during the beam time. Also, the values during the beam time are per-pixel and the triple-alpha source calibration provides data per-strip. This has a small impact on the resolution, as the differential energy loss dependent on the effective dead layer thickness cannot be accounted for in the strip calibration.
The resolution during in-beam measurements is mainly impacted by energy straggling in the target, as can be seen in the systematic increase of relative peak width towards higher scattering angles θ. Additional contributions are minor uncertainties in the beam energy as well as lattice defects introduced during the beam time. Additionally, charge carriers

generated by the impinging alpha particles can become trapped in the detector's dead layer, which can lead to a worsened energy resolution and increased leakage current [101]. The resolution results are detailed in Table 3.4. The table shows the energy resolution for the entire setup, not separate detectors. This is done, as opposed to providing a per-pixel energy-resolution, to also factor in variations between pixels and systematic effects such as minor position deviations which also increase the measured line thicknesses and impact the energies of all particles detected by the LYCCA setup. An additional observation on

Table 3.4: Absolute and relative energy resolution compared to the incident energy for the triple-alpha source and the in-beam measurements. This energy resolution is based on the Energy-θ plot, which sums up all pixels for a given scattering angle θ.

Energy [MeV]	Resolution (sigma) [keV]	Rel. resolution	Measurement
5.17	49.08	0.95%	3α: ^{239}Pu, det. 7
5.50	49.11	0.89%	3α: ^{241}Am, det. 7
5.81	48.47	0.83%	3α: ^{244}Cm, det. 7
5.16	42.30	0.82%	3α: ^{239}Pu, det. 25
5.49	43.32	0.79%	3α: ^{241}Am, det. 25
5.81	44.04	0.76%	3α: ^{244}Cm, det. 25
21.06	46.38	0.22%	2^+, $\theta = 24°$
17.06	75.29	0.44%	2^+, $\theta = 50°$
12.50	87.11	0.70%	2^+, $\theta = 75°$
17.78	42.96	0.24%	0_2^+ (Hoyle), $\theta = 24°$
14.01	71.28	0.51%	0_2^+ (Hoyle), $\theta = 50°$
9.85	117.36	1.19%	0_2^+ (Hoyle), $\theta = 75°$
15.67	54.78	0.35%	3^-, $\theta = 24°$
12.10	79.13	0.65%	3^-, $\theta = 50°$
8.20	102.31	1.25%	3^-, $\theta = 75°$

the energy-stability of the setup can be performed by evaluating the energy sum of the detected particles of one event, discussed in the following chapters, throughout the entire measurement campaign. This sum is expected to be constant for each event where all particles are detected and only alpha exit channels are available, since for them all energy should be accounted for. This energy should thus be equal to the energy of the incident alpha particle with the beam energy. The test is performed by monitoring the time evolution of this energy sum in the laboratory frame throughout the beam times. This is shown in Figure 3.15. The energy sum in the center-of-mass frame exceeds the beam energy, which is likely caused by a slight axis misalignment of the setup. This will be further discussed in Section 4.1.4. Additionally, a slight oscillation in the energy sum is observed which exceeds the expected energy resolution of the detectors and variance of the beam energy of approximately 30 keV. If the angular offset hypothesis is correct,

the oscillation could be caused by interplay of the reaction position reconstruction, discussed in Section 3.7, and the slight misalignment of the setup. Despite the visible effect in Figure 3.15, the variation of the energy resolution in the center-of-mass resolution in the laboratory and center-of-mass frame is below 9 % during the December measurement (22.19 keV vs 20.36 keV) and below 13 % during the January 2020 measurement (29.92 keV vs 26.65 keV), not counting the decrease in resolution between the December 2019 and January 2020 runs.

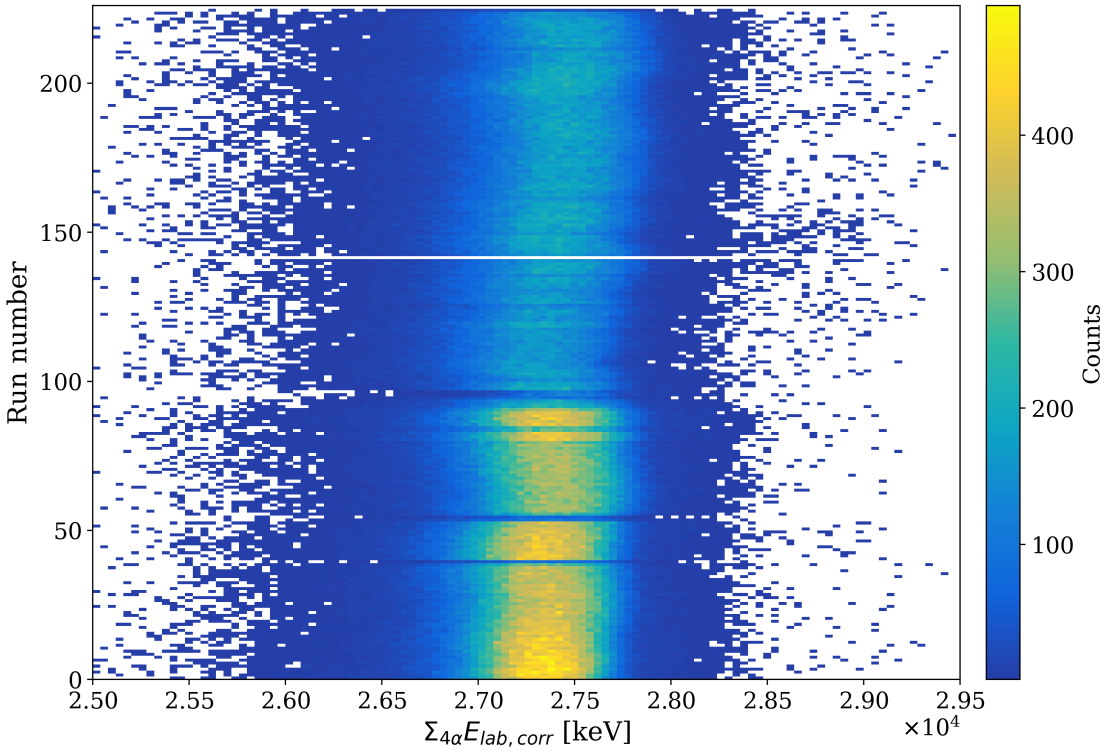

Figure 3.15: Time dependence of the energy-loss corrected energy sum of four particles detected in coincidence.

3.6 Energy loss

The energy of the alpha particles E is reduced by energy losses ΔE in the target material and the dead layer of the detectors. These losses depend on the energy of the alpha particle and the thickness of the material, and the angle of incidence. The energy loss functions are calculated using the SRIM software [81]. Since the detectors measure $E - \Delta E$, a two-dimensional function $\Delta E(E - \Delta E, d)$, where d is the path length through the material, is used to correct the energy of the alpha particles. For this, energy-loss functions are fitted to the SRIM-data for a range of thicknesses. In the analysis code the four neighboring thicknesses are then cubicly interpolated to obtain the energy loss for the given thickness of the target material.

3.6.1 Dead layer thickness

The dead layer thicknesses were provided by the DSSSD manufacturer in the specifications of the detectors (see Section 2.2.3). During the analysis, the dead layer thickness can be tested for consistency by systematically varying the thickness used in the energy loss function. The linearity of the DSSSD and DAC response, as well as of the front-end electronics, was demonstrated before. Using this premise, the optimum thickness value corresponds to the best energy resolution for a low-order polynomial calibration function. Using this approach a dead layer thicknesses between 2.45(25) µm and 3.10(31) µm of silicon oxide, SiO_2, was obtained. This corresponds to Si-equivalent thicknesses at the relevant energies of the experiment of below 10 MeV between 1.99(47) µm and 2.51(54) µm. Despite the simple core assumption of best linearity, the result is consistent with recent measurements performed at the Lund University [98], where two test detectors of the same type used in the LYCCA setup exhibited a dead layer thickness of 1.826(25) µm and 1.96(9) µm Silicon-equivalent respectively. Their measurements demonstrated that the dead layer variation over a detector surface can be even larger, as exemplified by a surface scan of a detector in Lund, which is shown in Figure 3.16b, indicating a variation of up to 0.3 µm in the dead layer thickness. The measurement in Lund was performed using three different isotopes: ^{244}Cm, ^{148}Gd, and ^{133}Ba, of which the ^{133}Ba source was used for the calibration, as it is an electron source, which has a neighboring energy loss in the dead layer compared to the alpha particles of the other sources. The source positions were then varied to obtain a surface scan of the detector and the dead layer thickness was obtained by comparing the energies of the calibration and the measured peaks. The obtained variation is due to the DSSSD manufacturing technology at production time. Throughout the analysis the dead layer was assumed to be equal for all employed detectors and constant over the detector surface, as a more detailed approach introduces too many degrees of freedom. This, however, leaves room for future improvements in the calibration, while ensuring a stable and consistent calibration for the current analysis.

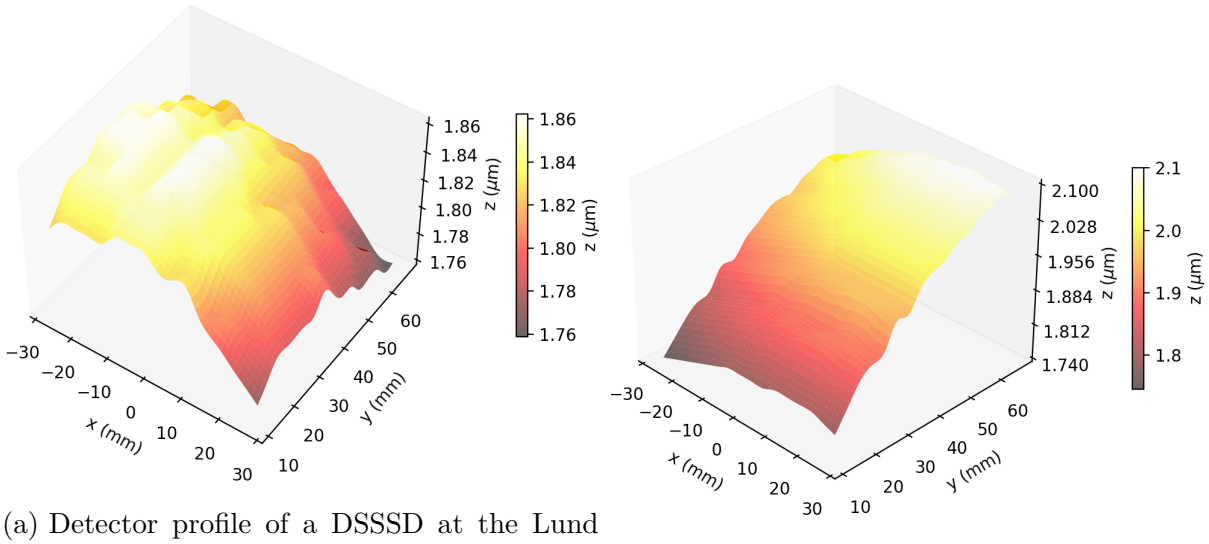

(a) Detector profile of a DSSSD at the Lund University. The thickness variation is approximately 0.1 µm over the detector surface.

(b) Detector profile of a second DSSSD at the Lund University. The thickness variation is approximately 0.34 µm.

Figure 3.16: Dead layer thickness profile of two DSSSDs measured at the Lund University [102].

Detector window effects

A subset of ten of the utilized 18 detectors have small rectangular windows in the dead layer, which covers the region of the backside strips 5 and 6. This can be seen in Figure 3.17a. These windows have a reduced dead layer thickness, but they do not cover the full area of the strip, which causes double peaks in the energy spectra, since the ions hitting the strip can either pass through the window or through the full dead layer. As the pixel resolution does not allow to distinguish between the two cases, the doubling of the peaks cannot be resolved for these strips. To prevent calibration issues and unclear energy assignment, any signal coinciding with data from these strips is excluded from further analysis.

3.6.2 Time walk

The most precise event timing signals captured by the AIDA FEE-modules are generated by the leading-edge triggers of their discriminators. This type of discriminator trigger is susceptible to the time-walk effect [75], which causes a systematic shift of the trigger signal depending on the amplitude of the signal. Considering two signals which originate at the same time, but have different energies, the signal with the higher energy will reach the trigger threshold earlier than the signal with the lower energy, causing a systematic deviation for the lower pulse. A visual representation of this effect can be seen in the figure inset 3.18 (b). This not only shifts the time of the trigger signal, but also degrades the time resolution as the shallower rising edge of the lower energy signal is more suscep-

(a) Frontal view of one of the LYCCA-DSSSDs with dead layer windows, visible as a vertical pattern of the dark rectangles. Also, on the left, the bonding wires contacting the strips on the front side are clearly visible. Adapted from [103].

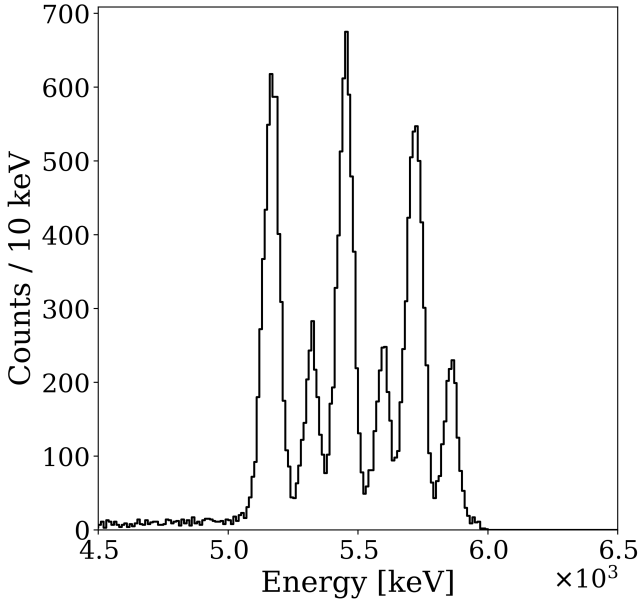

(b) Energy spectrum of a triple-alpha source of strip 5 on a detector (module 24) exhibiting a dead layer window. The spectrum shows a second, higher-energy peak for each of the Pu, Am, and Cm lines, where the incident alpha particle passed through the window.

Figure 3.17: An example triple-alpha source spectrum used for calibration for a strip with a dead layer window. Clearly visible are the doubled peaks caused by the different dead layer thicknesses.

tible to noise and statistical fluctuations.

The shift caused by the time-walk effect is observed in multiple places during the analysis: Initially it is visible in the time difference distributions between discriminator and ADC signals. Here it only impacts a small fraction of the events, as a broad time gate is used to combine the signals. During the later data anlysis stages, the results are more sensitive to the shift, as the gates are typically narrower than 100 ns. To mitigate this, a simple function,

$$f(x, a, b, c, d, e) = a + b \cdot \exp\left(-\frac{c + x}{d}\right) + e \cdot x,$$

is fitted to a Δt-E histogram, which is filled during a prior analysis step. The energy is the absolute energy of the measured alpha particle, and the time is the time difference to the scattered alpha, if the energy of the scattered alpha is above 10 MeV. This function is then used to shift the timestamps depending on their energy. Correcting this systematic shift narrows the time distribution of the coincident alpha particles. This is especially relevant for the Hoyle state decay, as the energy of the decay products is much lower than the energy of the scattered alpha particle used for the initial kinematic gate. In

addition, the broader time distribution for lower energies needs to be taken into account in the coincidence gate. To integrate this, another, similar, function is used to also fit the distribution widths. An example for this can be seen in Figure 3.18 (a), where the time-walk correction curve for one of the detectors is shown.

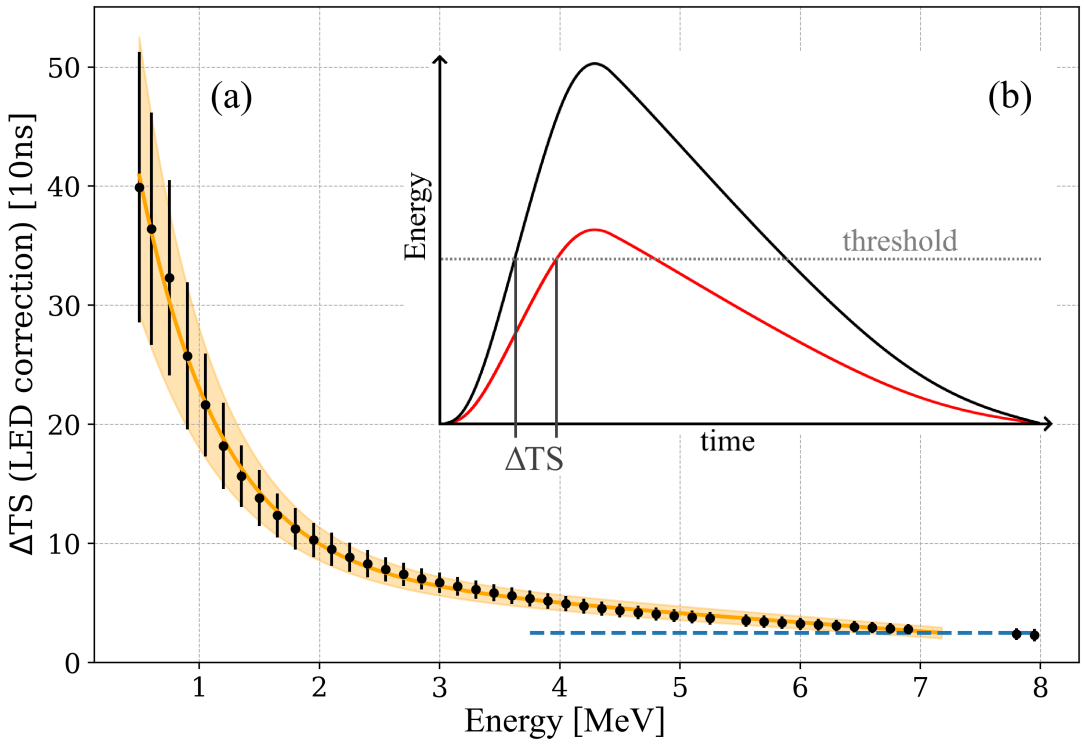

Figure 3.18: (a) Time-Walk correction curve for module 24 for the data of the second beam time. The data points are the fitted centroid of each slice (projection) of the measured 2D energy-ΔTS distributions. The fit function and its confidence interval, plotted in orange, are detailed in equation 3.6.2. The asymptote, shown in blue, is assumed to be constant and passes through the energy of the reference detection from which ΔTS is computed. (b) illustrates the cause of the shift: Two example signal pulses (black and red) with different energies are shown. The indicated discriminator trigger threshold is reached earlier by the higher pulse, causing a systematic shift in the time difference between incidence and trigger.

3.7 Beam spot position

Since the employed reconstruction approach is highly sensitive to the reaction angles, the beam spot movement during the beam time becomes a contributing factor to the systematic uncertainties. After an initial promising demonstration as part of the work of Mădălina Răvar [104], an updated approach was developed to determine the beam spot position. To reconstruct the beam spot position on the target, a reaction with an otherwise unwanted contaminant in the target can be used: Hydrogen. The reaction of

the alpha particles with the hydrogen in the target material causes scattering under low angles, producing a crescent-shaped distribution on the energy-theta plots. This shape can be seen in Figure 3.19. Since the kinematics limit the scattering angle of the alpha particles to below 14.6°, this maximum can be utilized to validate the relative offsets from the pixel to the reaction position, where the beam intersects the target. The pixels which

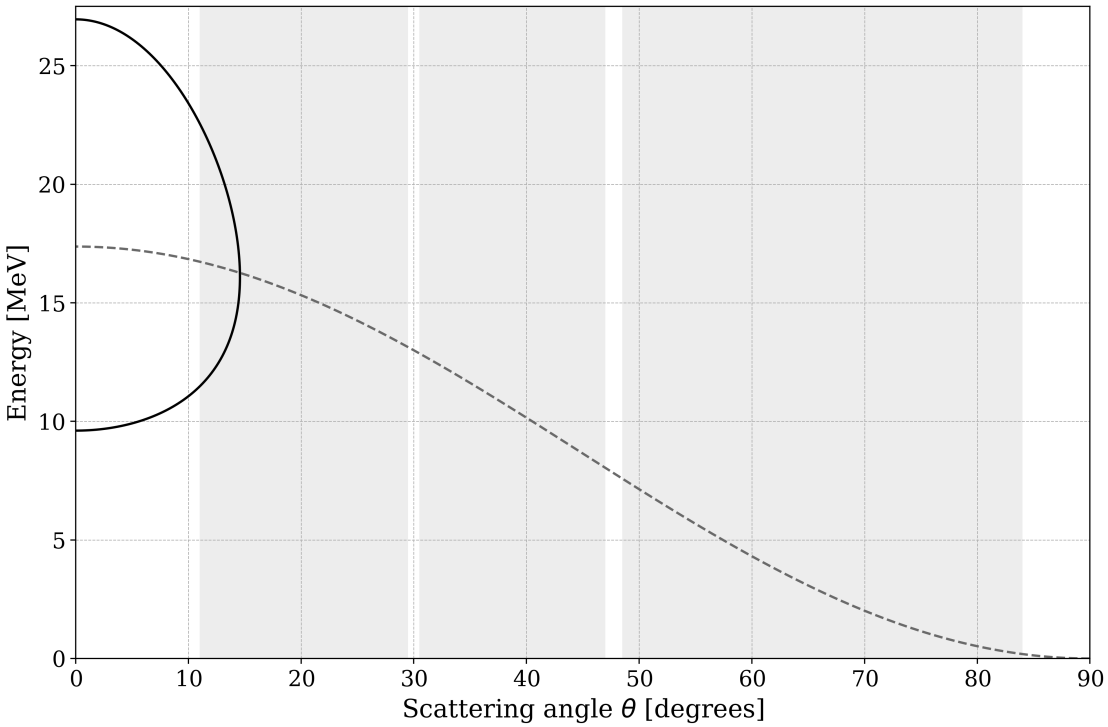

Figure 3.19: The alpha scattering kinematics on hydrogen embedded in the target. The solid line shows the expected kinematic line for the scattered alpha particles. As can be seen, these can only be detected inside the wall detectors. The dashed lines show the corresponding hydrogen scattering line.

registered the alpha particles at the scattering angle corresponding to the scattering on hydrogen are then selected and used to fit a circle to the pixel positions. The center of this circle is the beam spot position. Additional information can also be obtained by fitting the circle separately per wall detector. This can be used to refine the positions of the wall detectors and ensure alignment. The resulting position is obtained for each batch of ten subruns (to ensure the statistics are sufficient for fitting). This can be plotted over the course of the two beam times for each wall detector. As can be seen in Figures 3.21 and 3.22, the detector movements are parallel which indicates a global shift corresponding with movement of the beam spot. The discontinuity between the first and second beam time is caused by hardware changes: The mounting of the tantalum covers caused minor shifts in the wall detectors, which were corrected for in the analysis based on the discussed beam spot determination. Additionally, since the beam times were not continuous, the beam had to be focused onto the target again for the second beam time, resulting in a slightly different initial reaction position.

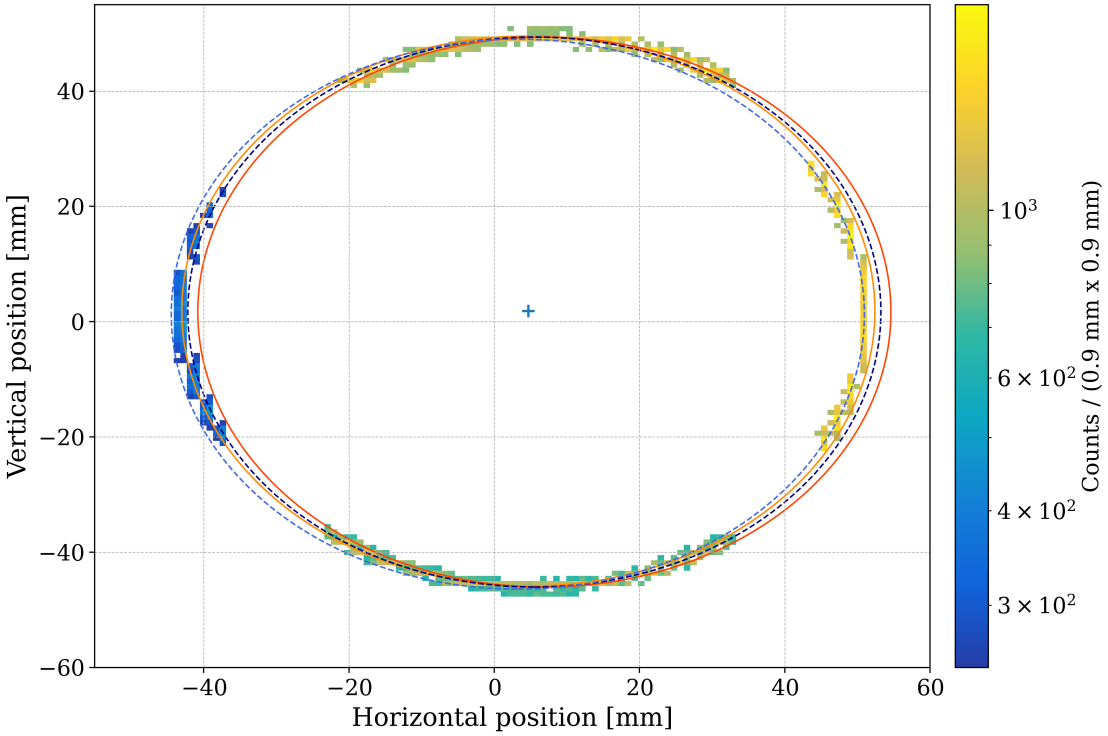

Figure 3.20: The pixels containing the kinematic line of the α on ^{1}H scattering process. The fits are shown for each detector. The blue (dashed) lines are the left and right wall detectors (module 14 and 25), the red (dotted) lines are the top and bottom wall detectors (module 15 and 24).

The effect of the beam spot position correction can be seen in Figure 3.23 when compared to the plots in Section 4.1.3, such as Figure 4.10. The angular deviations are reduced to a shape that is closer to the expected ellipse, which is caused by initial beam diameter and angular straggling of the beam particles. The remaining deviations are caused by the detector positions, which are further discussed in the next section.

3.8 Detector positions

When the setup was originally designed, the precision of the DSSSDs' positioning was specified to be within 0.1 mm. This precision is limited by the mechanical support of the DSSSD wafer and PCB, which is realized through connectors on the backside of the wafer. These allow for slight movement of the DSSSDs, and tilting, which reduces the precision of the setup. Since the measured reaction is overspecified, the geometry of the reaction and the physical constraints on the pixel positions can be used (the detectors are planar), to optimize the positions. This can be done using the inelastic scattering reactions in which the 2^+ state of ^{12}C is populated, since the alpha energies are low enough to be fully deposited in the DSSSDs, but the excited Carbon nucleus does not undergo a further decay. This eliminates the energy sensitivity which exists in

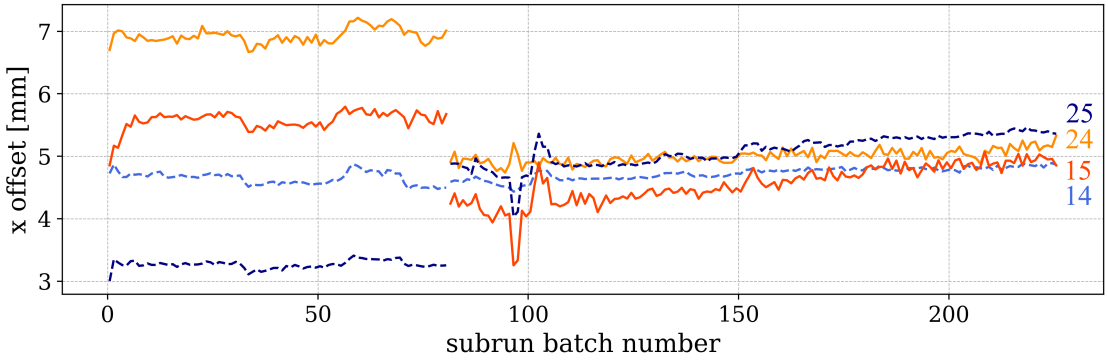

Figure 3.21: Determined horizontal beam spot position during the first and second beam time. Runs 1-80 are from the first, the later ones from the second beam time. The color scheme is the same as in Figure 3.20.

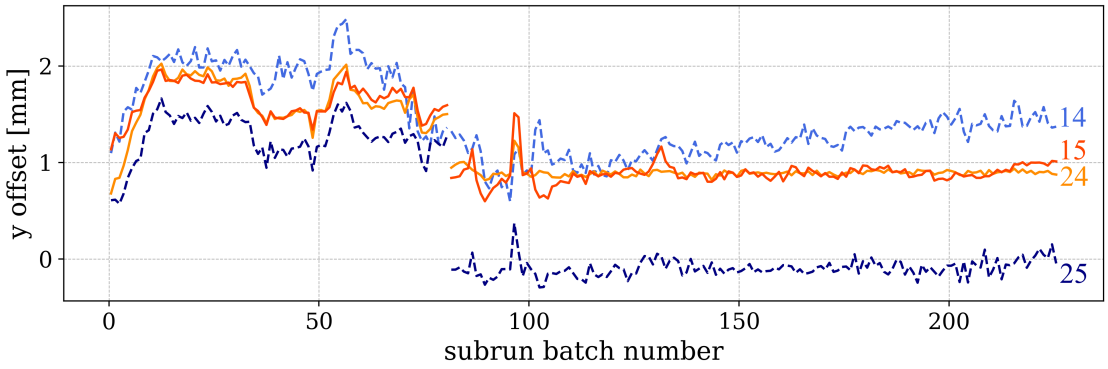

Figure 3.22: Determined vertical beam spot position during the first and second beam time. Runs 1-80 are from the first, the later ones from the second beam time. The color scheme is the same as in Figure 3.20.

our reconstruction approaches (e.g. for the Hoyle state decay), because the two-body kinematics only depend on the measured angles of the ^{12}C nucleus and the scattered alpha in the laboratory system. This allows to use the reaction plane ($\Delta\phi = 180\,\text{deg}$) and $\theta_{\alpha_{scatter}}$ vs $\theta_{^{12}\text{C}}$ dependency to compute the deviation between current and expected detector positions per pixel. Using these deviations, a chi-squared minimization can be performed to optimize the detector positions in a multi-step process. Initially only the angular positions are optimized, because the setup is not directly sensitive to radial components of measured vectors. The next step computes the rotations of the detector planes and can also approximate radial shifts, since these change the apparent opening angle of the detectors.

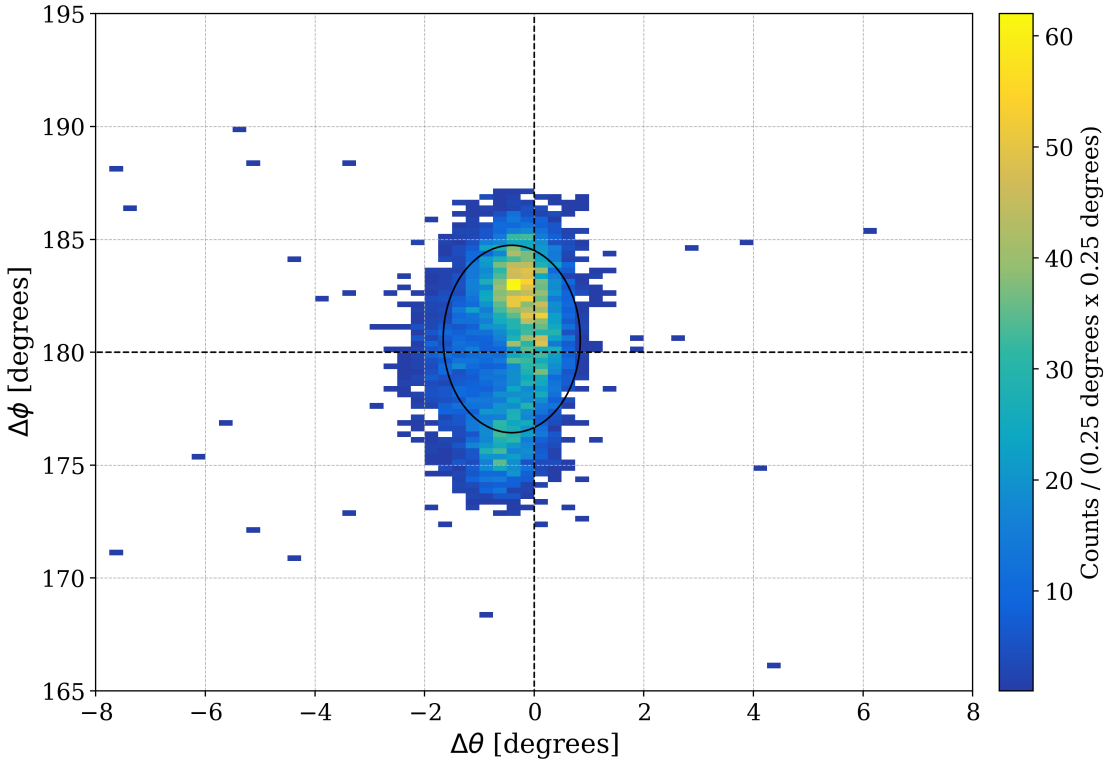

Figure 3.23: Angular deviations between the expected and measured reaction plane normal / scattering offset for one run file. The plot uses a reaction position offset of 1 mm off the chamber center, below the maximum beam spot movement during the analysis. The construction of this plot is further detailed in Section 4.1.3.

3.8.1 Position de-aliasing

Since each detector pixel only provides location information based on its own position within the detector, the position of the detected alpha particles is fixed to discrete positions. This can lead to alias effects, where the sharp distribution of the alpha particles' positions causes distortions in the angular distributions and center-of-mass frame energies.

These aliasing effects not only cause visual artifacts, but also interfere with the automatic gate finding algorithms. To mitigate this, each hit is assigned a random position within the pixel area, which is then used for further analysis. This effectively smooths the angular distributions and reduces the aliasing effects.

Chapter 4

Analysis of excitations above the α decay energy

With the data now in a suitable format, the primary physics analysis can be performed. To avoid confusion in the following sections, an *event* refers to a single reaction in the target of which at least one alpha particle was detected, while a single detection in a detector is referred to as a *hit*. The terms *condition* and *gate* are used interchangeably and refer to a selection criterion that is applied to the data.

After initial processing, $3.2 \cdot 10^9$ particle detections (hits) were recorded during a cumulative measurement time of 13.5 days. This data contains the reactions of interest, but also a plethora of background events, which need to be suppressed. These range from beam reactions on target contaminants or on residual gas to narrow angle scattering on installed slits and apertures, and even include rare events from natural background radiation. Additionally other excited states in ^{12}C are populated, which need to be suppressed using conditions, commonly referred to as *gates*.

A useful visualization of the obtained data is to plot the energy E of the detected particles against their detection angle θ. The angle is defined as the angle between the beam axis and the detector pixel, so it corresponds to the scattering angle of the particle. The E-θ plot of the obtained data during the beam times can be seen in Figure 4.1. The most prominent features in the plot are the distinct lines spanning from lower to higher scattering angles which are decreasing in energy towards the higher angles. These are the so called kinematic lines which contain the ejectiles of each reaction, the scattered projectile-like alpha particles, and are essential for the selection of events from a reaction of interest, as each line corresponds to a specific reaction. Parallel lines typically originate from reactions with the same target nucleus, but at different excitation energies, since energy conservation dictates that less energy is available for the ejectile if higher lying states are populated.

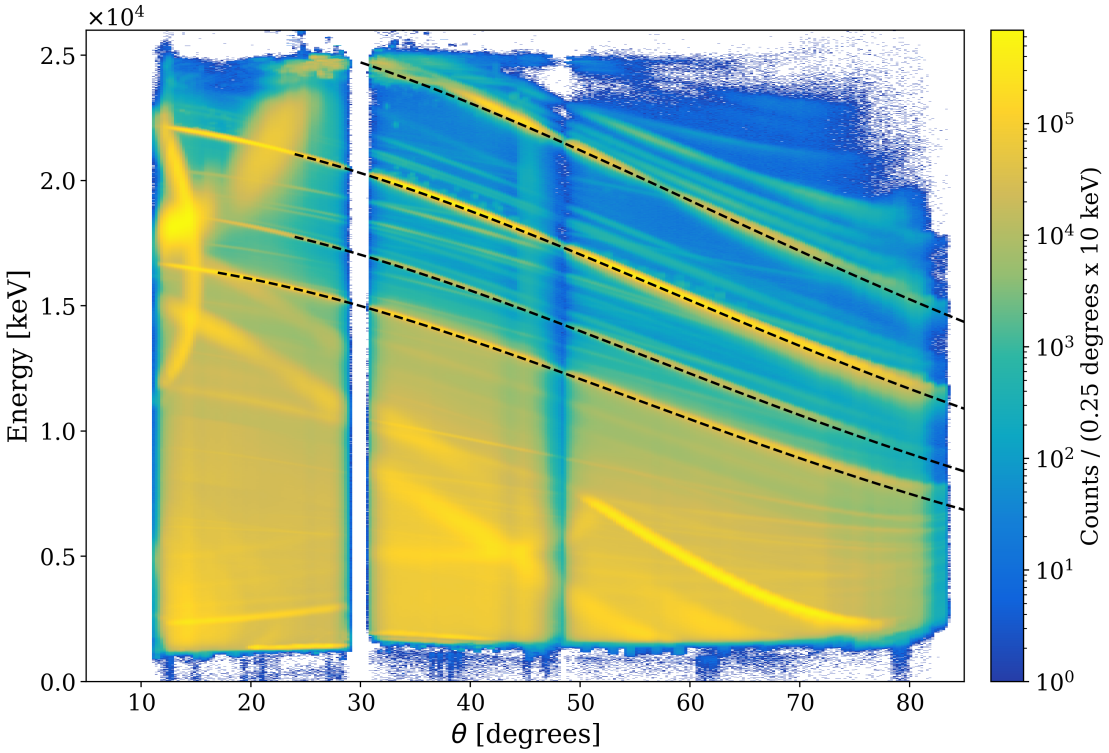

Figure 4.1: Energy of the scattered particles registered in the DSSSDs against the detection angle of the respective pixel to the beam axis. Highlighted by dashed lines are the kinematic lines corresponding to elastic and inelastic scattering in ^{12}C, involving the four lowest energy states in it. The states corresponding to each line are (top to bottom): The ground state, first 2^+ state, the Hoyle state, and the 3^- state.

4.1 Reaction selection

As a lot of different reactions occur in the target, the initial test condition should suppress as many unwanted reaction events as possible. One effective technique is the use of *kinematic conditions*, where the energy and angle dependency of one or more of the reaction products are used to select the reaction of interest.
This is based on the fact that each reaction populating an excitation in ^{12}C follows either

$$^{12}\mathrm{C}(\alpha,\alpha\prime)^{12}\mathrm{C}^{(*)} \tag{4.1}$$

for inelastic scattering and excitation of states below the particle separation threshold of 7.275 MeV, or

$$^{12}\mathrm{C}(\alpha,\alpha\prime)3\alpha \tag{4.2}$$

for higher lying states, such as the Hoyle state. The alternative radiative decay of the Hoyle state is in comparison highly unlikely (see 1.5).

It is thus expected to observe one scattered alpha particle on the kinematic scattering line corresponding to the state of interest (see Figure 3.10). The condition checks for

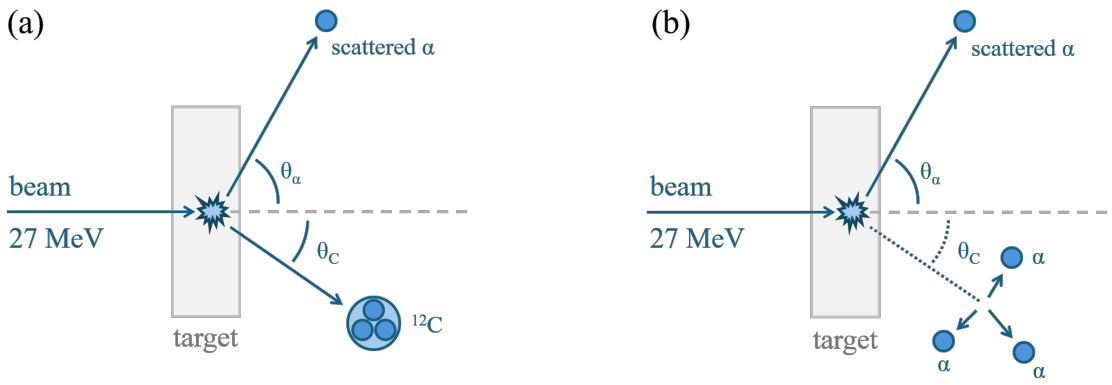

Figure 4.2: The two different reaction types in ^{12}C: (a) - scattering below the particle separation threshold and (b) - the decay of the Hoyle state and higher lying states. The beam enters from the left.

the energy difference for each detected alpha particle relative to the kinematic line of the Hoyle state for the scattering angle of the particle. The resulting energy distribution is shown in Figure 4.3. The typical energy difference for event selection is set to ±250 keV, which is a compromise to reduce the background while still allowing for a sufficient number of events to pass the condition. It is selected based on the energy straggling in the target and energy resolution of the setup, which were discussed in Section 3.5. For each ejectile, either three alpha particles, or a carbon nucleus will be emitted and can be registered in the detector array in coincidence with it. The time span between these events is called the *coincidence window*.

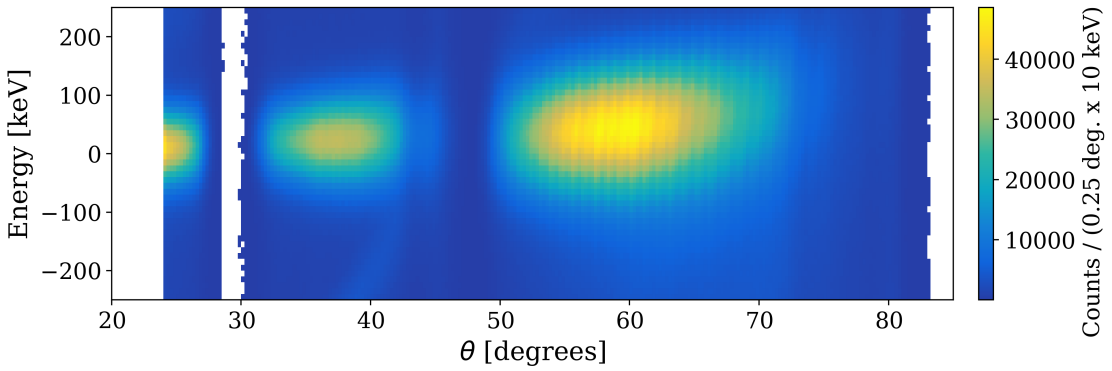

Figure 4.3: Energy difference between the scattered particles registered in the DSSSDs and the kinematic line of the Hoyle state evaluated at the scattering angle of the detected particle. To show this dependency, it is plotted against the scattering angle.

It is chosen based on the time resolution of the detectors and electronics at the particles' energies and other contributing factors, such as the time of flight of the particles. These only have a minor impact, compared to the leading-edge effects at low energies, though, as all flight times are sufficiently short: The longest flight distance in the setup is the

distance between the target and the wall detectors. The detection threshold in the wall detectors (mod. 14, 15, 24, and 25) is set to 800 keV and above. As this is the detected energy, the minimum particle energy before energy losses in the detector's dead layer is approximately 1.1 MeV, as can be seen in Figure 4.1. The resulting minimum alpha particle velocity is $v_{\alpha,\mathrm{min}} = 7.3\ \frac{\mathrm{mm}}{\mathrm{ns}}$. Since the maximum distance between the target and a detector pixel is $d_{\mathrm{max}} = 208$ mm, this would result in a maximum time of flight of

$$t_{\mathrm{ToF,min}} = \frac{d_{\mathrm{max}}}{v_{\alpha,\mathrm{min}}} = 28.4 \text{ ns}. \tag{4.3}$$

The minimum time of flight for an ejectile corresponding to an excitation energy above 7.654 MeV in ^{12}C at an energy of 15 MeV and a velocity of 26.8 $\frac{\mathrm{mm}}{\mathrm{ns}}$, is achieved for the minimum detector distance in the barrel detectors, at a distance of $d_{\mathrm{min}} = 83.5$ mm, resulting in a minimum time of flight of

$$t_{\mathrm{ToF,max}} = \frac{d_{\mathrm{min}}}{v_{\alpha,\mathrm{max}}} = 3.11 \text{ ns}. \tag{4.4}$$

Given the time resolution of the data acquisition system of 10 ns, this results in a maximum deviation of 3 ticks. Although this value is small, the following coincidence window is set slightly asymmetrically to compensate for this, as shown in Section 4.1.1.
To set a gating condition on events on a line in the E-θ plot, the relationship of energy and scattering angle is required. The computation of the required curves was performed using the LISE++ software [105] and the CATKIN calculation tool [106]. The derivation of the used relativistic scattering formula is given in [107].
Using the kinematic lines of the levels of interest, the analysis codes iterate over all detector hits and search for events that lie on the kinematic lines. If an event is found, the next analysis step is triggered, which is the coincidence condition. Since this requirement limits the possible energy-angle coordinates to a thin kinematic line, only a small fraction of the recorded events will pass this condition. This is an effective way to suppress contaminating background events.

4.1.1 Coincidence condition

For each detected ejectile $\alpha\prime$ on the kinematic line, the analysis code selects all other hits in a defined time span, the coincidence window. In the case of the Hoyle state, the coincidence window is set to -9 to $+12$ ticks, which corresponds to -90 ns to 120 ns. This range was chosen during the analysis, as it optimized the acceptance of the Hoyle state decay events while minimizing the background. This initial phase of the kinematic condition generates a list of all hits that occur within the coincidence window of the

detected ejectile. Plotting the time difference between the ejectile and all other registered hits shows a clear peak at zero, as expected. This can be seen in Figure 4.4.

The second phase of the coincidence condition additionally compensates for the time-

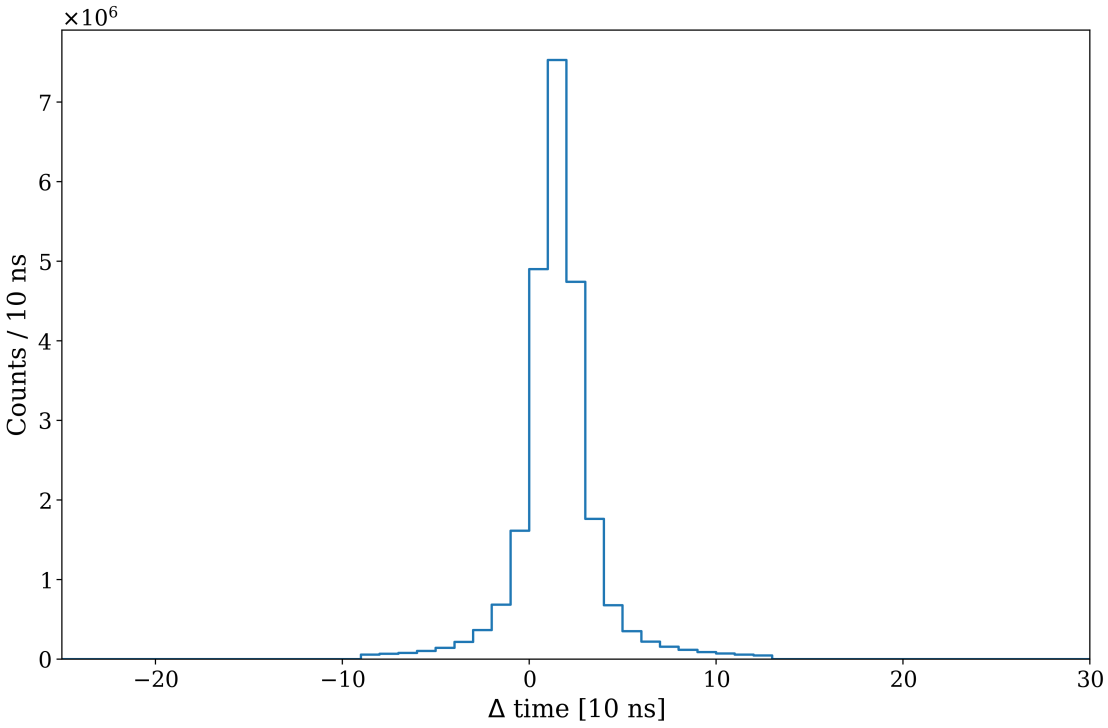

Figure 4.4: Time difference between the scattered alpha and all other registered hits for each event after applying the broad coincidence condition: Each event contributes as many points to the plot as its multiplicity contains.

walk effect caused by the used leading-edge discriminators. This is the *energy-dependent coincidence condition*. This topic was discussed in more detail in the prior Section 3.6.2, where individual event building was discussed. Since the energy of the ejectile is typically much higher (at least 5 MeV for the Hoyle state) than the alpha particles originating from the ^{12}C decay, the delay of its signal is much shorter. The applied correction function compensates for this systematic shift, but another effect needs to be considered: The time resolution of the detector and electronics degrades towards lower energies due to the time-walk, which results in a broadening of the time distribution of the detected events due to signal ripple, noise and statistical fluctuations of the detection process. Using this distribution, shown in Figure 4.5a, for each energy-bin, a projection of the time difference distribution is created, to which a normal distribution is then fitted. The energy-dependent gate condition-window function is then set to 3σ of the normal distribution corresponding to the energy range of the detected particle. The impact of the second phase is demonstrated in Figure 4.5.

A brief remark needs to be made on the implementation of the coincidence condition: Since large parts of the following processing have to be performed for every single reg-

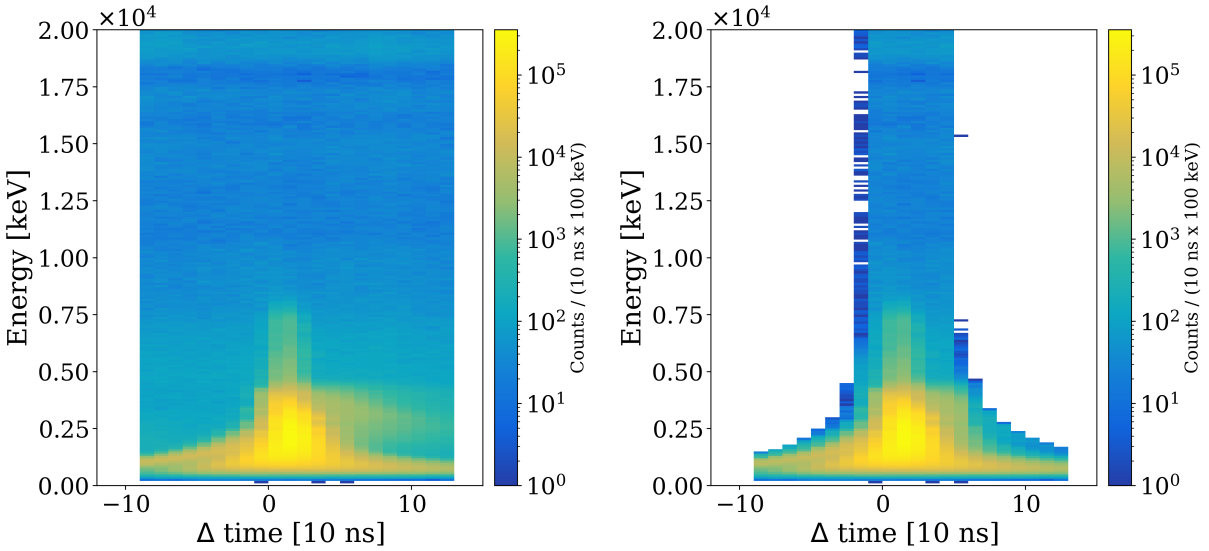

(a) Time differences of hits before the energy-dependent coincidence condition.

(b) Time differences of hits after the energy-dependent coincidence condition.

Figure 4.5: Time difference between the detected ejectile and all other registered detections within the initial coincidence window plotted dependent on the energy of the respective coincident particle. Note the broadening towards lower energies, which is similar to the time - energy plot in Figure 3.6, since the cause of the reduced time resolution in both cases is the time-walk effect.

istered detector hit, performance is a critical factor. As ROOT trees are optimized for sequential access, the coincidence condition uses two techniques to speed up the search. First, a ring-buffer constantly stores the last 32 events, which allows for a fast backwards search for coincident events at negative timestamp differences. The ring buffer size was optimized to allow for a wide search range while still fitting into the fastest cache of the available CPUs. This buffer is accessed every time a hit on the kinematic line is found and populates a buffer storing the coincident event up to the currently processed entry. The second technique is to store a list of open coincidence windows while iterating, which are then checked for each event. This allows one to fill the buffer with the coincident events that occurred after the entry containing the hit on the kinematic line. After each read event, the list of open windows is updated, and the code checks if the current event is outside of the updated window. If this is the case, the window is closed, and the buffer, now containing all hits that have timestamps within the defined coincidence window, is processed. Another optimization was the use of *SIMD* (Single Instruction, Multiple Data) instructions to speed up the test for the kinematic line, which allow for a parallel evaluation of the terms of the polynomial function used to define the kinematic line.
All parameters of the search, the conditions' gate functions, energy-width, and the coincidence window are fully configurable, enabling the analysis of higher lying states in ^{12}C, which is discussed in later parts of this thesis. Further details on the location of the source code and the implementation can be found in the appendix A.7.

4.1.2 Multiplicity of detected alpha particles

Since the reaction of interest is a three-body decay, the detection of four alpha particles (including the ejectile) is expected, as shown in Figure 4.2. After applying the coincidence condition, the multiplicity of the detected alpha particles is determined by counting the number of particles within the selection. The majority of events measured have a multiplicity of less than four. Compared to the expected multiplicity of four, which was observed 1.238×10^6 times, higher multiplicities were observed less often, as listed in Table 4.1, showing that the multiplicity of three was observed almost an order of magnitude more often. There are multiple reasons and combinations of reasons for the high fraction of low multiplicity events:

Multiplicity	Count
1	5.426×10^7
2	3.297×10^7
3	1.080×10^7
4	1.238×10^6

Table 4.1: Multiplicity of detected alpha particles after applying the coincidence condition.

- A substantial fraction of these events are elastic scattering reactions, only resulting in a multiplicity of two, where ejectile and recoil nucleus are detected.
- Excitations below particle separation energies can also only register as multiplicity two events: ejectile and recoil nucleus.
- Since the detectors have a limited solid angle coverage, some of the decay products' trajectories will not intersect a detector's active area, reducing the multiplicity.
- Comparable to the previous point, the energy losses in the dead layer of the detectors reduce the energy of the particles below the detection threshold of ≈ 700 keV.
- Dead time can also cause detector hits to not register.
- A high fraction of low-angle scattering events transfers very little energy and momentum to the recoil nucleus, causing the recoiling particle to be fully stopped in the target.
- Although most alpha particles deposit their entire energy in the detector, for some outer strips the efficiency is reduced by alpha particles scattered out of the sensitive depletion zone.

Apart from low-multiplicity events, there is also a low chance for multiple events to overlap, since the incident alphas are independent events, although this probability is very low, as seen in Figure 4.6, in which only few events have a multiplicity above four. Despite the fact that overall most detected events are elastic, the majority of the events that reach the multiplicity condition correspond to excitations of the Hoyle state.

A direct comparison of the multiplicity of the detected events with the expected mul-

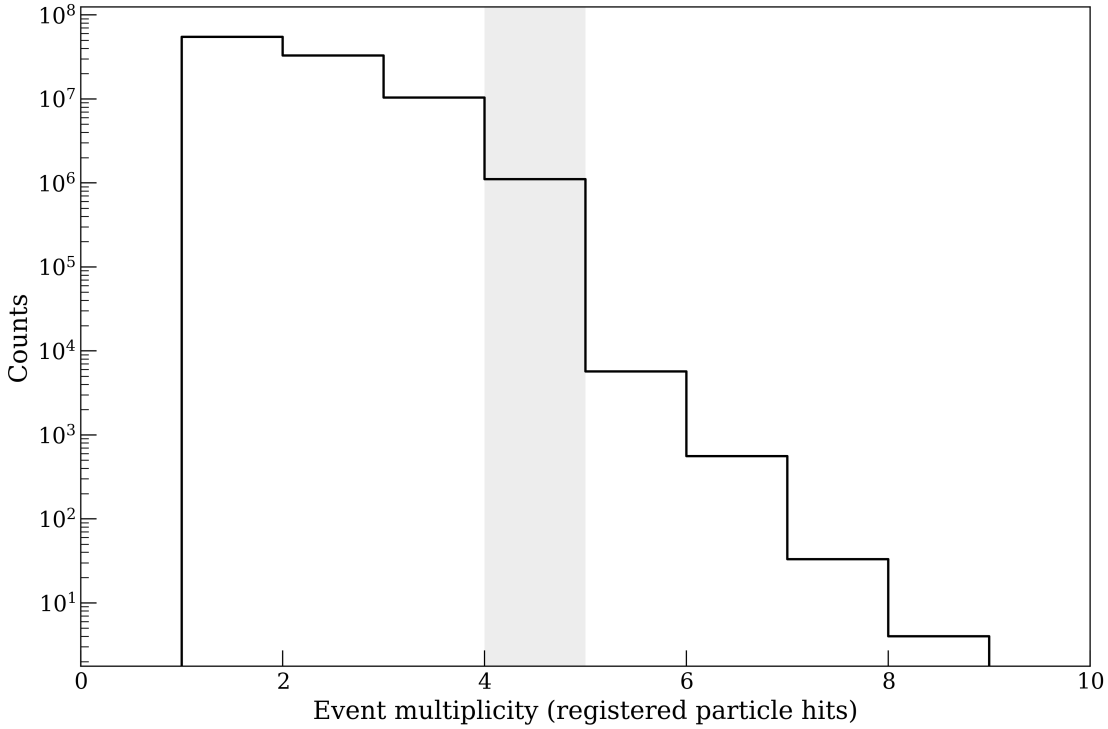

Figure 4.6: Multiplicity of the detected alpha particles in the DSSSDs. The gray region highlights multiplicity-4 events, which are expected for the Hoyle state decay.

tiplicity of the Hoyle state decay is non-trivial, as different angular configurations have vastly different detection probabilities. To estimate the number and distribution of undetected alpha particles, a Monte Carlo simulation was performed, which is discussed in Section 5. The condition's gate width is chosen based on the time distribution of the registered events. If a constant background is assumed, the ratio of the selected events to the total number of events can be directly controlled by the selection window width of the used conditions during the analysis.

As can be seen in the selected fraction of the data in the E-θ plot (Figure 4.12a) and the multiplicity plot (Figure 4.6), the coincidence condition in combination with the multiplicity criterion is a highly effective filter if applied to the obtained data: The plots visualize that only sparse events remain outside the expected kinematic line and the area containing the decay alphas. Note that in all E-θ plots, the area of the decay alphas is not continuous but interrupted by the gaps between the detector rings and the wall assembly and the rings themselves. The overall shape of it is determined by the kinematic

line of the recoiling ^{12}C, but is broadened by the momentum distribution of the decay alphas. This becomes more evident when comparing the distribution of the Hoyle state decay alphas with those of the 3^- state, which has a higher excitation energy and is thus further broadened.

To better visualize the obtained data and get an impression of the effects of detector coverage, the detected alpha particles can be plotted on a 2D mapping of the detector coverage. This mapping shows the position of each detected alpha particle in the DSSSDs in a θ-ϕ polar plot. This is shown in Figure 4.7.

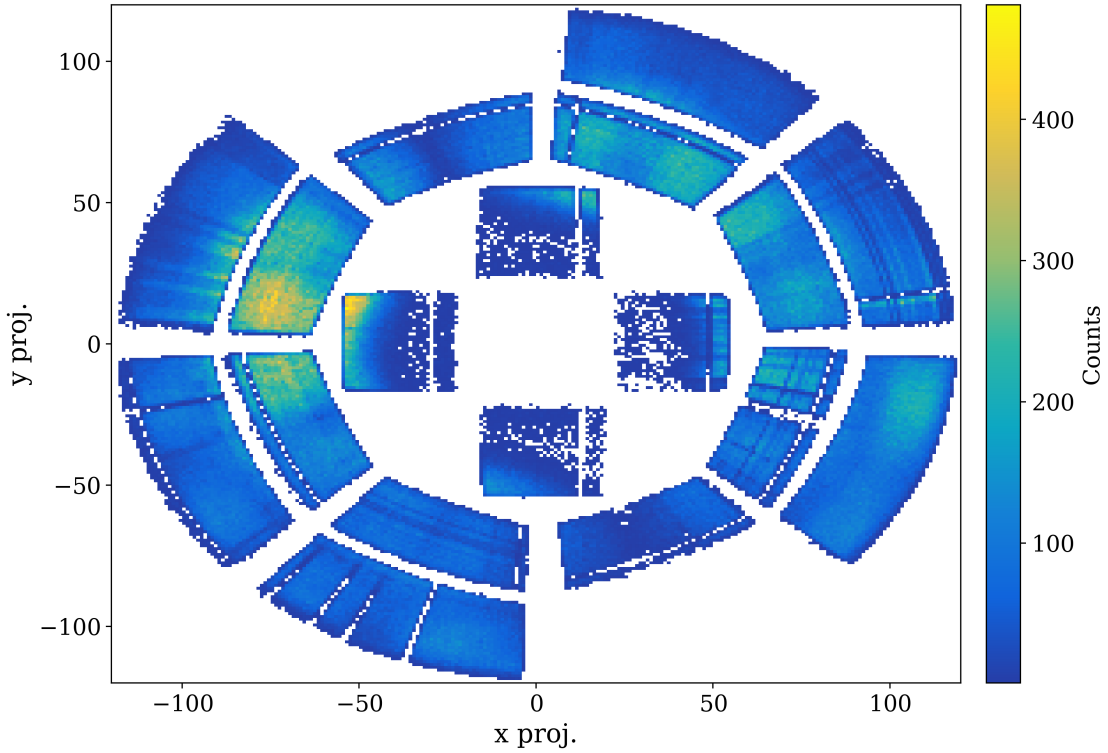

Figure 4.7: Detected alpha particles in the DSSSDs after applying the kinematics, coincidence and multiplicity gate conditions. Clearly visible are the barrel structure of the DSSSDs and the detector wall assembly. The perspective originates from the position of the target downstream along the beam trajectory towards the detectors.

4.1.3 Angular condition ($\Delta\theta$ and $\Delta\phi$)

The kinematic relationship between the ejectile and the recoiling carbon nucleus is well understood. This allows for the use of selection conditions on the angular distributions of the detected particles to further suppress background events. Since the excited carbon nucleus above the particle separation threshold decays into its three alpha constituents, its trajectory is not directly observable, and needs to be reconstructed from the measured

alpha particles. Since none of the three alpha particles' energies exceed 6 MeV, their velocities are below 5.7 % of the speed of light, resulting in $\gamma < 1.002$. This allows for the use of non-relativistic kinematics, which reduces the reconstruction of the trajectory of the recoiling nucleus to a direct vector sum of the momentum vectors of the three alpha particles.

Computing the direction vector of the carbon nucleus immediately yields its scattering angle $\theta_{^{12}\mathrm{C}}$ and azimuthal angle $\phi_{^{12}\mathrm{C}}$ relative to the beam axis. Furthermore, as the scattering angle of the scattered alpha particle is also known, the expected scattering angle of the carbon nucleus, $\theta_{^{12}\mathrm{C,calc}}$, can be calculated from the kinematics. Although we expect both angles to be equal and angular straggling in the target material should only cause slight broadening, the main intent of this condition is to suppress background events, where the ejectile's trajectory does not match the trajectory of the recoiling nucleus. The majority of the events at this point originate from the decay of the Hoyle state, as the previous conditions have already suppressed most other events.
The θ_α-$\theta_{^{12}\mathrm{C}}$ relationship was extracted using the LISE++ software [105] and is shown in Figure 4.8. Based on this, two conditions can be derived: One in the θ and one in

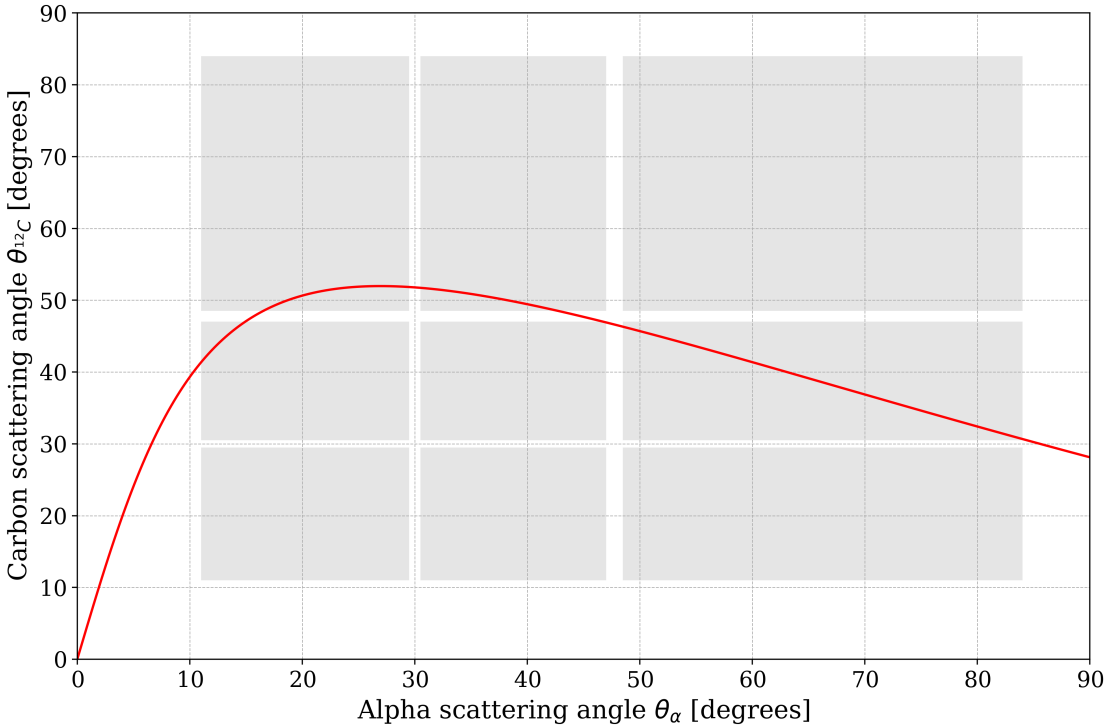

Figure 4.8: Scattering angle $\theta_{^{12}\mathrm{C}}$ of the carbon nucleus relative to the beam axis as a function of the scattering angle θ_α of the scattered alpha particle for a 27 MeV alpha beam exciting the Hoyle state (7.654 MeV). The shaded areas mark the angular coverage of the detectors.

the ϕ direction. These initial two conditions are demonstrated in Figure 4.9, which show the angular difference between the reconstructed ^{12}C nucleus and the computed θ and ϕ based on the scattered alpha particle.

Momentum conservation dictates that the initial scattering axis must form a reaction plane which passes through the beam axis. This results in an angle difference of 180° between the scattered alpha and the carbon nucleus in the laboratory frame, as can be seen in Figure 4.9b. Secondly, the difference in the scattering angle of the scattered alpha and the calculated scattering angle of the carbon nucleus should be small, as shown in Figure 4.9a.

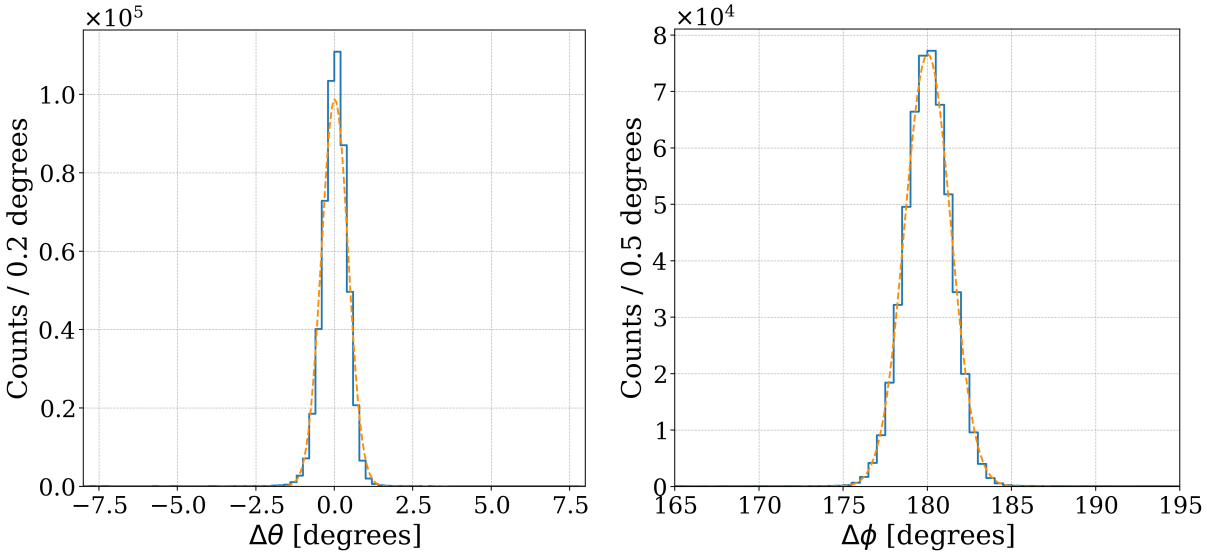

(a) Distribution of the scattering angle differences between ^{12}C and ejectile ($\theta_{^{12}\mathrm{C}} - \theta_{^{12}\mathrm{C,calc}}$).

(b) Distribution of the azimuthal angle differences between ^{12}C and ejectile ($\phi_{^{12}\mathrm{C}} - \phi_{^{4}\mathrm{He,scatter}}$).

Figure 4.9: The angular distribution of the difference between the scattering angle of the reconstructed ^{12}C nucleus and the computed θ based on the scattered alpha and the relationship of the azimuthal angles of ejectile and recoiling nucleus.

There is an additional improvement that can be made: The angular deviations, given by detector pixel size, angular straggling, beam width and energy loss in the target material before the reaction (changing the reaction energy), are not separated in θ and ϕ. Their scattering process results in a cone-shaped angular distribution, which is centered around the expected point. Projected onto the detector planes, this results in an elliptical distribution of events.
Gating on this shape can be used to improve the gate condition's efficiency, the measure of how well the condition separates the events of interest from the background. This is done by using a two-dimensional elliptical condition, which is demonstrated in Figure 4.10. As can be seen the data follows the expected elliptical shape and the filter condition's selection, indicated by a line, matches the data well.

These conditions are also automatically deduced by fitting the distributions shown in

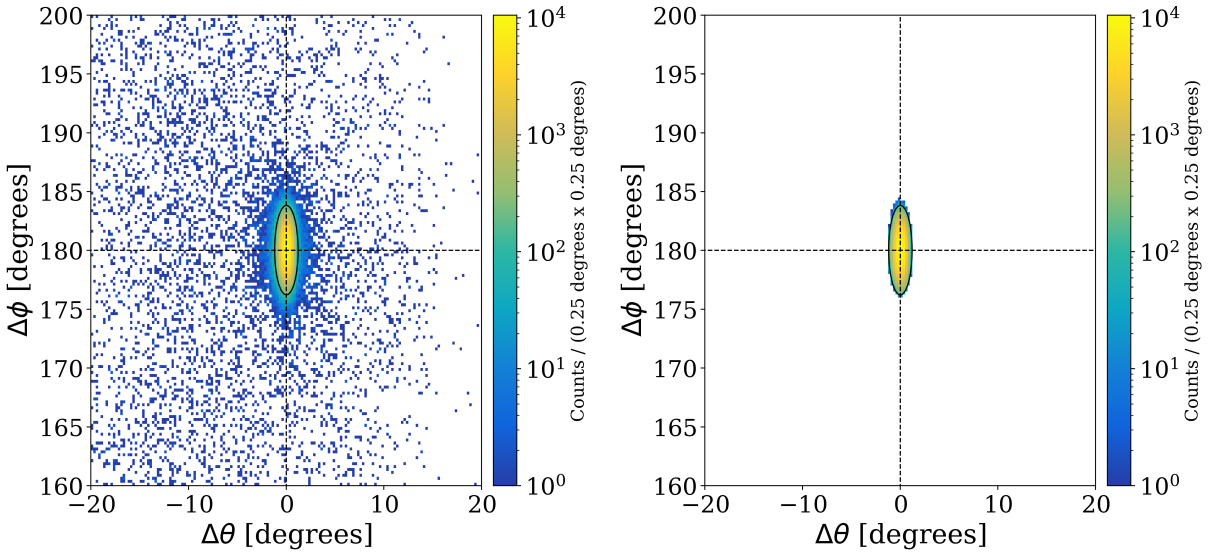

(a) Angular difference distribution before applying the angular condition.

(b) Angular difference distribution after applying the angular condition.

Figure 4.10: The angular distribution of the difference between the reconstructed ^{12}C nucleus and the computed θ and ϕ based on the scattered alpha

Figure 4.9 with Gaussian functions and using the mean in θ and ϕ as the center of the filter condition's ellipse. While the width can also be determined from the fit, it is set to the fixed values referenced in Table 4.2 to allow setting widths corresponding to expected straggling and detector resolution values during testing. The condition thresholds are set between 1.9 and 2σ for $\Delta\theta$ and between 2.3 and 2.6σ for $\Delta\phi$ of the fits of the measured $\Delta\theta$ and the $\Delta\phi$ distribution for the decay analysis. The exact values set to be more robust in fit-deviations between individual runs.

The reason to use the mean values determined via fit is to make the system more robust against deviations in the detector alignment and the beam energy at the time of reaction, which is directly dependent on the energy loss of the initial beam particle before the reaction. These offsets can be seen in Table 4.2, which shows a deviation towards lower angles for the $\Delta\theta$ condition and a minor offset in the $\Delta\phi$ condition.

The condition for the angular gate is defined as an elliptical region in the (θ, ϕ) plane. The area of this ellipse relative to the total area of the forwards facing semi-spherical surface is a measure of the gate condition's efficiency, if uniformly distributed background events are assumed, and can be used as an initial test for the suppression efficiency for random events. Although many background events follow kinematic dynamics, each of these events has its own reaction plane, resulting in a spread along the ϕ axis. Additionally, reactions where the scattered alpha particle does not match the reconstructed ^{12}C nucleus will also be suppressed by this gate condition as their relationship between $\theta_{\alpha'}$ and $\theta_{^{12}\mathrm{C}}$ will in most cases not follow the scattering dependency shown in Figure 4.8. This is visualized for a single event in Figure 4.11, where the opening angle of the cone

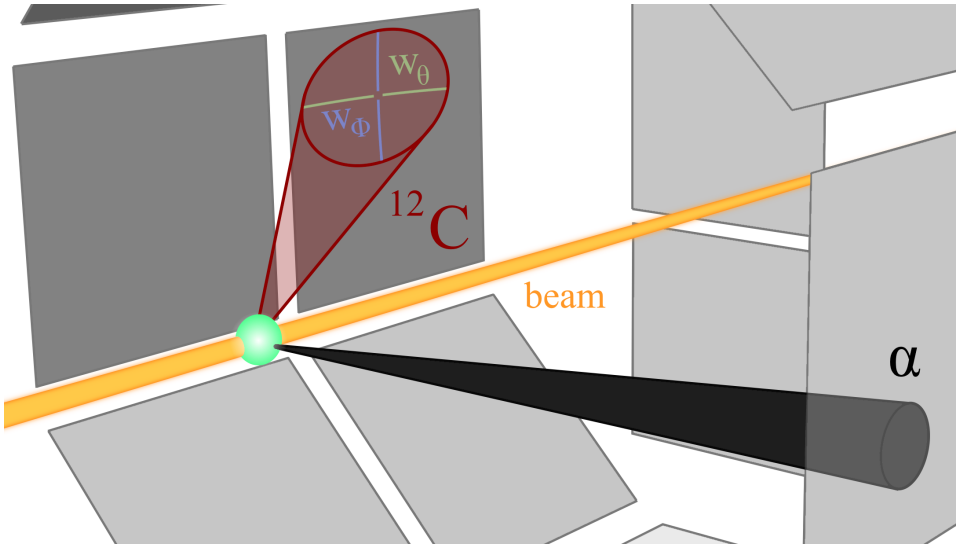

Figure 4.11: Schematic of a scattering reaction in the laboratory frame. The beam enters from the left. The grey outlines indicate the detector positions. The exaggerated opening angle of the ^{12}C cone shows the orientation of the angle differences in the $\Delta\theta$ and $\Delta\phi$ directions.

corresponding to the reconstructed ^{12}C nucleus shows the width of the angular gate condition.

Using these assumptions, the ratios between the angular deviation of an individual event, $\Delta\theta$ and $\Delta\phi$, and the width of the gate condition, w_θ and w_ϕ, which is based on the fit of the distribution of the angular deviations of the accumulated events, can be used to to test if an event passes the gate condition. An event satisfies the gate condition if:

$$\left(\frac{\Delta\theta}{w_\theta}\right)^2 + \left(\frac{\Delta\phi}{w_\phi}\right)^2 < 1.$$

This inequality defines an elliptical region in the (θ, ϕ) plane. The area A_{ellipse} of this ellipse is:

$$A_{\text{ellipse}} = \pi w_\theta w_\phi.$$

To estimate the gate efficiency, an elliptical cone with half-axes θ and ϕ is assumed. The isotropic background suppression efficiency is then given by the ratio of the area of the elliptical cone to the solid angle coverage of the detector array, Ω_{LYCCA}, which is given in Table 2.1.

For small angles, an elliptical cone with half-angles θ and ϕ can be used to approximate the area. Thus, the solid angle $\Omega_{\text{elliptical cone}}$ is given by

$$\Omega_{\text{elliptical cone}} \approx 2\pi \left(1 - \cos\theta \cos\phi\right). \tag{4.5}$$

To find the open angle coverage relative to the detector coverage

$$\text{Coverage} = \frac{\Omega_{\text{elliptical cone}}}{\Omega_{\text{LYCCA}}}, \tag{4.6}$$

substituting the respective solid angles, the following expression is obtained:

$$\text{Coverage} = \frac{2\pi\left(1 - \cos\theta\cos\phi\right)}{\Omega_{\text{LYCCA}}}. \tag{4.7}$$

The measured positions and used thresholds widths are listed in Table 4.2. For the given elliptical condition, the relative coverage is 1.88 % for the Hoyle state and 1.97 % of the solid angle of the setup for the 3^- state, corresponding to an isotropic background suppression of 98.12 % and 98.03 %, respectively.

As can be seen, the positions are in very good agreement, and only 0.114° off for the $\Delta\phi$ gate and 0.009° off for the $\Delta\theta$ gate for events matching the Hoyle state kinematics. For the next higher-lying excited state, the 3^- state, the deviations are 0.012° and 0.020°, respectively. These deviations demonstrate the robustness of the gate conditions and the quality of the detector position calibration discussed in Section 3.8. It is of note that the alignment procedure can only shift entire detectors, and not individual pixels, which makes the obtained result less prone to overfitting and systematic errors. One systematic dependency, however cannot be mitigated by this technique: If the beam vector is not perfectly parallel to the central symmetry axis, this cannot be corrected by the alignment procedure or registered in the angle-offset calibration. The reason for this is, that the angular theta-dependency between ejectile and recoil has a negative slope, as can be seen in Figure 4.8: As the recoil is emitted 180° opposite to the ejectile. A slight rotation of the beam axis would increase either the ejectiles' or the recoils' scattering angle and decrease the scattering angle of the other, shifting the event on the θ-θ curve.

Table 4.2: Measured positions and widths of the angular condition.

State	Condition	Mean [°]	Width [°]	Threshold [°] (Half gate width)
Hoyle state	$\Delta\theta$	-0.009	0.46	1.2
	$\Delta\phi$	180.114	1.68	3.8
3^- state	$\Delta\theta$	0.012	0.75	1.5
	$\Delta\phi$	180.020	1.98	3.75

Despite this shortcoming, the angular condition is still a helpful requirement to discriminate kinematic events not originating from the initial beam momentum: The Energy - θ plot after applying the angular gate demonstrates that the gate is effective in suppressing background events, as the remnants of background lines are reduced and the resulting distribution gets narrower, as seen in Figure 4.12.

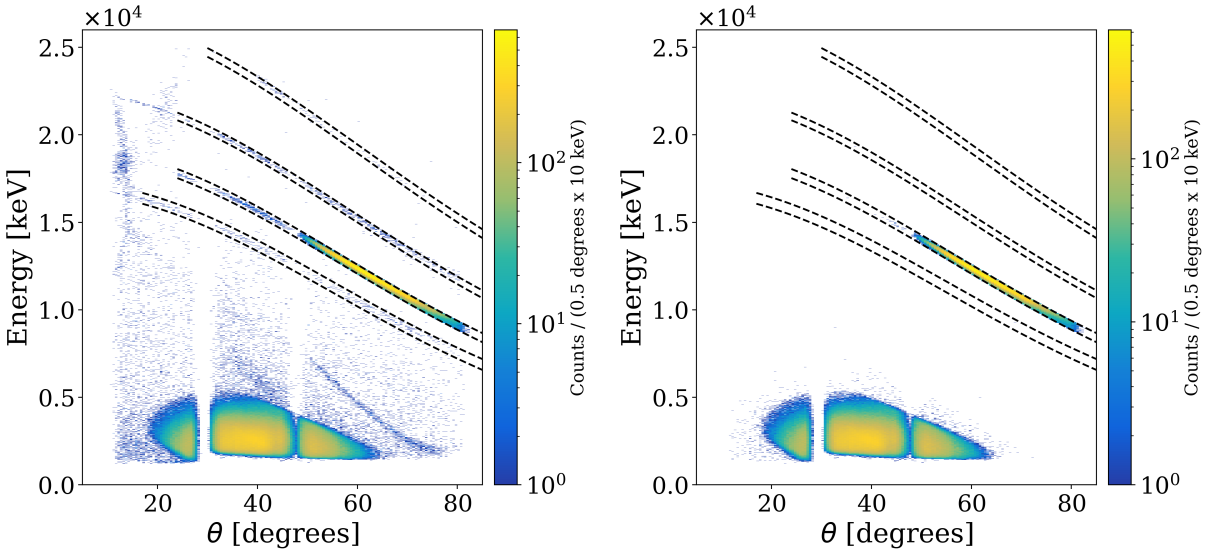

(a) Energy of the scattered particles against the detection angle of the respective pixel to the beam axis before applying the angular gate.

(b) Energy of the scattered particles against the detection angle of the respective pixel to the beam axis after applying the angular gate.

Figure 4.12: Energy of the scattered particles detected in the DSSSDs against the detection angle of the respective pixel to the beam axis.

4.1.4 Energy sum conditions

Another conserved quantity that can be used to suppress background events is the conservation of energy in all reference frames. This is used twice in the analysis: Once in the laboratory frame, the following relationship can be utilized:

$$\sum_{i=1}^{4} E_{\alpha_i} + E_{\alpha\prime} + \Delta_m = E_{\text{beam}}, \tag{4.8}$$

where E_{α_i} is the energy of the decay alpha particles, $E_{\alpha\prime}$ is the energy of the scattered alpha particle, Δ_m is the energy equivalent to the mass difference between ^{12}C and the three alpha particles, and E_{beam} is the initial beam energy. This can be seen in the energy sum plot in Figure 4.13. The mean value of the distribution is at 27.4 MeV, which is 1.5 % above the beam energy. This is caused by the energy loss correction term slightly overestimating the energy loss in the target material as well as minor coordinate deviations caused by the beam spot size. This distribution shifts the reference lines used for the energy calibration towards lower scattering angles, where they are erroneously shifted to higher energies. This effect is reduced by the reaction position correction, but not fully compensated. As all decay-related processes are easier to describe in the *center-of-mass* frame of the decaying ^{12}C nucleus, a transformation to this reference frame is performed for each event. To do this, the already computed velocity vector of the reconstructed ^{12}C nucleus is used to transform the energy and momentum of the detected

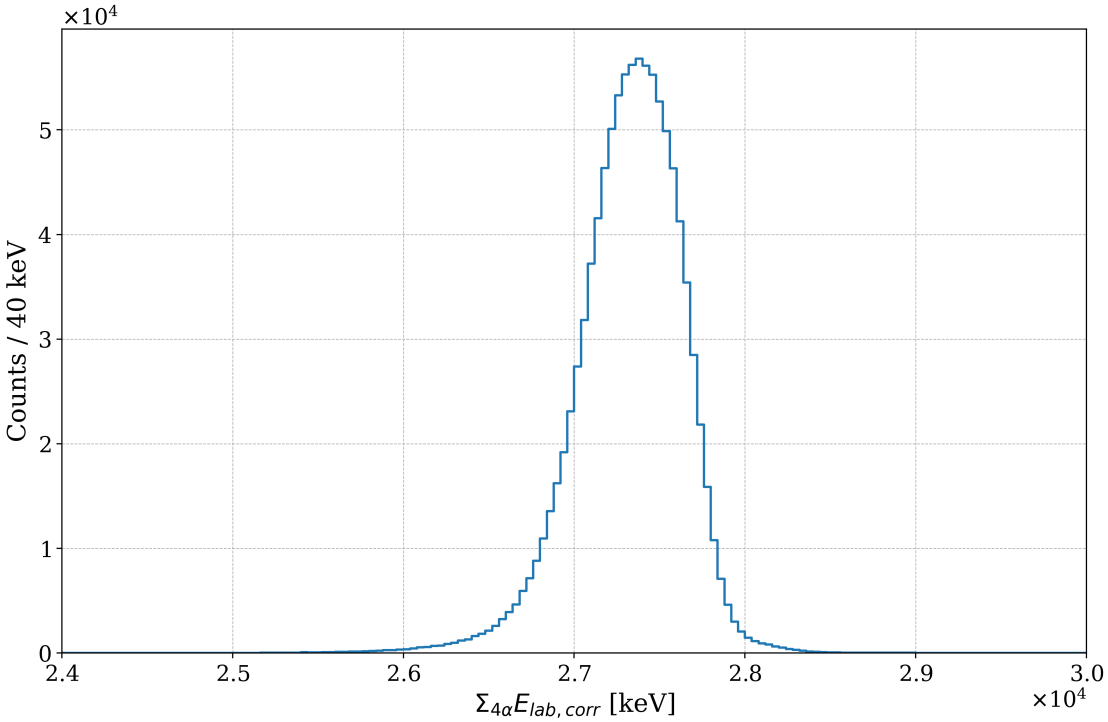

Figure 4.13: Energy sum of the four detected alpha particles in the laboratory reference frame with applied energy loss correction. The mean value of the distribution is at 27.4 MeV.

alpha particles into relative movement to the ^{12}C nucleus. Since the three alpha particles originate from the decay of this nucleus, all vector quantities are thus transformed into the center-of-mass frame. As discussed earlier (Section 4.1.3), these transformations are only valid due to the low velocities of the measured alpha particles. Using the velocity vectors, the kinetic energies of the alpha particles in the center-of-mass frame can also be calculated.

Based on this transformation, the second energy gate is applied in the center-of-mass frame, where the energy sum of the decay products must equal the excitation energy of the populated state in ^{12}C plus the Q-value of the break-up reaction:

$$\sum_{i=1}^{3} E_{\alpha_i} = E_{\text{exc}} + Q_{\text{break-up}}. \tag{4.9}$$

The Q-value for the Hoyle state is 379.6 keV [45]. These equations are only valid if the energy losses in the target material and the dead layer of the detectors are taken into account. Any deviation from the expected energy sum will still produce a peak in the energy spectrum that can be used for gating, but the peak position will be shifted and the peak broadened, reducing the gate efficiency. The energy gates are demonstrated in Figure 4.15. The used fit functions are *Voigt* functions, which are a convolution of a Gaussian and a Lorentzian distribution. The Voigt function is used to account for the

energy resolution of the detectors and the intrinsic width of the peaks.
For the energy gates, we use the energy sum of the four alpha particles in the laboratory reference frame plus the reaction Q-value and the three alpha energy sum of the decay products of the Hoyle state in the center-of-mass frame of the decay. As evident by the elliptical distribution in the energy sum- energy histogram (Figure 4.14a), the energy sums are generally independent, but a slight trend can be observed. This is caused by the energy loss in the target material and its impact on the reconstruction of the center-of-mass frame.

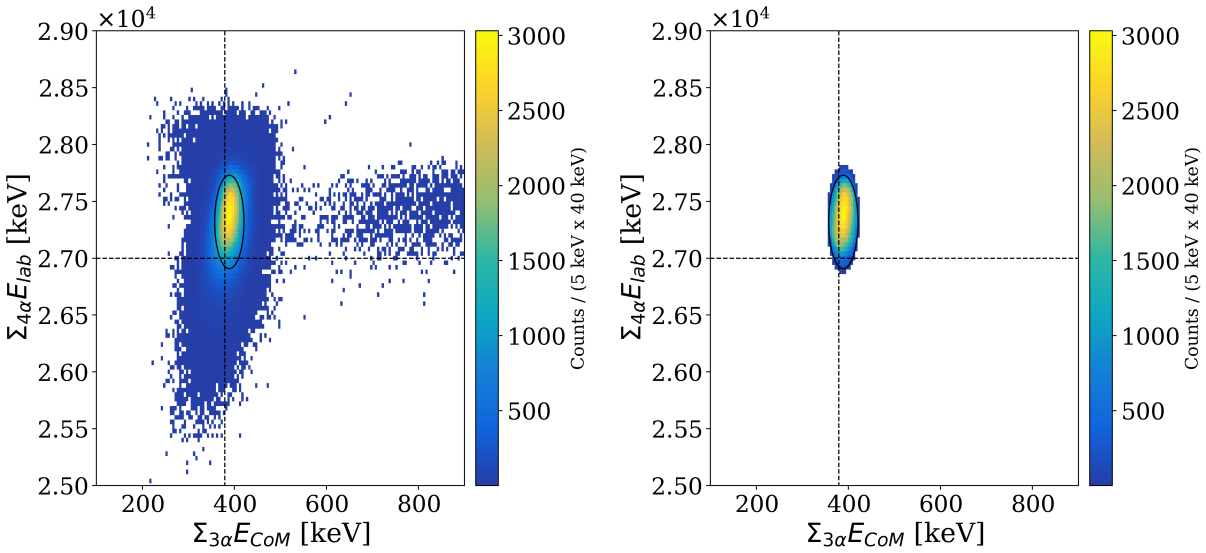

(a) Energy sum of the four detected alpha particles **before** applying the laboratory-frame and center-of-mass-frame energy conditions.

(b) Energy sum of the four detected alpha particles **after** applying the laboratory-frame and center-of-mass-frame energy conditions.

Figure 4.14: Comparison of the energy sums of the four detected alpha particles in the laboratory and in the center-of-mass frame before and after the energy-sum condition.

The obtained gate widths are displayed in Table 4.3.

Table 4.3: Measured positions and widths of the energy-sum selection conditions in the laboratory and center-of-mass frame for both experiments.

Condition	2019		2020	
Condition	Mean [keV]	Width [keV]	Mean [keV]	Width [keV]
$\Sigma_{4,\text{lab.}} E_\alpha$	27313.8	275.9	27349.5	304.1
$\Sigma_{3,\text{CoM.}} E_\alpha$	389.0	21.2	389.1	28.3

As can be seen in the energy-theta histogram in Figure 4.15, the gates suppresses all events outside the primary distribution.

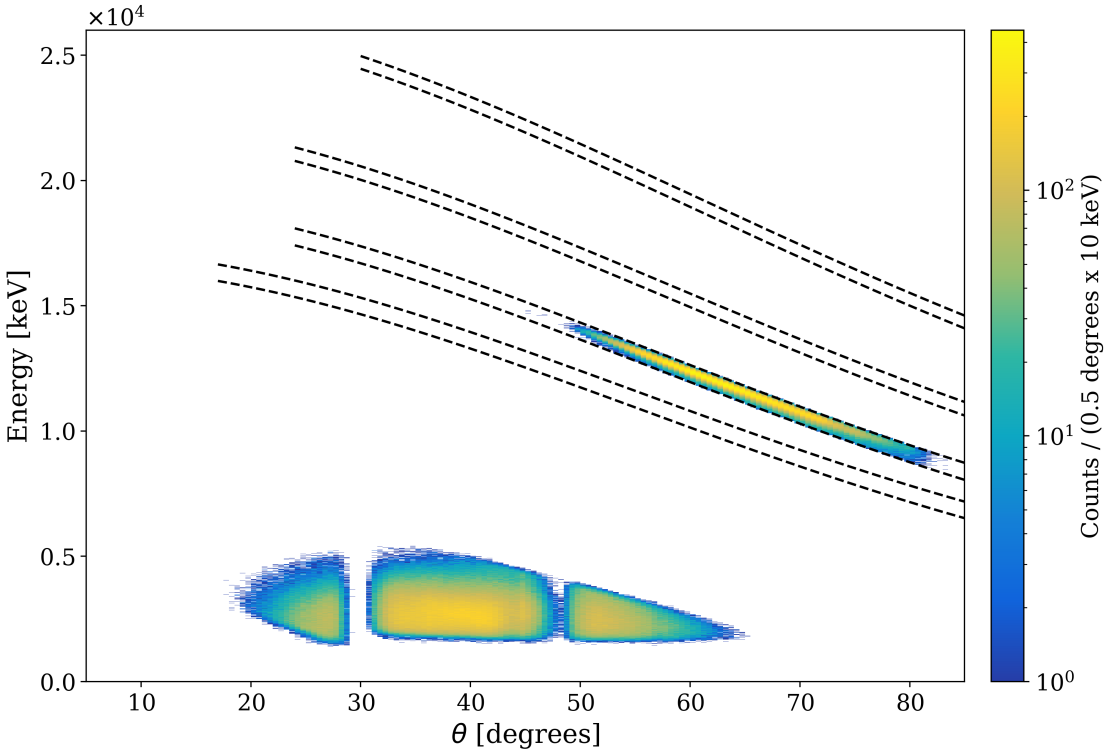

Figure 4.15: Energy of the scattered particles registered in the DSSSDs against the detection angle of the respective pixel to the beam axis after applying the coincidence gate after all utilized gate conditions (kinematics, coincidence, multiplicity, angular distribution, energy sum in laboratory and center-of-mass frame).

4.1.5 Event selection efficiency

Each gate applied to the data has an associated efficiency, which is governed by its sensitivity, the probability that a true decay event is accepted by the condition, as well as its specificity, which is the probability that a background event is rejected by the gate condition. The efficiency of the gates is crucial for the analysis, as it directly influences the statistics of the data. Both metrics are directly dependent on the width of the gate, which is always a trade-off between efficiency and specificity.

The most selective condition is the kinematic filter, followed by the multiplicity gate. The energy condition passes almost 85 % of the events. The efficiencies for the applied conditions are summarized in Table 4.4 for the combined December 2019 and January 2020 datasets.

Table 4.4: Gate efficiencies and detection counts for the applied gates for the combined dataset (December 2019 and January 2020). Four detected hits make up a final event.

Gate	Remaining registered hits	Efficiency [%]
Raw data	3.19×10^{10}	-
Kinematic	1.56×10^{8}	0.490
Multiplicity	4.45×10^{6}	2.844
Angular	4.12×10^{6}	92.646
Energy sum	3.46×10^{6}	84.030
Energy sum (COM)	2.61×10^{6}	75.374
Combinatorial veto	2.34×10^{5}	16.878

Since the values in the table count detector hits, the amount of Hoyle state decay events was only a quarter of the registered particle count. This results in $2.61 \times 10^6/4 = 6.52 \times 10^5$ remaining Hoyle state decay events after all gates have been applied. The resulting event counts for each beam time are summarized in Table 4.5.

Table 4.5: Total Hoyle state decay events (4 alpha particles each) after the final condition for complete events where all 4 particles were detected with a gate width of 1.5σ with and without the combinatorial veto, discussed in Section 4.1.6.

Dataset	Remaining decay events	Remaining events after veto
December 2019	3.31×10^{5}	2.95×10^{5}
January 2020	3.21×10^{5}	2.89×10^{5}
Total	6.52×10^{5}	5.84×10^{5}

4.1.6 Combinatorial mismatch

While the previously described gate conditions are effective in suppressing background events, some of the accepted events can still exhibit systematic deviations. As mentioned in Section 3.3.3, one source for position errors is the recombination-process of front- and back-side strip events. During this process two particles close energies enter one detector at the same time. The up to four activated strips can then no longer be unambiguously assigned to the two particles, introducing a potential mismatch. Since the acceptance-window for energy differences between the two strip-events forming one detector hit is relatively wide (typically between 109 keV and 152 keV), these mismatches can occur for the decay products of the Hoyle state.

To avoid this problem, multiple techniques can be employed: The easiest is to only accept events, where all four alpha particles are registered in different detectors. This removes the ambiguity of the event position, but also drastically reduces the statistics, as can be

seen in the comparison between Figures 4.23 and 4.16, with the four-detector distribution containing about 50.2 % less events. The statistics for three and four-detector events are

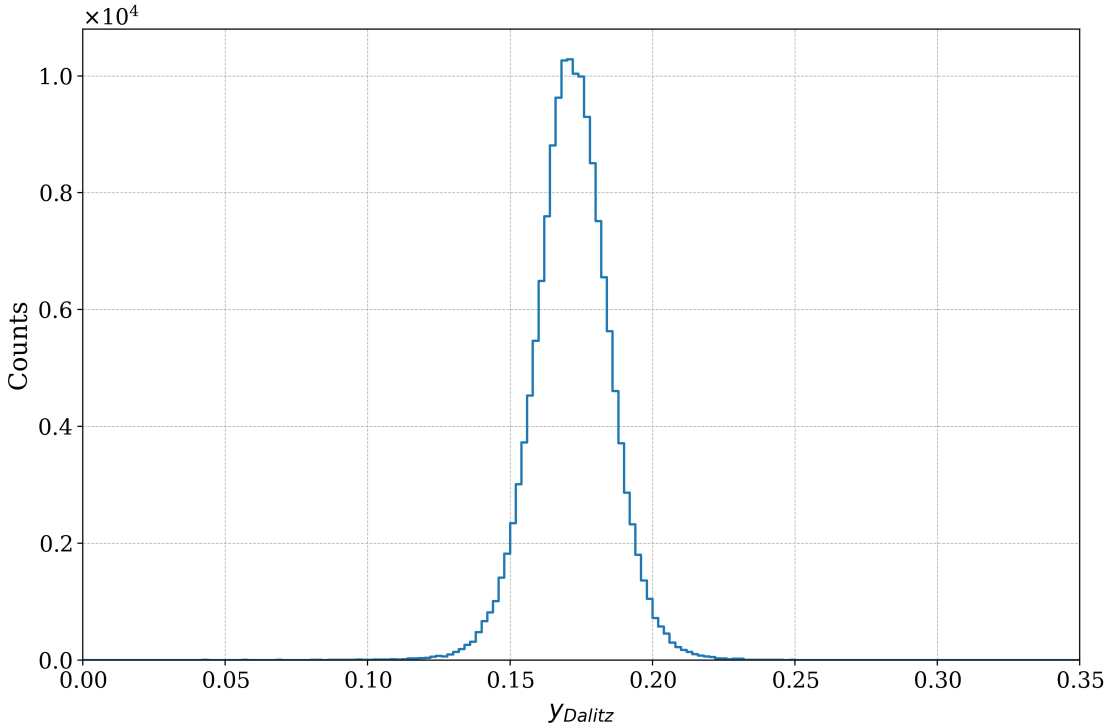

Figure 4.16: Y-component of the folded Dalitz plot of the three detected alpha particles of the Hoyle state break-up in the center-of-mass frame after all described conditions, projected onto the $(2\epsilon_{\alpha_3} - \epsilon_{\alpha_2} - \epsilon_{\alpha_1})$ plane. The plot shows the distribution for events where all four alpha particles are detected in different detectors.

summarized in Table 4.6. This shows a significant reduction in statistics, as almost half of the events are rejected by this condition. A more effective mitigation strategy is to

Table 4.6: Total Hoyle state decay events after the final gate condition for different event detector-counts and the combinatorial mismatch veto, here shown for an energy of 5 MeV and a ring detector.

Condition	Remaining decay events
Any detector combination	6.52×10^5
3 detectors	3.16×10^5
4 detectors	3.28×10^5
3 & 4 detectors with veto	5.84×10^5

pass all four-detector events, but to also include an additional check for events where the four particles hit only three detectors: As detailed in Section 3.3.3, the energy difference between front- and back-side strip entries is used as a condition when combining these to complete detector hits. Events are only accepted if the energies of both registered entries

differs by more than the front-back combination gate threshold plus a safety margin. In this case, a width of 250 keV was used as veto threshold. Given the maximum permissive veto of 152 keV, which corresponds to 3.0 σ of the Gaussian-shape approximated front-back energy difference distribution, this is a separation between the distributions of about 4 σ. Thus, the probability of a random event passing this condition can be estimated by the square of the integral of the Gaussian distribution below 2 σ, which is about 5.95×10^{-4}. This results in a reduction of the conflicting events while only rejecting 8.04 % of the measured events. As can be seen in Figure 4.17, applying this condition reduces the distribution width while maintaining the overall statistics. This especially

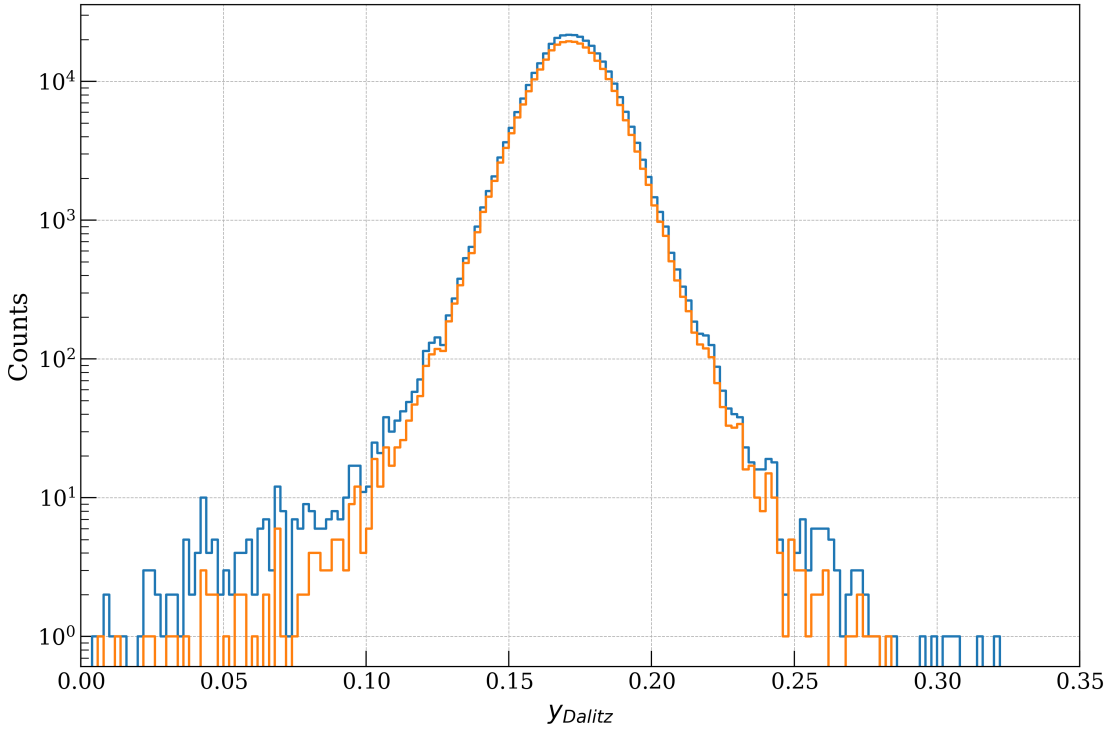

Figure 4.17: Comparison of the Y-component of the folded Dalitz plot of the three detected alpha particles of the Hoyle state break-up in the center-of-mass frame after all described gates, projected onto the $E_{\alpha_1} - E_{\alpha_2}$ plane. The plot shows the superimposed distributions with the combinatorial mismatch veto (orange) and without (blue).

improves the background suppression in the outer regions of the Gaussian peak that corresponds to the sequential decay mode. This region is of particular interest, as events corresponding to the direct decay modes are expected to be located in there. Thus, background suppression in this region is crucial for the analysis of the branching ratios of the Hoyle state decay. The veto gate demonstrates efficient background suppression, and its width of 250 keV is substantially wider than the typical 135 keV energy width in which front- and back-side strip events can be combined.

4.2 Hoyle state decay analysis

The initial data analysis has been completed, and at this point, the data from the experiment and the Monte Carlo simulation are ready to be analyzed. The data obtained from the previous gates shows no remaining significant background events. After the center-of-mass transformation into the decay frame of reference, the data can now be analyzed to study the decay properties of the Hoyle state. The following sections will discuss the analysis techniques, a selection of observables, and the results of the analysis.

4.2.1 Reduced energies

After the transformation to the center-of-mass reference frame, the absolute energies of the three decay alphas in the center-of-mass frame are of limited usefulness, as their sum is fixed by the decay energy of the ^{12}C nucleus. This was also used as a gate in the primary data analysis (see Section 4.1.4). Instead, the reduced energies ϵ_i were used, which are defined as the energy of the alpha particle divided by the measured decay energy of the ^{12}C nucleus. This approach offers multiple advantages:

- The reduced energies are dimensionless and scaled to their reaction Q-value, which makes it easier to compare between decays from different excited states.
- The reduced energies are invariant with respect to the exact decay energy of the ^{12}C nucleus, which reduces the systematic uncertainty of the energy calibration and the energy loss corrections. It also ensures that the only remaining dependency of the reduced energy is the decay process itself.

This ensures that the reduced energies only depend on the decay process of their respective excited state. As introduced in Section 1.5, the sequential decay of the ^{12}C nucleus is the dominant decay channel compared to the three different direct decay modes. The resulting distribution for the reduced energies of the three detected alpha particles is shown in Figure 4.18.

The distribution shows a distinct peak at $\epsilon = 1/2$ which corresponds to the initially emitted alpha particle in the sequential decay mode. The continuum at lower ϵ values primarily originates from the subsequent beryllium decay. The continuum exhibits an upward sloping shape, which can be explained by the low energy thresholds, as was demonstrated using the supporting Monte Carlo simulation, later discussed in Section 5.6. Since the angles in the center-of-mass frame are known, the angle difference ω between the velocity vector of the alpha with the highest energy in the center-of-mass frame and the vector between the two lower energy alphas can be calculated. For the prominent sequential decay mode, this corresponds to the angle difference between the alpha particle's velocity vector in the center-of-mass frame and the subsequent beryllium decay axis,

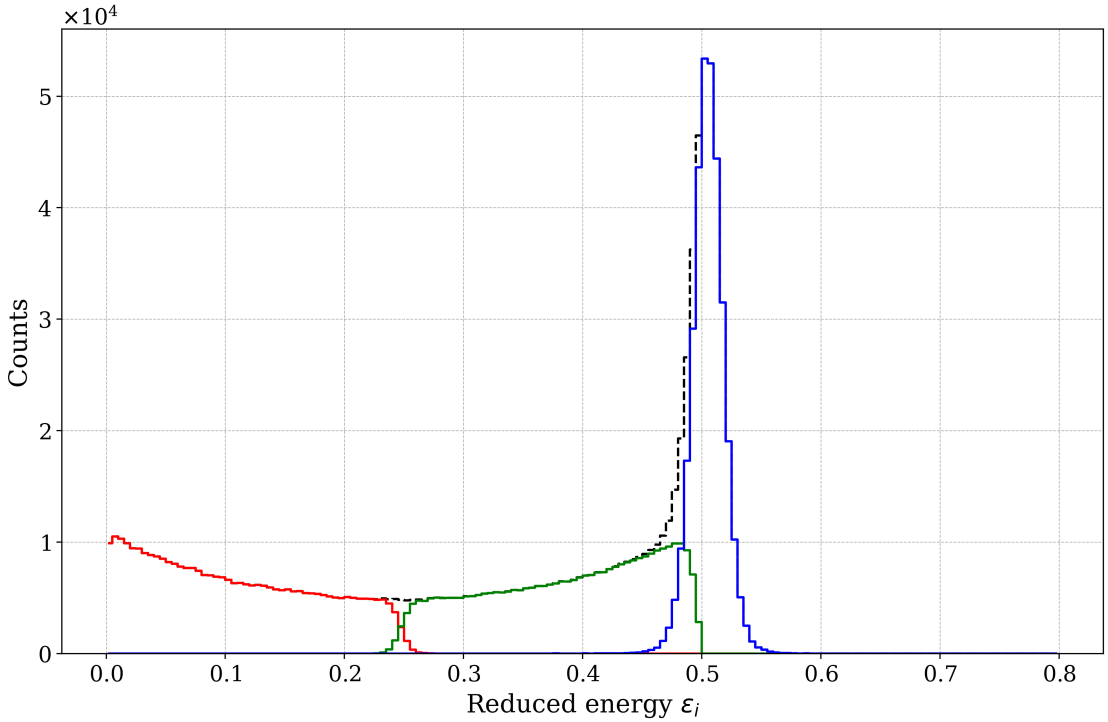

Figure 4.18: Comparison of the reduced energies of the three detected alpha particles in the center-of-mass frame for the Hoyle state decay. The dashed line indicates the sum of the distributions. The three alphas are ordered by their energy in the center-of-mass frame.

the connecting vector between the two lower energy alpha particles in the center-of-mass frame. As can be seen in Figure 4.19, this creates a clear dependence of the reduced energies on the angle difference, which can be seen in Figure 1.9. The plot in Figure 4.19 visualizes this degree of freedom of the sequential decay: The energy of the initial alpha is fixed by the $^{12}C \rightarrow ^{8}Be + \alpha$ decay, as energy and momentum conservation only provide one solution for the energy partition of the initial reaction products. This can be seen in the vertical line at $\epsilon = 0.505$ in the plot (derivation provided in appendix Section A.6). During the secondary decay step the alpha particles of the beryllium decay have to be emitted antiparallel in the center-of-mass frame of the beryllium nucleus to conserve momentum.

When the opening angle between the initial alpha's emission trajectory and the subsequent beryllium decay axis is 90°, both beryllium alpha particles have the same energy in the center-of-mass frame of the decaying ^{12}C nucleus.

This can be easily understood from a geometrical perspective, as their perpendicular momentum relative to the initial decay axis must cancel out. As the angle ω between the initial alpha emission and the subsequent beryllium decay decreases, the emission vector of one of the beryllium alphas aligns more closely with the initially emitted alpha, as illustrated before in Figure 1.9. This alignment reduces the energy of the second alpha particle in the center-of-mass frame due to the counteracting momentum contribution

from the beryllium nucleus following the initial decay. Conversely, the second alpha particle from the beryllium decay is emitted in the opposite direction relative to the motion of the beryllium nucleus, thereby increasing its energy by a similar magnitude. This splitting towards lower axis angle differences of the energies between the two beryllium-alpha particles can be seen in Figure 4.19: At 90° the energy of the two alpha particles is equal at approximately $\epsilon = 0.247$, which separates into two distinct lines with a sinusoidal shape as the angle difference ω decreases. The energy of the third alpha particle is fixed by the energy conservation of the initial decay process and is constant at $\epsilon = 0.505$.

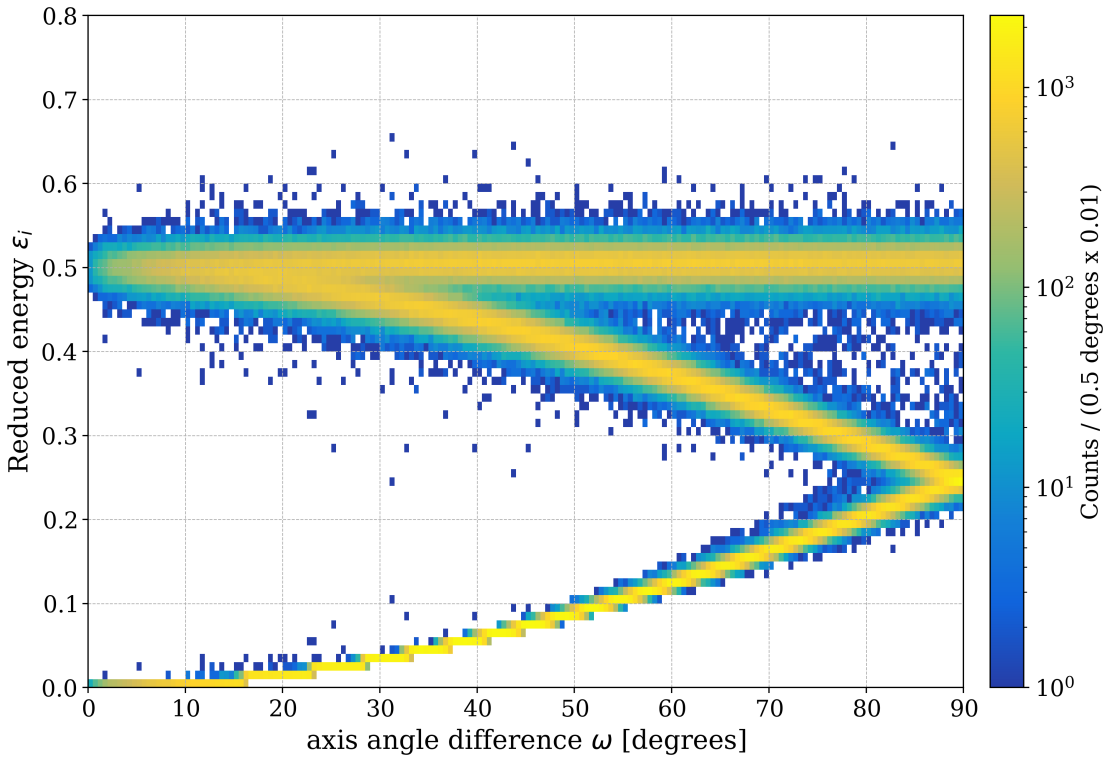

Figure 4.19: Reduced energies of the three detected alpha particles in the center-of-mass frame plotted against the angle difference between the alpha particle with the highest energy and the vector between the other two alpha particles.

Dalitz plots

The most prominent feature of the obtained Dalitz plot is the large triangle shape which contains most detected events. As discussed in Section 1.6 these originate from sequential decays of the Hoyle state. As at this stage no inherent distinction between the different alpha particles is made, the Dalitz plot is symmetric with respect to the exchange of the alpha particles. This symmetry allows one to fold the Dalitz plot along its symmetry axes, which results in a more compact representation of the data with higher statistics per bin. The folded Dalitz plot is shown in Figure 4.22.

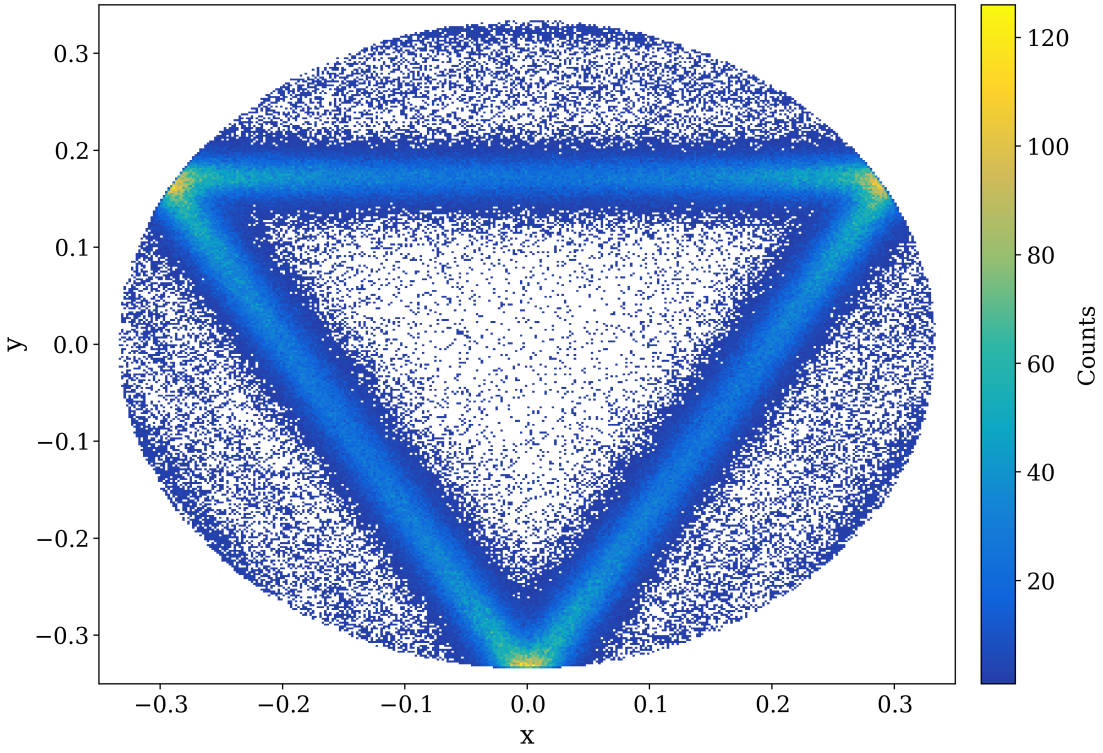

Figure 4.20: Dalitz plot of the three detected alpha particles from the Hoyle state break-up in the center-of-mass frame. The plotted events were selected by the using the Hoyle state's kinematic line to find a reaction's ejectile and the decay alphas were identified using the coincidence window and multiplicity condition. No other conditions, such as angular or energy gates, were applied.

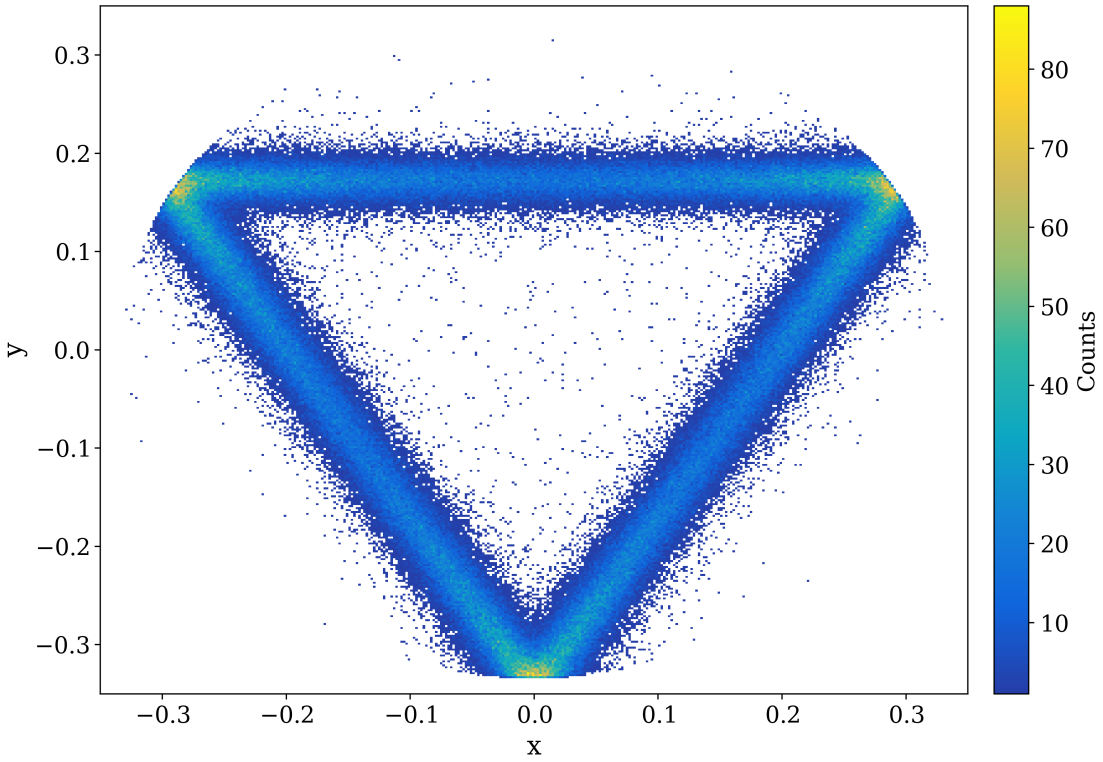

Figure 4.21: Dalitz plot of the three detected alpha particles from the Hoyle state break-up in the center-of-mass frame after all described conditions: Kinematic selection, coincidence filtering, multiplicity condition, angular gate, and energy sum gate. The employed thresholds are listed in the respective sections.

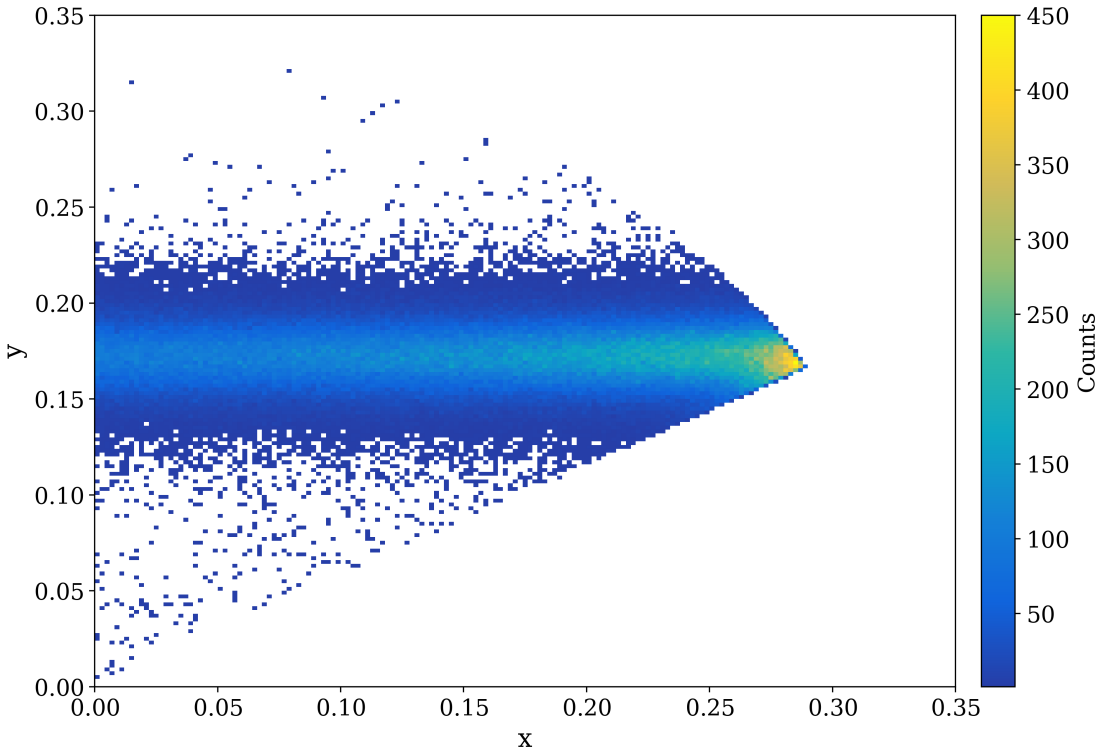

Figure 4.22: Folded Dalitz plot of the three detected alpha particles from the Hoyle state break-up in the center-of-mass frame after all described conditions.

As the key interest of the presented study is the distinction of the branching channels of the Hoyle state, the separation between the aforementioned triangle and the rest of the data should be maximized. To facilitate this, the projection of the Y-axis of the folded Dalitz plot can be used: It clearly shows a main peak, a cross section of one of the triangle's sides. The direct decay events are expected to be located around it, forming a wide enhancement of the underlying continuum. This was demonstrated by the supporting Monte Carlo simulation, which will be discussed in Section 5.6.

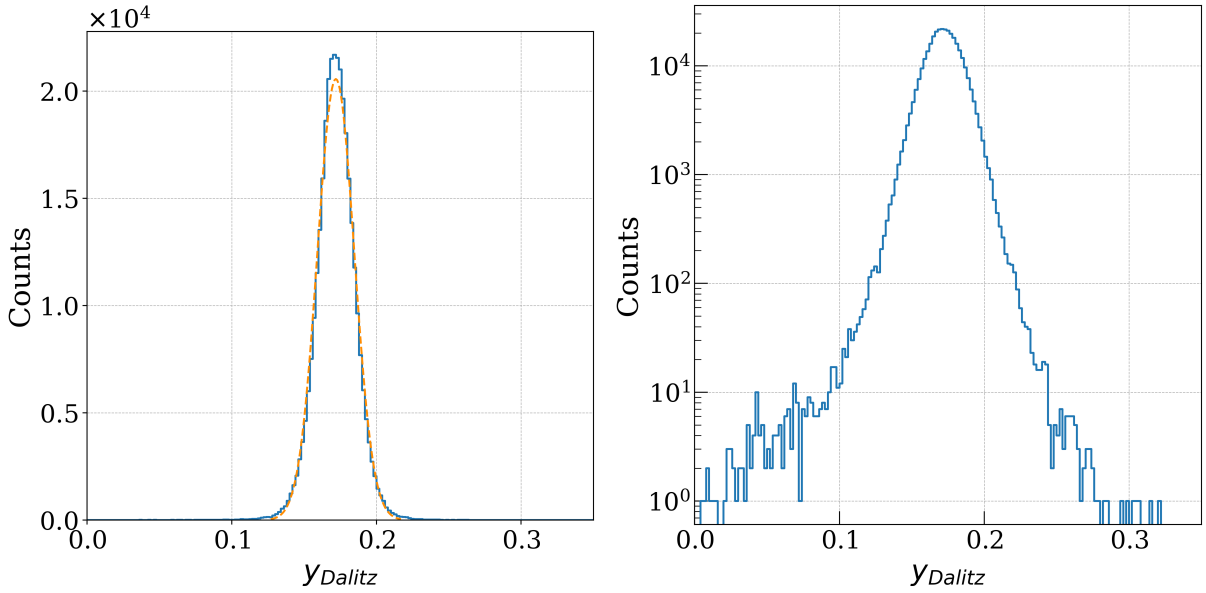

(a) Y-projection of the folded Dalitz plot after the application of all described conditions.

(b) Logarithmic plot of the Y-projection of the folded Dalitz plot after all conditions.

Figure 4.23: Y-projection of the folded Dalitz plot of the three detected alpha particles from the Hoyle state break-up in the center-of-mass frame after all described conditions, projected onto the $E_{\alpha_1} - E_{\alpha_2}$ plane.

4.2.2 Systematic deviations

Studying this projection, the standard deviation of each run can be used to test the energy resolution in the center-of-mass reference frame. The result of this test is presented in Figure 4.24 showing a clear difference between the resolution during the December and January campaign. Multiple reasons, such as slightly different detector alignment or wider beam dispersion can be the cause of this degradation. Radiation damage of the detectors is less likely, as the expected behavior would be a continuous regression towards higher run indices or even a slight improvement after the beam interruption due to passive annealing and migration of trapped charge carriers.

Since the simulated peak-shape only corresponds to a singular setup resolution, the data were split into the December and January section to be analyzed separately in the subsequent steps. The core reason for this is that the wider distribution of sequential

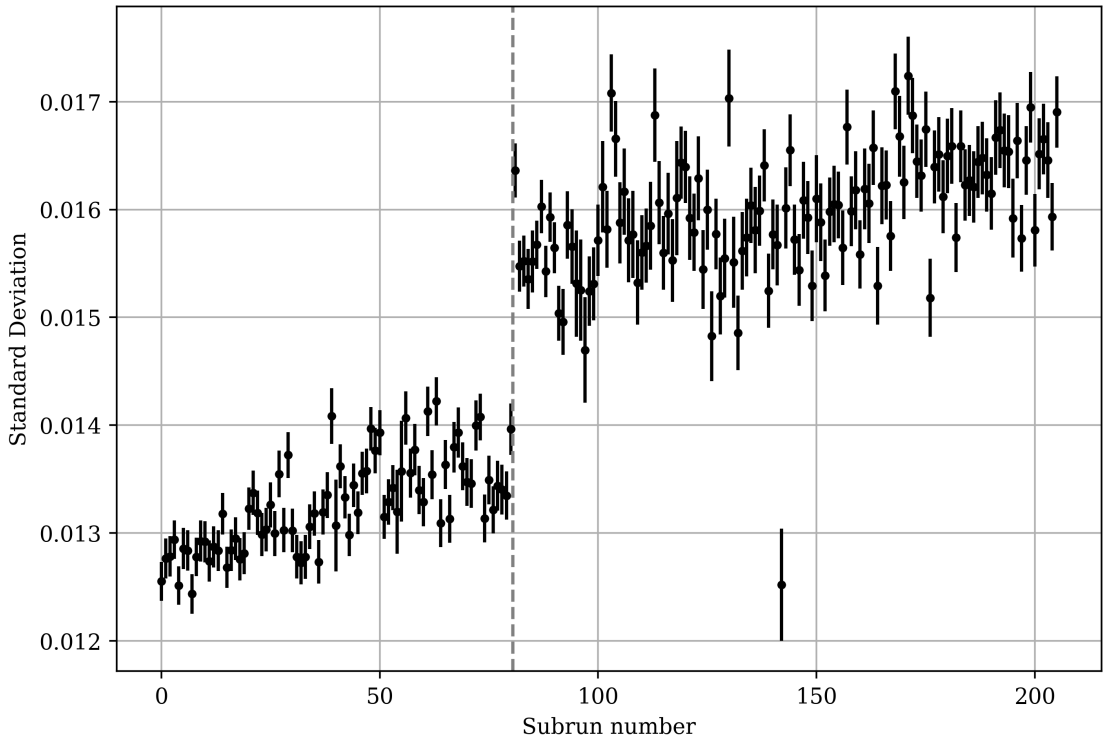

Figure 4.24: Standard deviation of the Y-component of the folded Dalitz plot of the three detected alpha particles from the Hoyle state break-up in the center-of-mass frame after all described conditions plotted against the run number.

decay events from the January campaign further overlap the distribution formed by the direct decay events compared to the December campaign creating a systematic deviation in the data. This will be further discussed in the Chapter 6.

4.2.3 Reconstructed Events

Based on the number of registered particles per event, which was determined when applying the multiplicity condition (see Section 4.1.2), events with a multiplicity of three were recorded 9.04 times more frequently than those with a multiplicity of four. A list of potential causes for this is stated in Section 3.3.3. Since a large fraction of the events with a multiplicity of three are expected to be Hoyle state decay events, an attempt was made to salvage as many of these events as possible. The system of four detected alpha particles, the ideal analysis case, is overspecified. Events with a multiplicity of three, however, in which one alpha particle was not detected, contain just sufficient information to reconstruct the missing alpha particle. To facilitate this, momentum conservation in the laboratory frame is used:

$$\vec{p}_{\text{beam}} + \vec{p}_{\text{target}} = \vec{p}_{\text{beam}} = \vec{p}_{\alpha\prime} + \vec{p}_{^{12}\text{C}} = \vec{p}_{\alpha\prime} + \sum_{i=1}^{3} \vec{p}_{\alpha_i} \tag{4.10}$$

Since the beam energy, and thus the beam momentum, is known and the initial momentum of the target nucleus is zero (on the scale of the beam momentum), the momentum-sum of the four alpha particles after the reaction is known. Since one of the alpha particles is not detected, the momentum of the missing alpha particle can be reconstructed by subtracting the sum of the momenta of the three detected alpha particles from the beam momentum. This is done for each event with multiplicity three during the analysis, and the reconstructed alpha particle is added to the event, which is then stored separately. The reconstructed alpha particle is then treated as a detected alpha particle in the subsequent analysis, as described in the previous sections. The reconstructed events are then transformed to the center-of-mass frame and the reduced energies are calculated. Using the reconstructed vector in the laboratory frame, a polar mapping of its position in the detector array positions can be created, as shown in Figure 4.25 (for comparison, a polar detector map of multiplicity four events is shown in Figure 4.7). While this approach

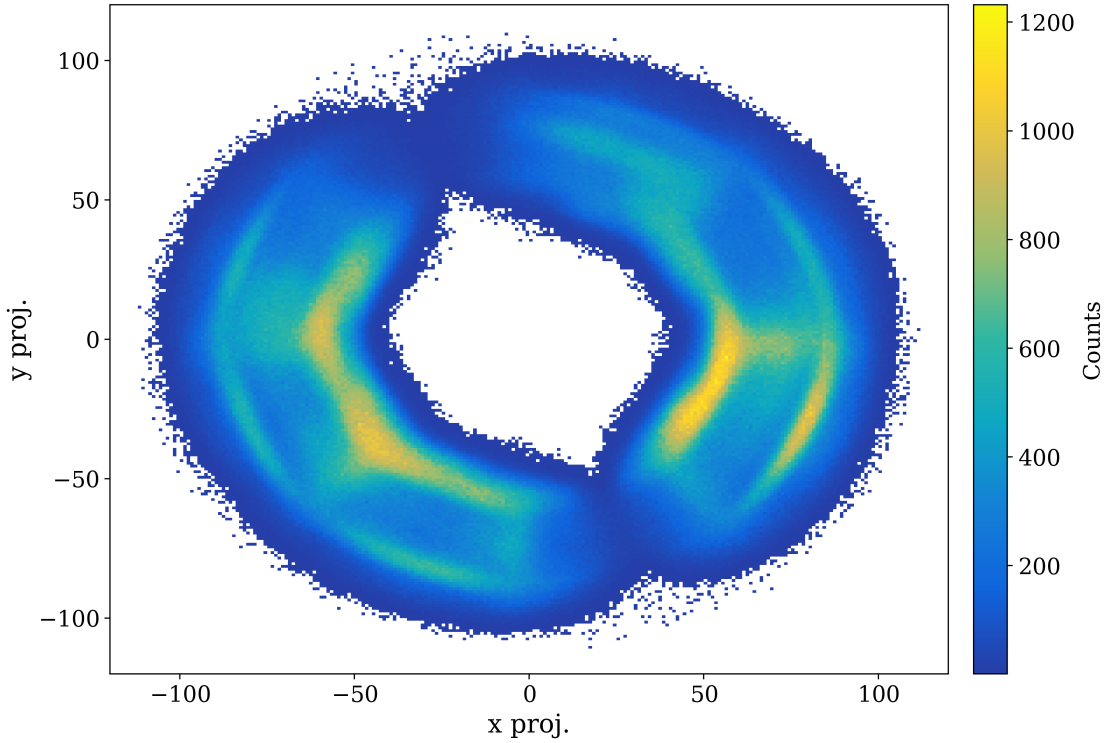

Figure 4.25: Detector map of the reconstructed alpha particle. The detector positions are visible as depletion zones, since the probability for an event to be reconstructed is lower if a detector was at the position where the alpha particle was not detected.

allows for the reconstruction of the missing alpha particle, it also introduces additional uncertainties. A disadvantage of this approach is the increased error of the reconstructed alpha particle compared to a directly detected alpha particle, as its momentum vector's error depends on the three detected alpha particles' momenta and uncertainties in reaction position and beam energy. Another problem is that after the loss of one alpha

particle, some quantities that were previously used to gate are now constraints (such as the energy sum in the laboratory frame). Since all prior conditions were used to achieve the high level of background suppression observed in the data (see Section 4.1.5), the reconstructed events are expected to have a higher background level, as some conditions are implicitly satisfied by the reconstruction: The energy sum in the laboratory frame, for example, is a reconstruction constraint and thus cannot be used to discriminate between valid detections and background events. These assumptions are confirmed by the Dalitz plot of the reconstructed events, which shows a less well-defined distribution and higher background level, which is further detailed in the appendix Section A.2.

4.3 3^- state decay analysis

Similarly to the previously discussed techniques, the decay of the 3^- state in ^{12}C can be analyzed. The higher energy in the center-of-mass frame of the decay compared to the Hoyle state decay results in a different distribution of the reduced energies, reducing the relative uncertainties. The resulting Energy-Theta plots before and after application of the same gate conditions as for the Hoyle state decay are shown in Figures 4.26a and 4.26b. The resulting Dalitz plot is shown in Figure 4.28. As can be seen in Table 4.7, the

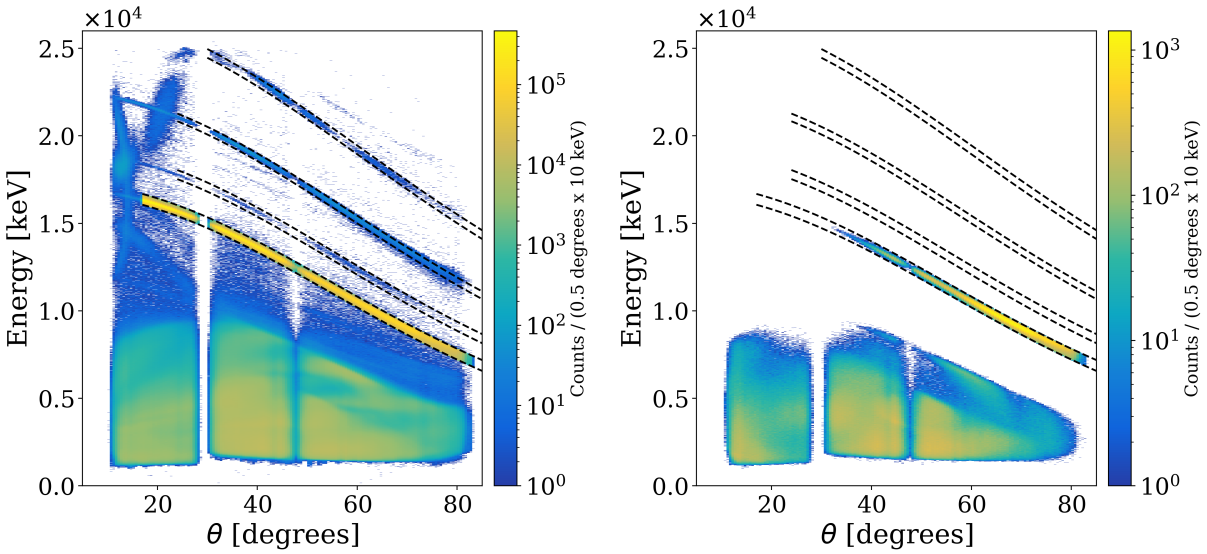

(a) Energy - θ plot after the initial kinematics gate.

(b) Energy - θ plot after kinematics, coincidence, angular, and energy gates.

Figure 4.26: Energy of the scattered particles registered in the DSSSDs against the detection angle of the respective pixel to the beam axis, gated on the kinematics line of the 3^- state in ^{12}C.

total number of decay events for the 3^- state is substantially higher than for the Hoyle state. In combination with the visible direct decay component, seen in the Dalitz plot in Figure 4.28, this significantly reduces the uncertainties of the analysis of the particle-

decay branching ratio of the 3^- state decay. As the analysis of the 3^- state is analogous

Table 4.7: Particle decay event statistics of the 3^- state for multiplicity = 4 events after the final gate, shown with and without the combinatorial veto condition.

Dataset	Remaining decay events	Remaining events after veto
December 2019	1.47×10^6	1.35×10^6
January 2020	1.42×10^5	1.30×10^5
Total	2.90×10^6	2.65×10^6

to the Hoyle state decay analysis, the same analysis conditions are applied. While most of the gates perform exactly as during the Hoyle state decay analysis, the energy sum conditions show a larger shift from their expected values than the Hoyle state decay events. This can be seen in Figures 4.27a and 4.27b, which even exhibit a diagonal trend towards higher energies. This is caused by the improved dead layer thickness, which optimizes the resolution for the Hoyle state analysis. The obtained energy gate widths are displayed in Table 4.8.

Table 4.8: Measured positions and widths of the energy-sum selection conditions in the laboratory and center-of-mass frame for both experiments.

Condition	2019		2020	
Condition	Mean [keV]	Width [keV]	Mean [keV]	Width [keV]
$\Sigma_{4,\text{lab.}} E_\alpha$	27430.1	304.3	27519.0	335.4
$\Sigma_{3,\text{CoM.}} E_\alpha$	2432.8	93.3	2439.4	112.3

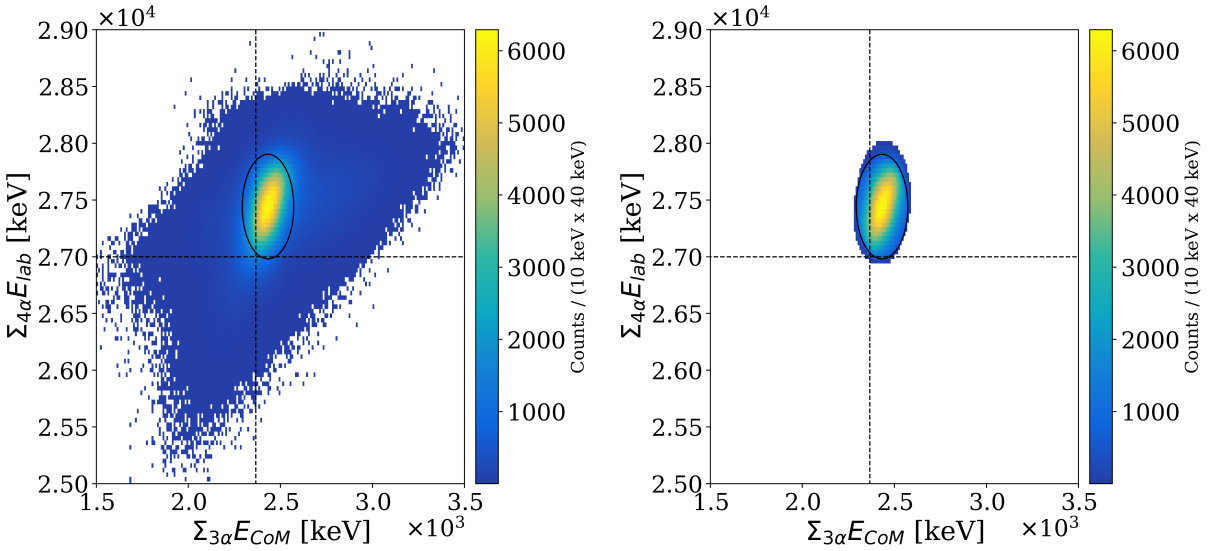

(a) Energy sum distributions before applying the corresponding condition for the 3^- state decay.

(b) Energy sum distributions before applying the corresponding condition for the 3^- state decay.

Figure 4.27: Energy sum gate for the 3^- state decay in ^{12}C.

The resulting Dalitz plot is shown in Figure 4.28, and the Y-projection of the Dalitz plot is shown in Figure 4.29. The Y-projection shows a sharp peak near the expected position at $\epsilon = 0.64$, as derived in Section A.6. This peak corresponds to the sequential decay mode of the 3^- state, which is expected to be the dominant decay mode.

Given the focus of this thesis on the analysis of the Hoyle state decay, the analysis of the 3^- state decay is only briefly discussed and the resulting distributions are provided in the appendix.

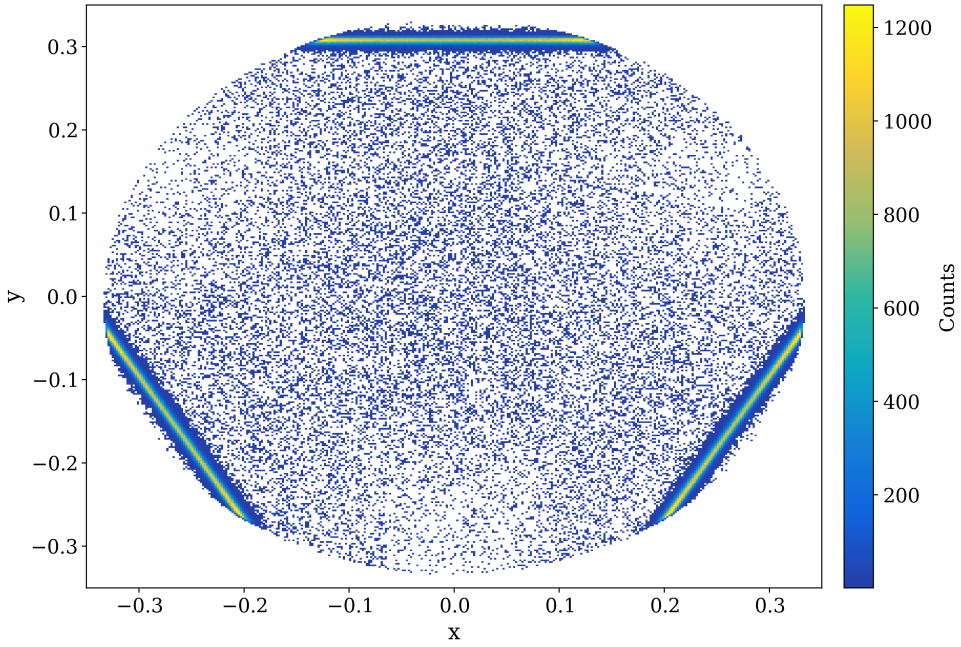

Figure 4.28: Experimental Dalitz plot of the 3^- state decay in ^{12}C. The higher Q-value of the decay compared to the Q-value of the ^{8}Be decay moves the triangle legs corresponding to the sequential decay events outward, causing them to not connect anymore.

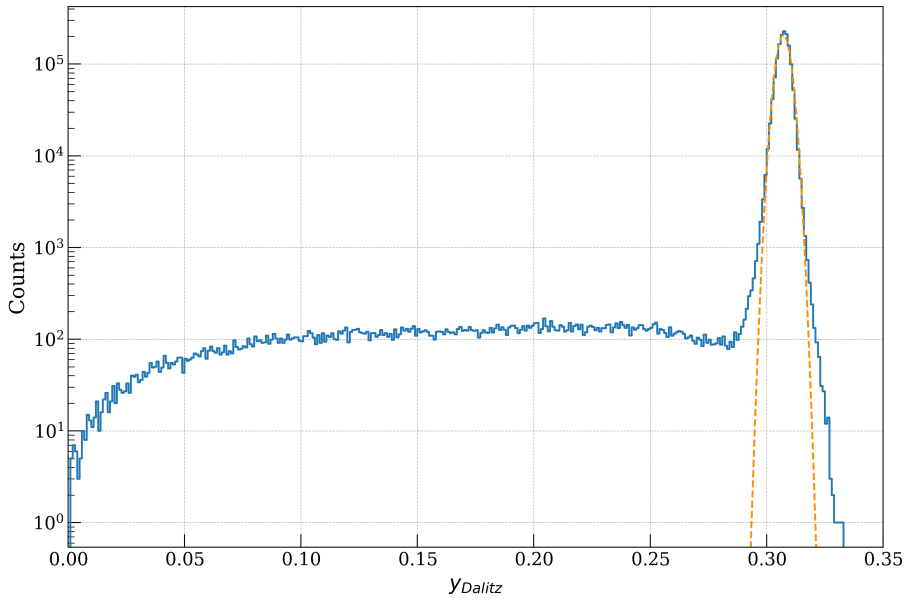

Figure 4.29: Y-projection of the Dalitz plot of the 3^- state's particle decay.

4.4 Future improvements

Based on the foundation laid by the current analysis, multiple improvements can be made to further enhance the analysis of the Hoyle state decay and the 3^- state decay. The following sections will discuss potential improvements and their expected impact on the analysis.

4.4.1 Kinematic fitting

Since the decay measurement is overspecified, as shown in the reconstruction of the missing alpha particle, the kinematic fitting can be used to improve the energy resolution of the detected alpha particles. The idea behind this is that each measured variable has a given error, but that certain combinations of variables are more or less likely than others for given sets of constraints. Using this, the input variables can be adjusted to minimize the error of the output variables within their respective errors. In comparable experiments, such as the study by Smith et al. [59], this technique improved the resolution by more than 10 %. One fundamental prerequisite of many kinematic fitting techniques is that the constraint distributions, in the case of the given experiment, the energy sum in the laboratory frame, the energy sum in the center-of-mass frame, and the momentum conservation, are centered around their expectation value. This prerequisite is not fulfilled in the current data. Still, the implementation of the algorithm has been integrated into the analysis software and can be used once the data satisfies the requirements.

4.4.2 Machine learning

A recent development in the field of nuclear physics is the use of machine learning algorithms to support and enabled data analysis of complex high-dimensional data. The direct branching ratio of the Hoyle state decay is a prime candidate for such an analysis, as we have a finite number of decay modes and multiple input dimensions per event, such as the reduced energies and the angular distributions for each particle. Machine learning techniques generally separate into two categories: supervised and unsupervised learning algorithms. Supervised learning algorithms are used to classify data into predefined classes, while unsupervised learning algorithms are used to find patterns in the data without predefined classes. Since in our case the decay modes are known, a supervised learning algorithm is the most suitable choice.

Machine learning model

The machine learning model employed in this test is the XGBoost algorithm, which is based on Gradient-Boosted decision trees [108]. The algorithm is widely used in the field of machine learning and is known for its high performance and robustness. The

model was trained using $2 \cdot 10^9$ simulated events, which is lower than the total number of simulated events, but sufficient to obtain a good classification accuracy. The training data were split into a training and a test set, with a ratio of 80:20. A challenge in the training of the model is the very low branching ratio of the direct decay modes, which caused a class imbalance in the training data. Especially the direct decay mode of the Hoyle state is underrepresented in the training data. To mitigate this, multiple techniques were used, such as oversampling of the direct-decay minority class using the Synthetic Minority Over-sampling Technique (SMOTE) and weighting of the classes in the training algorithm. The model was initially tested on the 3^- state direct decay modes, as the separation between the sequential decay and the direct decay modes is more pronounced there.
To further improve the classification accuracy, the model was trained using a grid search to optimize the hyperparameters of the model. The hyperparameters were optimized using a 3-fold cross-validation, which is a common technique to prevent overfitting of the model. Additionally, synthetic features were generated to improve the classification performance: The energy sum of the three decay alpha particles was used as a feature, as well as the sinuses and cosines of the angles between the decay alpha particles. The training performance is shown in the confusion matrix in Figure 4.31. A confusion matrix is a tool used to visualize the performance of a classification algorithm, as it shows the true class of the data points against the predicted class and thus the misclassification rate. The learning curve of the model is shown in Figure 4.30.

The performance of the classification model was evaluated using three key metrics: **Precision**, **Recall**, and **Accuracy**. These metrics are widely used in machine learning to assess the effectiveness of classification algorithms [109]:

- **Precision** is defined as the ratio of correctly predicted positive observations to the total predicted positives. High precision indicates a low false positive rate.
- **Recall**, also known as sensitivity, is the ratio of correctly predicted positive observations to all observations in the actual class. High recall is corresponds to a higher amount of true positives.
- **Accuracy** measures the overall correctness of the model, calculated as the ratio of correctly predicted observations to the total observations. While accuracy provides a broad measure of model performance, it is less informative in cases of class imbalance such as the one in this analysis.

The provided classes are *DDE* for the equal energy direct decay mode, *DDF*, commonly referred to as $DD\phi$ for the free direct decay mode, and *SD* for the sequential decay mode. The *NoDecay* class is used for events that do not belong to any of the decay modes. The performance metrics for each class are shown in Table 4.9. These results

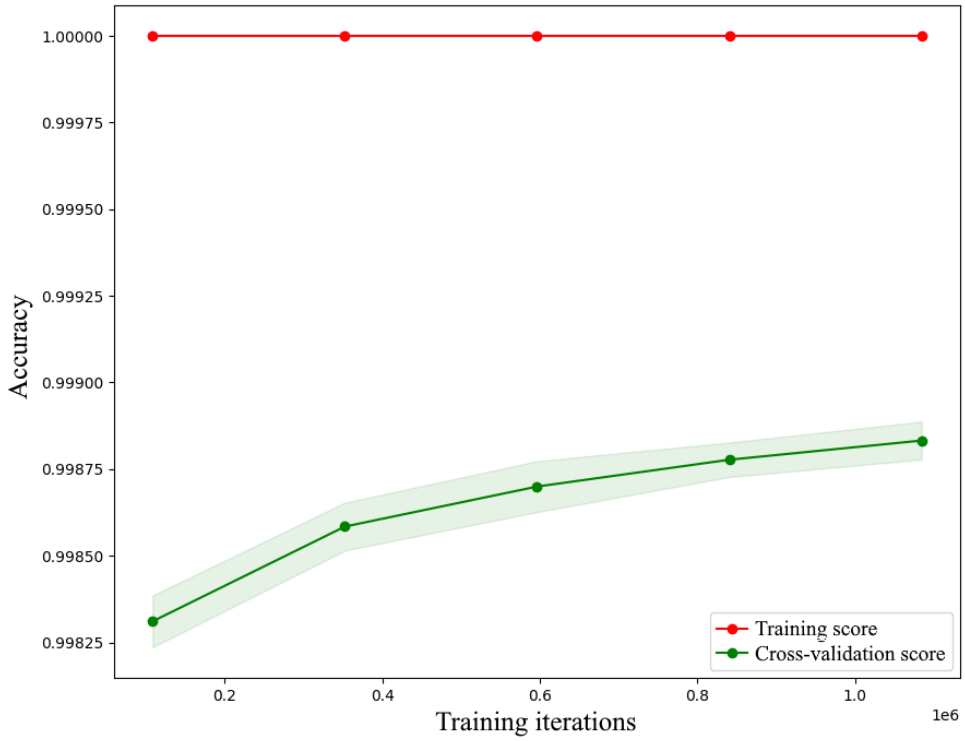

Figure 4.30: Learning curve of the XGBoost classifier for the classification of the decay modes of the Hoyle state.

Metric	NoDecay	SD	DDE	DDF
Precision	0.1351	0.9993	0.9506	0.9711
Recall	0.0735	0.9996	0.9872	0.9507
Accuracy		0.9988		

Table 4.9: Performance metrics for each class.

show that the model achieves high precision and recall for the **SD**, **DDE**, and **DDF** classes, with values exceeding 0.95. However, the **NoDecay** class has significantly lower precision (0.1351) and recall (0.0735), indicating difficulties in accurately predicting this class, possibly due to class imbalance. This suggests that the model approach cannot yet be used to discriminate between background events and decay events, but can be used to classify the decay modes of the Hoyle state. Despite this challenge, the overall accuracy of 0.9988 suggests that the model performs well, but may need further refinements, and more training data to better classify the decay events. Given the low branching ratio of the direct decay modes of below 10^{-4}, the model's performance is not yet sufficient to determine the branching ratios of the Hoyle state decay.

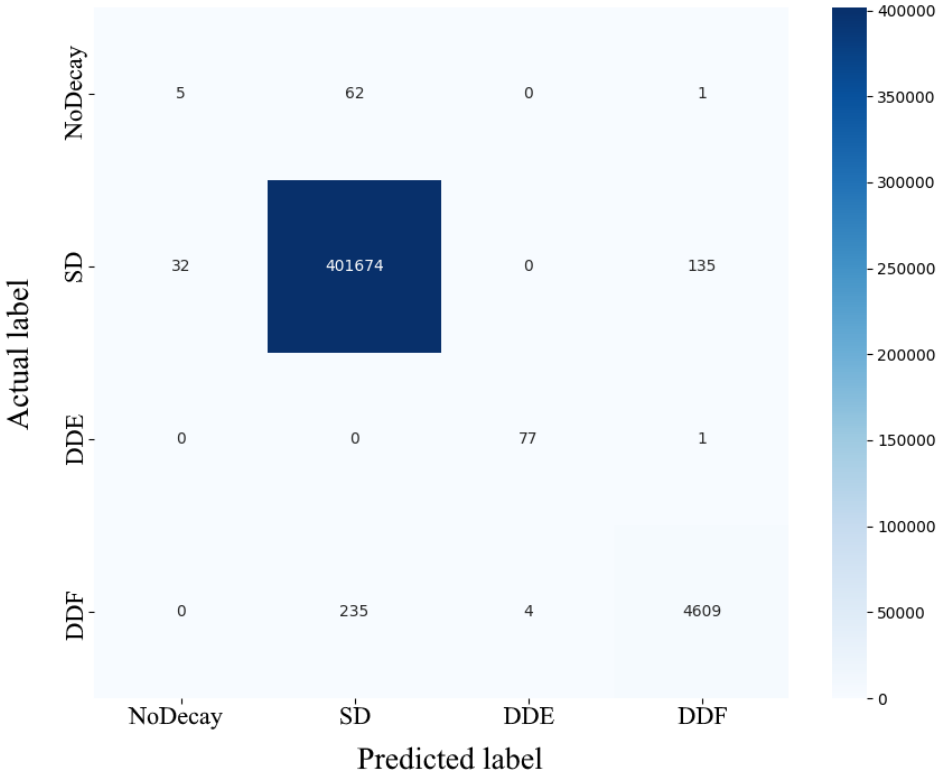

Figure 4.31: Confusion matrix of the XGBoost classifier for the classification of the decay modes of the Hoyle state.

Chapter 5

Monte Carlo simulation

The determination of the probabilities for the detection of events with a combination of reaction-specific and isotropic angular distributions is a non-trivial problem. A primary cause is the multitude of detector combinations that satisfy the kinematic constraints of the reaction, but also effects such as angular straggling and energy losses contribute to the challenge. Additionally, the exact gate characteristics for particles originating from different decay modes and their detection efficiencies, as well as the effects of the energy loss in the target material on the events in the center-of-mass frame reveal complex behavior.
An elegant solution to this is the use of Monte Carlo simulations, which can be used to generate distributions of measured quantities for a given set of input parameters, which can then be compared to the measured data. Thus, in conjunction to the previously detailed work, a Monte Carlo simulation was developed to investigate the decay of the Hoyle state and of the higher lying states in ^{12}C in conjunction to this thesis. The simulation was primarily implemented by Timo Biesenbach but received contributions and support from the author of this thesis. Due to its integral role in the analysis of the data, the simulation is presented in this chapter.

5.1 The Geant4 framework

The presented simulation code was developed using the Geant4 framework, which is a toolkit for the simulation of the passage of particles through matter [110]. It is used in a large number of analyses in nuclear and particle physics, as well as in medical physics, aeronautics and space science. Geant4 is developed and supported by the Geant4 Collaboration, which consists of numerous institutes and universities from around the world. The Geant4 toolkit is open-source software.

5.2 Simulation setup

The simulation uses the same overall detector geometry as the experimental setup. The target is modeled as a thin layer of ^{12}C with a thickness of 0.114 $\frac{\text{mg}}{\text{cm}^2}$. The detectors are modeled as silicon pixel volumes, as the strip-like geometry of the DSSSDs is not relevant for the simulation and would introduce unnecessary uncertainties.
Each detector is modeled with a flat dead layer of 19.68 µm. The simulation also artificially introduces (tagged) mismatched events (see Section 4.1.6) to study the effect of the combinatorial mismatch on the angular distributions. Furthermore, all strips that were inactive during the experiment are also masked in the simulation to analyze the consequences of the reduced solid angle coverage on the angular distributions.

5.3 Decay simulation

The simulation of decay processes for a carbon nucleus in a state with available particle-decay modes generates decay events probabilistically for each mode. The momentum distribution of the decay particles is initially determined in the center-of-mass (CM) frame of the ^{12}C nucleus. The decay plane is randomly oriented, and the resulting vectors are then transformed into the laboratory frame to reflect realistic experimental conditions. This approach ensures accurate modeling of the decay dynamics and facilitates comparison with experimental data.
For an excited ^{12}C nucleus (7.2747 MeV), several decay channels are considered, including Sequential Decay (SD) and Direct Decays (DDE, DDL, DDΦ, DDP). Each decay mode results in the emission of alpha particles, with their kinematic properties derived from initial conditions and energy distributions. Considering these modes provides a comprehensive understanding of the decay mechanisms and their implications for nuclear physics.

5.3.1 Sequential Decay

In the sequential decay process, the excited ^{12}C nucleus decays into an ^{8}Be nucleus and an alpha particle (^{4}He). The ^{8}Be nucleus subsequently decays into two additional alpha particles. The excitation energy E_{exc} of the ^{12}C nucleus is distributed among the decay products as follows

$$E_{\text{exc}} = E_{^{12}\text{C}} - E_{^{8}\text{Be}} - E_{^{4}\text{He}} = E_{\text{CM}} + E_{\text{kin}},$$

where E_{CM} is the center-of-mass energy and E_{kin} is the kinetic energy of the decay products. The velocity vector of the first alpha particle in the lab frame, $\vec{v}_{\alpha_1}$, is given by

$$\vec{v}_{\alpha_1} = \vec{v}_{\mathrm{parent}} + \vec{v}_{\mathrm{CMS},\alpha_1}.$$

Here, $\vec{v}_{\mathrm{parent}}$ represents the velocity of the parent ^{12}C nucleus, and $\vec{v}_{\mathrm{CMS},\alpha_1}$ is the velocity in the center-of-mass system. To ensure an isotropic distribution, the angles θ and ϕ are computed using:

$$\theta = \cos^{-1}(1 - 2R_1), \quad \phi = 2\pi R_2,$$

where R_1 and R_2 are uniformly distributed random numbers between 0 and 1 to achieve the isotropic emission pattern, which is essential to not introduce unintentional biases.

5.3.2 Direct Decay Modes

The Direct decay modes of ^{12}C involve the direct emission of three alpha particles from the parent nucleus without forming intermediate states. The kinetic energy of each alpha particle, $E_{\alpha,i}$, is determined by the fractional energy distribution specific to each mode

$$E_{\alpha,i} = \epsilon_i E_{\mathrm{CM}},$$

where ϵ_i is the fractional energy for each particle.

DDE Mode

In the direct decay mode with equal-energy distribution (DDE), which corresponds to an equilateral triangle configuration, each alpha particle receives one-third of the excitation energy

$$\epsilon_i = \frac{1}{3},$$

resulting in a symmetric energy distribution among the decay products, which is centered in the Dalitz plot. Like the DDL mode, this decay has no inherent degree of freedom, making it a useful reference when fitting to the experimental data.

DDL Mode

The linear mode, where one alpha particle is at rest in the center-of-mass frame and the other alpha particles are emitted antiparallel, is known as the DDL mode. In this decay mode, the excitation energy is equally shared between the two moving alpha particles due to momentum conservation, resulting in the following energy distribution

$$\epsilon_1 = 0, \quad \epsilon_2 = \frac{1}{2}, \quad \epsilon_3 = \frac{1}{2}.$$

DDΦ Mode The decay mode least restrictive in terms of energy distribution is the DDΦ mode, which allows for a more general energy distribution among the decay products. It generally assumes that all combinations of energies and momenta generally allowed by the conservation laws are possible. This mode is implemented using an initial configuration derived from the circular area of allowed momenta in the Dalitz plot, to ensure complete phase space coverage and momentum conservation.
Using energy conservation, the initial configuration is limited to the triangular area of allowed energies in the Dalitz plot. While this guarantees energy conservation is, momentum conservation dictates that the decay products lie within a circular area in the Dalitz plot [111]. This circular area can be parametrized using the maximum allowed radius $\frac{1}{3}$, which follows from the maximum energy range of an alpha particle in the decay process, ranging from 0, where both other particles are emitted antiparallel, to $\frac{2}{3}$, where one particle is emitted in one direction and the other two in the opposite direction. This is derived in appendix Section A.4. This gives the diameter $\frac{1}{3}$ of the allowed circle in the Dalitz plot.
In order to uniformly distribute points within a circle, two independent random variables, U_1 and U_2, each uniformly distributed on the interval $[0, 1]$, are generated. These variables are used to compute the polar coordinates (r, θ) and subsequently the Cartesian coordinates (x, y). The radius r is derived from U_1 as:

$$r = \sqrt{U_1} \times \frac{1}{3}$$

This ensures that the points are uniformly distributed within the circle, as the square root transformation compensates for the non-linear area growth of the circle with increasing radius.
The angle θ is determined by the second random variable U_2 using

$$\theta = 2\pi U_2$$

Given r and θ, the Cartesian coordinates (x, y) of the point are then computed as

$$X = r\cos(\theta)$$
$$Y = r\sin(\theta).$$

These are then used to compute the energy fractions ϵ_i of the decay products using the inverse Dalitz transformation:

$$\epsilon_1 = \frac{1}{3} - \frac{1}{3}X - \frac{1}{\sqrt{3}}Y, \tag{5.1}$$

$$\epsilon_2 = \frac{1}{3} - \frac{1}{3}X + \frac{1}{\sqrt{3}}Y, \tag{5.2}$$

$$\epsilon_3 = 1 - \epsilon_1 - \epsilon_2. \tag{5.3}$$

DDP Mode The DDP mode, also known as Coulomb-corrected "free" direct decay, allows for a more general energy distribution among the decay products while applying a Coulomb correction to account for the interactions between the decaying particles. While it generally assumes that all combinations of energies and momenta generally allowed by the conservation laws are possible, the Coulomb interaction between the decay products is considered, as the decay products are charged particles and subject to Coulomb interactions. The Coulomb interactions impacts the initial arrangement of the constituent alpha particles up until the break-up and even influences their kinematics briefly afterwards. To account for this, the simulation incorporates more advanced scattering theory to model the Coulomb interaction between the decay products, which will be discussed in more detail in the following Section 5.3.3. The approach was introduced by Smith *et al.* [59]. As discussed there, it does not completely fill the available phase space, as the so called "DDΦ" mode would, but it is a more realistic approach to the decay process.
To generate events adhering to the DDP mode, the simulation uses a two step process: The initial energy distribution is selected analogously to the DDΦ mode, but the energy fractions must then be transformed to accurately reflect the simulated probability density function. To implement this distributions, obtained by the decay simulation code, rejection sampling is used. An alternative approach of using the inverse cumulative distribution function (CDF) for direct sampling was tested, but was found to be more computationally expensive, so the aforementioned, faster sampling approach was chosen:

Generate random point (x, y) within the probability threshold:
$x = r\cos(\theta), \quad y = r\sin(\theta)$
$r = \sqrt{R_1} \cdot 0.5, \quad \theta = 2\pi R_2$

accepting the point if $R <$ threshold. Here R is a uniformly distributed random number and the threshold is based on a predefined probability density function. This approach ensures that the sampled points strictly adhere to the physical constraints imposed by the Coulomb interaction. The lab frame velocity vectors of the alpha particles are calculated

as

$$\vec{v}_{\alpha,i} = \sqrt{\frac{2E_{\alpha,i}}{m_\alpha}} \begin{pmatrix} \sin\theta_i \cos\phi_i \\ \sin\theta_i \sin\phi_i \\ \cos\theta_i \end{pmatrix} + \vec{v}_{\text{parent}},$$

where m_α is the mass of the alpha particle, and θ_i and ϕ_i ensure isotropic emission. This representation captures the rotation and transformation to the laboratory frame, providing a clear and elegant mathematical description.

5.3.3 Energy Distribution of direct three-body decays

Instead of assuming an equal distribution of energy across the available phase space, the hyperspherical harmonics method is used to account for the interactions between particles, particularly the Coulomb interactions, which significantly influence the decay process. This method is chosen because it effectively describes the dynamics of three-body systems by transforming the problem into a single-coordinate problem [112]. It has also been successfully demonstrated by Smith *et al.* [59] to accurately model the free decay of the Hoyle state in ^{12}C.

The system's overall size is defined by the hyperradius ρ, which is a measure of the system and is given by

$$\rho^2 = \frac{1}{mM} \sum_{i<k} m_i m_k r_{ik}^2,$$

where m is a normalization mass, M is the total mass of the system, and r_{ik} are the pairwise distances between particles. This transformation simplifies the analysis of the three-body problem by reducing the complexity associated with multiple interacting particles.

The effective potential $U_{\text{eff}}(\rho)$ includes contributions from the Coulomb potential $V_C(\rho)$ and the centrifugal barrier $V_L(\rho)$:

$$V_C(\rho) = \sum_{i<k} \frac{Z_i Z_k e^2}{r_{ik}},$$

$$V_L(\rho) = \frac{\hbar^2 (K + 3/2)(K + 5/2)}{2m\rho^2},$$

where Z_i and Z_k are the charges of the particles, and K is the hypermomentum quantum number. The hypermomentum, analogous to angular momentum in classical mechanics, is a quantum number that arises in the description of the motion of particles in a hyperspherical coordinate system. Combining these, the total effective potential is

$$U_{\text{eff}}(\rho) = V_C(\rho) + V_L(\rho).$$

To estimate the probability density of different energy distributions, the decay width

Γ is calculated using the WKB (Wentzel-Kramers-Brillouin) approximation. The action S is computed along the classically forbidden region between the classical turning points ρ_0 and ρ_t:

$$S = \frac{1}{\hbar} \int_{\rho_0}^{\rho_t} \sqrt{2m \left(U_{\text{eff}}(\rho) - E\right)} \, d\rho,$$

where E is the total energy of the system. The transmission coefficient T, representing the probability of tunneling through the potential barrier, is given by:

$$T = \exp(-2S).$$

The decay width is then:

$$\Gamma \approx T \cdot f,$$

where f is a pre-factor that includes the knocking rate, which is the frequency of attempts to penetrate the barrier, and the density of final states available for the decay products. By applying the hyperspherical harmonics method and the WKB approximation, the energy distributions of the emitted α particles are effectively predicted. While this method still has limitations, such as a systematic overestimation of the decay width [112]. One additional limitation is that while the approach integrates over multiple different decay distribution, it is initialized to an equal-energy distribution, which can lead to a bias in the results. Despite this, the overall probability density is far more accurate than the equal-probability phase space distribution, as demonstrated in prior studies [59].
These relative decay probabilities for given input energy distributions can be used to generate the probability density function for the decay process, ensuring that the simulation reflects the physical constraints of the system. To generate a random point on the probability density distribution, an energy fraction for each particle of a decay is generated using the approach discussed in 5.3.2. The velocities $\vec{v}_i$ and momenta $\vec{p}_i$ of the α particles with masses $m_i = m_\alpha$ are calculated based on the energy fractions and masses of the particles using

$$p_i = \sqrt{2m_i E_i}, \quad v_i = \frac{p_i}{m_i}.$$

To link these values to the probability density, the pairwise distances and hyperradius for the generated particle velocities are determined as follows.
First, the pairwise distances squared, r_{12}^2, r_{13}^2, and r_{23}^2 are calculated using the velocities $\vec{v}_i$ of the particles:

$$r_{ij}^2 = (\vec{v}_i - \vec{v}_j)^2.$$

Next, the hyperradius ρ can be calculated using:

$$\rho^2 = \frac{1}{m_s M} \left(m_1 m_2 r_{12}^2 + m_1 m_3 r_{13}^2 + m_2 m_3 r_{23}^2 \right),$$

where $M = m_1 + m_2 + m_3$.

Finally, the normalized pairwise distances s are determined

$$s_1 = \frac{r_{12}}{\rho}, \quad s_2 = \frac{r_{13}}{\rho}, \quad s_3 = \frac{r_{23}}{\rho}.$$

Using these, the combined Coulomb and centrifugal potential at a given hyperradius ρ can be obtained. This contributes to the effective potential of the system by

$$V_{\text{Coul}} = \frac{Z_1 Z_2 e^2}{s_1} + \frac{Z_1 Z_3 e^2}{s_2} + \frac{Z_2 Z_3 e^2}{s_3}, \quad V_{\text{cent}} = \frac{\hbar^2 (K + 1.5)(K + 2.5)}{2 m_s \rho^2}.$$

Finally, the WKB approximation (see equation 5.3.3) is used to integrate the action over the classically forbidden region, calculating the transmission coefficient. This provides the decay width, which estimates the probability density of different energy distributions. By iterating over many decay events, the simulation models the statistical energy distribution of the emitted α particles, providing insights into the underlying physical decay process. This approach, leveraging the hyperspherical harmonics method and WKB approximation, assures that the predicted energy distributions accurately reflect the physical constraints and interactions within the system. The resulting probability distributions are shown in Figure 5.1 in their Dalitz plot coordinates.

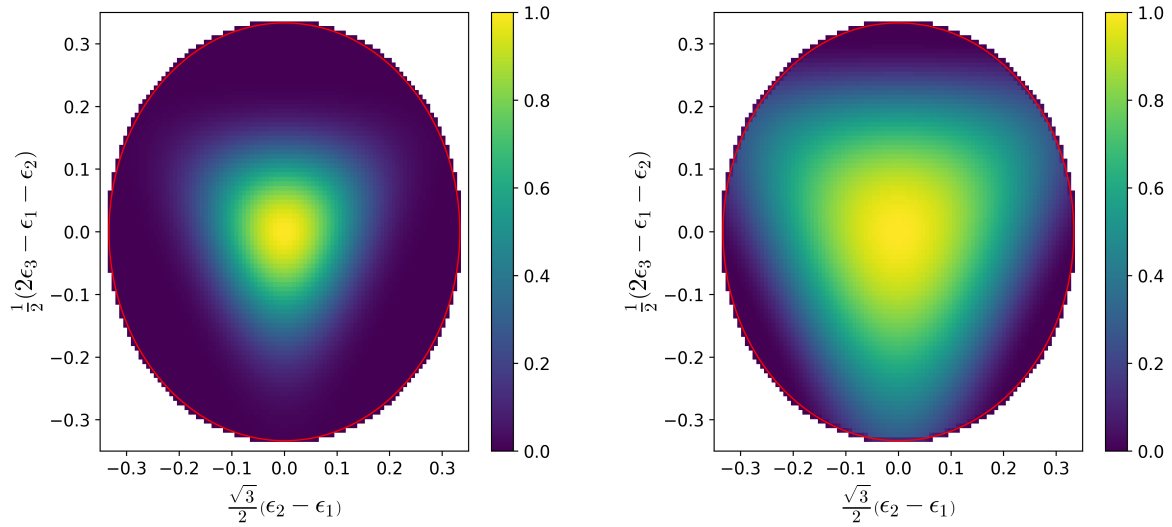

(a) Dalitz plot of the Hoyle state direct decay density distribution simulation.

(b) Dalitz plots of the direct decay density simulation of the 3^- state.

Figure 5.1: Probability density distributions of the direct decay channels of the Hoyle state and the 3^- state in ^{12}C. The red circles indicate the available phase space. The displayed values are scaled probability densities where the maximum value is set to 1.

5.3.4 Branching Ratios for Decay Modes

To obtain a realistic representation of the experimental data, the simulation incorporates branching ratios for each decay mode. These ratios are based on theoretical predictions and experimental data, but are increased to ensure that even rare decay events are adequately represented in the simulation. Lower ratios can always be computed from simulated higher ratios using undersampling or scaling, but the reverse is not possible. The simulated branching ratios for each decay mode for the states of interest are summarized in Table 5.1. During the simulation, the selection of the decay mode is performed using weighted sampling based on these branching ratios. A random number R is generated and compared against the cumulative probabilities of each decay mode. For example, if R is less than the cumulative probability for SD, then the sequential decay mode is selected. Otherwise, the selection process continues with the next mode.

Decay Mode	0^+	3^-	2_2^+	1^-	...
SD	0.9769	0.920	0.920	0.920	...
DDE	0.0078	0.001	0.001	0.001	...
DDL	0.0012	0.000	0.000	0.000	...
DDΦ	0.0141	0.079	0.079	0.079	...

Table 5.1: Simulated branching ratios for each particle-decay mode and a set of excited states of ^{12}C. During the simulation, events for higher lying states are generated too, to ensure a robust background estimation in the particle-decay energy ranges.

5.4 Simulation of combinatorial mismatch

To account for the potential mis-identification of particles in the experimental data, introduced in Section 4.1.6, the simulation is extended to generate mismatched events. This is achieved by testing if two particles are detected in the same detector within a certain energy range. To account for the intrinsic resolution and gate width, the following condition is used

$$|E_{\text{Detector 2}} - E_{\text{Detector 1}}| < 250 \text{ keV} + \mathcal{N}(0, \sigma_{E,\text{Detector 1}}),$$

where $\mathcal{N}(0, \sigma_{E,\text{Detector 1}})$ is a normally distributed random number with a standard deviation of $\sigma_{E,\text{Detector 1}}$ for the energy of the first particle. If this condition is satisfied, in 50 % of the cases, the particle's interaction strips are swapped to simulate the combinatorial mismatch event, which is then processed in the same way as the correctly identified events.

5.5 Simulated statistics

The simulation is run for a total of $1.01 \cdot 10^{11}$ events, of which $3.003 \cdot 10^{9}$ particles are detected in the simulated detectors. The simulated amount of events was chosen as large as possible to improve the statistical accuracy of the simulation, but had to be limited due to computational constraints. To compensate for the overall lower statistics than in the experimental data, the reaction probabilities for inelastic scattering are biased towards higher interaction rates, as most of the simulated alpha particles in the experiment pass through the target without interacting. Additionally, the direct decay branching ratios are increased by a factor of 30× compared to the prior deduced upper limits, which is sufficient to obtain a good statistical accuracy. The choice against further increasing the statistics was made to not impact the analysis process, as the used level of direct events of about 1.3 % cannot impact the automatic gate-condition finding process which uses fitting of normal distributions to the data. Larger event fractions, however, could lead to a bias in the analysis process which would skew the results and make them less comparable to the experimental data.

To ensure that the simulated data is as close to the experimental data as possible, the simulated data is processed using the same primary data analysis code as the experimental data (see 4). This ensures that all corrections and gates which might be dependent on the observed decay branch are also applied to the simulated data as well. To not compromise this, the simulated data can not be too different from the experimental data, and since upper limits for the direct decay branch exist, these limits must not be exceeded by an amount that could impact analysis processes such as automatic gate finding.

The resulting plots of the analysis of the simulation are be presented and discussed in the following Section 5.6, to highlight differences and similarities and explain features of the experimental data. The obtained statistics and gate efficiencies are summarized in Table 5.2. The simulation efficiencies deviate from the experimental values: The initial and secondary conditions are much more efficient in the simulation, as the simulation not contains all potential background decay modes due to computational constraints. Additionally, the reaction probability of the simulation was biased towards the state of interest to ensure a sufficient number of events for the decay mode study. The three latter conditions, where checks on angular distribution, on the energy sum in the laboratory frame, and on the energy in the center-of-mass frame are applied, have a combined efficiency of 60.73 % for the simulation and 58.68 % for the experimental data seen in Table 4.4, which shows very good agreement. Due to the angular dependency of the calibration, the energy resolution and angular resolution are closely linked, providing a plausible explanation for the efficiency shifts between the three gate conditions.

Table 5.2: Gate efficiencies and detection counts for the applied gates on the Hoyle state for the simulation dataset. Four detected hits make up a final event.

Gate	Remaining registered hits	Efficiency [%]
Raw data	3.00×10^9	-
Kinematic	8.75×10^7	2.912
Multiplicity	7.16×10^6	8.185
Angular	5.29×10^6	73.902
Energy sum	4.89×10^5	92.349
Energy sum (COM)	4.35×10^5	88.978

5.6 Simulation results

The simulated Energy-θ distribution, shown in Figure 5.2, demonstrates the expected behavior of the scattered particles. The events were analyzed using the same analysis code as the experimental data to obtain histograms that can be directly compared to the experimental data. To allow testing of even rare decay modes and to adjust for statistical fluctuations, the simulation is initially run with a substantially higher branching ratio, 30× higher than the upper limit deduced by J. Bishop *et al.* [69]. This is required, since fitting of the model to the experimental data is not possible without a sufficient number of events per decay mode. To facilitate later analysis and comparison steps, all generated events are tagged with the decay mode they originate from.

As previously discussed (Section 4.2), the distribution of the reduced energies of the three detected alpha particles in the center-of-mass shows a relative enhancement of events towards $\epsilon = 0$ and $\epsilon = 1/2$. The reason for this is the reduced detection efficiency of particles in the $\epsilon = 0.2$ region due to the detector energy thresholds. This effect can be seen when comparing Figures 5.3a and 5.3b.

The Dalitz plots obtained from the simulation show the same features as the experimental data as can be seen in Figures 5.4 and 5.5. The employed decay simulation code is based on the work of Garrido *eg al.* [112] which was also employed by Smith *et al.* [59]. Its implementation into the Monte Carlo simulation uses a two-step approach: first, the probability-density function (PDF) is generated in the center-of-mass frame of the decaying nucleus. This PDF is then sampled during the decay simulation to generate the resulting alpha particles.

Moreover, the same code, including the Coulomb interaction theory, was used to simulate the DDP decay mode of the 3^- state in ^{12}C in addition to the DDϕ mode with equal phase space distribution. While the separation between sequential and direct decay modes is much more pronounced in the 3^- state, and the branching ratio is higher, the 3^- state is significantly more complex to simulate, as its non-zero angular momentum impacts the decay process. This was demonstrated in the B.1 section, where it is shown that the

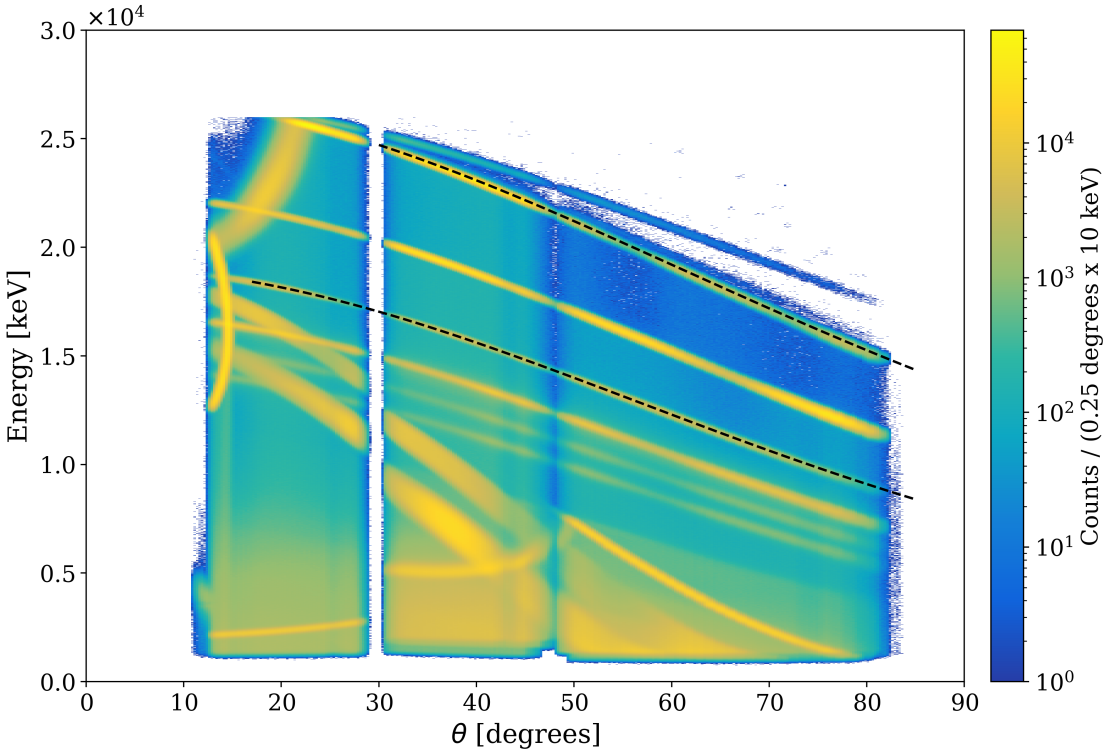

Figure 5.2: Energy of the simulated scattered particles registered in the DSSSDs against the detection angle of the respective pixel to the beam axis. From [113].

existing DDP simulation code does not produce a realistic energy distribution for the 3^- state.

The DDF decay mode of the 3^- state shows better agreement with the experimental data, which can be seen in Figure 5.6, as it reproduces the overall structure of the experimental data, shown in Figure 4.28.

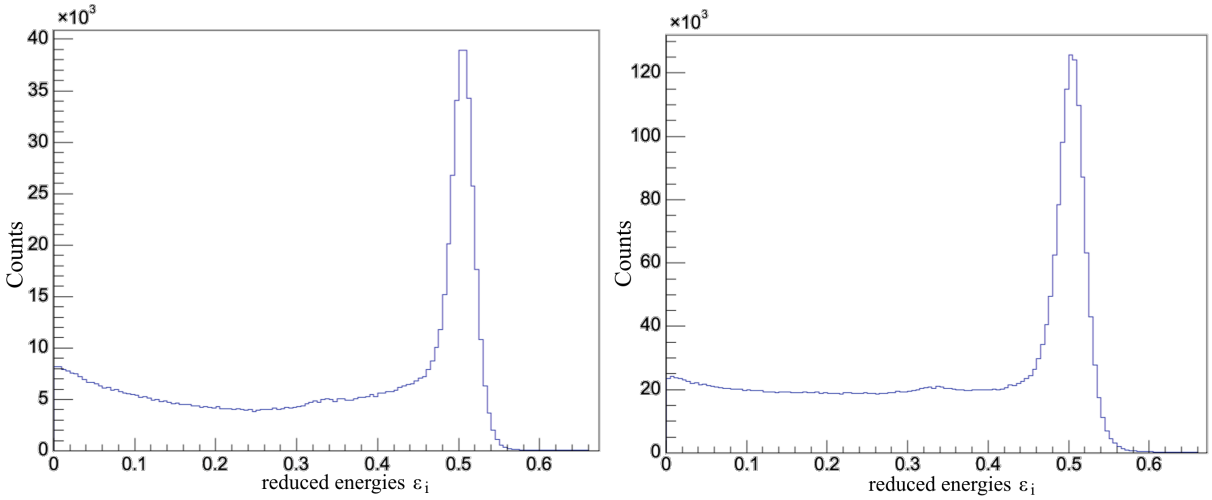

(a) Reduced energies of the three decay alpha particles in the center-of-mass frame without low-energy thresholds.

(b) Reduced energies of the three decay alpha particles in the center-of-mass frame using per-detector energy thresholds.

Figure 5.3: Reduced energies of the three detected alpha particles in the center-of-mass frame after introducing a per-detector detection cutoff between 0.45 MeV (module 3) and 1.45 MeV (module 13). Figures from [113].

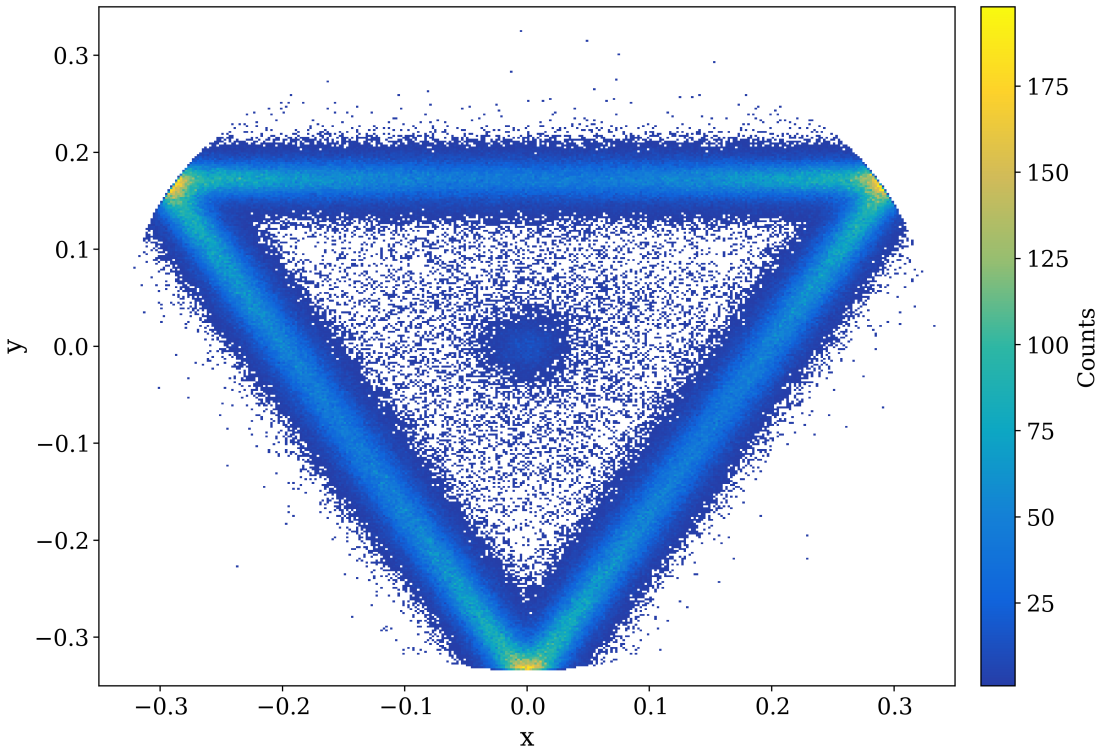

Figure 5.4: Dalitz plot of the simulated Hoyle state decay data with a 30× increased direct branching ratio compared to literature values.

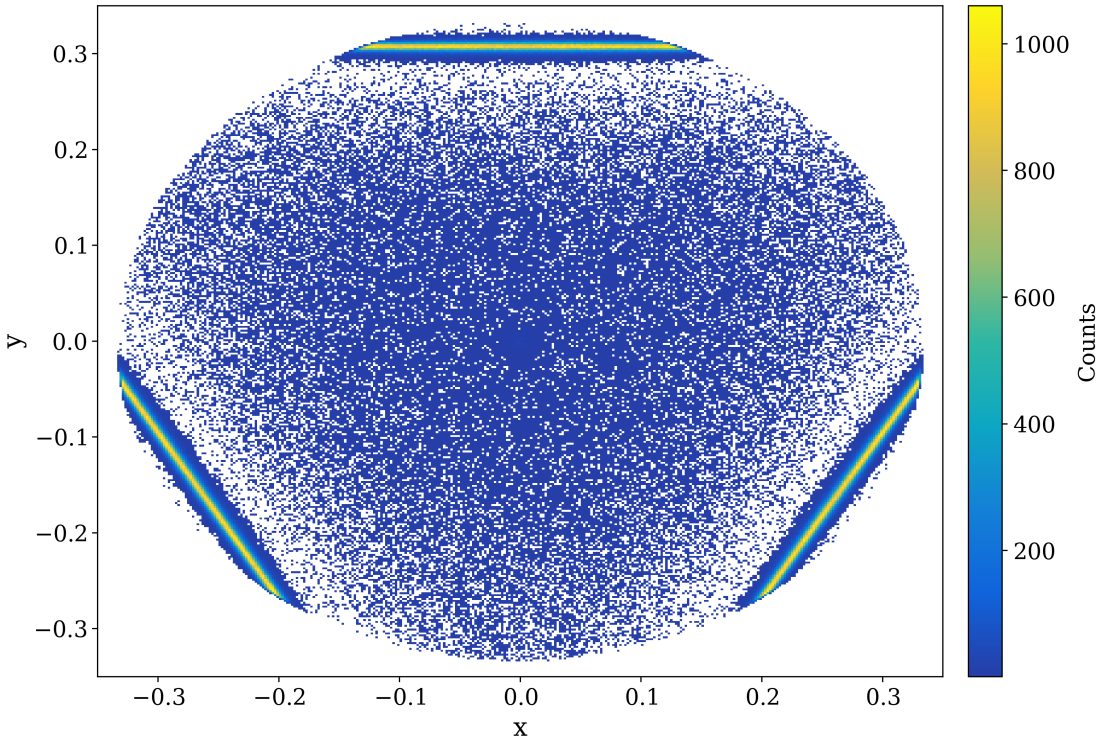

Figure 5.5: Dalitz plot of the simulated 3^- state decay data.

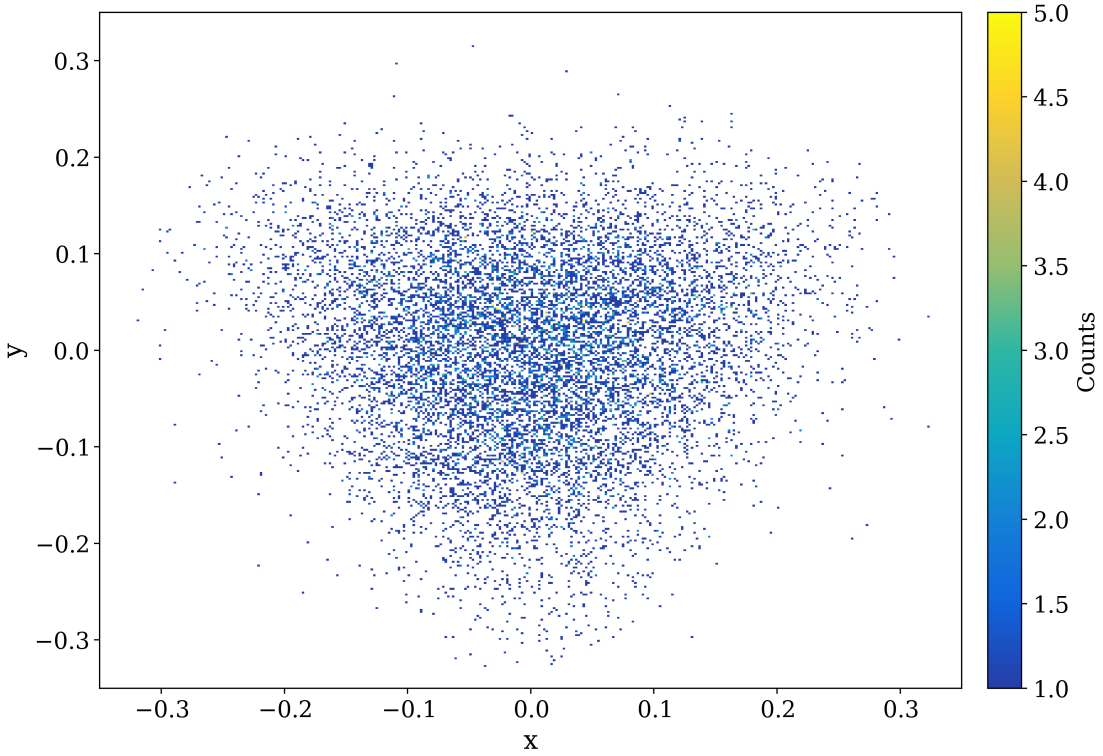

Figure 5.6: Dalitz plot of the simulated Hoyle state decay data showing the free direct decay mode (DDF). Clearly visible is the Coulomb induced triangular shape, described by the hyperspherical harmonics approach.

5.6.1 Simulated Hoyle state direct decay components

The Y-projection of the folded Dalitz plot for the simulated sequential decay mode is shown in Figure 5.7. The direct decay modes, discussed in Section 1.5, are shown in Figure 5.8. The shown projections are used to reproduce the experimental data using fitting, which will be discussed in the following Section 6.

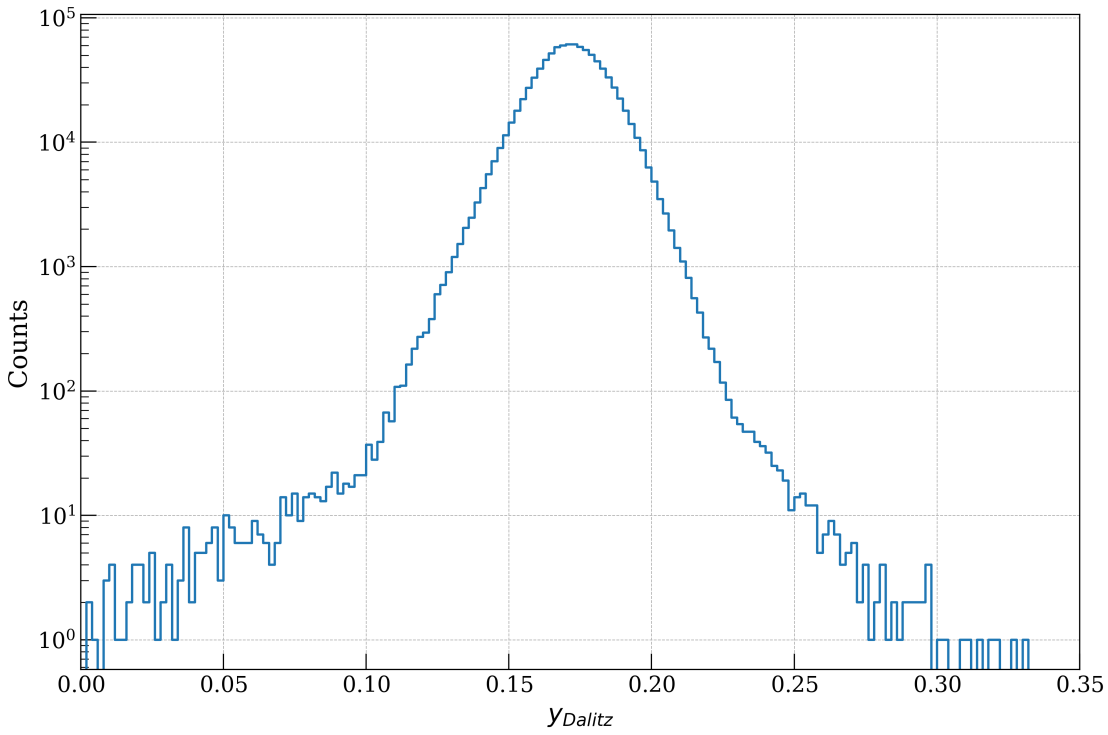

Figure 5.7: Y-projection of the folded Dalitz plot for simulated sequential Hoyle state decay mode data.

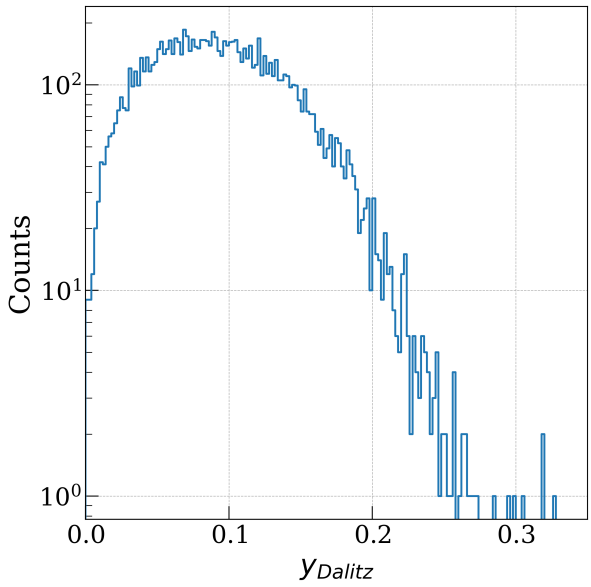

(a) Simulated Hoyle state DDP decay mode.

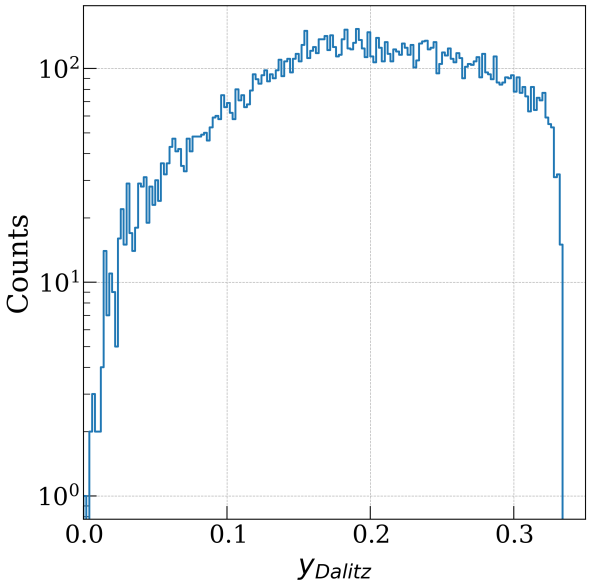

(b) Simulated Hoyle state DDF decay mode.

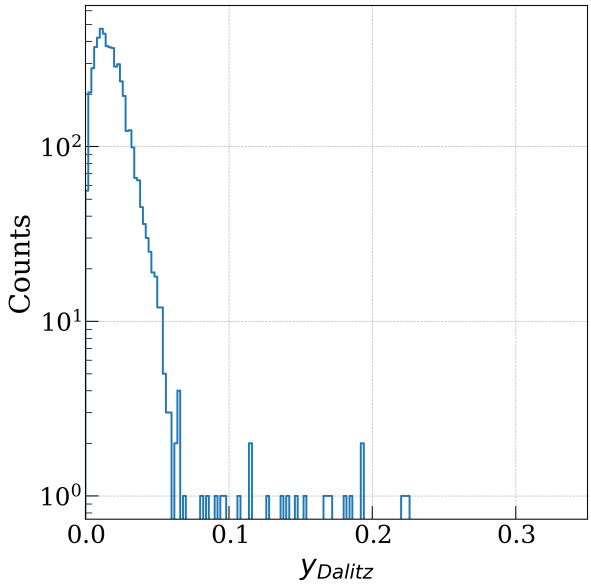

(c) Simulated Hoyle state DDE decay mode.

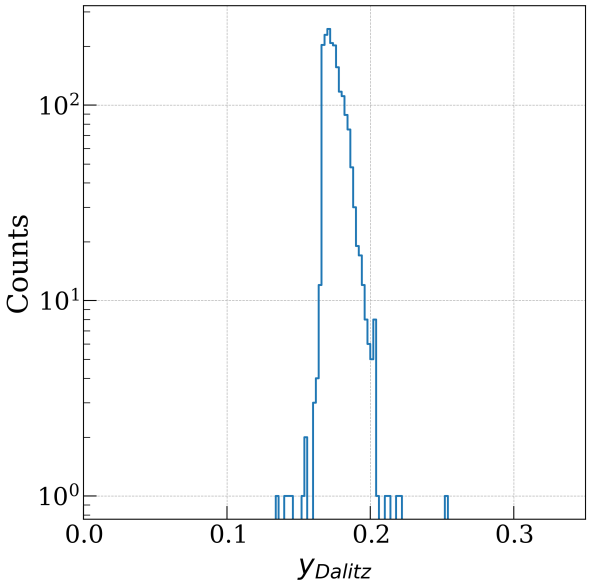

(d) Simulated Hoyle state DDL decay mode.

Figure 5.8: Y-projections of the folded Dalitz plot for the simulated direct Hoyle state decay modes.

5.6.2 Simulated 3^- state direct decay components

For the 3^- state, the Y-projection of the folded Dalitz plot of the simulated events for the sequential decay (SD) mode, the DDE mode, the DDP mode, and the DDϕ mode are shown in Figure 5.9.

The narrow SD peak is well resolved, as is the sharp distribution created by the DDE decay. The DDP and DDϕ modes, conceptually only differing in their treatment of the Coulomb barrier, show a broader distribution, with different centroids.

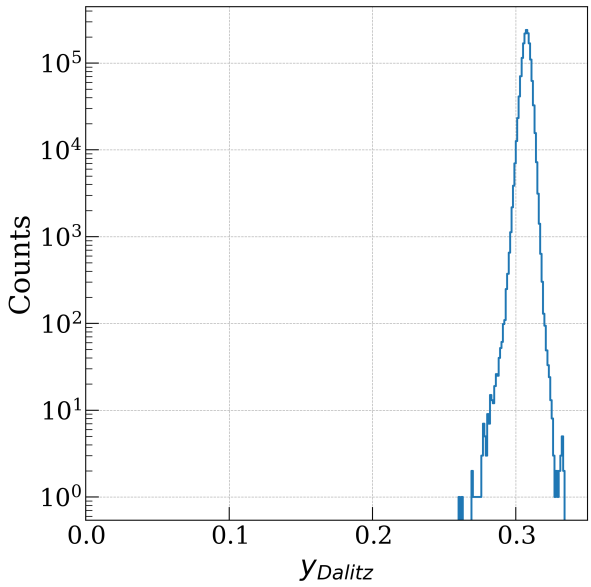

(a) Simulated 3^- state sequential decay mode.

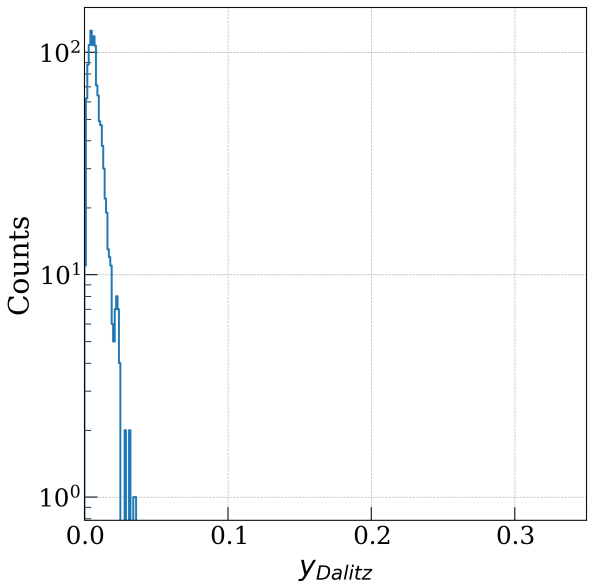

(b) Simulated 3^- state decay mode DDE.

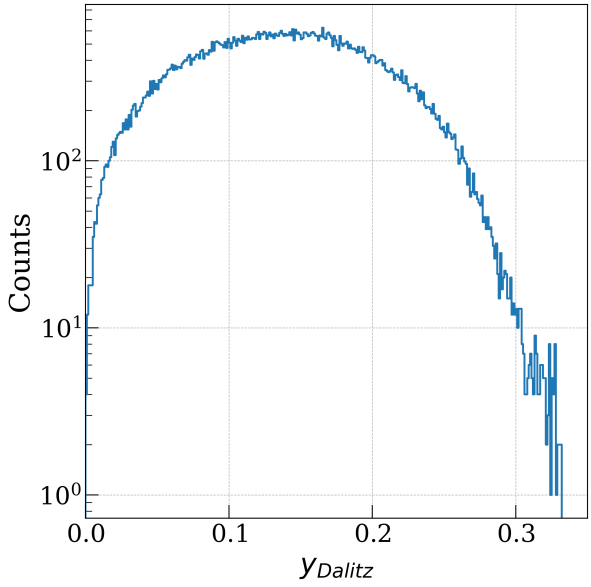

(c) Simulated 3^- state decay mode DDP.

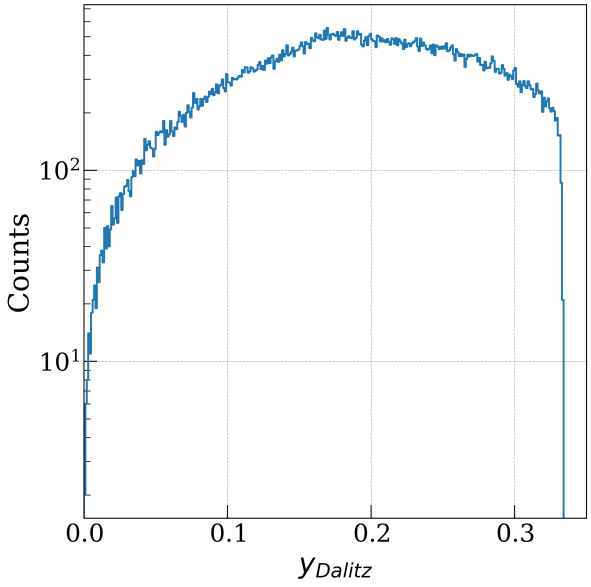

(d) Simulated 3^- state decay mode DDF.

Figure 5.9: Simulated 3^- state decay mode projections.

Chapter 6

Direct particle-decay branching ratios

To determine the branching ratio of the three-alpha decay modes from simulation and experimental data, an approach based on the frequentist analysis technique [114] is used. The premise of the applied method is to compare the observed data to the simulated data with respect to one or multiple free parameters, in this case, the branching ratios of the three decay modes. The likelihood function, defined as the probability of obtaining the observed data given the model represented by the simulation, is used to quantify the agreement between the two datasets [114]. The likelihood function is maximized to find the best fit parameters.
The application of this approach will be introduced in the following sections and the results of the analysis will be presented.
While the underlying method is a well-established technique [115], it must be used with caution, as its results can be sensitive to systematic deviations between the observations and the model such as skewed distributions or different resolutions. To account for these systematic deviations, additional consistency checks were performed, which will be discussed in the later parts of this chapter in Section 4.2.2.

6.1 Methodology

The branching-ratio analysis uses the Y-projection of the folded Dalitz plots for simulation and experimental data, which is introduced in Section 4.2.1, after both datasets were processed using the same analysis codes as discussed in the prior chapters. The simulation data is split by its tagging information, which contains the branching channel it is generated from.
Histograms are built for the simulated data, multiplied by amplitude parameters to represent the probability distribution of the observed values. The scaling approach is chosen over approaches such as random undersampling of the individual events, as it allows for a more accurate representation of the experimental data and utilizes all data points. The likelihood evaluation involves combining the obtained histogram for each decay mode

linearly, scaled by the branching ratio under investigation to fit the experimental data. A likelihood function that maps the agreement between the observed data and fit of the simulated data is then used to determine the optimal parameters. In this analysis, the negative log-likelihood function is used, which will be discussed in more detail in Section 6.1.1.
A parameter optimization is performed to minimize this negative log-likelihood, identifying the best-fit branching ratios: For an ideal fit, the individual components of the simulated data should match the experimental data. This can be described by

$$f_i \cdot A_{i,\mathrm{sim}} = A_{i,\mathrm{exp}}, \tag{6.1}$$

where f_i is the scaling fit parameter of the individual simulated component $A_{i,\mathrm{sim}}$, and $A_{i,\mathrm{exp}}$ is the experimental component associated with the decay mode i. As the simulated components' volumes are given by

$$A_{i,\mathrm{sim}} = N_{\mathrm{sim}} \cdot b_{i,\mathrm{sim}}, \tag{6.2}$$

where N_{sim} is the total number of simulated events and $b_{i,\mathrm{sim}}$ is the branching ratio of the decay mode i in the simulation, and

$$A_{i,\mathrm{exp}} = N_{\mathrm{exp}} \cdot b_{i,\mathrm{exp}}, \tag{6.3}$$

with the total number of experimental events N_{exp}, the condition that

$$N_{\mathrm{sim}} \cdot \sum f_i b_{i,\mathrm{sim}} = N_{\mathrm{exp}} \cdot \sum_i b_{i,\mathrm{exp}} \tag{6.4}$$

must be fulfilled. This results in

$$\frac{1}{\sum f_i b_{i,\mathrm{sim}}} = \frac{N_{\mathrm{sim}}}{N_{\mathrm{exp}}}. \tag{6.5}$$

Using this, the branching ratio can be obtained from the fit parameter f_i by

$$b_{i,\mathrm{exp}} = f_i \cdot b_{i,\mathrm{sim}} \cdot \frac{N_{\mathrm{sim}}}{N_{\mathrm{exp}}} = f_i \cdot \frac{b_{i,\mathrm{sim}}}{\sum f_j b_{j,\mathrm{sim}}}, \tag{6.6}$$

which only depends on known quantities.
The expected peak position of the sequential decay component after the Y-projection, previously introduced in Figure 4.23a, is shown in Table 6.1, as its high statistics allow for direct measurement of the peak position. The direct decay modes have more degrees of freedom, forming a wider non-Gaussian distribution of events instead. The derivation of these values is discussed in the appendix (Section A.6). To fit the model to the observed

Table 6.1: Expected relative energy ϵ_3 of the alpha particle with the highest center-of-mass energy for the the sequential decay component of different states in ^{12}C.

Decay mode	Expected relative energy (ϵ_3)
Hoyle state	0.17193
3^-	0.30746

data, the likelihood function under the Poisson distribution has to be maximized, which is a common technique in statistical inference [115]. Apart from the statistical uncertainties (see Section 6.1.2), systematic uncertainties are only implicitly introduced by the constant energy resolution and angular precision of the detector setup. This aspect of the simulation only accounts for a part of the systematic uncertainties, as the experimental resolution slightly varies per detector and with time, creating a large amount of possible free parameters. This was further discussed in Section 4.2.2.
Additionally, all direct decay modes were analyzed separately, as fitting multiple direct decay modes simultaneously increases the number of free parameters and broadens the likelihood function, making the fit less robust. In addition, multiple direct decay modes are contradictory: The DDP mode, for example, covers only a subset of the $DD\phi$ mode's phase space by factoring in the Coulomb barrier penetration in the decay process, while the $DD\phi$ mode does not. This is a clear conceptual contradiction, which is why the direct decay modes were analyzed separately.

6.1.1 Likelihood Functions

As the underlying data consists of count data, where events occur independently and the data represent the number of occurrences within fixed intervals, the Poisson distribution is an appropriate statistical model [114]. Applying its properties, the probability of an observation is given by

$$P(y_i;\lambda_i) = \frac{\lambda_i^{y_i} e^{-\lambda_i}}{y_i!}, \tag{6.7}$$

where λ_i is the expected number of occurrences and y_i is the observed number of occurrences. The likelihood function for the entire dataset is then the product of the individual Poisson probabilities:

$$\mathcal{L}(\mathbf{Y};\boldsymbol{\lambda}) = \prod_{i=1}^{N} \frac{\lambda_i^{y_i} e^{-\lambda_i}}{y_i!}, \tag{6.8}$$

where N is the total number of data points, $\mathbf{Y}$ represents the observed data, and $\boldsymbol{\lambda}$ represents the model prediction. This function quantifies the probability of reproducing the data given the model predictions, serving as a measure of how well the model explains the observed counts.

To simplify computation, especially with large datasets, the log-likelihood function is used instead of the product of Poisson distributions, since the logarithm is a monotonic transformation and does not affect the maximum likelihood estimate of the parameters, transforming the product into a sum:

$$\log \mathcal{L}(\mathbf{Y}; \boldsymbol{\lambda}) = \sum_{i=1}^{N} \left[y_i \log(\lambda_i) - \lambda_i - \log(y_i!) \right]. \tag{6.9}$$

To avoid the logarithm of zero when λ_i is very small, a small constant $\epsilon > 0$ is added, which is orders of magnitude smaller than the smallest expected count:

$$\log \mathcal{L}(\mathbf{Y}; \boldsymbol{\lambda}) = \sum_{i=1}^{N} \left[y_i \log(\lambda_i + \epsilon) - \lambda_i - \log(y_i!) \right]. \tag{6.10}$$

Finally, the deviance of the negative log-likelihood is defined as

$$-2 \log \mathcal{L}(\mathbf{Y}; \boldsymbol{\lambda}), \tag{6.11}$$

which is the function minimized during parameter optimization. The factor of 2 is included by convention to ensure that $\Delta(-2 \ln \mathcal{L})$ is asymptotically χ^2-distributed, as will be discussed in the following Section 6.1.2.
As discussed previously in Section 4.2.2, the data from the December and January runs were found to deviate in resolution and had to be analyzed separately, as the fit is highly sensitive to the resolution to discriminate between the decay modes.

6.1.2 Uncertainty Computation

To obtain robust error ranges for the measured branching ratios, the properties of the used negative log-likelihood function were utilized to derive confidence intervals for the estimated parameters.
The negative log-likelihood function, defined as $-2 \log \mathcal{L}$, where $\mathcal{L}$ is the likelihood of the observed data given the model parameters (amplitudes of the sequential and direct decay components), forms the basis for this approach. This method is applicable because the likelihood function and its parameters satisfy the following regularity conditions [116]:

- **Identifiability**: The true parameter value must be uniquely identifiable within the parameter space, ensuring that different parameter values yield distinct likelihoods. This is shown by the clear optimum visible in the likelihood curve, as for example shown in Figure 6.4b.
- **Smoothness**: The log-likelihood function should be twice continuously differentiable with respect to the parameters, providing a smooth surface for analysis, which

follows from the differentiability of the used likelihood function 6.10.

- **Positive Definiteness of the Fisher Information**: The Fisher information matrix, defined as the expected value of the second derivative (Hessian) of the log-likelihood, must be positive definite. This condition ensures that the likelihood surface is convex around the maximum likelihood estimates (MLEs). This is verified using the Hessian matrix of the log-likelihood function, which is positive definite at the MLEs.

- **Asymptotic Normality of MLEs**: The general assumption of the given statistical test and overall analysis is that the measured values follow the Poisson statistics, which converges to a normal distribution for large sample sizes.

The confirmation of these criteria enables the application of Wilks' theorem which states, that the distribution of $-2\log\mathcal{L}$ approaches a χ^2-distribution asymptotically as the sample size increases [117]. However, when a parameter is constrained by a physical boundary (e.g., a nonnegative amplitude with the MLE at zero), the likelihood–ratio statistic follows a mixture of χ^2 distributions rather than a pure χ^2; in such cases the standard χ^2 thresholds yield conservative one-sided limits [**PDGStatistics2024**]. This allows to use the properties of the χ^2 distribution to determine confidence intervals for the parameters. Specifically, for a model with k degrees of freedom, the likelihood-ratio test statistic will asymptotically follow a χ^2 distribution with k degrees of freedom. In practical terms, this means that the increase in the negative log-likelihood function from its minimum value, $\Delta(-2\log L)$, can be compared directly to critical values from the χ^2 distribution to determine confidence intervals. The intercept of the likelihood curve with the critical χ^2 values is tested in both directions to determine the confidence intervals and account for skewness in the likelihood curve and the logarithmic sampling of the branching ratio. When the value falls between two branching ratio values, an interpolation is performed to determine the intersection point of the likelihood curve with the critical χ^2 value, as shown in Figure 6.3.
For the employed two-parameter model, where the amplitudes of the sequential and direct component are the free parameters, the relationship between the difference of a likelihood value to the minimum of the likelihood distribution in the negative log-likelihood, $\Delta\chi^2$, and the corresponding confidence levels is summarized in Table 6.2. These values can be directly obtained by evaluating the percent point function, the inverse of the cumulative distribution function, of the χ^2-distribution [114]. These critical values are derived from the cumulative distribution function (CDF) of the χ^2 distribution, which for k degrees of freedom is given by

$$P(\chi^2 \leq x) = \frac{1}{2^{k/2}\Gamma(k/2)} \int_0^x t^{k/2-1} e^{-t/2} dt, \tag{6.12}$$

Table 6.2: Critical values of $\Delta\chi^2$ for confidence intervals in a two-parameter fit.

Standard Deviations	Confidence Level	$\Delta\chi^2$
1σ	68.3%	2.3
2σ	95.4%	6.18
3σ	99.7%	11.8

where $\Gamma(\cdot)$ denotes the Gamma function, k is the number of degrees of freedom, and x is the critical value.

For a two-parameter model ($k = 2$), the $\Delta\chi^2$ values listed in Table 6.2 correspond to the commonly used 1σ, 2σ, and 3σ confidence intervals.

The theoretical foundation of this approach, grounded in likelihood-based inference and the properties of the χ^2 distribution, ensures that the derived confidence intervals are both statistically rigorous and interpretable within the frequentist framework. It is a standard method for uncertainty estimation in likelihood-based analyses [114].

The obtained uncertainty intervals, however, only account for the statistical uncertainties of the model parameters and do not include systematic uncertainties. While parts of the systematic uncertainties are accounted for in the Monte Carlo simulation, effects like the energy sum deviations, discussed in Section 4.1.4, are not fully accounted for. As these general model improvements require simulating a larger parameter space, they could not be included in the current analysis, but will be addressed in future studies.

Another important aspect of the method employed is that only one direct decay distribution is fitted at a time. Since all bin counts are zero or positive, as are the fitted amplitudes, the introduction of other direct decay modes can only decrease the relative event fraction of a given decay mode. This is a clear limitation of the method, which restricts it to providing upper limits for the branching ratios of the direct decay modes.

6.2 Hoyle state branching ratio results

The application of the general method, as described in the previous section, can exemplary be seen in Figure 6.1, where the Y-projection of the Dalitz plot with the experimental data from the December 2019 campaign is drawn superimposed with the simulated sequential decay and DDP direct decay data. The plot shows an exaggerated direct decay branching ratio of $b_{\text{Hoyle,DDP}} = 1.125 \times 10^{-3}$ to more clearly show the direct decay component.

For each configuration the run files with average laboratory and center-of-mass energy sums and distribution width within 2σ of the run average were selected. This was done because a small subset of outlier runs exhibited a significantly different resolution. Adding these files would compromise the fit quality, as the assumption of the simulated model is

a uniform resolution.

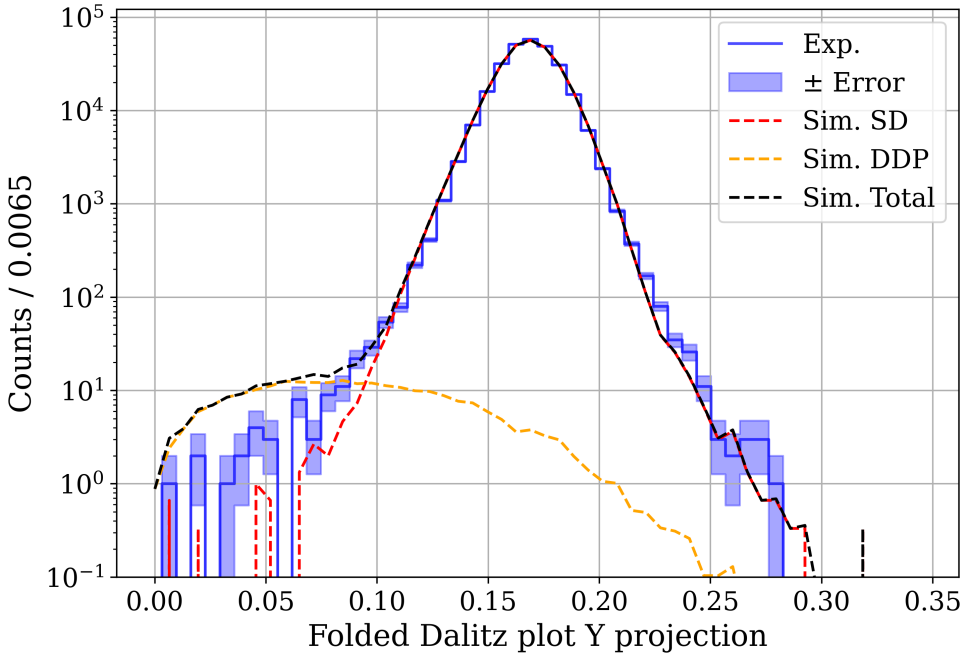

Figure 6.1: Example of the simulated sequential and DDP decay events of the Hoyle state and the experimental data using an exaggerated direct decay branching ratio of $b_{\text{DDP, Hoyle}} = 1.125 \times 10^{-3}$ for demonstration using the December 2019 data.

To demonstrate the scale-relation between sequential and direct decay components, the same data, now with the branching ratio obtained from the likelihood analysis, is shown on a linear scale, as well as amplified by a factor of 10^3 in Figures 6.2a and 6.2b, respectively. This visualization demonstrates the high influence of the sequential decay branch, as, even when amplified by a factor of 10^3, the direct decay component is the minority component. The overall simulated distribution of the sequential decay component shows very good agreement with the experimental data, as does the contribution of the direct decay component. The latter component has very low statistics, caused by the low branching ratio of the direct decay modes. The figures also clearly show the overlap of the expected sequential and direct decay components, which is a known limitation of relative-energy-based analysis methods. This overlap is caused by the energies of the direct decay alpha particles, which can distribute their energy over a wide range between the three alpha particles. This can also create configurations that are indistinguishable from the sequential decay mode. As all decay components have the same Q-value, and the components only vary in their relative energies, the highest sensitivity of the analysis can be achieved on the non-overlapping regions of the decay components.

Using the likelihood function obtained by scanning the fit parameter space, the optimum branching ratios and their confidence intervals can be obtained. The likelihood function is evaluated over a logarithmic range of the branching ratio to cover the full range of possible

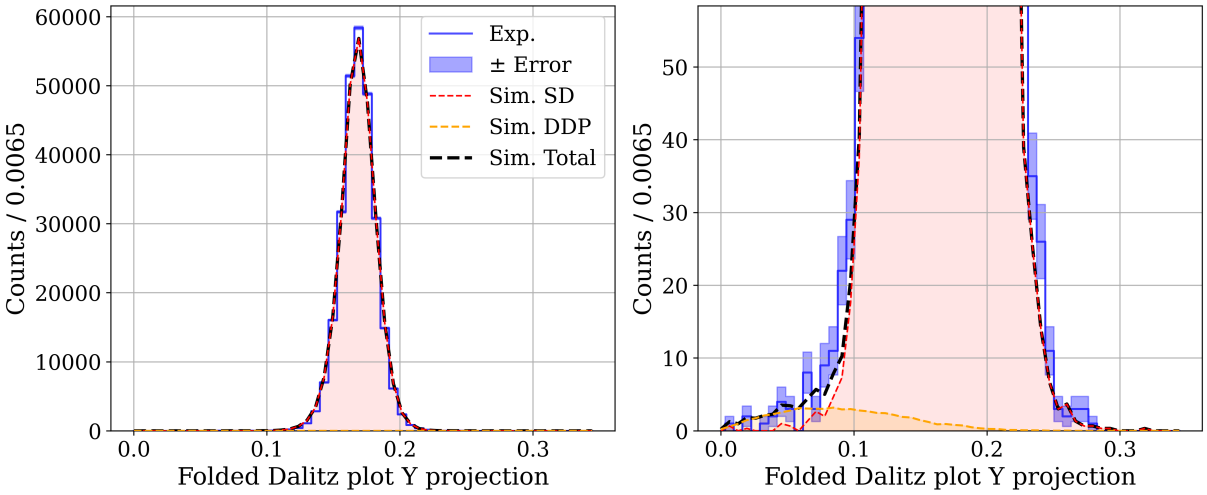

(a) Fit of the simulated Hoyle state decay mode data for the DDP decay mode to the experimental data on a linear scale, showing the full data range.

(b) Fit of the simulated DDP decay mode data to the experimental data on a linear scale, scaling to 10^3 of the sequential peak amplitude.

Figure 6.2: Fits of the Hoyle-state DDP and SD decay modes to the experimental data plotted on a linear scale, showing the full data range and a zoomed-in view to demonstrate the low amplitude of the direct decay component.

values. The obtained curve shows a minimum at the obtained value of $b_{\text{Hoyle,DDP}} = 2.8 \times 10^{-4}$ for the DDP decay mode. The likelihood function is shown in Figure 6.3.

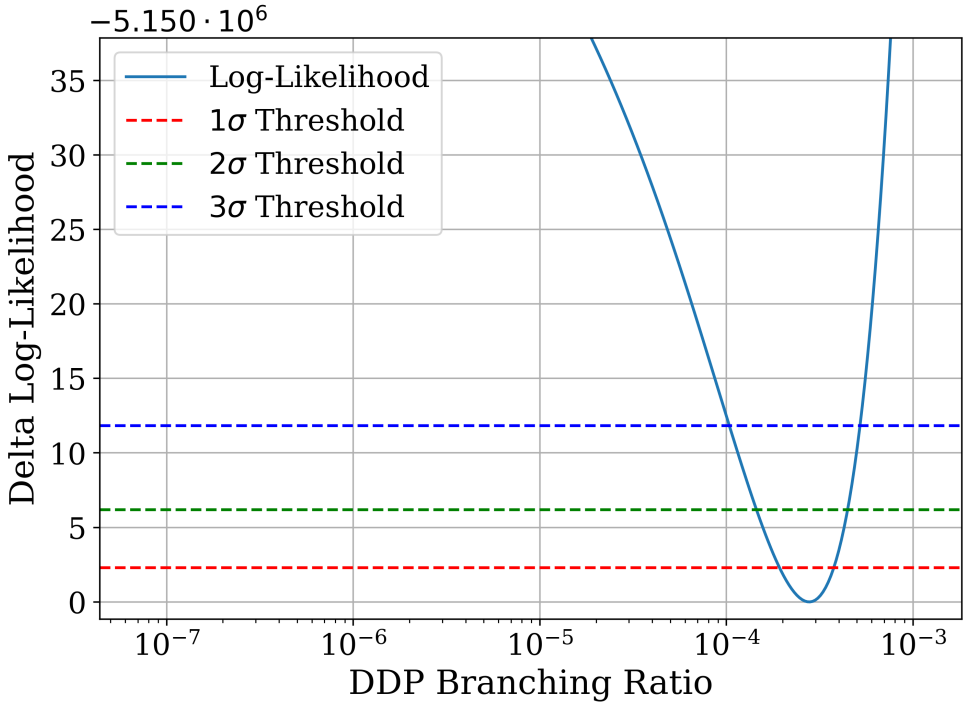

Figure 6.3: Likelihood curve for the DDP decay mode of the Hoyle state. The horizontal lines indicate the confidence levels of 1σ, 2σ, and 3 σ.

6.2.1 DDP branching ratio

The DDP decay mode of the Hoyle state is the augmented free decay mode, where the available phase space is limited by the Coulomb repulsion of the alpha particles previously shown in Figure 5.1a.

For this decay mode, a branching ratio of $b_{\text{Hoyle,DDP}} = 2.800^{+1.653}_{-1.352} \cdot 10^{-4}$ is obtained in the December 2019 data. In the January measurement the obtained optimum branching ratio is $b_{\text{Hoyle,DDP}} = 2.625^{+1.694}_{-1.296} \cdot 10^{-4}$ with uncertainty ranges at the 95.4 % confidence level. The detailed results with best fit, lower, and upper limits for the Hoyle state decay mode are shown in Table 6.3. The best obtained fit for the December 2019 data is shown in Figure 6.4a and the corresponding likelihood curve is presented in Figure 6.4b. The shaded areas in the likelihood-curve plots show, from dark to light orange, the confidence levels of 1σ, 2σ, and 3σ, respectively. The optimal fit for the January 2020 data is shown in Figure 6.5a and the corresponding likelihood curve is given in Figure 6.5b.

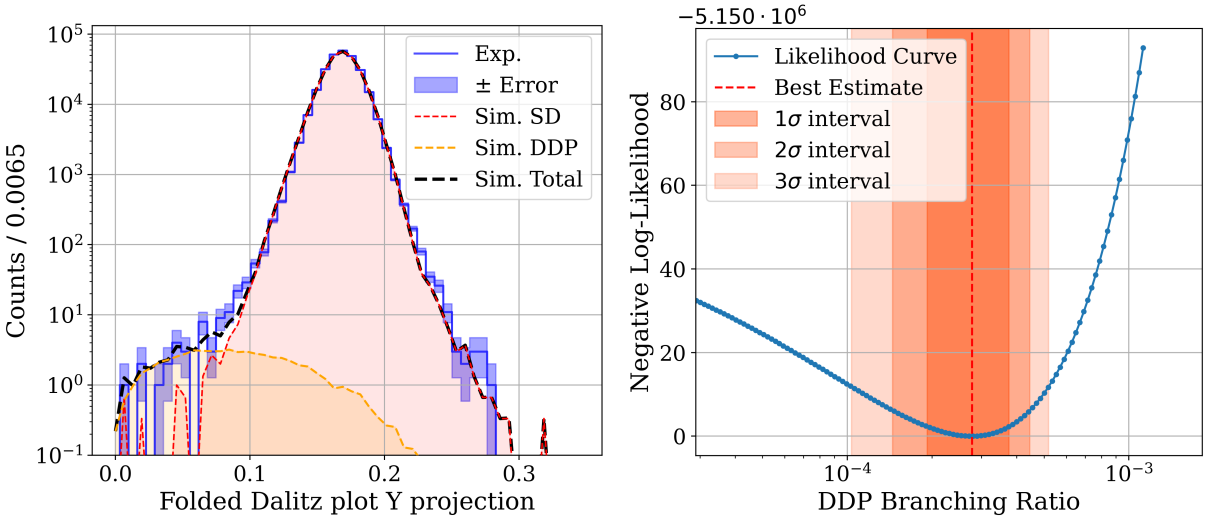

(a) Histogram showing the fit of the simulated sequential and DDP decay events to the experimental data for the December 2019 data.

(b) Likelihood curve with confidence intervals for the DDP decay mode of the Hoyle state for the December 2019 data.

Figure 6.4: Fit of the simulated sequential and DDP decay events to the experimental data for the December 2019 data.

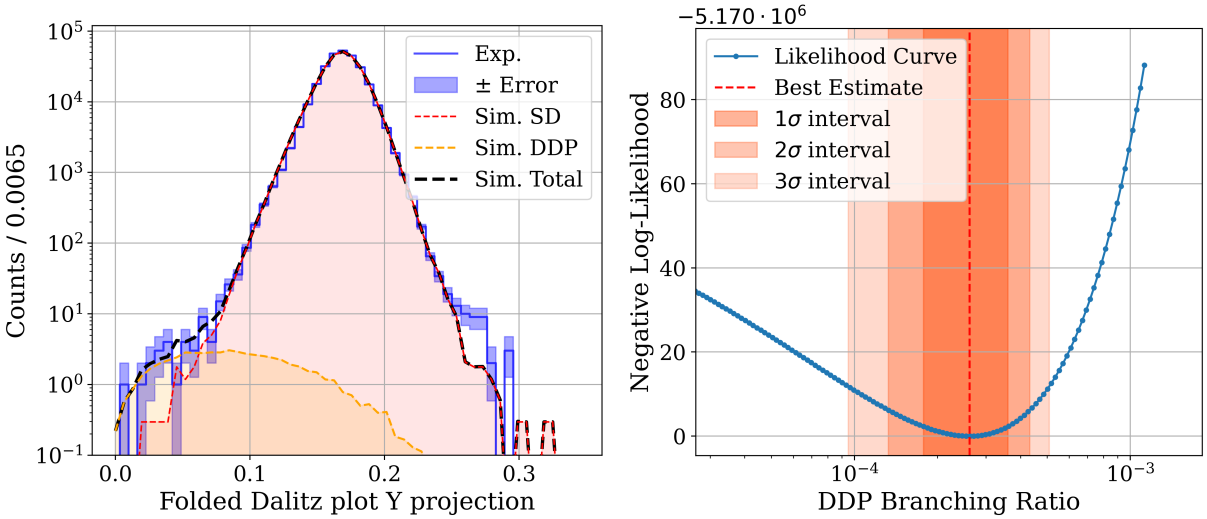

(a) Histogram showing the fit of the simulated sequential and DDP decay events to the experimental data for the January 2020 data.

(b) Likelihood curve with confidence intervals for the DDP decay mode of the Hoyle state for the January 2020 data.

Figure 6.5: Fit of the simulated sequential and DDP decay events to the experimental data for the January 2020 data.

Table 6.3: Upper and lower limits of the branching ratio of the DDP three-alpha decay mode of the Hoyle state for different confidence levels for 92 % (2019) and 95 % of the data of the December and January measurements. These are the files within the 2σ range of the energy sum and distribution width of the run average, as described in the beginning of this section.

Experiment	HS DDP Branching ratio		Confidence level
	Lower limit	Upper Limit	
December 2019	2.800×10^{-4}		Best fit
	1.924×10^{-4}	3.757×10^{-4}	1 σ (68.3 %)
	1.449×10^{-4}	4.454×10^{-4}	2 σ (95.4 %)
	1.035×10^{-4}	5.192×10^{-4}	3 σ (99.7 %)
January 2020	2.625×10^{-4}		Best fit
	1.780×10^{-4}	3.603×10^{-4}	1 σ (68.3 %)
	1.329×10^{-4}	4.320×10^{-4}	2 σ (95.4 %)
	9.492×10^{-5}	5.086×10^{-4}	3 σ (99.7 %)

6.2.2 DDϕ branching ratio

The DDϕ decay mode of the Hoyle state is the direct decay mode where the alpha particles are allowed to distribute their energy freely and cover the full phase space. This enables any possible energy combination, only restricted by energy and momentum conservation. Without considering the Coulomb repulsion of the alpha particles, as discussed in the previous DDP decay mode section, the branching ratio of the DDϕ direct decay mode of the Hoyle state is found to be $b_{\text{Hoyle,DD}\phi} = 5.234^{+2.627}_{-2.228} \cdot 10^{-4}$ for the December 2019 experiment and $b_{\text{Hoyle,DD}\phi} = 5.593^{+2.783}_{-2.434} \cdot 10^{-4}$ for the January 2020 experiment. This result is substantially higher than the branching ratio of the DDP decay mode. The overall fit quality is lower, especially in the relative energy range above $0.28 \cdot Q$, where Q is the Q-value of the Hoyle state. As the general curve shape in the sensitive area below $0.10 \cdot Q$ is similar to the DDP decay mode, the increase in the branching ratio is primarily caused by the wider distribution of the direct decay component. The results are shown in Table 6.4. The best fit for the data taken in December 2019 is shown in Figure 6.6a and in Figure 6.7a for the January 2020 data. The likelihood curve for the DDϕ decay mode is shown in Figure 6.6b for the December 2019 data and in Figure 6.7b for the January 2020 data.

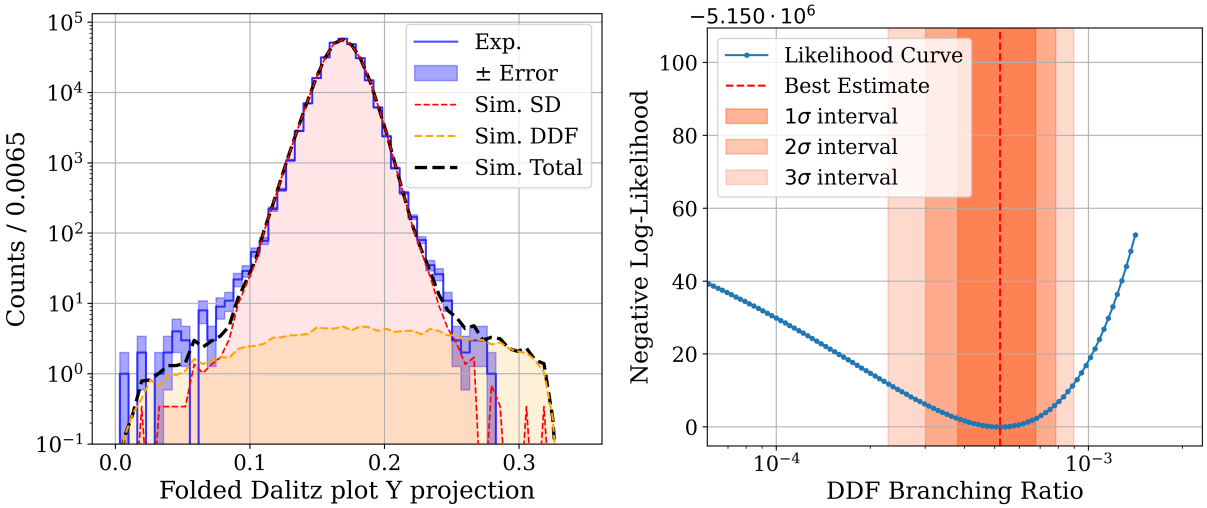

(a) Fit of the simulated sequential and DDϕ decay mode data to the experimental data of the 2019 experiment.

(b) Likelihood curve with confidence intervals for the DDϕ decay mode of the Hoyle state for the December 2019 data.

Figure 6.6: Fit of the DDϕ mode of the Hoyle state for the December 2019 data.

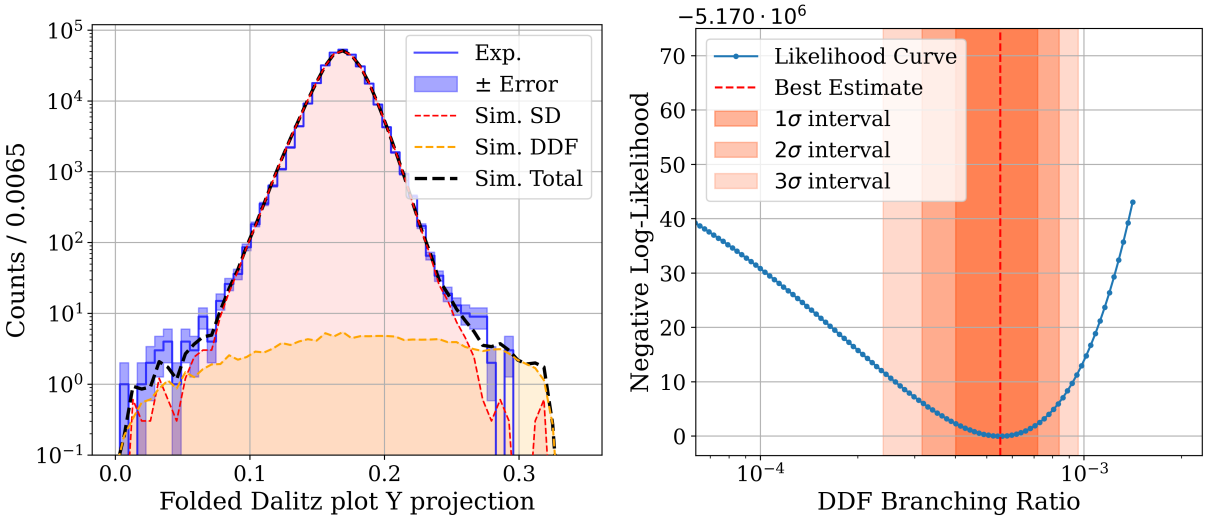

(a) Fit of the simulated sequential and DDϕ decay mode data to the experimental data of the 2020 experiment.

(b) Likelihood curve with confidence intervals for the DDϕ decay mode of the Hoyle state for the January 2020 data.

Figure 6.7: Fit of the DDϕ mode of the Hoyle state for the January 2020 data.

Table 6.4: Upper and lower limits of the branching ratio of the $DD\phi$ three-alpha decay mode of the Hoyle state for different confidence levels for 92 % and 95 % of the data of the December 2019 and January 2020 measurements, respectively.

Experiment	HS DDϕ Branching ratio Lower limit	Upper Limit	Confidence level
December 2019	5.234×10^{-4}		Best fit
	3.815×10^{-4}	6.775×10^{-4}	1 σ (68.3 %)
	3.006×10^{-4}	7.861×10^{-4}	2 σ (95.4 %)
	2.282×10^{-4}	8.990×10^{-4}	3 σ (99.7 %)
January 2020	5.593×10^{-4}		Best fit
	4.016×10^{-4}	7.196×10^{-4}	1 σ (68.3 %)
	3.159×10^{-4}	8.376×10^{-4}	2 σ (95.4 %)
	2.395×10^{-4}	9.605×10^{-4}	3 σ (99.7 %)

6.2.3 DDE branching ratio

The DDE decay mode assumes equal energy distribution of the three alpha particles, which results in the direct decay events being distributed in the center of the Dalitz plot. This results in an event population at low relative energies in the Y-projection plot, as shown in the best fit for the December 2019 data in Figure 6.8a. The branching ratio of the DDE decay mode is found to be $b_{\text{Hoyle}} = 2.857^{+4.579}_{-2.234} \cdot 10^{-5}$ for the December 2019 data and $b_{\text{Hoyle}} = 4.011^{+5.517}_{-3.299} \cdot 10^{-5}$ for the January 2020 data. The likelihood curve for the DDE decay mode is shown in Figure 6.8b. The best fit of the DDE decay mode for the data from 2020 is shown in Figure 6.9a and the corresponding likelihood curve is shown in Figure 6.9b.

The fits show good agreement for the sensitive area but are not able to produce a continuous fit for the full range of the data, as the model underestimates the experimental data at relative energies around 0.05. This feature could be an indicator that multiple direct decay components are present, which are not accounted for in the model. This aspect could be mitigated by employing a multi-component model, which fits multiple direct decay components simultaneously. This approach has been tested, but does not provide a smooth likelihood curve, which is a requirement for the employed confidence analysis technique. The results of the two performed experiments where sequential and DDE component were taken into account are shown in Table 6.5.

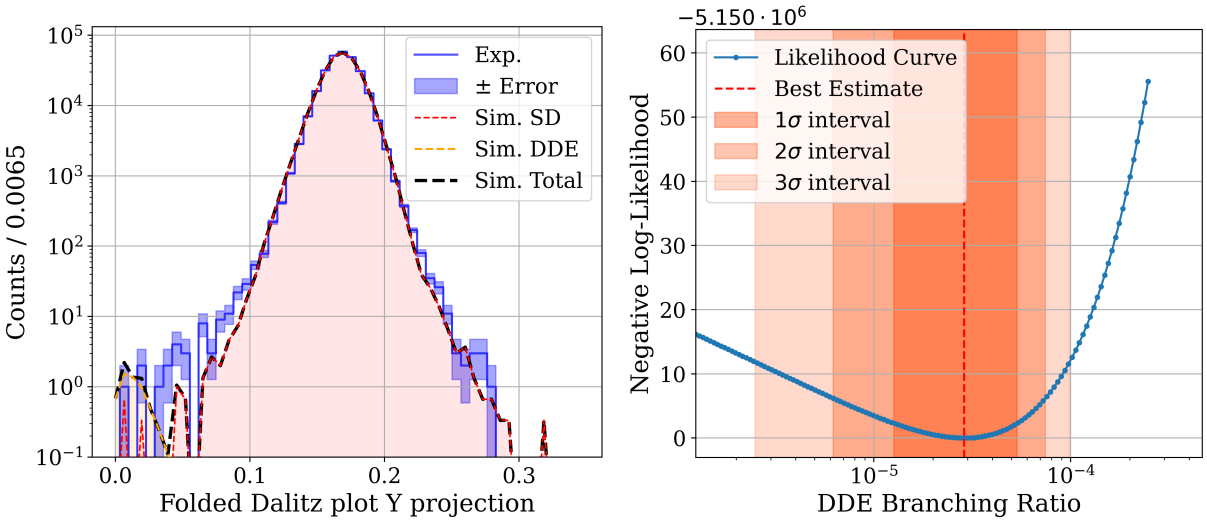

(a) Fit of the simulated sequential and DDE decay mode data to the experimental data of the 2019 experiment.

(b) Likelihood curve with confidence intervals for the DDE decay mode of the Hoyle state for the December 2019 data.

Figure 6.8: Fit of the DDE mode of the Hoyle state for the December 2019 data.

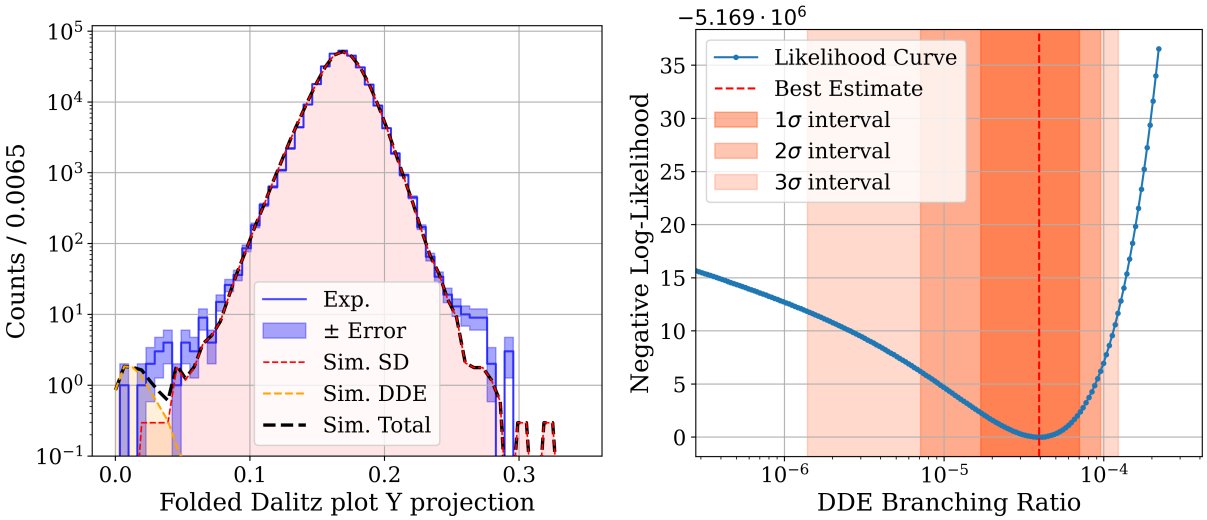

(a) Fit of the simulated sequential and DDE decay mode data to the experimental data of the 2020 experiment.

(b) Likelihood curve with confidence intervals for the DDE decay mode of the Hoyle state for the January 2020 data.

Figure 6.9: Fit of the DDE mode of the Hoyle state for the January 2020 data.

Table 6.5: Upper and lower limits of the branching ratio of the DDE three-alpha decay mode of the Hoyle state for different confidence levels for 92 % (2019) and 95 % of the data of the December and January measurements.

Experiment	HS DDE Branching ratio Lower limit	Upper Limit	Confidence level
December 2019	2.857×10^{-5}		Best fit
	1.263×10^{-5}	5.355×10^{-5}	1 σ (68.3 %)
	6.225×10^{-6}	7.437×10^{-5}	2 σ (95.4 %)
	2.500×10^{-6}	9.881×10^{-5}	3 σ (99.7 %)
January 2020	4.011×10^{-5}		Best fit
	1.696×10^{-5}	7.048×10^{-5}	1 σ (68.3 %)
	7.117×10^{-6}	9.528×10^{-5}	2 σ (95.4 %)
	1.394×10^{-6}	1.235×10^{-4}	3 σ (99.7 %)

6.2.4 DDL branching ratio

The DDL decay mode of the Hoyle state is the direct decay mode where one alpha particle after the decay is at rest in the center-of-mass frame of the decaying ^{12}C nucleus and the other two alpha particles are emitted antiparallel to each other with equal energy. Contrasting a more broad definition of the DDL event decay, which was for example chosen by Smith et al. [59], where all decays close enough to a linear configuration are considered as DDL decay events, here, only antiparallel decay configurations were considered.

A test fit of this decay path was performed, but the results showed a very high sensitivity to the model uncertainties: The Monte-Carlo simulation (see Figure 6.10) and general constraints of the Dalitz plots show that the DDL events overlap with the corners of the sequential decay triangle in the Dalitz plot, where the statistics of the sequential decay mode is highest. The large sequential component at the overlap range made the fit very sensitive to the exact energy resolution, as the outer edges of the sequential decay component are implicitly scaled up or down by introduction of the DDL decay mode as the fitting algorithm is most sensitive to the data close to the peak.

For this reason, the DDL decay mode was not included in the likelihood analysis, as the model uncertainties changed the resulting branching ratio by more than two orders of magnitude. An example fit is shown in Figure 6.11. The corresponding branching ratio is $b_{\text{Hoyle, DDL}} = 2.619^{+0.483}_{-0.453}\times10^{-2}$ for the typical energy resolution of the December 2019 data. Reducing the data selection threshold has a strong impact on the obtained branching ratio, as the lowest threshold yields a branching ratio of $b_{\text{Hoyle, DDL}} = 4.533^{+0.655}_{-0.774} \times 10^{-2}$. This indicates that at the current sensitivity of the experiment, the DDL decay mode cannot be resolved.

Given the dependency of the branching ratio on the systematic errors and since the study of the systematic uncertainties of the model is beyond the scope of this work, the DDL decay mode was not included in the final analysis, but was included in the likelihood analysis for completeness.

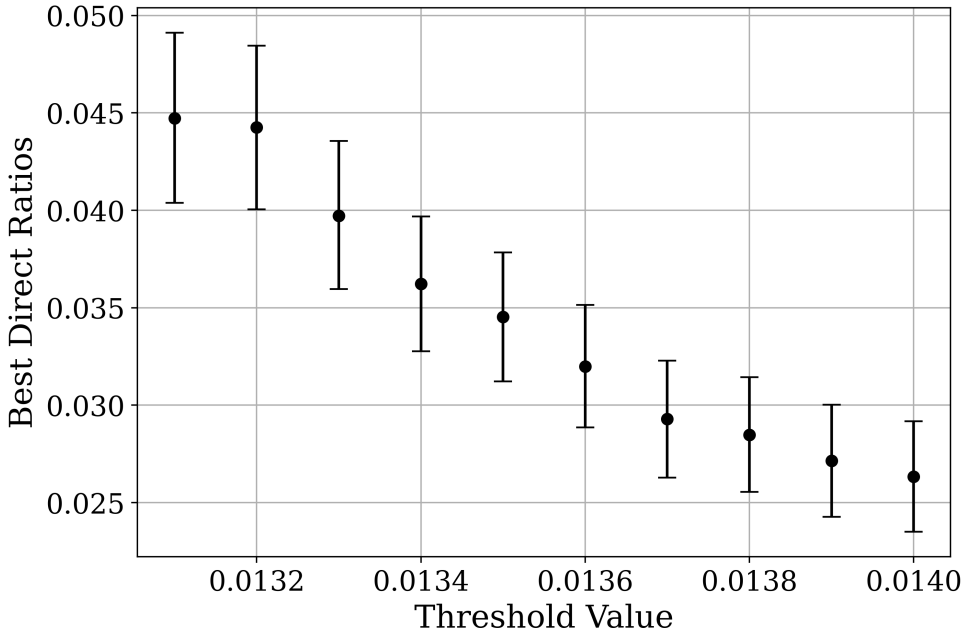

Figure 6.10: Fit of the simulated sequential and DDL decay mode data to the experimental data of the 2019 experiment.

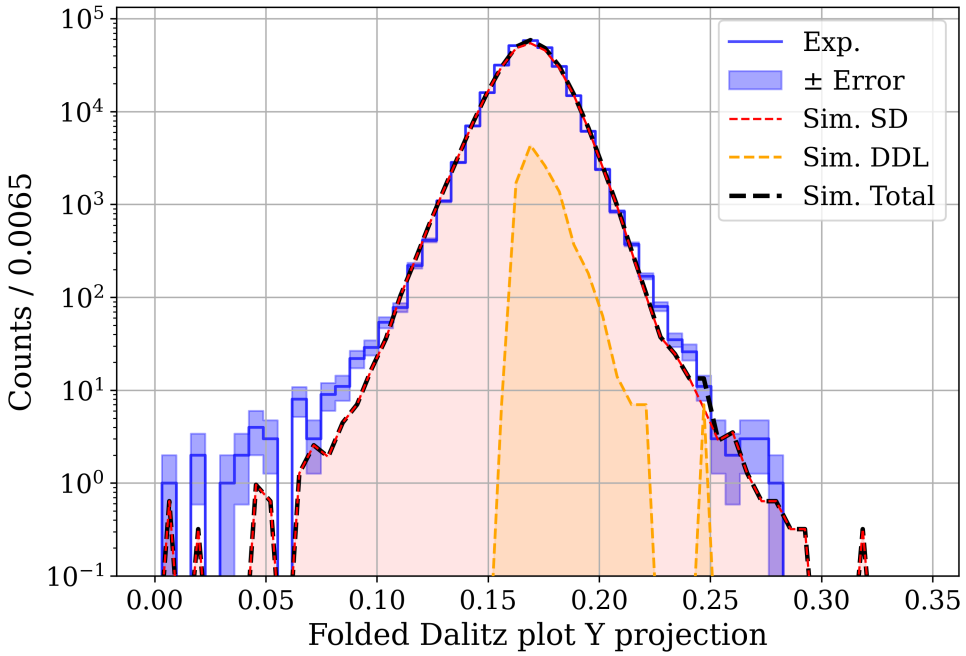

Figure 6.11: Fit of the simulated sequential and DDL decay mode data to the experimental data of the 2019 experiment.

6.2.5 Summary

In total, the branching ratios of the DDP, DDϕ, and DDE decay modes of the Hoyle states were measured. The resulting values are summarized in Table 6.6. The shown values only include statistical uncertainties and only partially account for systematic uncertainties that were implicitly included in the Monte Carlo simulation.

Table 6.6: Upper and lower limits of the branching ratio of the direct three-alpha decay modes of the Hoyle state at a 2σ confidence level for 92 % of the data of the December and 95 % of the data of the January measurements. The given uncertainties are statistical only.

Decay mode	Hoyle State Branching ratio 2019	2020
DDE	$2.857^{+4.579}_{-2.234} \cdot 10^{-5}$	$4.011^{+5.517}_{-3.299} \cdot 10^{-5}$
DDϕ	$5.234^{+2.627}_{-2.228} \cdot 10^{-4}$	$5.593^{+2.783}_{-2.434} \cdot 10^{-4}$
DDP	$2.800^{+1.653}_{-1.352} \cdot 10^{-4}$	$2.625^{+1.694}_{-1.296} \cdot 10^{-4}$

The relative uncertainties of the branching ratios of particle decay of the Hoyle state are summarized in Table 6.7.

Table 6.7: Relative uncertainties of the branching ratios of the 3^- state decay modes for the 2σ confidence interval.

Decay mode	Relative uncertainty 2019 -	+	Relative uncertainty 2020 -	+
DDϕ	−42.6 %	50.2 %	−43.5 %	49.8 %
DDP	−48.3 %	59.0 %	−49.4 %	64.5 %
DDE	−78.2 %	160.3 %	−82.3 %	137.6 %

6.3 Systematic Deviations

Since the overlap of the sequential and direct decay components is directly related to the resolution of the sequential decay component, a test for a systematic relationship between the resolution and the branching ratio is performed. To test the sensitivity of the approach to the resolution, the fit is performed on subsets of the December and January datasets: As each dataset consists of multiple runs, which were combined to form the analyzed datasets.

As the sequential component extends over parts of the direct decay components, the subsets were selected by the resolution of the prominent relative-energy peak of the sequential decay component. As the resolution slightly varies between the subruns due to beam-spot fluctuations, the measurement provided a wide range of resolutions, as

previously shown in Figure 4.24. The results of this analysis for the DDP decay mode are shown in Figure 6.12.

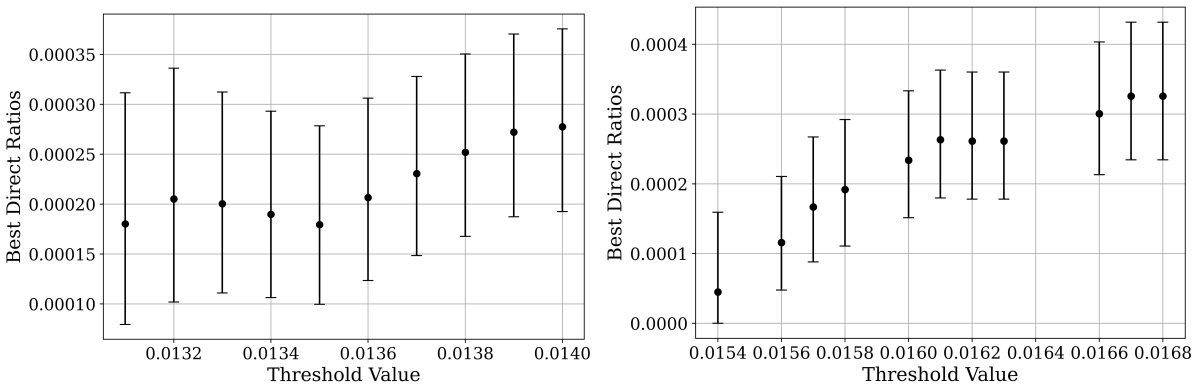

(a) Branching ratios of the DDP direct Hoyle state decay mode as a function of the resolution threshold for the December 2019 data.

(b) Branching ratios of the DDP decay mode for the January 2020 data. The gaps are created when the same file-count is obtained for multiple resolution thresholds.

Figure 6.12: Branching ratio of the Hoyle state decay mode as a function of the resolution threshold for the December 2019 and January 2020 data.

It should be noted that the resolution selection is performed using a Gaussian fit on the inner part of the sequential decay component to ensure that the selection is not influenced by the direct decay component. Since for the measured branching ratios of $b_{\text{Hoyle}} \approx 3{\cdot}10^{-4}$, the DDP decay component is almost two orders of magnitude smaller than the sequential decay component in the fringe of the fit and almost five orders of magnitude smaller in the center of the sequential peak, as can be seen in the fit in Figure 6.5a. The dependency of the selected subruns on the resolution is shown in Figure 6.13.

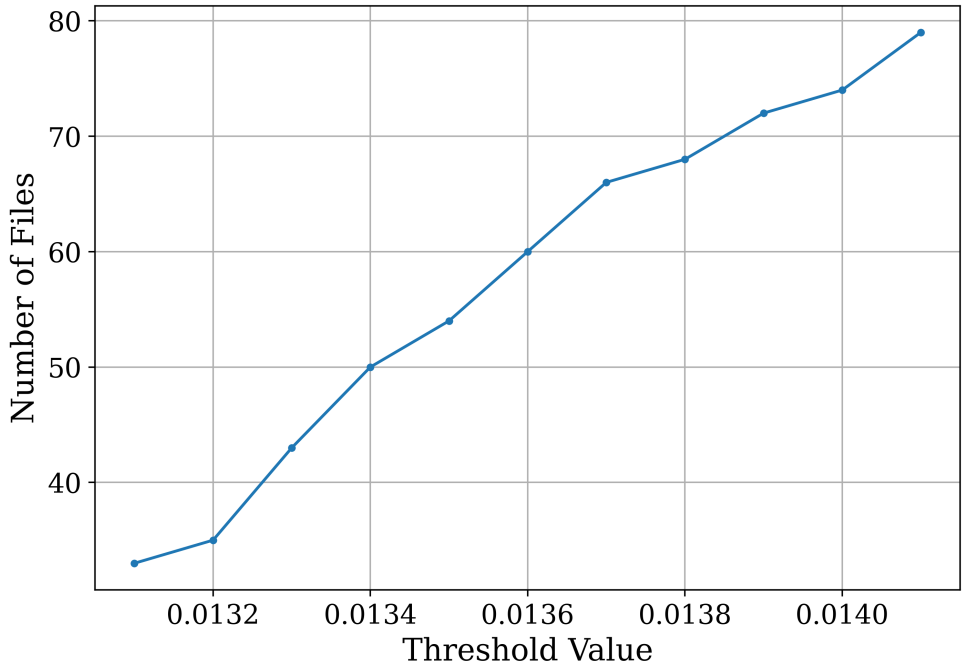

Figure 6.13: Number of run files used as a function of the resolution threshold for the December 2019 data.

The graph shows a gradual increase of the branching ratio for higher resolution thresholds, which is consistent with the expected behavior, as including runs with poorer resolution can artificially broaden the tail of the sequential decay peak, which the fit may attribute to the direct decay component. For the data taken in December 2019, the branching ratio increases from $b_{\text{Hoyle}} = 1.794^{+0.990}_{-0.799} \cdot 10^{-4}$ to $b_{\text{Hoyle}} = 2.774^{+0.982}_{-0.850} \cdot 10^{-4}$. The effect is, however, especially pronounced for the data taken in January 2020, where the best-fit branching ratio increases from $b_{\text{Hoyle}} = 4.469^{+1.146}_{-4.469} \cdot 10^{-5}$ to $b_{\text{Hoyle}} = 3.258^{+1.061}_{-0.913} \cdot 10^{-4}$.

Conclusion and Outlook

This thesis presents an analysis of the particle-decay behavior of excited ^{12}C states. To enable this, the LYCCA setup was upgraded to 24 mounted detectors with 18 AIDA FEE data-acquisition modules. Two experiments were planned, conducted, and more than $3 \cdot 10^{10}$ particle events were recorded. The data were analyzed and the results were compared to state-of-the-art Monte-Carlo simulations. The main objectives of this work were to provide analysis tools and methods for the LYCCA setup, demonstrate the capabilities of the upgraded array and apply them to study the case of the particle-decay behavior of excited ^{12}C states.

During this work, two measurement campaigns to determine the branching ratios of the direct decay modes of the Hoyle state and the 3^- state in ^{12}C were performed. Given the high angular coverage and resolution of the LYCCA setup, of the $3 \cdot 10^{10}$ detected particles, more than $6 \cdot 10^6$ particle-decay events of the Hoyle state, comprising $2.4 \cdot 10^7$ alpha particles, were detected in the two experiments, yielding one of the largest single-sample Hoyle triple-α datasets reported in the literature. The results of the analysis are summarized in Table 6.8. Although the optimization process provides best-fit values with confidence intervals, only the upper limits can be stated as robust constraints. This is because potential, unmodeled decay modes that overlap in phase space could contribute to the observed signal, meaning the true branching ratio for a specific direct decay mode could be lower than the best-fit value, as explained in Section 6.1.2. In addition to the presented values, a test of the DDL decay mode of the Hoyle state was performed, but the results were inconclusive due to the phase-space location of the DDL event which is entirely contained within the sequential-decay domain.

While the energy resolution in the center-of-mass frame did not allow for establishing a new conclusive upper limit, the resulting branching ratios still lie within the range of previous measurements, providing new data points for structure studies on the elusive nature of the configuration of higher-lying states in ^{12}C. Additionally, the source of a detected detrimental influence on the energy resolution was narrowed down to positional deviations, which will be corrected in future analyses, as this was beyond the scope of this thesis.

Significant advancements were achieved through a series of technical and methodological improvements: The test measurements and enhanced electrical grounding of the detectors contributed to the reduction of electronic noise before the beam time. Key developments

Table 6.8: Summary of the measured branching ratios for the direct decay modes of the Hoyle state in ^{12}C.

Decay mode	Experiment	Optimum branching ratio ($\pm 2\sigma$)	Upper limit ($\pm 2\sigma$)
DDP	2019	$(2.800^{+1.653}_{-1.352}) \cdot 10^{-4}$	$4.454 \cdot 10^{-4}$
	2020	$(2.625^{+1.694}_{-1.296}) \cdot 10^{-4}$	$4.320 \cdot 10^{-4}$
DDϕ	2019	$(5.234^{+2.627}_{-2.228}) \cdot 10^{-4}$	$7.861 \cdot 10^{-4}$
	2020	$(5.593^{+2.783}_{-2.434}) \cdot 10^{-4}$	$8.376 \cdot 10^{-4}$
DDE	2019	$(2.857^{+4.579}_{-2.235}) \cdot 10^{-5}$	$7.437 \cdot 10^{-5}$
	2020	$(4.011^{+5.517}_{-3.299}) \cdot 10^{-5}$	$8.827 \cdot 10^{-5}$

included an event-analysis pipeline built from the ground up, leading to improved, much faster, and more efficient event building with higher combination efficiency. This pipeline now offers a robust foundation for handling larger-scale datasets, significant for future experiments.

A time-walk correction was implemented (Section 3.6.2) to mitigate the amplitude-dependent variations in signal propagation, which improved timing accuracy across the detectors and enhanced the background suppression capabilities of the detector array. Additionally, the fit logic was refined in collaboration with Joe Roob, resulting in a more robust and reliable fitting procedure, which was necessary due to the high number of measured quantities. New gate conditions were implemented (sections 4.1.3, 4.1.4) to allow for more efficient data selection, enabling an almost background-free analysis. A new detector-position offset correction technique was implemented and demonstrated (Section 4.1.3), further optimizing the spatial resolution of the experiment.

To obtain a more robust understanding of the target properties, an RBS measurement was performed at the *RUBION* facility, which, alongside consistency measurements of the used alpha source, confirmed the target parameters and increased the reliability of the detectors' energy calibrations, which are based on the alpha source and target properties. New tools were developed to accelerate the analysis process, with the time from acquisition to center-of-mass frame analysis for future experiments reduced from multiple full days to less than three hours. A new pixel calibration code was built, which was further improved upon by Alessandro Salice. The decay simulation code was also enhanced, to support the work of Timo Biesenbach, and ensure a highly accurate modeling of the particle-decay process.

The branching ratio calculation code, used in the analysis, as discussed in chapter 6, was also newly developed, providing a systematic method to determine the probabilities of various particle-decay channels. Finally, new consistency checks were established to ensure data quality, thereby increasing the reliability of the experimental outcomes.

The new analysis codes and hardware improvements provide a solid foundation for the

next experiments performed with the LYCCA setup. The high angular resolution and good solid angle coverage of approximately π sr in the current configuration offer unique opportunities for particle-decay studies. These developments not only enhance the experimental capabilities of the LYCCA array but also open new avenues for the study of excited nuclear states and their decay pathways.
The obtained results agree with the contemporary picture that the Hoyle state decays overwhelmingly via the sequential $^{8}\mathrm{Be}_{\mathrm{g.s.}} + \alpha$ path: recent dedicated searches report no positive signal for a direct 3α branch and set experimental upper limits at the $\mathcal{O}(10^{-4})$ level [59, 69]. Semiclassical considerations linked to the 2^+ excitation suggest that any direct component is likely below present sensitivity (i.e. $\lesssim 10^{-5}$) [67]. For the competing radiative de-excitation channel, recent measurements place the branching ratio around a few times 10^{-4} [28]. The upper limits established in this work for direct particle-decay modes are of a similar order of magnitude.

Ongoing and future improvements

The shown analyses of the decay behavior of the Hoyle state and the excited 3^- state in ^{12}C (the latter provided in the Appendix B.1) states was a first step in the analysis of the structure and decay behavior of ^{12}C using the LYCCA setup. The results of the analysis show that the setup is capable of measuring the decay behavior of excited states in ^{12}C with good precision. During the analysis, several possible improvements and optimizations were identified that are currently being implemented. The following sections will discuss these improvements and provide an outlook on future analyses.

Completed detector setup

The current measurement was performed using 18 DSSSD modules. While all 24 detectors of the full LYCCA setup are installed, six DAQ FEE modules are currently in the process of being repaired. Once the full setup is operational, the angular coverage will be increased, which will significantly improve the detection efficiency of high-multiplicity events. As a high-multiplicity event consists of multiple individual detections with a given detection probability, increasing this probability has an amplified effect on the total detection probability. Simulation studies suggest that improving the detector coverage by 30 % and lowering the detection thresholds is expected to increase the detection probability of high-multiplicity events by a factor of up to 3.

Positional improvements

While the LYCCA setup was originally planned for use at FAIR, the requirements for angular precision and resolution for a complete-kinematics measurement such as the one presented in this thesis are substantially higher, especially for the detector position along the beam axis. A more sophisticated analysis approach to compensate for position deviations is currently under development and shows promising results. The approach is energy-invariant as it uses the intersection points of different kinematic lines of alpha particles in the energy-θ plane. This approach then provides a fixed θ-position for each intersection, which can be used to develop the 2D beam-tracking employed in the analysis to a full 3D tracking approach. This would allow for a more precise determination of the decay vertex and the beam momentum vector. This can be seen in Figure 6.14, where a systematic sinusoidal deviation of the intersection points is visible, hinting at a beam-axis deflection of 0.5° in the laboratory frame.

The automatic fitting of the intersection points has already been implemented and

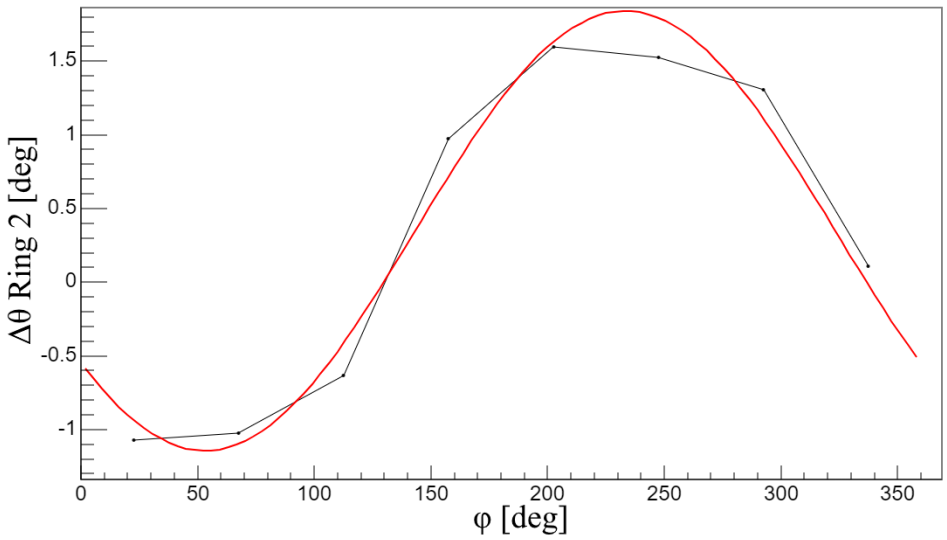

Figure 6.14: Detection position deflection on detectors in ring 2. Figure provided by Alessandro Salice [100].

tested by Alessandro Salice, and the integration into the analysis is currently in progress. The most likely cause for energy deviations lies in the rotation of the beam axis, which shifts the kinematic lines required for the energy calibration. This introduces a dependency of the energies on the beam axis. This could also explain the deviations of the gold calibration, mentioned in Section 3.4.2. Correcting the energy shifts is also expected to compensate the energy offset of the energy sum in the laboratory and center-of-mass frames, which in turn would allow for the application of kinematic fitting. Kinematic fitting is a powerful tool to improve the precision of the analysis by taking into account the kinematic constraints of the decay process and varying the individual parameters within their uncertainties. During this thesis a kinematic fitting approach was developed

and tested, but due to the energy offset, the results could not be integrated into the final analysis, as was discussed in Section 4.4.1.

Improved branching ratio calculation

The technique used to obtain branching ratios from the measured and simulated spectra itself offers several possibilities for improvement: A better approximation of the systematic errors can be obtained and incorporated into the Monte-Carlo simulation. Since the branching ratio calculation technique was found to be sensitive to the energy resolution, a mapping of the simulation energy resolution to the experimental data resolution for each run could be performed.
Additionally, the use of a more refined, unified confidence belt metric as proposed by [118] could be employed to obtain more robust confidence intervals for the branching ratios where upper limits are concerned. Additionally, a Bayesian approach could be used to further refine the confidence intervals.

Machine learning for event classification

The current analysis approach uses a two-component fit onto a 1D projection to identify the fraction of direct decay events in relation to the amount of sequential decays. As some direct decay modes have more degrees of freedom, this approach does not utilize the full information contained in the data. A machine learning approach could be used to classify the events into different decay modes, which would allow for a more detailed analysis of the decay process. This was previously introduced in the Section 4.4.2. A test of machine learning algorithms for event classification of the particle decays of the 3^- state was conducted using the XGBoost algorithm. While the overall accuracy on simulated test data were found to be 99.88 %, the key challenge lies in correctly identifying the rare direct-decay events. This approach demonstrated promising results in classifying the minority decay modes, establishing its general feasibility. The performance, particularly for the rare direct decays, is expected to improve further as more simulated training data becomes available to better train the model on this imbalanced dataset. The technique consists of a two-step approach: first, the model is trained on simulated data, and then the model is applied to the experimental data. The training code has been implemented and tested for the 3^- state and will next be applied to the Hoyle state data, and the integration of the classifier that tags the experimental data using the trained model into the data processing pipeline is currently in progress.

A Appendix A

A.1 Target analysis using Rutherford backscattering

The Rutherford Backscattering Spectrometry (RBS) technique is an ion beam based analysis approach used to determine elemental composition and depth profiles of materials. The method involves directing an ion beam, typically composed of alpha particles, onto a target material. The backscattering of these ions, which occurs due to elastic collisions with the nuclei of the target atoms, results in backscattered ions whose energy is indicative of the mass and depth of the scattering atoms due to the kinematics of the collision and the energy loss of the ions as they penetrate the target material [119]. A schematic overview and an example spectrum are shown in Figure A.1.

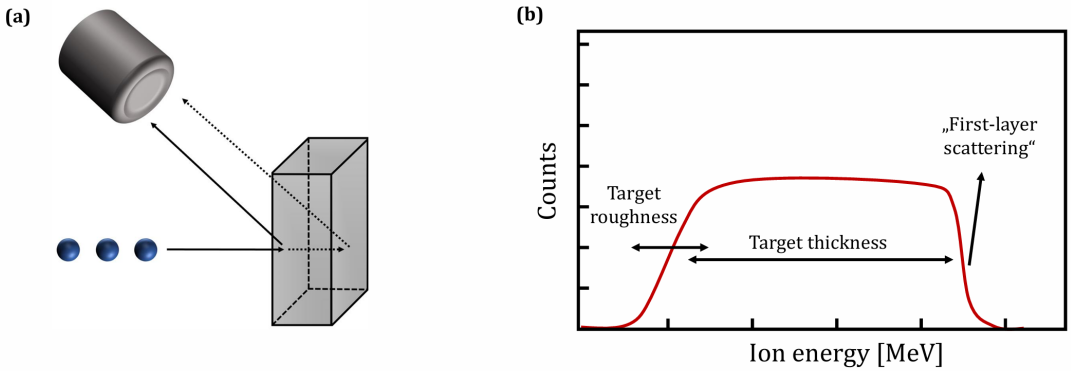

Figure A.1: (a) Schematic of the Rutherford backscattering method, showing the incident ion beam and the backscattered ions registered in the detector. (b) Example energy spectrum of backscattered ions, showing the energy of the ions as they scatter on the target material. Taken from [17].

In the performed RBS analysis, energy spectra were taken at RUBION [91] using 2 MeV alpha particles measured with a silicon detector at a scattering angle of 159.3° with respect to the incident beam direction. The obtained spectra were compared to simulated spectra using the SIMNRA software package [120]. Generally, RBS provides high resolution for surface and near-surface analysis, making it suitable for studying thin films, such as the target foil employed during the experiments discussed in this thesis. The experimental spectrum, as well as the simulated spectrum, are shown in Figure A.2 displaying

the energies of the alpha particles scattered on the ions in the target and the substrate below it. The data were calibrated using backscattering on four different reference foils, consisting of ^{27}Al, ^{12}C, ^{180}Ta, and ^{120}Sn, respectively The shown data corresponds to

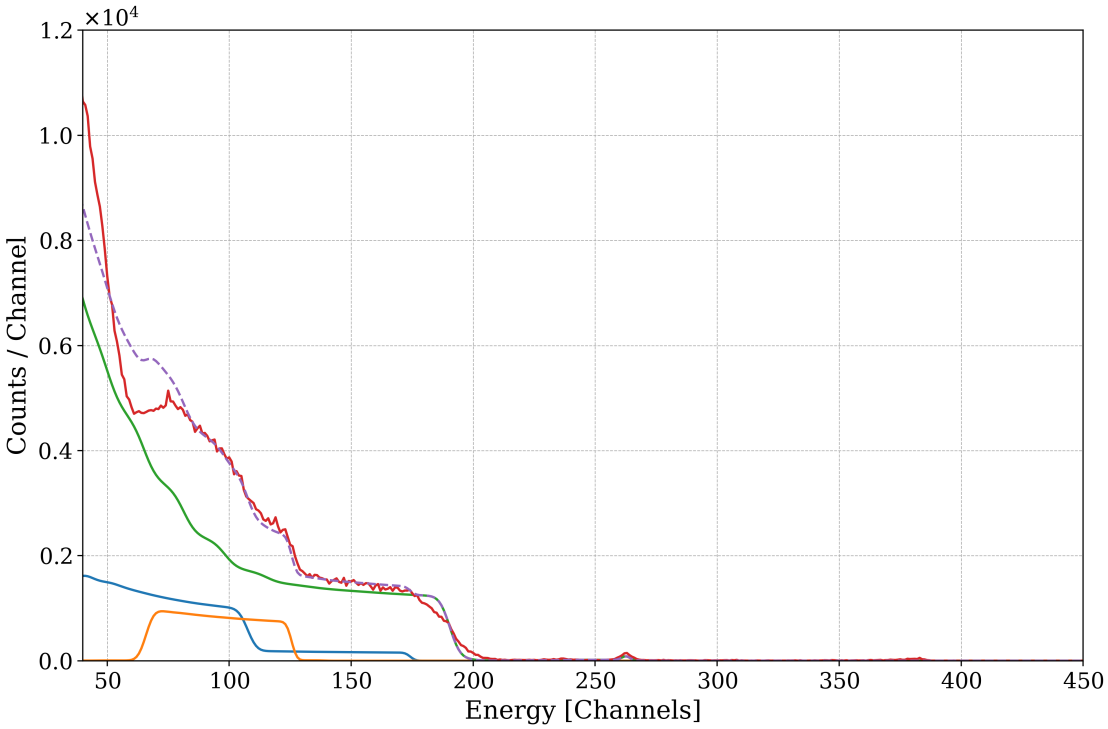

Figure A.2: Rutherford backscattering spectrum of the target. The target is a carbon foil of 0.1155(58) $\frac{\text{mg}}{\text{cm}^2}$ thickness. The blue line shows the obtained experimental spectrum, while the orange dashed linie denotes the simulated spectrum. The violet line corresponds to the silicon substrate the target is mounted on, the green line below to the simulated contribution of oxygen in the silicon substrate. The contribution of the carbon in the target is shown in red.

a target thickness of $5.8 \times 10^1 8$ carbon atoms per square centimeter, corresponding to a mass area density of 0.1155(58) $\frac{\text{mg}}{\text{cm}^2}$, which is within 1.4 % of the value obtained by weighing the target foil. Still, the simulated RBS spectrum shows a deviation from the measured spectrum towards lower energies, due to surface impurities in the target and a silicon-substrate onto which the target is placed during the measurement to stop the beam at the RUBION facility. Since this only impacts the surface layer of the target, it falls estimated 5 % uncertainty of RBS measurements like these[17]. Main contributions to deviations between the measured and simulated spectra are caused by the presence of the silicon and silicon oxide of the substrate below the target. Since the exact deposition depth of the oxygen in the silicon substrate is unknown, the simulated spectrum peaks are slightly shifted and excess counts are observed at lower energies. Since the target thickness only depends on the positions of the edges of the peaks, this effect can be neglected for the determination of the target thickness within the given uncertainty.

A.2 Reconstruction of incomplete events

Using the reconstructed alpha particle from the Hoyle state decay, the Dalitz plot of the four detected alpha particles can be reconstructed. This is shown in Figure A.3.

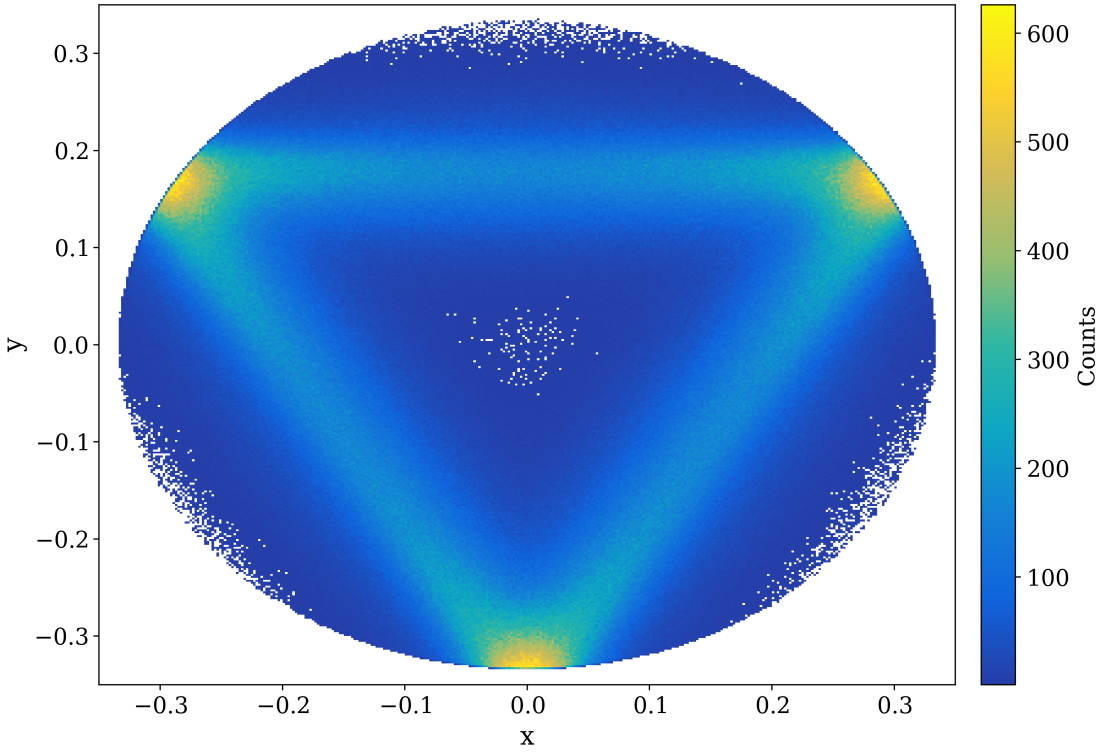

Figure A.3: Dalitz plot for events with three detected alpha particles and one reconstructed alpha particle. One of the reconstructed alpha particles is a fragment of the ^{12}C nucleus Despite the broader distribution the triangle shape is still visible.

The obtained statistics for the reconstructed events are summarized in Table A.1. They show a significant increase in the number of events compared to events with a multiplicity of four, containing 8.2 times more events. This suggests that the current gaps between the rings and the efficiency of the event combination stage offer potential for future improvements.

Table A.1: Total Hoyle state decay events after the final gate for multiplicity-3 events using reconstruction of the missing decay alpha.

Dataset	Remaining decay events
December 2019	3.63×10^6
January 2020	3.86×10^6
Total	7.49×10^6

A.3 Detector leakage current measurement

During the data acquisition, the leakage current of the detectors was monitored per MHV distribution unit with data taken every hour. Most detectors are read out individually, but since fewer MHV units are available than detectors, some detectors are supplied in groups of two. The following Figure, A.4, shows the examplary leakage current of four MHV units over the course of the first experiment in December 2019. Detector group **A** is at a lower scattering angle, causing a significantly stronger increase in the leakage current.

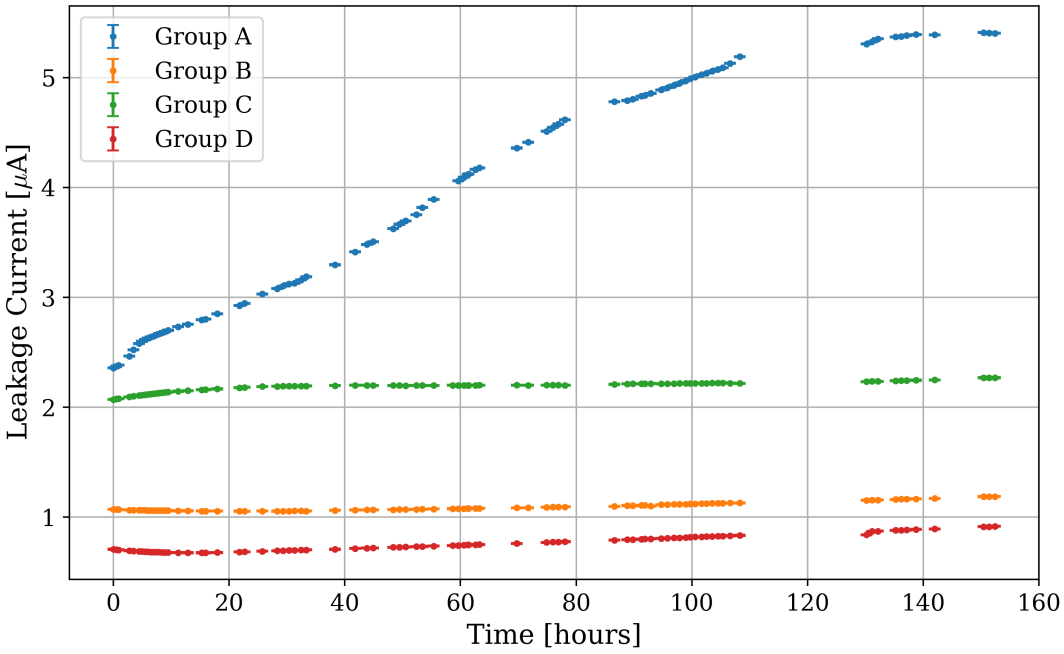

Figure A.4: Leakage current of four detector groups for the first experiment in December 2019. The detectors are grouped in pairs, with the detectors in group A being at the lowest scattering angle.

A.4 Dalitz Derivation

Consider three particles with normalized energies $\epsilon_i = \frac{e_i}{Q}$, where $\sum_{i=1}^{3} \epsilon_i = 1$ with Q being the total energy. The Dalitz plot coordinates are:

$$X = \frac{1}{\sqrt{3}}(\epsilon_2 - \epsilon_1), \tag{A.1}$$

$$Y = \frac{1}{3}(2\epsilon_3 - \epsilon_2 - \epsilon_1). \tag{A.2}$$

Energy Conservation (Triangle)

Energy conservation implies:

$$\epsilon_1 + \epsilon_2 + \epsilon_3 = 1, \tag{A.3}$$

which can be rewritten as:

$$\epsilon_3 = 1 - \epsilon_1 - \epsilon_2. \tag{A.4}$$

Each ϵ_i fulfills the following constraints:

$$0 \leq \epsilon_i \leq 1. \tag{A.5}$$

To express a limiting range on X for a given Y, the formula

$$Y = \frac{1}{3}(2\epsilon_3 - \epsilon_2 - \epsilon_1), \tag{A.6}$$

can be changed to only depend on ϵ_3 by adding $(0 = \epsilon_1 + \epsilon_2 + \epsilon_3 - 1)$:

$$Y = \epsilon_3 - \frac{1}{3}, \tag{A.7}$$

$$\epsilon_3 = Y + \frac{1}{3}. \tag{A.8}$$

Putting in the constraints for ϵ_3 sets a range on Y:

$$-\frac{1}{3} \leq Y \leq \frac{2}{3}. \tag{A.9}$$

For a fixed Y (and thus ϵ_3), ϵ_1 is also limited:

$$\epsilon_1 + \epsilon_2 = 1 - \epsilon_3, \tag{A.10}$$

$$\epsilon_2 = 1 - \epsilon_3 - \epsilon_1. \tag{A.11}$$

Using these relationships, X can be expressed in terms of ϵ_1 and Y:

$$X = \frac{1}{\sqrt{3}}(\epsilon_2 - \epsilon_1) \tag{A.12}$$

$$= \frac{1}{\sqrt{3}}\left(1 - \epsilon_3 - 2\epsilon_1\right) \tag{A.13}$$

$$= \frac{1}{\sqrt{3}}\left(1 - Y - \frac{1}{3} - 2\epsilon_1\right) \tag{A.14}$$

$$= \frac{1}{\sqrt{3}}\left(\frac{2}{3} - Y - 2\epsilon_1\right). \tag{A.15}$$

Since ϵ_1 ranges from 0 to $1 - \epsilon_3 = \frac{2}{3} - Y$, X is limited by:

$$\frac{1}{\sqrt{3}}\left(\frac{2}{3} - Y - 2 \cdot (\frac{2}{3} - Y)\right) \leq X \leq \frac{1}{\sqrt{3}}\left(\frac{2}{3} - Y - 2 \cdot (0)\right), \tag{A.16}$$

$$-\frac{1}{\sqrt{3}}\left(\frac{2}{3} - Y\right) \leq X \leq \frac{1}{\sqrt{3}}\left(\frac{2}{3} - Y\right). \tag{A.17}$$

This forms a triangular plane constrained by $X \in \left(-\frac{1}{\sqrt{3}}, \frac{1}{\sqrt{3}}\right)$, and $Y \in \left(-\frac{1}{3}, \frac{2}{3}\right)$ with linear boundaries. The vertices of the resulting triangle are:

$$A = (0, \frac{2}{3}), \tag{A.18}$$

$$B = (-\frac{1}{\sqrt{3}}, -\frac{1}{3}), \tag{A.19}$$

$$C = (\frac{1}{\sqrt{3}}, -\frac{1}{3}). \tag{A.20}$$

Another useful approach to show this property is the use of Viviani's theorem, named after the Italian mathematician Vincenzo Viviani. It states that the sum of the perpendicular distances from any interior point to the sides of an equilateral triangle is constant and the same as the height of the triangle. For the given triangle, this sum is always 1, matching the height of the triangle with side length 1, confirming the triangular constraint.

A.5 Energy range of direct decay alpha particles

In the center-of-mass frame, the total momentum sum of the three particles must be zero:

$$\mathbf{p}_1 + \mathbf{p}_2 + \mathbf{p}_3 = 0. \tag{A.21}$$

Consider the scenario where one particle, has maximum possible energy. In this case, the other two particles (particles 2 and 3) must have momenta that exactly cancel the momentum of particle 1. Their momenta are each comprised of a component parallel to particle 1's momentum and a component perpendicular to it. As the perpendicular components do not contribute to the compensation of particle 1's momentum and the momentum is given by the square sum of the components

$$p = \sqrt{p_{\parallel}^2 + p_{\perp}^2}, \tag{A.22}$$

the maximum parallel momentum is achieved when the perpendicular components are zero. This reduces the problem to one dimension, where the parallel components of particles 2 and 3 must sum to the negative of the parallel component of particle 1. For

a fixed energy of particle 1, on gets the following constraints

$$\epsilon_{23} = \epsilon_2 + \epsilon_3, \tag{A.23}$$

$$p_{23} = p_2 + p_3 \qquad = n(\sqrt{\epsilon_2} + \sqrt{\epsilon_3}), \tag{A.24}$$

with n being a constant containing mass and the $\frac{1}{2}$ term.

The equation (A.24) can be expressed dependent on the energy of particle 3

$$p_{23} = n(\sqrt{\epsilon_{23} - \epsilon_3}). \tag{A.25}$$

This equation can be solved for its maximum value by taking the derivative with respect to ϵ_3 and setting it to zero

$$\frac{d}{d\epsilon_3} p_{23} = n\left(\frac{1}{2}\right)(\epsilon_{23} - \epsilon_3)^{-\frac{1}{2}} = 0, \tag{A.26}$$

$$(\epsilon_{23} - \epsilon_3)^{-\frac{1}{2}} = 0, \tag{A.27}$$

$$\epsilon_{23} - \epsilon_3 = 0, \tag{A.28}$$

$$\epsilon_{23} = \epsilon_3. \tag{A.29}$$

Validating that this is a maximum, the second derivative is calculated

$$\frac{d^2}{d\epsilon_3^2} p_{23} = -n\left(\frac{1}{2}\right)(\epsilon_{23} - \epsilon_3)^{-\frac{3}{2}} < 0. \tag{A.30}$$

This shows that the maximum momentum of particles 2 and 3 is achieved when their relative energies - and subsequently their absolute energies are equal.

This result provides two limiting cases on ϵ_1: If ϵ_1 is zero, then $\epsilon_2 = \epsilon_3$, resulting in the DDL decay configuration. The maximum for ϵ_1 is achieved by computing the momenta

$$p_1 = p_2 + p_3, \tag{A.31}$$

$$p_1 = 2p_2. \tag{A.32}$$

$$\tag{A.33}$$

which can be expressed in terms of velocities (using $p = mv$):

$$v_1 = 2v_2. \tag{A.34}$$

The energies

$$\epsilon_1 = 1 - \epsilon_2 - \epsilon_3, \tag{A.35}$$

$$\epsilon_1 = 1 - 2\epsilon_2. \tag{A.36}$$

can be expressed in terms of velocities using

$$\epsilon_i = \frac{E_i}{Q} = \frac{m v_i^2}{2Q}, \tag{A.37}$$

which, using (A.36), results in

$$\frac{m v_1^2}{2Q} = 1 - 2\frac{m v_2^2}{2Q}, \tag{A.38}$$

$$v_1^2 = \frac{2Q}{m} - 2v_2^2. \tag{A.39}$$

Combining this with (A.34) yields

$$v_1^2 = \frac{2Q}{m} - 2\left(\frac{1}{2}v_1\right)^2, \tag{A.40}$$

$$v_1^2 = \frac{2Q}{m} - \frac{1}{2}v_1^2, \tag{A.41}$$

$$v_1^2 = \frac{4Q}{3m}. \tag{A.42}$$

$$\tag{A.43}$$

This gives the upper limit for the energy of particle 1 as

$$\epsilon_1 = \frac{m v_1^2}{2Q}, \tag{A.44}$$

$$\epsilon_1 = \frac{m}{2Q}\frac{4Q}{3m}, \tag{A.45}$$

$$\epsilon_1 = \frac{2}{3}. \tag{A.46}$$

A.6 Dalitz Plot Sequential Component Position Derivation

To compute the expected peak position of the sequential decay component in the Y-projection of the folded Dalitz plot, the energies of the decay particles must be computed, as it is formed by the energies of the initially emitted alpha particles in the

$$^{12}\mathrm{C}^* \rightarrow \alpha + ^{8}\mathrm{Be} \tag{A.47}$$

process. As both decay steps of the sequential decay are 2-body processes, the kinetic energy partitioning is fixed by energy and momentum conservation.
The Q-value for the first decay channel ($^{12}\mathrm{C}^* \rightarrow {}^{8}\mathrm{Be} + \alpha$) and the total decay Q-value

($^{12}C^* \rightarrow 3\alpha$) can be computed using

$$\begin{aligned} Q_{\text{first}} &= m_{^{12}C^*} - (m_\alpha + m_{^8\text{Be}}), \\ Q_{\text{total}} &= m_{^{12}C^*} - 3 \times m_\alpha. \end{aligned} \tag{A.48}$$

The kinetic energy of the alpha particle in the first decay, E_3, is calculated using the mass ratio of the products

$$E_3 = Q_{\text{first}} \times \left(\frac{1}{1 + \frac{m_\alpha}{m_{^8\text{Be}}}} \right). \tag{A.49}$$

The relative energies are obtained by

$$\epsilon_3 = \frac{E_3}{Q_{\text{total}}}, \tag{A.50}$$

with the resulting values in the folded Dalitz plot given by

$$Y = \epsilon_3 - \frac{1}{3}. \tag{A.51}$$

The results for the Q-values and the relative kinetic energy of the alpha particle with respect to the total Q-value are given in Table A.2.

Table A.2: Values for the sequential decay component calculation.

State	Q-value first step	Q-value total	E_3	ϵ_3	Y value
Hoyle state	287.5 keV	379.3 keV	191.7 keV	0.50526	0.17193
3- state	2274.4 keV	2366.3 keV	1516.3 keV	0.64080	0.30746

A.7 Software developed for the analysis of the experiment

During the course of the analysis, several software tools were developed to facilitate the analysis of the data as described in chapter 3. The source code for these tools is available on the Institute's GitLab server split into two repositories, one for the analysis and one for the simulation.
The analysis repository, `lycca-analysis`, is available at the following URL:
`https://gitlab.ikp.uni-koeln.de/lycca/lycca-analysis`. It contains the following analysis programs:

- `Converter`: Convert the raw data from the binary format from the DAQ to a more accessible ROOT format.

- `timetest`: Obtain reliable gate widths for the EventBuilder.
- `EventBuilder`: Combine the ADC and discriminator data into strip events.
- `CalibrationStrips`: Generate an initial strip calibration using the triple-alpha source data.
- `CalibrationPixels`: Generate the per-pixel calibration using a combination of the triple-alpha source and kinematic line data.
- `CombineStrips`: Combine the strip data into pixel data.
- `AnalysisGateKinematics2`: Apply the final gate conditions to the combined pixel data and calculate the kinematics of the events in the laboratory and center-of-mass frame and generate Dalitz plots.
- `AnalysisGateClassifier`: Classify the events into different categories using the XGBoost machine learning algorithm.
- `DetPos`: Calculate the position of the detectors in the laboratory frame.
- `HistoAdd`: More efficiently add up histograms.

It also contains a library of header files containing utility functions required by the LYCCA analysis programs.
In addition, the repository contains a selection of tools:

- `AnalysisDiagnostics`: Generate diagnostic plots to compare different analysis runs.
- `CompareCalibration`: Compare different generated calibrations.
- `CurveFitETht`: Obtain an energy-θ curve for a scattering reaction of interest, using data obtained from LISE++.
- `Prettify`: Automatically extract plots from ROOT files and rebuild them more consistently.

The simulation repository, `lycca-simulation2`, is available at the following URL: `https://gitlab.ikp.uni-koeln.de/lycca/lycca-simulation2` and contains different revisions of the simulation code used to generate the Monte Carlo data used in the analysis.
All provided programs and scripts are written in C++, python, bash and a few newer programs in Julia. The programs are designed to be run on the Linux operating system and can be accessed by members of the Institute for Nuclear Physics at the University of Cologne.

B Appendix B

B.1 3^- state branching ratio results

To analyze the next higher lying state in ^{12}C, namely the 3^- state at 9.64 MeV, the same technique as for the Hoyle state was applied. The results are summarized in the following sections. As previously discussed in Section 4.3, a large amount of data were collected for the decay of the 3^- state and analyzed in the same way as the Hoyle state decay data. The obtained statistics for the 3^- state decay are significantly higher than for the Hoyle state decay ($2.65 \cdot 10^6$ events for the 3^- state compared to $5.84 \cdot 10^5$ events for the Hoyle state, after all cuts and using the veto-energy for same-detector events). Also, the higher energy in the center-of-mass system of the 3^- state of 2.37 MeV compared to the Hoyle state's 0.38 MeV results in a better relative energy resolution. As seen during analysis chapter 4.3, the 3^- state was found to have a substantially higher direct decay probability than the Hoyle state, which can be seen in the comparison of the Dalitz plots in Figures 4.28 and 4.29. Another prominent feature is the existence of depletion regions in the Dalitz plot, which are suppressed by angular momentum effects [121]. The Y-projection of the Dalitz plots of the 3^- state decay clearly shows the low-energy continuum, which is a result of the direct decay of the 3^- state.
The obtained branching ratios are summarized in tables B.1, B.2, and B.3. Since no events for the DLL mode were simulated, as it is expected to be suppressed by the angular momentum depletion, no branching ratio could be determined for this mode. The resulting branching ratios for the December and January measurements are not in agreement within 3σ confidence intervals. This is likely due to an underlying systematic component that was not fully accounted for in the analysis, as the current confidence intervals are only based on the statistical uncertainties of the fit. Further information on the systematic uncertainties are provided in Section 6.3.
The study of the 3^- state and the study of the direct particle decay of higher lying states in ^{12}C, such as the 1^- state, will be further expanded upon in the master's thesis of Joe Roob.

B.1.1 DDϕ branching ratio

The DDϕ decay mode of the 3^- state, where the only limitation on the energy distribution of the alpha particles are energy and momentum conservation, was analyzed in the same way as the DDϕ decay mode of the Hoyle state. The results of the fits are shown in Figures B.1a and B.2a. The likelihood curves with confidence intervals are shown in Figures B.1b and B.2b. The results of the branching ratios are summarized in Table B.1. The results of the December and January measurements are not in agreement within 3σ confidence intervals, which is likely due to an underlying systematic component that was not accounted for in the analysis. The results deviate by 11.6 % between the two measurements, but the statistical confidence intervals (relative uncertainties between 1.33 % and 1.64 %) are very narrow compared to the deviation. The planned inclusion of systematic uncertainties will increase the confidence interval width, which will likely lead to an agreement between the two measurements.

Another very important aspect is, that during the data preparation, the analysis of the Hoyle state was the priority, and the detector configuration was optimized to ensure that the resolution of the Hoyle-state decay events was as high as possible. Given the energy offsets, discussed in Section 4.1.4, the optimum configuration providing the best resolution at the Hoyle-state energy did not necessarily provide the best resolution for the 3^- state decay events. For consistency reasons, the same detector configuration and dead-layer thicknesses were used for the 3^- state analysis as for the Hoyle state analysis. A more detailed analysis of the systematic uncertainties will be performed in the future to investigate the discrepancy between the two measurements.

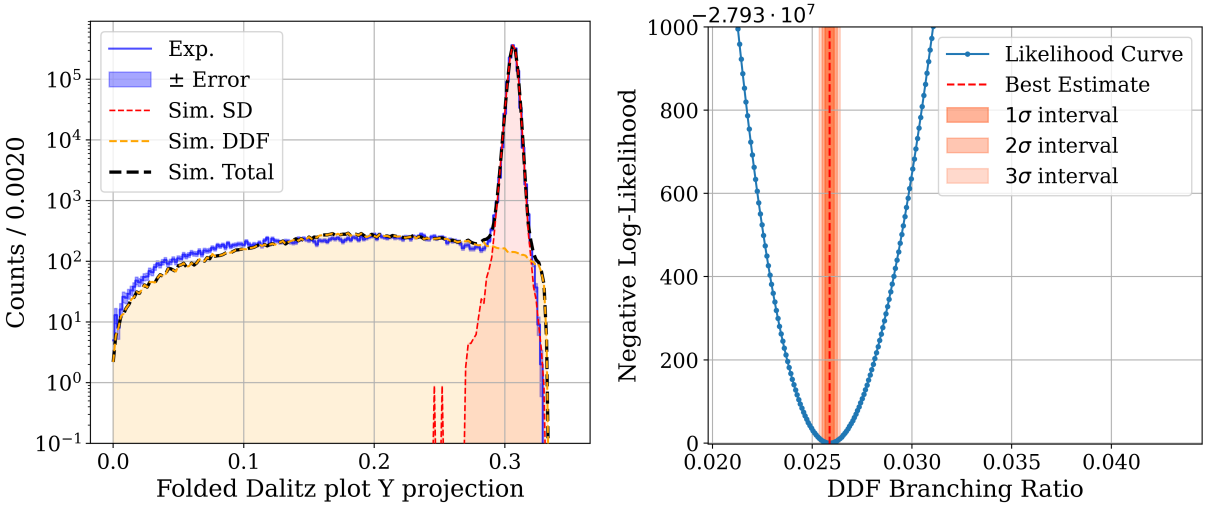

(a) Fit of the simulated sequential and DDϕ decay mode data to the experimental data of the 2019 experiment.

(b) Likelihood curve with confidence intervals for the DDϕ decay mode of the 3^- state for the December 2019 data.

Figure B.1: Fit of the DDϕ mode of the 3^- state for the December 2019 data.

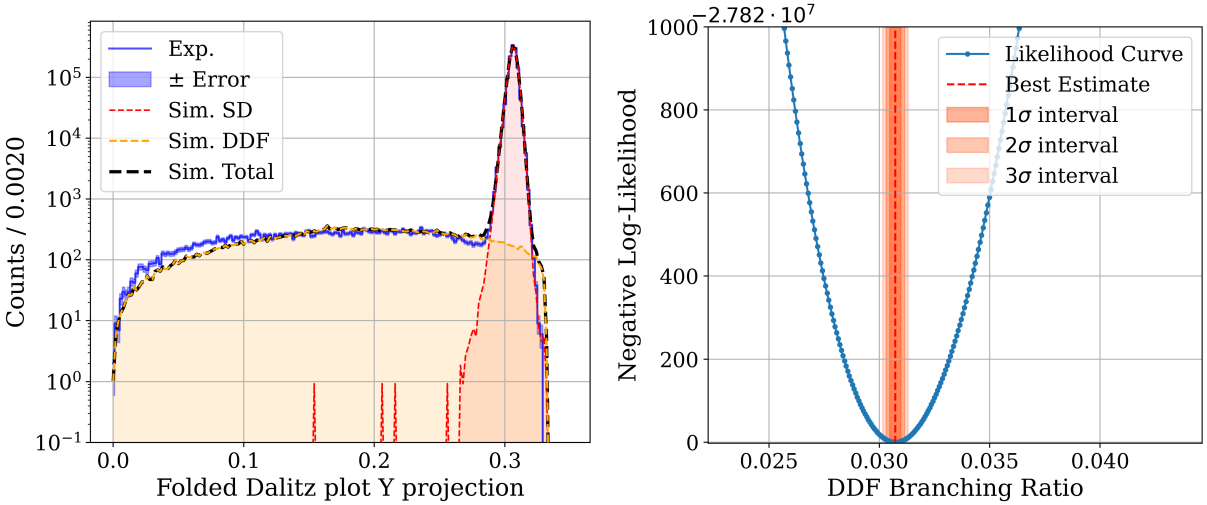

(a) Fit of the simulated sequential and DDϕ decay mode data to the experimental data of the 2020 experiment.

(b) Likelihood curve with confidence intervals for the DDϕ decay mode of the 3^- state for the January 2020 data.

Figure B.2: Fit of the DDϕ mode of the 3^- state for the January 2020 data.

Table B.1: Upper and lower limits of the branching ratio of the $DD\phi$ three-alpha decay mode of the 3^- state for different confidence levels for 92 % (2019) and 95 % of the data of the December and January measurements.

Experiment	DDϕ Branching ratio Lower limit	Upper Limit	Confidence level
December 2019	2.577×10^{-2}		Best fit
	2.566×10^{-2}	2.608×10^{-2}	1 σ (68.3 %)
	2.550×10^{-2}	2.625×10^{-2}	2 σ (95.4 %)
	2.534×10^{-2}	2.640×10^{-2}	3 σ (99.7 %)
January 2020	2.876×10^{-2}		Best fit
	2.817×10^{-2}	2.925×10^{-2}	1 σ (68.3 %)
	2.781×10^{-2}	2.960×10^{-2}	2 σ (95.4 %)
	2.748×10^{-2}	2.996×10^{-2}	3 σ (99.7 %)

B.1.2 DDP decay mode

The DDP mode of the 3^- state was analyzed in the same way as the DDP mode of the Hoyle state: A WKB-approximation based density matrix was used to obtain a distribution of relative energies for the DDP decay mode. As can be seen in the fits in Figures B.3a and B.4a, the model is unable to reproduce the amount of higher relative energy events of the direct decay component visible in the experimental data. Due to the shifted centroid of the distribution compared to the DDϕ distribution, the results are still close to the values obtained for the $DD\phi$ decay mode in the corresponding measurement and in agreement within 2σ confidence intervals with them. Like the DDϕ branching ratio results, they are not in agreement with each other and exhibit a similar shift towards larger branching ratios in the January dataset, which is likely due to the same systematic reason as for the DDϕ decay mode.

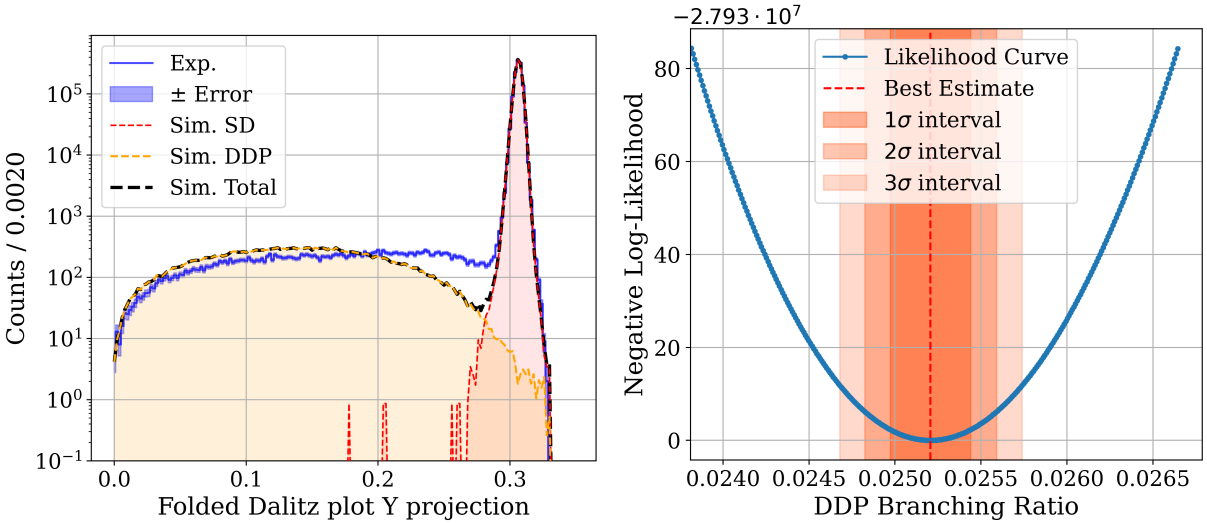

(a) Fit of the simulated sequential and DDP decay mode data to the experimental data of the 2019 experiment.

(b) Likelihood curve with confidence intervals for the DDP decay mode of the 3^- state for the December 2019 data.

Figure B.3: Fit of the DDP mode of the 3^- state for the December 2019 data.

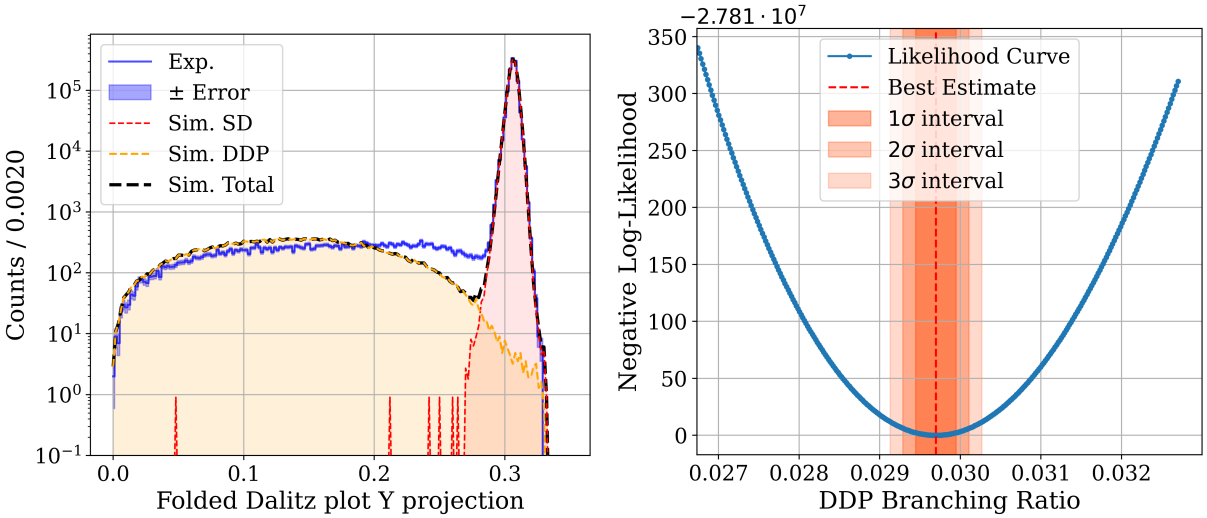

(a) Fit of the simulated sequential and DDP decay mode data to the experimental data of the 2020 experiment.

(b) Likelihood curve with confidence intervals for the DDP decay mode of the 3^- state for the January 2020 data.

Figure B.4: Fit of the DDP mode of the 3^- state for the January 2020 data.

Table B.2: Upper and lower limits of the branching ratio of the DDP three-alpha decay mode of the 3^- state for different confidence levels for 92 % (2019) and 95 % of the data of the December and January measurements.

Experiment	DDP Branching ratio Lower limit	Upper Limit	Confidence level
December 2019	2.521×10^{-2}		Best fit
	2.497×10^{-2}	2.544×10^{-2}	1 σ (68.3 %)
	2.482×10^{-2}	2.559×10^{-2}	2 σ (95.4 %)
	2.468×10^{-2}	2.574×10^{-2}	3 σ (99.7 %)
January 2020	2.970×10^{-2}		Best fit
	2.945×10^{-2}	2.994×10^{-2}	1 σ (68.3 %)
	2.929×10^{-2}	3.011×10^{-2}	2 σ (95.4 %)
	2.913×10^{-2}	3.027×10^{-2}	3 σ (99.7 %)

B.1.3 DDE branching ratio

Analogous to the DDE decay model of the Hoyle state a separation between the sequential and DDE decay components can be seen, which does not match the continuous experimental energy distribution, as can be seen in the fits in Figures B.5a and B.6a. The resulting likelihood curves are shown in Figures B.5b and B.6b. The separation between the two distributions is much more pronounced in the 3^- state data, as the direct decay component is much more prominent and the higher absolute decay energy of the state provides a much better resolution of the relative energies resulting in a narrow sequential decay peak in the Y-projection of the Dalitz plot. This suggests that, if the DDE decay mode is present, it must be accompanied by another direct decay mode, as the DDE decay mode alone cannot explain the observed data. The method employed, however, does only support the determination of one direct decay mode at a time, as introduced in Section 6.1. The approach of fitting the direct decay modes separately has also been employed in comparable analyses, such as the work of Smith et al. [59].
The resulting branching ratios obtained in the DDE decay mode study are summarized in Table B.3. As each contribution of other direct decay modes would reduce the branching ratio of the DDE decay mode, the obtained branching ratios can be considered as upper limits for the DDE decay mode. The results obtained in the December and January measurements are not in agreement within 3σ confidence intervals, which is likely due to other direct decay modes superimposed on the experimental spectrum.

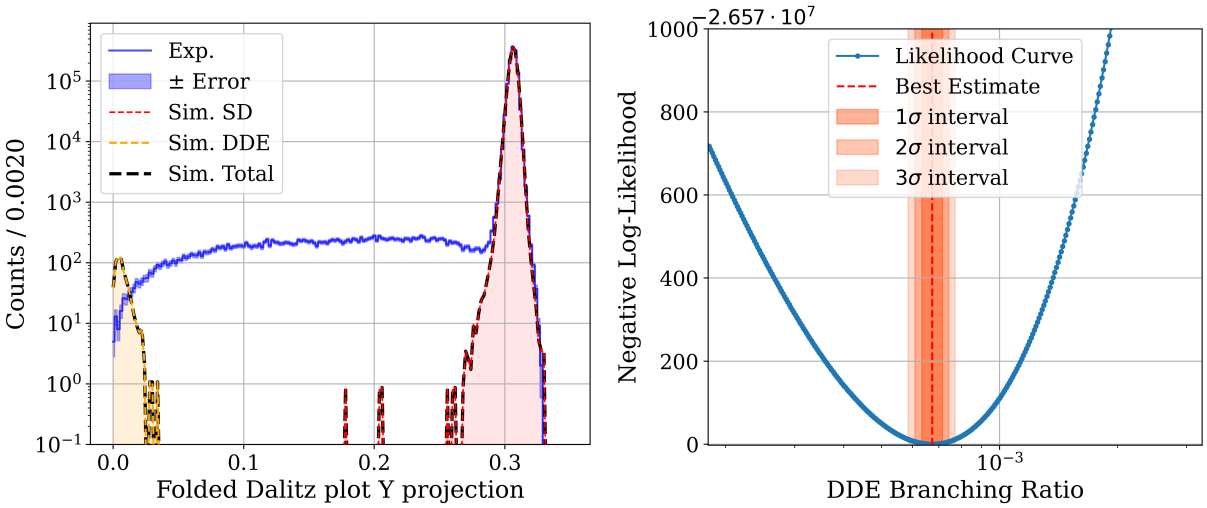

(a) Fit of the simulated sequential and DDE decay mode data to the experimental data of the 2019 experiment.

(b) Likelihood curve with confidence intervals for the DDE decay mode of the 3^- state for the December 2019 data.

Figure B.5: Fit of the DDE mode of the 3^- state for the December 2019 data.

The relative uncertainties of the branching ratios of the 3^- state decay modes are summarized in Table B.4. In comparison to the relative uncertainties of the Hoyle state branching ratios, as shown in Table 6.7, the statistical uncertainties are significantly lower

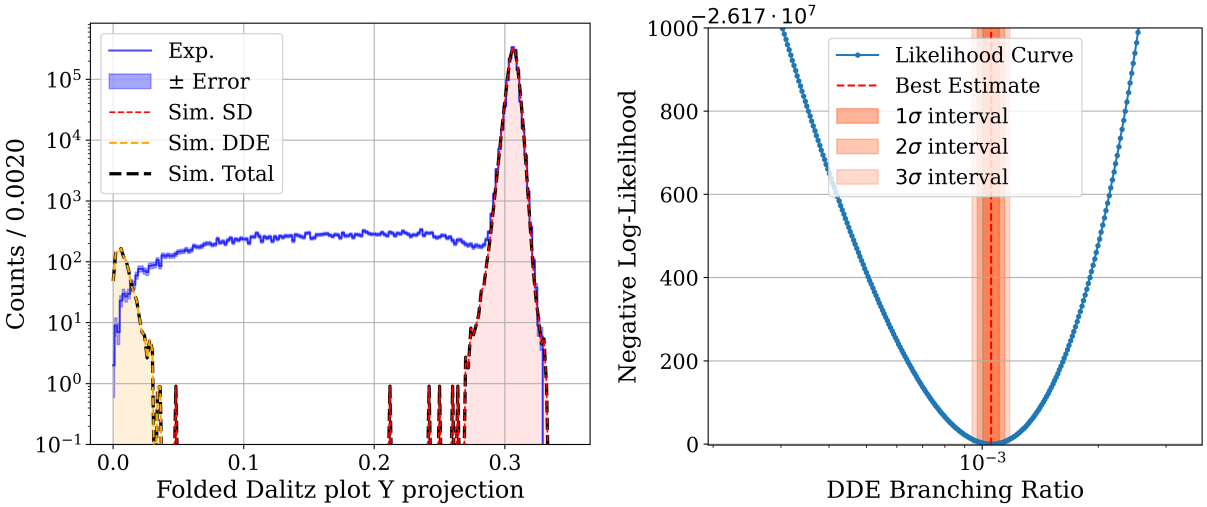

(a) Fit of the simulated sequential and DDE decay mode data to the experimental data of the 2020 experiment.

(b) Likelihood curve with confidence intervals for the DDE decay mode of the 3^- state for the January 2020 data.

Figure B.6: Fit of the DDE mode of the 3^- state for the January 2020 data.

for the 3^- state decay modes. This is due to the higher statistics and better resolution, which allows to resolve the difference between the December and January measurements.

Table B.3: Upper and lower limits of the branching ratio of the DDE three-alpha decay mode of the 3^- state for different confidence levels for 92 % (2019) and 95 % of the data of the December and January measurements.

Experiment	DDE Branching ratio Lower limit	Upper Limit	Confidence level
December 2019	6.736×10^{-4}		Best fit
	6.3352×10^{-4}	7.1543×10^{-4}	1 σ (68.3 %)
	6.0850×10^{-4}	7.4322×10^{-4}	2 σ (95.4 %)
	5.8472×10^{-4}	7.7115×10^{-4}	3 σ (99.7 %)
January 2020	1.059×10^{-3}		Best fit
	1.0043×10^{-3}	1.109×10^{-3}	1 σ (68.3 %)
	9.7209×10^{-4}	1.144×10^{-3}	2 σ (95.4 %)
	9.4131×10^{-4}	1.179×10^{-3}	3 σ (99.7 %)

Table B.4: Relative uncertainties of the branching ratios of the 3^- state decay modes for the 2σ confidence interval.

Decay mode	Relative uncertainty 2019 -	+	Relative uncertainty 2020 -	+
DDϕ	-1.33 %	1.64 %	-1.33 %	1.40 %
DDP	-1.52 %	1.52 %	-1.39 %	1.37 %
DDE	-9.66 %	10.3 %	-8.23 %	7.97 %

B.1.4 Summary

The branching ratios of the 3^- state of ^{12}C were determined for the DDϕ, DDP, and DDE decay modes and are summarized in Tables B.1, B.2, and B.3, respectively. A summary is provided in Table B.5. The results of the December and January measurements of the DDϕ and DDP decay modes are not in agreement within 3σ confidence intervals of their statistical errors. As systematic errors increase the width of the confidence intervals, this disagreement does not necessarily imply that the results themselves are incompatible. A minor underlying systematic shift that was not accounted for in the analysis, such as a slight beam angle offset between the two measurement campaigns or a minor shift of the wall detectors during the mounting of the protective tantalum apertures, could also be the cause of the discrepancy. To further investigate this, a more detailed analysis of the systematic uncertainties will be performed, but was out of the scope of this work.

Table B.5: Summary of the measured branching ratios for the direct decay modes of the 3^- state in ^{12}C.

Decay mode	Experiment	Branching ratio ($\pm 2\sigma$)	Upper limit ($\pm 2\sigma$)
DDP	2019	$(2.521^{+0.038}_{-0.038}) \cdot 10^{-2}$	$2.559 \cdot 10^{-2}$
	2020	$(2.970^{+0.041}_{-0.041}) \cdot 10^{-2}$	$3.019 \cdot 10^{-2}$
DDϕ	2019	$(2.583^{+0.042}_{-0.034}) \cdot 10^{-2}$	$2.625 \cdot 10^{-2}$
	2020	$(3.072^{+0.043}_{-0.041}) \cdot 10^{-2}$	$3.115 \cdot 10^{-2}$
DDE	2019	$(6.736^{+0.697}_{-0.651}) \cdot 10^{-4}$	$7.432 \cdot 10^{-4}$
	2020	$(1.059^{+0.084}_{-0.087}) \cdot 10^{-3}$	$1.176 \cdot 10^{-3}$

As both decay modes, DDP and DDϕ, describe a relatively similar decay process, given that both can populate the same energy configurations of the three alpha particles, only with different likelihoods, the results could be affected by the same systematic component. While the DDP component underestimates the amount of direct-decay alpha particles with higher relative energies, the DDϕ component overestimates this population. A core issue in the DDP description of the decay is the neglected angular momentum of the 3^- state, which could impact the distribution. The simple uniform distribution of the DDϕ decay mode is, however, also an oversimplification of the Coulomb barrier penetration process. Since the 2σ uncertainty band of the DDP mode is wider than the DDϕ confidence interval, which can be attributed to the larger absolute deviation of the DDP fit from the data, even encompassing the DDϕ uncertainty band, the free direct decay branching ratio is likely to be in the range of the DDϕ decay modes between 2.482×10^{-2} and 3.011×10^{-2}.

The DDE decay mode results are also not in agreement. The best fit of the DDE mode without any other direct decay contribution also insufficiently describes the experimental data. This again confirms the approach to use the direct decay mode results only be as an upper limit. For the DDE decay mode this limit is thus 1.144×10^{-3}.

All these results only contain statistical uncertainties and are, as shown before, affected by systematic deviations, and thus preliminary.

List of Tables

List of Figures

Bibliography

[1] R. H. Cyburt, B. D. Fields, K. A. Olive, and T.-H. Yeh, *Big bang nucleosynthesis: Present status*, Rev. Mod. Phys. **88** (1 2016) 015004 (cit. on p. 10).

[2] R. A. Alpher, H. Bethe, and G. Gamow, *The Origin of Chemical Elements*, Physical Review **73** (1948) 803 (cit. on p. 10).

[3] E. M. Burbidge, G. R. Burbidge, W. A. Fowler, and F. Hoyle, *Synthesis of the Elements in Stars*, Rev. Mod. Phys. **29** (4 1957) 547 (cit. on pp. 10, 11).

[4] C. Iliadis, *Nuclear physics of stars: Second Edition*, 2015. ISBN: 9783527336487 (cit. on pp. 11, 12, 17).

[5] B. W. Carroll and D. A. Ostlie, *An Introduction to Modern Astrophysics*, 2nd ed. Cambridge University Press, 2017 (cit. on p. 11).

[6] B. E. J. Pagel, *Nucleosynthesis and Chemical Evolution of Galaxies*, Cambridge, UK: Cambridge University Press, 1997. ISBN: 978-0521550611 (cit. on p. 11).

[7] D. D. Clayton, *Principles of stellar evolution and nucleosynthesis: with a new preface*, 1983. ISBN: 0-226-10953-4 (paperback), 0-226-10952-6 (hardcover) (cit. on p. 12).

[8] A. Karakas and J. Lattanzio, *The Dawes Review 2: Nucleosynthesis and Stellar Yields of Low- and Intermediate-Mass Single Stars*, Publications of the Astronomical Society of Australia **31** (2014) (cit. on p. 12).

[9] R. Kippenhahn and A. Weigert, *Stellar Structure and Evolution*, 1990 (cit. on pp. 12, 14).

[10] H. Fynbo, C. Diget, U. Bergmann, M. Borge, J. Cederkall, P. Dendooven, L. Fraile, S. Franchoo, V. Fedosseev, B. Fulton, W. Huang, J. Huikari, H. Jeppesen, A. Jokinen, P. Jones, B. Jonson, U. Koster, K. Langanke, M. Meister, T. Nilsson, G. Nyman, Y. Prezado, K. Rilsager, S. Rinta-Antila, O. Tengblad, M. Turrion, Y. Wang, L. Weissman, K. Wilhelmsen, J. Aysto, and ISOLDE Collaboration, *Revised rates for the stellar triple-alpha process from measurement of C-12 nuclear resonances*, Nature **433** (2005) 136. (Cit. on p. 12).

[11] D. Luong, M. Dasgupta, D. Hinde, R. du Rietz, R. Rafiei, C. Lin, M. Evers, and A. Diaz-Torres, *Insights into the mechanisms and time-scales of breakup of 6,7Li*, Physics Letters B **695** (2011) 105. (Cit. on p. 12).

[12] F. Hoyle, *On Nuclear Reactions Occuring in Very Hot STARS.I. the Synthesis of Elements from Carbon to Nickel.* apjs **1** (1954) 121 (cit. on pp. 12, 19).

[13] C. Kobayashi, A. I. Karakas, and M. Lugaro, *The Origin of Elements from Carbon to Uranium*, The Astrophysical Journal **900** (2020) 179 (cit. on p. 13).

[14] O. R. Pols, *Stellar Structure and Evolution*, Fundamentals of Astrophysics (2021) (cit. on p. 15).

[15] U. Greife, C. Arpesella, E. Bellotti, K. Brand, C. Broggini, L. Campajola, P. Corvisiero, A. D'Onofrio, G. Fiorentini, A. Fubini, G. Gervino, L. Gialanella, C. Gustavino, E. Huttel, M. Junker, R. Kavanagh, R. Kubat, J. Lambert, G. Oliviero, P. Prati, H. Rebel, V. Roca, W. Rodney, C. Rolfs, M. Romano, M. Romoli, S. Schmidt, W. Schulte, F. Strieder, F. Terrasi, H. Trautvetter, D. Zahnow, and S. Zavatarelli, *Further direct approaches to the nuclear reactions in the Sun*, Nuclear Physics A **621** (1997). Nuclei in the Cosmos 603. (Cit. on p. 15).

[16] R. Depalo, "New direct measurement of the 6Li(p,γ)7Be cross section at LUNA". *Proceedings, 5th International Solar Neutrino Conference: Dresden, Germany, June 11-14, 2018*. Ed. by M. Meyer and K. Zuber. 2019 pp. 233–237 (cit. on p. 15).

[17] F. Heim, *The Statistical γ Decay Behavior and Nuclear Reaction Rates of Heavy Nuclei Relevant for Explosive Nucleosynthesis*, PhD thesis. Universität zu Köln, 2021 (cit. on pp. 15, 17, 162, 163).

[18] C. E. Rolfs and W. S. Rodney, *Cauldrons in the Cosmos*, The University of Chicago Press, 1988 (cit. on pp. 16, 18).

[19] M. Aliotta, M. Junker, P. Prati, O. Straniero, and F. Strieder, *Helium burning and neutron sources in the stars*, The European Physical Journal A **52** (2016) 76. (Cit. on p. 17).

[20] K. Langanke and M. Wiescher, *Nuclear reactions and stellar processes*, Reports on Progress in Physics **64** (2001) 1657 (cit. on p. 18).

[21] M. Freer and H. Fynbo, *The Hoyle state in 12C*, Progress in Particle and Nuclear Physics **78** (2014) 1. (Cit. on pp. 18, 21).

[22] F. C. Adams and E. Grohs, *Stellar helium burning in other universes: A solution to the triple alpha fine-tuning problem*, Astroparticle Physics **87** (2017) 40. (Cit. on p. 18).

[23] I. J. Iben, *STELLAR EVOLUTION. VII. THE EVOLUTION OF A 2.25 SOLAR MASSES STAR FROM THE MAIN SEQUENCE TO THE HELIUM-BURNING PHASE.* Astrophys. J., 147: 650-63(Feb. 1967). (1967) (cit. on p. 18).

[24] E. E. Salpeter, *Nuclear Reactions in Stars Without Hydrogen*, Astrophysical Journal **115** (1952) 326 (cit. on p. 18).

[25] E. J. Öpik. Proceedings of the Royal Irish Academy **A54** (1951) 49 (cit. on p. 18).

[26] D. N. F. Dunbar, R. E. Pixley, W. A. Wenzel, and W. Whaling, *The 7.68-MeV State in* ^{12}C, Phys. Rev. **92** (3 1953) 649 (cit. on pp. 19, 34).

[27] C. W. Cook, W. A. Fowler, C. C. Lauritsen, and T. Lauritsen, B^{12}, C^{12}, *and the Red Giants*, Phys. Rev. **107** (2 1957) 508 (cit. on pp. 19, 34).

[28] Z. Luo, M. Barbui, J. Bishop, G. Chubarian, V. Z. Goldberg, E. Harris, E. Koshchiy, C. E. Parker, M. Roosa, A. Saastamoinen, D. P. Scriven, and G. V. Rogachev, *Radiative decay branching ratio of the Hoyle state*, Phys. Rev. C **109** (2 2024) 025801 (cit. on pp. 19, 31, 159).

[29] P. Adsley, M. Heine, D. G. Jenkins, S. Courtin, R. Neveling, J. W. Brümmer, L. M. Donaldson, N. Y. Kheswa, K. C. W. Li, D. J. Marín-Lámbarri, P. Z. Mabika, P. Papka, L. Pellegri, V. Pesudo, B. Rebeiro, F. D. Smit, and W. Yahia-Cherif, *Extending the Hoyle-State Paradigm to* ^{12}C $+^{12}$ C *Fusion*, Phys. Rev. Lett. **129** (10 2022) 102701 (cit. on p. 19).

[30] H. Morinaga, *Interpretation of Some of the Excited States of 4n Self-Conjugate Nuclei*, Phys. Rev. **101** (1 1956) 254 (cit. on pp. 19, 26).

[31] Y. Funaki, A. Tohsaki, H. Horiuchi, P. Schuck, and G. Röpke, *Analysis of previous microscopic calculations for the second* 0^+ *state in* ^{12}C *in terms of* $3-\alpha$ *particle Bose-condensed state*, Phys. Rev. C **67** (5 2003) 051306 (cit. on pp. 19, 21, 25).

[32] Y. Funaki, A. Tohsaki, H. Horiuchi, P. Schuck, and G. Röpke, *Inelastic form factors to alpha-particle condensate states in 12C and 16O: What can we learn?*, The European Physical Journal A - Hadrons and Nuclei **28** (2006) 259. (Cit. on pp. 19, 25).

[33] N. B. Nguyen, F. M. Nunes, I. J. Thompson, and E. F. Brown, *Low-Temperature Triple-Alpha Rate in a Full Three-Body Nuclear Model*, Phys. Rev. Lett. **109** (14 2012) 141101 (cit. on p. 19).

[34] C. Angulo, M. Arnould, M. Rayet, P. Descouvemont, D. Baye, C. Leclercq-Willain, A. Coc, S. Barhoumi, P. Aguer, C. Rolfs, R. Kunz, J. W. Hammer, A. Mayer, T. Paradellis, S. Kossionides, C. Chronidou, K. Spyrou, S. degl'Innocenti, G. Fiorentini, B. Ricci, S. Zavatarelli, C. Providencia, H. Wolters, J. Soares, C. Grama, J. Rahighi, A. Shotter, and M. Lamehi Rachti, *A compilation of charged-particle induced thermonuclear reaction rates*, Nuc. Phys. A **656** (1999) 3 (cit. on p. 19).

[35] C. Angulo, M. Arnould, M. Rayet, and et al., *NACRE: Nuclear Astrophysics Compilation of REaction rates*. `http://www.astro.ulb.ac.be/nacre`. Accessed: 2023-07-08. 2023 (cit. on p. 19).

[36] N. B. Nguyen, F. M. Nunes, and I. J. Thompson, *Investigation of the triple-α reaction in a full three-body approach*, Phys. Rev. C **87** (5 2013) 054615 (cit. on p. 19).

[37] E. Garrido, R. de Diego, D. V. Fedorov, and A. S. Jensen, *Direct and sequential radiative three-body reaction rates at low temperatures*, The European Physical Journal A **47** (2011) 102. (Cit. on p. 20).

[38] S. Karataglidis, P. J. Dortmans, K. Amos, and R. de Swiniarski, *Fully microscopic model of 200 MeV proton–^{12}C elastic and inelastic scattering*, Phys. Rev. C **52** (2 1995) 861 (cit. on p. 21).

[39] M. Freer, H. Horiuchi, Y. Kanada-En'yo, D. Lee, and U.-G. Meißner, *Microscopic clustering in light nuclei*, Rev. Mod. Phys. **90** (3 2018) 035004 (cit. on p. 21).

[40] A. Tohsaki, H. Horiuchi, P. Schuck, and G. Röpke, *Alpha Cluster Condensation in ^{12}C and ^{16}O*, Phys. Rev. Lett. **87** (19 2001) 192501 (cit. on pp. 21, 23, 24).

[41] H. Margenau, *Statistics of Excited Energy States of Nuclei*, Phys. Rev. **59** (8 1941) 627 (cit. on p. 21).

[42] D. Brink and E. Boeker, *Effective interactions for Hartree-Fock calculations*, Nuclear Physics A **91** (1967) 1. (Cit. on p. 21).

[43] R. Bijker and F. Iachello, *Cluster states in nuclei as representations of a* $\mathrm{U}(\nu+1)$ *group*, Phys. Rev. C **61** (6 2000) 067305 (cit. on pp. 22, 23, 25).

[44] D. J. Marín-Lámbarri, R. Bijker, M. Freer, M. Gai, T. Kokalova, D. J. Parker, and C. Wheldon, *Evidence for Triangular $\mathcal{D}_{3h}$ Symmetry in* ^{12}C, Phys. Rev. Lett. **113** (1 2014) 012502 (cit. on p. 23).

[45] J. Kelley, J. Purcell, and C. Sheu, *Energy levels of light nuclei A=12*, Nuclear Physics A **968** (2017) 71. (Cit. on pp. 23, 98).

[46] W. von Oertzen, M. Freer, and Y. Kanada-En'yo, *Nuclear clusters and nuclear molecules*, Physics Reports **432** (2006) 43. (Cit. on p. 24).

[47] H. Horiuchi and K. Ikeda, *A Molecule-like Structure in Atomic Nuclei of 16O* and 10Ne*, Progress of Theoretical Physics **40** (1968) 277 (cit. on p. 24).

[48] A. N. Danilov, T. L. Belyaeva, A. S. Demyanova, S. A. Goncharov, and A. A. Ogloblin, *Determination of nuclear radii for unstable states in* ^{12}C *with diffraction inelastic scattering*, Phys. Rev. C **80** (5 2009) 054603 (cit. on pp. 24, 26, 29).

[49] E. P. Gross, *Structure of a quantized vortex in boson systems*, Il Nuovo Cimento (1955-1965) **20** (1961) 454 (cit. on p. 24).

[50] E. Uegaki, S. Okabe, Y. Abe, and H. Tanaka, *Structure of the Excited States in 12C.* Progress of Theoretical Physics **57** (1977) 1262. (Cit. on p. 25).

[51] M. Chernykh, H. Feldmeier, T. Neff, P. von Neumann-Cosel, and A. Richter, *Structure of the Hoyle State in* ^{12}C, Phys. Rev. Lett. **98** (3 2007) 032501 (cit. on pp. 25, 26).

[52] Y. Kanada-En'yo and H. Horiuchi, *Structure of Light Unstable Nuclei Studied with Antisymmetrized Molecular Dynamics*, Progress of Theoretical Physics Supplement **142** (2001) 205. (Cit. on p. 26).

[53] Y. Kanada-En'yo, *The Structure of Ground and Excited States of* ^{12}C, Progress of Theoretical Physics **117** (2007) 655. (Cit. on p. 26).

[54] E. Epelbaum, H. Krebs, T. A. Lähde, D. Lee, and U.-G. Meißner, *Structure and Rotations of the Hoyle State*, Phys. Rev. Lett. **109** (25 2012) 252501 (cit. on pp. 27, 28).

[55] I. Brida, S. C. Pieper, and R. B. Wiringa, *Quantum Monte Carlo calculations of spectroscopic overlaps in* $A \leq 7$ *nuclei*, Phys. Rev. C **84** (2011) 024319 (cit. on p. 28).

[56] J. Carlson, S. Gandolfi, F. Pederiva, S. C. Pieper, R. Schiavilla, K. E. Schmidt, and R. B. Wiringa, *Quantum Monte Carlo methods for nuclear physics*, Rev. Mod. Phys. **87** (2015) 1067 (cit. on p. 28).

[57] J. Carlson, S. Gandolfi, F. Pederiva, S. C. Pieper, R. Schiavilla, K. E. Schmidt, and R. B. Wiringa, *Quantum Monte Carlo methods for nuclear physics*, Rev. Mod. Phys. **87** (3 2015) 1067 (cit. on p. 28).

[58] A. C. Dreyfuss, K. D. Launey, T. Dytrych, J. P. Draayer, and C. Bahri, *Hoyle state and rotational features in Carbon-12 within a no-core shell-model framework*, Physics Letters B **727** (2013) 511. (Cit. on p. 29).

[59] R. Smith, T. Kokalova, C. Wheldon, J. E. Bishop, M. Freer, N. Curtis, and D. J. Parker, *New Measurement of the Direct* 3α *Decay from the* ^{12}C *Hoyle State*, Phys. Rev. Lett. **119** (13 2017) 132502 (cit. on pp. 30, 35–37, 116, 124–126, 130, 152, 159, 177).

[60] R. Dalitz, *CXII. On the analysis of* τ*-meson data and the nature of the* τ*-meson*, The London, Edinburgh, and Dublin Philosophical Magazine and Journal of Science **44** (1953) 1068 (cit. on p. 32).

[61] M. G. Holloway and B. L. Moore, *The disintegration of* ^{14}N *and* ^{15}N *by deuterons*, Physical Review **58** (1940) 847 (cit. on p. 34).

[62] M. Freer, A. H. Wuosmaa, R. R. Betts, D. J. Henderson, P. Wilt, R. W. Zurmühle, D. P. Balamuth, S. Barrow, D. Benton, Q. Li, Z. Liu, and Y. Miao, *Limits for the 3 α branching ratio of the decay of the 7.65 MeV, 0_2^+ state in* ^{12}C, Phys. Rev. C **49** (4 1994) R1751 (cit. on p. 35).

[63] A. Raduta, B. Borderie, E. Geraci, N. Le Neindre, P. Napolitani, M. Rivet, R. Alba, F. Amorini, G. Cardella, M. Chatterjee, E. De Filippo, D. Guinet, P. Lautesse, E. La Guidara, G. Lanzalone, G. Lanzano, I. Lombardo, O. Lopez, C. Maiolino, A. Pagano, S. Pirrone, G. Politi, F. Porto, F. Rizzo, P. Russotto, and J. Wieleczko, *Evidence for α-particle condensation in nuclei from the Hoyle state deexcitation*, Physics Letters B **705** (2011) 65. (Cit. on p. 35).

[64] T. K. Rana, S. Bhattacharya, C. Bhattacharya, S. Kundu, K. Banerjee, T. K. Ghosh, G. Mukherjee, R. Pandey, P. Roy, V. Srivastava, M. Gohil, J. K. Meena, H. Pai, A. K. Saha, J. K. Sahoo, and R. M. Saha, *Estimation of direct components of the decay of the Hoyle state*, Phys. Rev. C **88** (2 2013) 021601 (cit. on p. 35).

[65] O. S. Kirsebom, M. Alcorta, M. J. G. Borge, M. Cubero, C. A. Diget, L. M. Fraile, B. R. Fulton, H. O. U. Fynbo, D. Galaviz, B. Jonson, M. Madurga, T. Nilsson, G. Nyman, K. Riisager, O. Tengblad, and M. Turrión, *Improved Limit on Direct α Decay of the Hoyle State*, Phys. Rev. Lett. **108** (20 2012) 202501 (cit. on pp. 35, 37).

[66] D. Dell'Aquila, I. Lombardo, G. Verde, M. Vigilante, L. Acosta, C. Agodi, F. Cappuzzello, D. Carbone, M. Cavallaro, S. Cherubini, A. Cvetinovic, G. D'Agata, L. Francalanza, G. L. Guardo, M. Gulino, I. Indelicato, M. La Cognata, L. Lamia, A. Ordine, R. G. Pizzone, S. M. R. Puglia, G. G. Rapisarda, S. Romano, G. Santagati, R. Spartà, G. Spadaccini, C. Spitaleri, and A. Tumino, *High-Precision Probe of the Fully Sequential Decay Width of the Hoyle State in* ^{12}C, Phys. Rev. Lett. **119** (13 2017) 132501 (cit. on pp. 35, 37).

[67] R. Smith, M. Gai, M. W. Ahmed, M. Freer, H. O. U. Fynbo, D. Schweitzer, and S. R. Stern, *Stringent upper limit on the direct* 3α *decay of the Hoyle state in* ^{12}C, Phys. Rev. C **101** (2 2020) 021302 (cit. on pp. 35–37, 159).

[68] T. Rana, S. Bhattacharya, C. Bhattacharya, S. Manna, S. Kundu, K. Banerjee, R. Pandey, P. Roy, A. Dhal, G. Mukherjee, V. Srivastava, A. Dey, A. Chaudhuri, T. Ghosh, A. Sen, M. Asgar, T. Roy, J. Sahoo, J. Meena, A. Saha, R. Saha, M. Sinha, and A. Roy, *New high precision study on the decay width of the Hoyle state in 12C*, Physics Letters B **793** (2019) 130. (Cit. on pp. 35–37).

[69] J. Bishop, G. V. Rogachev, S. Ahn, E. Aboud, M. Barbui, A. Bosh, C. Hunt, H. Jayatissa, E. Koshchiy, R. Malecek, S. T. Marley, E. C. Pollacco, C. D. Pruitt, B. T. Roeder, A. Saastamoinen, L. G. Sobotka, and S. Upadhyayula, *Almost*

medium-free measurement of the Hoyle state direct-decay component with a TPC, Phys. Rev. C **102** (4 2020) 041303 (cit. on pp. 35, 37, 130, 159).

[70] J. Sakurai and J. Napolitano, *Modern Quantum Mechanics*, Cambridge University Press, 2017. ISBN: 9781108422413 (cit. on p. 36).

[71] University of Cologne, *Accelerators at the Institute for Nuclear Physics*. Accessed: 2024-07-06. 2021 (cit. on p. 38).

[72] A. Wendt, J. Taprogge, P. Reiter, P. Golubev, H. Grawe, S. Pietri, and e. a. Boutachkov, *Isospin symmetry in the sd shell: Transition strengths in the neutron-deficient sd shell nucleus* ^{33}Ar, Phys. Rev. C **90** (5 2014) 054301 (cit. on pp. 39, 40).

[73] B. Fu, K. Wolf, P. Reiter, M. Bentley, P. Coleman-Smith, S. Fox, C. Goergen, P. Golubev, I. Lazarus, C. Lorenz, D. Rudolph, L. Scruton, and S. Thiel, "Upgrade and Commissioning of the Lund-York-Cologne CAlorimeter". *GSI Scientific Report 2016*. Ed. by K. Große. Vol. 2017-1. GSI Scientific Report. GSI Scientific Report 2016, RESEARCH-NUSTAR-GS-5. 2017 pp. 190–191 (cit. on pp. 41, 47, 51, 52, 54).

[74] P. Golubev, A. Wendt, L. Scruton, J. Taprogge, D. Rudolph, P. Reiter, M. Bentley, V. Avdeichikov, P. Boutachkov, S. Fox, J. Gerl, C. Görgen, R. Hoischen, N. Kurz, B. Nara Singh, G. Pascovici, S. Pietri, H. Schaffner, M. Taylor, S. Thiel, and H. Wollersheim, *The Lund-York-Cologne Calorimeter (LYCCA): Concept, design and prototype developments for a FAIR-NUSTAR detector system to discriminate relativistic heavy-ion reaction products*, Nuclear Instruments and Methods in Physics Research Section A: Accelerators, Spectrometers, Detectors and Associated Equipment **723** (2013) 55. (Cit. on p. 44).

[75] G. Knoll, *Radiation Detection and Measurement*, 4th ed. Hoboken, NJ: John Wiley, 2010. ISBN: 978-0-470-13148-0 (cit. on pp. 44–46, 76).

[76] H. Kolanoski and N. Wermes, "8 Halbleiterdetektoren". *Teilchendetektoren: Grundlagen und Anwendungen*. Berlin, Heidelberg: Springer Berlin Heidelberg, 2016 pp. 269–383. ISBN: 978-3-662-45350-6 (cit. on pp. 45, 47).

[77] A. Örbom, J. Ahlstedt, T. Serén, I. Auterinen, P. Kotiluoto, H. Hauge, K. Östlund, T. Olafsen, A. Wu, M. Dahlbom, and S.-E. Strand, *Characterization of a double-sided silicon strip detector autoradiography system*. Medical Physics **42** (2015) 575. (Cit. on p. 45).

[78] e. a. D. Rudolph, *Technical Design Report of LYCCA*, (2008) (cit. on pp. 46, 50).

[79] D. Torresi, D. Stanko, A. Di Pietro, P. Figuera, M. Fisichella, M. Lattuada, M. Milin, A. Musumarra, M. Pellegriti, V. Scuderi, E. Strano, and M. Zadro, *Influence of the interstrip gap on the response and the efficiency of Double Sided Silicon Strip Detectors*, Nuclear Instruments and Methods in Physics Research Section A: Accelerators, Spectrometers, Detectors and Associated Equipment **713** (2013) 11. (Cit. on p. 47).

[80] K. S. Krane, *Introductory Nuclear Physics*, 3rd. New York: Wiley, 1991. ISBN: 978-0-471-80553-3 (cit. on p. 47).

[81] J. F. Ziegler, M. D. Ziegler, and J. P. Biersack, *SRIM - The stopping and range of ions in matter (2010)*, Nuclear Instruments and Methods in Physics Research B **268** (2010) 1818 (cit. on pp. 47, 50, 74).

[82] J. F. Ziegler, *INTERACTIONS OF IONS WITH MATTER*. `http://srim.org/`. Accessed: 2024-06-20. 2024 (cit. on p. 47).

[83] e. a. Tom Davinson, *Technical Design Report of AIDA*. Tech. rep. On behalf of the AIDA collaboration. University of Edinburgh, University of Liverpool, STFC Daresbury Laboratory, and Rutherford Appleton Laboratory, 2006 (cit. on p. 51).

[84] D. Braga, P. J. Coleman-Smith, T. Davinson, I. H. Lazarus, R. D. Page, and S. Thomas, "AIDA: A 16-channel amplifier ASIC to read out the Advanced Implantation Detector Array for experiments in nuclear decay spectroscopy". *2011 2nd International Conference on Advancements in Nuclear Instrumentation, Measurement Methods and their Applications*. 2011 pp. 1–5 (cit. on p. 51).

[85] mesytec GmbH & Co. KG, *MHV-4 4-Channel High Precision Bias Supply Unit Datasheet*. Accessed: 2024-06-21. 2023 (cit. on p. 52).

[86] C. J. Griffin, T. Davinson, A. Estrade, D. Braga, I. Burrows, P. J. Coleman-Smith, T. Grahn, A. Grant, L. J. Harkness-Brennan, G. Kiss, M. Kogimtzis, I. H. Lazarus, S. C. Letts, Z. Liu, G. Lorusso, K. Matsui, S. Nishimura, R. D. Page, M. Prydderch, V. H. Phong, V. F. E. Pucknell, S. Rinta-Antila, O. J. Roberts, D. A. Seddon, J. Simpson, S. L. Thomas, and P. J. Woods, "β-Decay Studies of r-Process Nuclei Using the Advanced Implantation Detector Array (AIDA)". *Proceedings of the 14th International Symposium on Nuclei in the Cosmos (NIC2016)*. 2017 (cit. on p. 53).

[87] P. J. Coleman-Smith, *Specification for the MACB*. Nuclear Physics Group STFC Daresbury UK. 2016 (cit. on p. 53).

[88] D. Laff, V. Pucknell, *et al.*, *Multi Instance Data Acquisition System (MIDAS)*, UKRI STFC Daresbury Laboratory (2023) (cit. on p. 54).

[89] C. Griffin and A. Estrade, *High data rate - Pause/Resume*. `https://elog.ph.ed.ac.uk/AIDA/30`. Accessed: 2024-07-13. 2015 (cit. on p. 54).

[90] M. Wieser and T. Coplen, *Atomic weights of the elements 2009*, Pure and Applied Chemistry **83** (2011) (cit. on p. 57).

[91] RUBION, *RBS - Rutherford Backscattering Spectrometry*. Accessed: 2024-06-19. 2024 (cit. on pp. 57, 162).

[92] F. Rademakers, P. Canal, A. Naumann, O. Couet, L. Moneta, V. Vassilev, S. Linev, D. Piparo, G. GANIS, B. Bellenot, E. Guiraud, G. Amadio, wverkerke, P. Mato, TimurP, M. Tadel, wlav, E. Tejedor, J. Blomer, A. Gheata, S. Hageboeck, S. Roiser, marsupial, S. Wunsch, O. Shadura, A. Bose, CristinaCristescu, X. Valls, R. Isemann, and K. Albertsson, *root-project/root: v6.20/06*. Version v6-20-06. 2020 (cit. on p. 60).

[93] R. Brun and F. Rademakers, *ROOT — An object oriented data analysis framework*, Nuclear Instruments and Methods in Physics Research Section A: Accelerators, Spectrometers, Detectors and Associated Equipment **389** (1997). New Computing Techniques in Physics Research V 81. (Cit. on p. 60).

[94] E. Browne and J. Tuli, *Nuclear Data Sheets for A = 239*, Nuclear Data Sheets **122** (2014) 293. (Cit. on p. 68).

[95] M. Basunia, *Nuclear Data Sheets for A = 237*, Nuclear Data Sheets **107** (2006) 2323. (Cit. on p. 68).

[96] B. Singh and E. Browne, *Nuclear Data Sheets for A = 240*, Nuclear Data Sheets **109** (2008) 2439. (Cit. on p. 68).

[97] T. Grahn, *AIDA FEE64 NON-LINEARITY TESTS*, (2010) (cit. on p. 70).

[98] P. Golubev, *Private Communication*. Lund University. 2024 (cit. on pp. 71, 75).

[99] A. Salice, *Verbesserung der Energiekalibrierung der LYCCA Si-Streifendetektoren auf Pixel-Ebene*. 2022 (cit. on p. 71).

[100] A. Salice. Private Communication. 2024 (cit. on pp. 71, 160).

[101] G. Kramberger, V. Cindro, I. Mandic, M. Mikuž, and M. Zavrtanik, *Effective trapping time of electrons and holes in different silicon materials irradiated with neutrons, protons and pions*, Jozef Stefan Institute and Department of Physics, University of Ljubljana, Jamova 39, SI-1000 Ljubljana, Slovenia (2001). Received 22 January 2001; received in revised form 3 May 2001; accepted 10 May 2001 (cit. on p. 73).

[102] P. G. M.A. Mohamed, *LYCCA Detector Profile measurement, Private Communication*. Lund University. 2024 (cit. on p. 76).

[103] J. Taprogge, *First in-beam measurements with the ΔE-E-TOF LYCCA-Array at relativistic energies*, MA thesis. University of Cologne, 2011 (cit. on p. 77).

[104] M. Răvar, *The Study of the* 3α*-Decay of* 0_2^+ *in* ^{12}C *Using the Lund-York-Cologne Calorimeter*, MA thesis. University of Cologne, 2020 (cit. on p. 78).

[105] O. Tarasov and D. Bazin, *LISE++ : design your own spectrometer*, Nuclear Physics A **746** (2004). Proceedings of the Sixth International Conference on Radioactive Nuclear Beams (RNB6) 411. (Cit. on pp. 86, 92).

[106] W. Catford, *Catkin Calculation Spreadsheet*. `https://personalpages.surrey.ac.uk/w.catford/kinematics/`. Accessed: 2024-06-16. 2019 (cit. on p. 86).

[107] C. Wheldon, *Derivations for two-body kinematics (both relativistic and non-relativistic)*. 2012 (cit. on p. 86).

[108] T. Chen and C. Guestrin, "XGBoost". *Proceedings of the 22nd ACM SIGKDD International Conference on Knowledge Discovery and Data Mining*. KDD '16. ACM, 2016 (cit. on p. 116).

[109] D. Powers and Ailab, *Evaluation: From precision, recall and F-measure to ROC, informedness, markedness & correlation*, J. Mach. Learn. Technol **2** (2011) 2229 (cit. on p. 117).

[110] S. Agostinelli *et al.*, *Geant4—a simulation toolkit*, Nuclear Instruments and Methods in Physics Research Section A: Accelerators, Spectrometers, Detectors and Associated Equipment **506** (2003) 250. (Cit. on p. 120).

[111] U. Galster, F. Baumgartner, U. Muller, H. Helm, and M. Jungen, *Experimental and quantum-chemical studies on the three-particle fragmentation of neutral triatomic hydrogen*, Physical Review A **72** (2005) 062506 (cit. on p. 123).

[112] E. Garrido, D. Fedorov, A. Jensen, and H. Fynbo, *Anatomy of three-body decay I: schematic models*, Nuclear Physics A **748** (2005) 27. (Cit. on pp. 125, 126, 130).

[113] T. Biesenbach. Private Communication. 2024 (cit. on pp. 131, 132).

[114] G. Casella and R. Berger, *Statistical Inference*, Duxbury Resource Center, 2001. ISBN: 0534243126 (cit. on pp. 137, 139, 141, 142).

[115] Y. Pawitan, *In All Likelihood: Statistical Modelling and Inference Using Likelihood*, Oxford University Press, 2001. ISBN: 9780198507659 (cit. on pp. 137, 139).

[116] E. L. Lehmann and G. Casella, *Theory of Point Estimation*, 2nd ed. Vol. 2. Springer Texts in Statistics. New York, NY: Springer, 1998. ISBN: 978-0-387-98502-2 (cit. on p. 140).

[117] S. S. Wilks, *The Large-Sample Distribution of the Likelihood Ratio for Testing Composite Hypotheses*, Annals of Mathematical Statistics **9** (1938) 60 (cit. on p. 141).

[118] G. J. Feldman and R. D. Cousins, *Unified approach to the classical statistical analysis of small signals*, Physical Review D **57** (1998) 3873 (cit. on p. 161).

[119] J. R. Tesmer and M. Nastasi, *Handbook of Modern Ion Beam Materials Analysis*, ed. by J. R. Tesmer and M. Nastasi. Pittsburg, PA: Materials Research Society, 1995. ISBN: 978-1-559-37867-3 (cit. on p. 162).

[120] M. Mayer, *SIMNRA: a simulation program for the analysis of NRA, RBS and ERDA*. Version 7.03. 2023 (cit. on p. 162).

[121] C. Zemach, *Three-Pion Decays of Unstable Particles*, Physical Review **133** (1964) B1201 (cit. on p. 172).